# THE DEVELOPMENT OF A NOVEL ELECTRO-MAGNETIC FORCE MICROSCOPE

By

JAMES FREDERICK CHARLES WINDMILL

A thesis submitted to the University of Plymouth

in partial fulfilment for the degree of

DOCTOR OF PHILOSOPHY

Department of Communication and Electronic Engineering

Faculty of Technology

**James Frederick Charles Windmill**

**The Development of a Novel Electro-Magnetic Force Microscope**

## Abstract

This thesis describes the development of a new type of Magnetic Force Microscope (MFM) probe based on a unique electromagnetic design. In addition the design, construction and testing of a new MFM system, complete in both hardware and software, is also described. The MFM allowed initial tests on prototypes of the new probe, and is to provide a base for future new probe integration. The microscope uses standard MFM micro-cantilever probes in static modes of imaging. A new computer hosted DSP control system, software, and its various interfaces with the MFM have been integrated into the system. The system has been tested using standard probes with various specimens and satisfactory results have been produced.

A novel probe has been designed to replace the standard MFM magnetic coated tip with a field generated about a sub-micron aperture in a conducting film. The field from the new probe is modelled and its imaging capability investigated, with iterative designs analysed in this way. The practical construction and potential problems therein, of the probe are also considered. Test apertures have been manufactured, and an image of the field produced when operating is provided as support to the theoretical designs. Future methods of using the new probe are also discussed, including the examination of the probe as a magnetic write mechanism.

This probe, integrated into the MFM, can provide a new method of microscopic magnetic imaging, and in addition opens a new potential method of magnetic storage that will require further research.

# List of Abbreviations

| | | |
|---|---|---|
| AFM | - | Atomic Force Microscope/Microscopy |
| CRIST | - | Centre for Research in Information Storage Technology (University of Plymouth) |
| DAQ | - | Data Acquisition (card) |
| DSP | - | Digital Signal Processor/Processing |
| eMFM | - | Electro-Magnetic Force Microscope/Microscopy |
| FEM | - | Finite Element Model |
| FIB | - | Focussed Ion Beam (milling) |
| GPIB | - | General Purpose Interface Bus |
| MFM | - | Magnetic Force Microscope/Microscopy |
| MRFM | - | Magnetic Resonance Force Microscope/Microscopy |
| MO | - | Magneto Optic |
| OBD | - | Optical Beam Deflection |
| PID | - | Proportional, Integral, Derivative (control system) |
| PZT | - | Lead (Pb) Zirconium Titanate |
| RMS | - | Royal Microscopical Society |
| SEM | - | Scanning Electron Microscope/Microscopy |
| SLM | - | Scanning Laser Microscope/Microscopy |
| SNOM | - | Scanning Near-field Optical Microscope/Microscopy |
| SPM | - | Scanning Probe Microscope/Microscopy |
| STM | - | Scanning Tunnelling Microscope/Microscopy |

# Table of Contents

# Table of Figures

# List of Tables

# Acknowledgements

I have always loved to learn and discover new things; by undertaking a PhD I was able to do this whilst also contributing my own part to science and engineering knowledge. I would like to acknowledge the following for their support during this work.

Prof. Warwick Clegg, CRIST, University of Plymouth, UK, my Director of Studies.

Dr. David Jenkins, CRIST, University of Plymouth, UK, my second supervisor.

My parents and brother for their continuing support and encouragement.

Winnie Ijomah for all her support while writing this thesis.

Glen Tunstall, Nick Fry, Kay Rydyger, Zaki Ahmed, Chibesa Chilumbu, Xinqun Liu and Amei Li, my fellow researchers at CRIST, and Simon Thorpe.

Dr. Paul Davey, CRIST, University of Plymouth, UK.

Klaus Hoffer, Vector Fields Ltd., Oxford, UK.

Prof. David Wright, School of Engineering & Computer Science, University of Exeter, UK.

The Department's technical staff, including John, Phil, Lee, David, Bill, Adrian, Bob, Sheila, and also the University technical services staff, Brian and Adrian.

The Department's administrative staff, including Barbara, Nicole, Sarah, Sue, Susan, Shirley & Jeanette.

The Engineering & Physical Sciences Research Council (EPSRC), and the Royal Society Paul Instrument Fund for financial support during this work.

# Author's Declaration

At no time during the registration for the degree of Doctor of Philosophy has the author been registered for any other University award.

This study was financed with the aid of a Research Studentship from the Engineering and Physical Science Research Council. A programme of advanced study was undertaken, which included supervised clean room machine operation instruction and an introduction to laser safety.

Relevant scientific seminars and conferences were regularly attended at which work was often presented; external institutions were visited for consultation purposes and several papers have been published, are awaiting publication, or have been submitted.

**Publications (or presentation of other forms of creative work):**

J. F. C. Windmill, W. W. Clegg, "A Novel Magnetic Force Microscope Probe Design", IEEE Transactions on Magnetics, vol. 36 (5), pp. 2984-2986 (Part 1), September 2000.

D. F. L. Jenkins, W. W. Clegg, L. He, J. Windmill, G. Tunstall, X. Liu, C. Chilumbu, A. Li, "Sensors For Dynamic Characterisation Of Magnetic Storage Systems", Sensor Review, vol. 20 (4), pp. 307-317, 2000 (invited paper).

F. Wang, N. Helian, W. W. Clegg, J. F. C. Windmill, D. Jenkins, "A current-modulating magnetic force microscope probe", Journal of Applied Physics, vol. 89 (11), pp. 6778-6780, 2001.

J. F. C. Windmill, W. W. Clegg, D. F. L. Jenkins, P. Davey, "A New Theoretical Probe for the Magnetic Force Microscope", Journal of Magnetism and Magnetic Materials, vol. 226-0, pp. 1267-1269, 2001.

W. W. Clegg, D. F. L. Jenkins, L. He, J. F. C. Windmill, N. Fry, R. Atkinson, W. R. Hendren, C. D. Wright, "A Scanning Laser Microscope System to Observe Static and Dynamic Magnetic Domain Behaviour", IEEE Transactions on Instrumentation and Measurement, vol. 51 (1), pp. 10-13, 2002.

W. Clegg, D. Jenkins, N. Helian, J. Windmill, R. Windmill, R. Atkinson, B. Hendren, C. D. Wright, "Scanning Laser Techniques For Dynamic Thermo-Magnetic Recording Onto Stationary Media", Journal of Magnetism and Magnetic Materials, vol. 249-3, pp. 42-45, 2002.

**Presentations and Conferences Attended:**

W. W. Clegg, J. F. C. Windmill, "A Novel Scanning Force Microscope Head Configuration Compatible With Vacuum Operation", Poster Presentation, CMMP 98 Conference, Manchester, UK.

J. F. C. Windmill, "A Scanning Laser Microscope System for Magnetic Imaging", Poster Presentation, Seagate '99, EPSRC Seminar, November 1999.

W. Clegg, L. He, D. Jenkins, J. Windmill, "A Magneto-Optic Scanning Laser Microscope to Characterise Static and Dynamic behaviour in Magnetic Materials", Poster Presentation, CMMP 99 Conference, Leicester, UK.

W. W. Clegg, L. He, D. F. L. Jenkins, J. F. C. Windmill, "A Magneto-Optic Scanning Laser Microscope Facility for the Time-Resolved Examination of Domain Dynamics", Poster Presentation, FOM 2000 Conference, Shirahama, Japan.

W. W. Clegg, D. F. L. Jenkins, L. He, J. F. C. Windmill, N. Fry, "A Scanning Laser Microscope System to Observe Static and Dynamic Magnetic Domain Behaviour", Oral Presentation, IEEE IMTC 2000 Conference, Baltimore, USA. Published in Proceedings of the 17th IEEE IMTC, vol. 2, pp. 559-561, 2000.

J. F. C. Windmill, W. W. Clegg, "A Novel Magnetic Force Microscope Probe Design", Oral Presentation, IEEE InterMag 2000 Conference, Toronto, Canada.

W. W. Clegg, D. F. L. Jenkins, J. F. C. Windmill, "A Magnetic Force Microscope Incorporating a Controllable Electromagnetic Probe", Oral Presentation, EPSRC Non-linear Magneto-Optics Meeting, University of Leeds, June 2000.

J. F. C. Windmill, W. W. Clegg, D. F. L. Jenkins, P. Davey, "A New Theoretical Probe for the Magnetic Force Microscope", Poster Presentation, ICM 2000 Conference, Recife, Brazil.

W. W. Clegg, L. He, D. F. L. Jenkins, J. F. C. Windmill, N. Fry, R. Atkinson, C. D. Wright, "Dynamic Thermo-Magnetic Recording using a Magneto-Optic Scanning Laser Microscope on Stationary Media", Oral Presentation, PELS 2000, Southampton, 2000.

J. F. C. Windmill, W. W. Clegg, D. F. L. Jenkins, P. J. Davey, "Next Generation Magnetic Force Microscope Probe Design?", Poster Presentation, CMMP 2000 Conference, Bristol, UK.

W. W. Clegg, R. Windmill, J. Windmill, D. F. L. Jenkins, N. Helian, R. Atkinson, C. D. Wright, "A Magneto-Optic Scanning Laser Microscope to Simulate the Write Process of a Magneto-Optical Drive", Poster Presentation, CMMP 2000 Conference, Bristol, UK.

F. Wang, N. Helian, W. W. Clegg, J. F. C. Windmill, D. Jenkins, "A current-modulating magnetic force microscope probe", Oral Presentation, IEEE-MMM 2001 Conference, San Antonio, USA.

Warwick Clegg, David Jenkins, Na Helian, James Windmill, Robert Windmill, Ron Atkinson, Bill Hendren, C David Wright, "Scanning Laser Techniques For Dynamic Thermo-Magnetic Recording Onto Stationary Media", Oral Presentation, IMST 2001, Grenoble, France.

W. Clegg, D. Jenkins, N. Helian, J. Windmill, R. Windmill, R. Atkinson, B. Hendren, C. D. Wright, "Real-Time Synchronous Observation of Switching Dynamics in Magneto-Optical Media", Oral Presentation, 12th Annual Symposium on Information Storage and Processing Systems (2001), Santa Clara, USA.

J. F. C. Windmill, W. W. Clegg, D. F. L. Jenkins, P. J. Davey, "An Electromagnetic Read/Write MFM Probe", Oral Presentation, 12th Annual Symposium on Information Storage and Processing Systems (2001), Santa Clara, USA.

W. W. Clegg, D. F. Jenkins, N. Helian, J. Windmill, R. Windmill, "Versatile optical system for static and dynamic thermo-magnetic recording using a scanning laser", Oral Presentation, Optical Metrology Roadmap for the Semiconductor, Optical, and Data Storage Industries Conference (part of SPIE's 46th Annual Meeting - 2001), San Diego, USA. Published in Proceedings of SPIE, vol. 4449, pp. 205-211, 2001.

D. Jenkins, W. Clegg, J. Windmill, G. Tunstall, S. Edmund, C. D. Wright, D. Newman, R. Atkinson, B. Hendren, M. Loze, P. Nutter, "Advanced Optical and Magneto-Optical Recording Techniques", Invited Presentation, 13th Annual Symposium on Information Storage and Processing Systems (2002), Santa Clara, USA.

External Contacts:

Prof. C. D. Wright, University of Exeter.

Prof. J. Pethica, University of Oxford.

Date 18/10/02 Signed J. Windmill

# 1 Introduction to Microscopic Magnetic Imaging

## *1.1 The Need for Magnetic Microscopy*

Computer technology has been a growth industry for the last several decades. This has led to a huge demand for data storage devices, the most common of which are those based on magnetic principles. A number of companies are in competition, fighting for their share of the profits that can be made. This has led to enormous pressure within the market to improve and innovate. Because of this, research into magnetic media and systems has expanded rapidly in all areas.

Magnetic recording requires the positioning of a domain of a certain size and orientation on the magnetic layer of a disk. This orientated domain corresponds to a 'bit' of written information, which must maintain this state until it is rewritten. To produce data storage systems with greater capacity and faster access times, domain imaging instruments have had to be refined and developed to further our understanding of the underlying physical mechanisms. Thus the main area that has provided the impetus for the development of magnetic microscopy from an interesting research concept to a practical commercial instrument is magnetic data storage. The continuing effort to increase data density has led to commercially available densities of 48.8 $Gb/in^2$, i.e. 2.5" drive platter capacity of 30GB, with research levels now reaching 100 $Gb/in^2$ [1] [2]. Current discussions regard 1 $Tb/in^2$ as a potential target in the near future [3]. As a result, the imaging instruments used in data recording research have had to improve, especially in terms of spatial resolution. A large amount of research continues into this field, in both the theoretical and practical issues.

## *1.2 Magneto-Optic Imaging Methods*

The interaction between magnetic media and electromagnetic radiation allows the creation of an image of the magnetisation state of a sample. The magneto-optical effects were

discovered by Michael Faraday (transmission through a material) and Rev J C Kerr (reflection from a material), as shown in Figure 1 [4] [5].

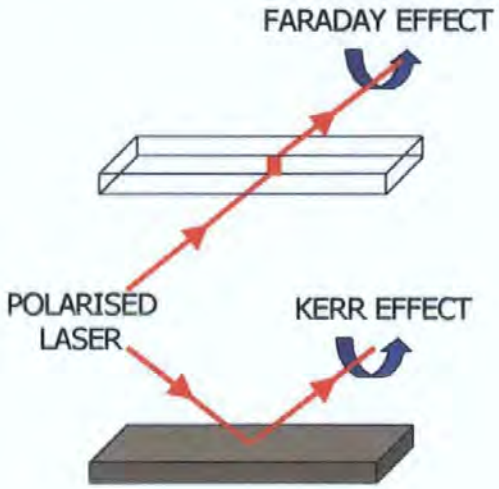


**Figure 1. Kerr and Faraday Magneto-Optic Effects.**

The basic premise is that the plane of polarised light is rotated when it is reflected from, or passes through a magnetic material. Both of these magneto-optic effects are accounted for by the same inherent material properties, however it is convention that reflection effects are known as the Kerr effects, and transmission effects as Faraday effects.

### *1.2.1 Far-Field Imaging*

Conventional optical microscopy (far-field) generally consists of a system of lenses that focus light reflected from a sample into a virtual, magnified image. This type of system can be used to utilise the effects described in Section 1.2. One example of this is a Scanning Laser Microscope (SLM), where the sample illumination is confined to a diffraction limited spot on the surface of the sample (or even within the sample) [6] [7]. The laser is scanned point by point in a raster across the sample, and the image built up electronically, pixel by pixel, from a signal derived from suitable photo-detectors. Laser scanning can be accomplished using either an XY table to move the sample under the laser, or by beam scanning optics, e.g. galvanometer scan mirrors. When using these effects,

different laser imaging modes can be selected according to the application to acquire different information. For example, a pulsed laser could be used for time-resolved imaging of domain wall motion [8]. By changing the power of a laser, and producing a pulse, Thermo-Magneto-Optic writing can be accomplished [9]. Imaging can be via photo-detector with various configurations (point by point imaging), or use of a CCD camera to capture either still frame images of the sample, or moving images of domain changes, although these would generally require illumination of the entire sample (full-field illumination) [10].

### *1.2.2 Near-Field Imaging*

One of the latest developments in optical imaging is the near-field microscope. In the late 19th century, the German Ernst Abbe and the Englishman Lord Rayleigh introduced a concept that is known as the diffraction limit of spatial resolution. This fundamental law states that with light, as with any other wave phenomenon used for microscopy, it is not possible to resolve spatial details that are located closer together than approximately half of the probing wavelength. This is described by the Rayleigh criterion equation,

$$d = 0.61\frac{\lambda}{NA}$$

where, $NA$ is the numerical aperture of the microscope objective lens, $\lambda$ is the wavelength of the illuminating source and $d$ is the resolving distance [11]. This occurs when a 26.5% dip in brightness appears between the two details, a value adopted as the general Rayleigh criterion for the resolution of two points in a conventional optical system, based on the ability of the human eye to distinguish differences in illumination intensity. For optical microscopy, typically operating at a wavelength of 500 nm (the visible spectrum ranges from 400 nm to 700 nm), the spatial resolution is thus limited to about 250 nm, although this is not strictly true for electronic and confocal imaging systems. A method to improve

this resolution to below 50 nm using an optical aperture was first discussed by Synge in 1928 [12]. This eventually developed into the Scanning Near-field Optical Microscope (SNOM), which is based on the premise that, for a given illuminating wavelength, only low spatial frequency information can propagate away from the object, whilst high spatial frequency information is contained in evanescent wave components. The amplitudes of these evanescent components decay exponentially away from the object. So, by probing into the near-field of a sample, i.e. within a small fraction of a wavelength away from its surface, these components can be detected with a resolution beyond the diffraction limit, as demonstrated by Betzig and Trautman in 1992 [13].

**Figure 2. SNOM Probe mounted on tuning fork for Shear-Force control.**



A SNOM system brings a small optical probe, as shown in Figure 2, very close to the sample surface, into the near-field region. This is usually a tapered optical fibre, with a very small aperture at its end, for example less than 100 nm in diameter, or an apertured Scanning Probe Microscopy (SPM) probe [14] [15]. Magnetic images can be created using the effects discussed in 1.2, with resolutions as low as 30 nm reported [16]. However, there are practical problems as the optical fibre aperture, and following optical system, can affect the polarisation of the imaging light [17]. To control the height of the probe above

the surface, typically 10 nm, a Shear-Force method can be used. In simple terms this is where the probe is resonated with a minute amplitude, that interacts, possibly by Van der Waals fields, with the sample, such that the distance between the two affects the amplitude or frequency [18]. In this way a feedback signal can be derived to stabilise the probe's scanning height.

## *1.3 Scanning Probe Microscopy*

Conventional far-field optical microscopy takes a single picture of the entire sample; this has the inherent resolution problem of the spatial diffraction limit. In Scanning Probe Microscopy, where the sample is scanned point by point, attempts are made to circumvent this law. This is either done optically, using the near-field, or other aperture, techniques. Or it can be done by using the interaction of a physical probe with the sample being scanned. This was first introduced by Binnig and Rohrer, with their invention, the Scanning Tunnelling Microscope (STM) in 1982 [19]. This uses electron tunnelling between a very sharp conducting tip and a surface as a topographical imaging process with atomic resolution. This stimulated the development of other Scanning Probe Microscopes, such as the Atomic Force Microscope (AFM) and Magnetic Force Microscope (MFM), with a variety of different probes replacing the tunnelling tip to image different surface forces.

Within the Centre for Research in Information Storage Technology (CRIST), University of Plymouth, work on a new 'home-built' AFM/MFM instrument had been initiated. This required substantial development in both the hardware, and software control systems, to reach a useful level of imaging proficiency. Based upon the research application of magnetic data storage, the focus of the contribution to knowledge is novel and innovative research on a new type of microscope probe, its associated modes of operation, and the potential for probe storage.

## *1.4 Outline of this Thesis*

The areas covered in the thesis can be split into two distinctive parts. The first part covers the initial work to produce an operational MFM instrument. Chapter 2 gives an overview of magnetic force microscopes, including atomic resolution sample scanning, a review of the different methods of detecting cantilever-sample interaction, and a brief outline of the different modes of operation in a MFM. Chapter 3 describes the design and construction of the MFM system hardware, including mechanical construction, detection methods and their implementation, sample scanning and approach mechanisms and also user observation of the probe. Chapter 4 covers the instrument's computer control system and related electronics hardware. The cantilever digital feedback control system design, implementation and testing is described in particular detail. Chapter 5 deals with work on system noise and calibration, with an overview of the entire system from a user perspective and finally a discussion of possible further work. Chapter 6 is the final element of this part of the thesis. Here topographic (AFM) and magnetic results from the MFM are shown and compared with previous work.

The second part of the thesis describes the design and development of a novel type of electromagnetic (apertured) MFM probe, referred to as an eMFM. Chapter 7 covers the initial work on the idea, providing results from field models of the new probe and simulation of the interaction between the probe and a magnetic sample. Chapter 8 continues the description of the theoretical development and simulation of the new probe, with a discussion of the preliminary practical design issues, aperture design, and modelling the probe with a three-dimensional tip. Chapter 9 concludes this part of the thesis with an exploration of the first work carried out to create the new probe, and the possible future work to implement it. This begins with discussion of prototype apertures made, and shows preliminary results from practical tests on the prototypes, comparing them against the theoretical work of the previous Chapters. Then, the next generation of prototypes, made

by altering commercial SPM cantilevers, is considered and the future potential of this method discussed. Work on using the probe as a hybrid recording mechanism is briefly examined, followed finally by a brief discussion of other possible avenues of research with the new probe.

Finally, Chapter 10 summarises the main aspects of the work, highlights the principle contributions to knowledge and proposes future work on the new probe.

# 2. Review of Magnetic Force Microscopes

The Magnetic Force Microscope (MFM) is based on the Atomic Force Microscope (AFM) reported by Binnig et al. in 1987 [20]. In an AFM a small probe, whose tip is atomically sharp, is brought either into contact with a sample surface, or near contact (i.e. 10 nm), and scanned across it. The resultant deflection of the tip is recorded and used to create an image of the surface topography or close range forces, such as Van der Waals forces. The MFM is a development of this, where the tip is coated with a ferromagnetic material, and scanned several tens of nanometres from the surface of a magnetic specimen where magnetostatic (rather than Van der Waals) forces are dominant.

The MFM was first successfully reported in 1987, when Martin and Wickramasinghe imaged forces from a magnetic recording head [21]. The basic concept of a MFM system is shown in Figure 3 below. Stray magnetic fields from the surface of a sample interact with the magnetic tip, generating a force. The tip is mounted on a flexible micromachined cantilever (100-200 x 40 x 1-2 μm), and hence the cantilever deflects relative to the force applied, or the force gradient if resonating. This deflection is monitored, and an image constructed by mapping the deflection relative to the tip's position above the sample.

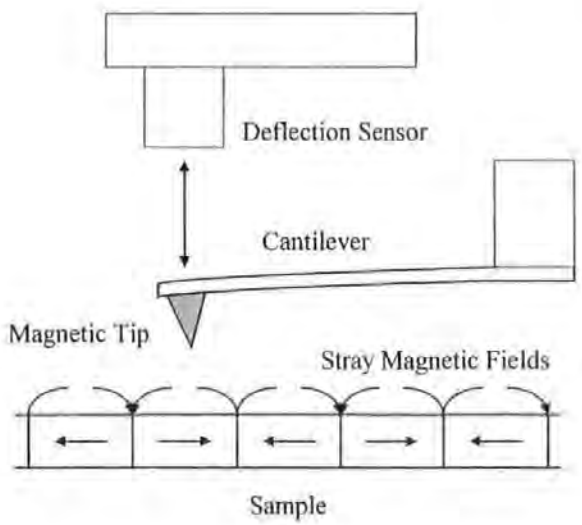


**Figure 3. The Basic Concept of MFM.**

## 2.1 *Method of Scanning*

Practically all SPMs use a piezoelectric scanner to achieve the sub-nanometre positioning required for probe or sample motion. The scanner is driven in a standard raster scan pattern, such that it moves across the first scan line, in the fast scan direction, then returns back, before stepping, in the slow scan direction, perpendicularly to the next scan line. This process is repeated until the entire image is captured. Data is sampled digitally at equally spaced intervals to create the image; this interval is the step size, usually equal to that of the slow scan direction increment. A piezoelectric is a ceramic that changes dimensions in response to an applied voltage. The scanner can be designed to move in three dimensions giving expansion and contraction in different directions. The piezoelectric material used in most SPMs is lead zirconium titanate (PZT), with various dopants to control certain properties [22].

The tube scanner design is prevalent in SPMs due to its simplicity, as shown in Figure 4. The inside and outside of the tube are coated with nickel electrodes, and the outer coating is split into four vertical segments, providing ±x and ±y motion. By applying a voltage between one of the outer segments and the inner electrode that part of the tube can be made to expand or contract depending on the voltage polarity, as is described in detail in Section 3.3.2. By grounding the internal (centre) electrode, and applying the same voltage to all four external electrodes, the tube can be made to move in the vertical (z) direction. When a voltage is applied to only a single external electrode (centre always ground), then the tube will bend in that axis. Applying the opposite voltage simultaneously to the opposite electrode can increase this motion. This bend causes the top of the tube, and so the sample, to tilt slightly, which, for a large scanning area causes a noticeable bowing effect in each scan line. The maximum scan size for a particular scanner depends on its length, wall thickness, strain coefficient and drive voltage.

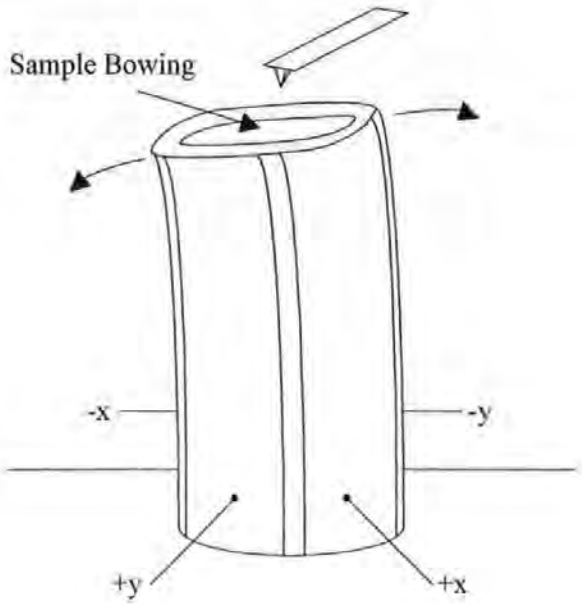


**Figure 4. PZT Tube Scanner.**

Theoretically a tube scanner's strain, i.e. change in length / original length, can be approximated as a linear relationship with the applied voltage. However, in practice the relationship has an intrinsic deviation from ideal linearity. This is shown in Figure 5, where an exaggerated s-shaped response is depicted.

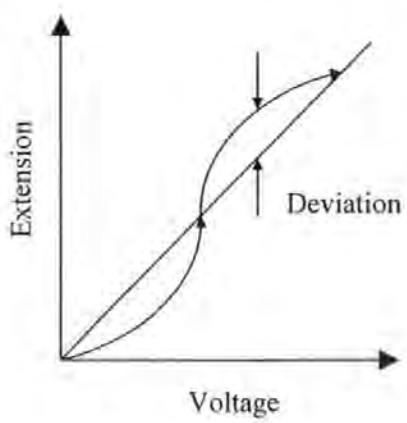


**Figure 5. PZT scanner non-linearity.**

**Typically 2-25% in SPM tube scanners, e.g. 25 nm deviation (10%) with 100 V applied.**

As the scanner motion is non-linear, so the image measurement points are unequally spaced. The non-linearity can range between 2 and 25% in SPM scanners. Different

techniques have been developed to overcome this problem, for example post imaging software correction or feedback control [23] [24].

This non-linearity is further complicated by another inherent piezoelectric problem, that of hysteresis, which can be as high as 20% in some materials. Figure 6 shows a plot of the hysteretic behaviour of the piezoelectric expansion and contraction, versus the applied voltage. This problem can be minimised by only sampling data in a single direction, as described previously.

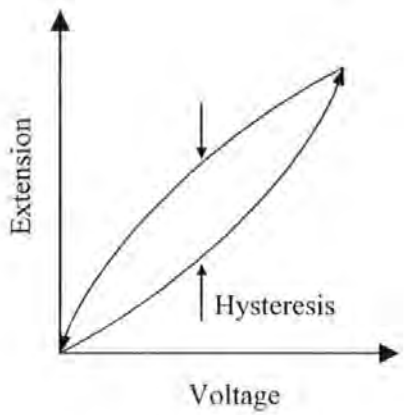


**Figure 6. PZT scanner hysteresis performance.**

**As high as 20% in SPM tube scanners, e.g. 12.5 nm deviation (5%) with 100 V applied.**

Piezoelectric material does not change shape completely when an abrupt change in voltage is applied. Rather, two marked steps in the motion occur, the first step taking place in less than a millisecond, the second on a much longer time scale. This second step is known as creep, as illustrated in Figure 7. Creep is the ratio of the second step change to the first, and is expressed as a percentage (usually quoted with the characteristic time interval $T_{CR}$ over which the creep occurs). Typical values of creep range from 1% to 20%, over times ranging from 10 to 100 seconds. The result of this is that two scans taken at different scan speeds can show slightly different length scales (magnifications) when creep is present. Therefore only measurements made at the scan speed used during calibration should be considered accurate, and hence multiple scan speed calibrations, combined with software

interpolation, or hardware scanner positioning feedback, are required to remove this non-linearity from images.

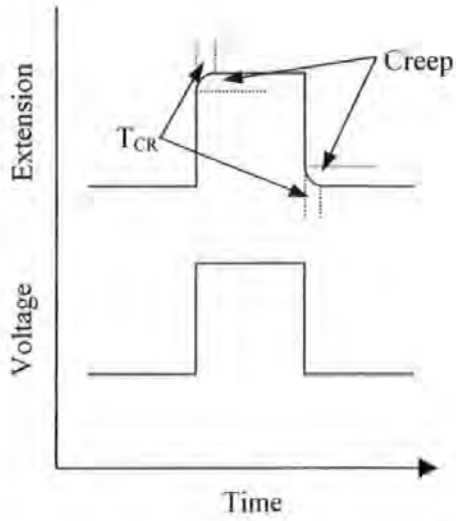


**Figure 7. PZT scanner creep.**

**Ranging from 1-20%, e.g. 50 nm creep after a 5 μm step, over 10 seconds.**

A PZT scanner also suffers from ageing, whereby the strain coefficient of piezoelectric materials changes exponentially with both time and use. This is shown in Figure 8, which shows the ageing of a piezoelectric scanner, for cases of both high and low usage. When a scanner is not used, the deflection achieved for a given voltage gradually decreases. However, if a scanner is used regularly, the deflection achieved for a given voltage actually increases slowly with use and time. These joint processes are both due to the piezoelectric material's polycrystalline structure. Each of the crystals that compose a scanner has its own dipole moment. Repeated application of voltage in the same direction, such as the voltage applied during scanning, causes more and more of the dipoles to align themselves along the axis of the scanner. The amount of deflection achieved for a given voltage depends upon how many dipoles are aligned. Thus, the more the scanner is used, the farther the scanner will travel. Conversely, if the scanner is not used, the dipole moments of the crystals will gradually become randomly oriented, i.e. depolarised. As a result, fewer dipoles contribute to the deflection of the scanner. When new, the scanner material

has already been polarised, which means that the crystals have already been exercised to the point where the deflection of the scanner is close to its maximum. The dependence of the scanner deflection on time and usage means that the scanner may not be extending the same distance for a given applied voltage as it did when it was first calibrated. As a result, when a feature on an SPM image is measured, the values of lateral and vertical dimensions may be in error.

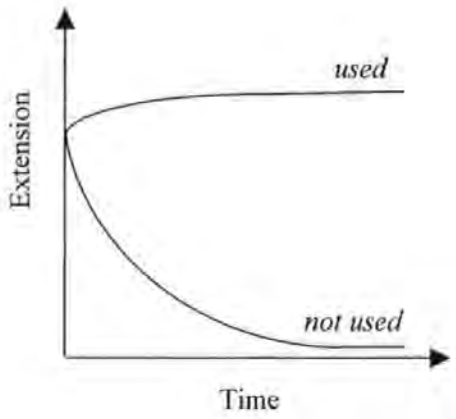


**Figure 8. PZT scanner ageing, typically μm against months.**

## *2.2 Methods of Detection*

Several different methods of detecting the deflection of the cantilever have been employed over the lifetime of AFM and MFM instrument development and implementation. These include tunnelling current, capacitance, laser diode feedback, interferometry and optical beam deflection. Each of these methods is reviewed in the following sections. This review is followed by a comparison of all the methods, and a choice of method for the instrument described in this work.

### 2.2.1 *Tunnelling Current*

This method, shown in Figure 9, is the same as using a STM to measure the deflections of the cantilever [20] [25] [26]. A bias voltage is applied between the conductive rear-side of the cantilever and tunnelling tip, so producing a tunnelling current through the air gap.

The tunnelling current density $j$ can be approximated as $j = \frac{e^2}{\hbar}\frac{\kappa_0}{4\pi^2 z}V\exp(-2\kappa_0 z)$, where $z$ is the effective tunnelling distance in Å, $V$ is the bias voltage, $e^2/\hbar = 2.44\times10^{-4}\Omega^{-1}$ and $\kappa_0$ is the inverse decay length given of the wave function density outside the surface.

This current changes according to the air gap, attributed to the deflections in the cantilever. Unfortunately the method suffers certain disadvantages. For example, the current is sensitive to which specific atom(s) the tunnelling is between, such that contamination of the cantilever or tunnelling tip can easily alter the current significantly. This can result in the image of the cantilever being imprinted on the sample image.

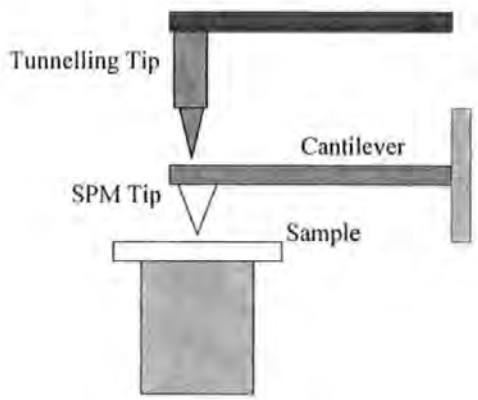


**Figure 9. Tunnelling Current Detection Method.**

### 2.2.2 *Capacitance*

The capacitance system, as shown in Figure 10, monitors the cantilever's deflections by the changes in capacitance between it and a reference plate [27] [28]. A high Q tuned circuit is used to detect the very small changes in capacitance. This method suffers from

noise due to drift in the tip-sample capacitance and also from stray capacitance; however, using capacitor transformer bridges this can be limited such that the sensitivity is determined by the drift of a reference capacitor [29]. The method is non-linear, and is easily affected by the 'local' environment, e.g. humidity, pressure and temperature, although this can be compensated for.

The current generated by the capacitance detection system is given by $i = \alpha\gamma \frac{i_0}{C} \frac{f_0}{B} \varepsilon_0 \frac{wl}{z_0^2} A\sin(\Omega t)$, where $\alpha\gamma = \sqrt{3}/8$, $C$ is the lever-reference plate capacitance whose separation is $z_0$, $f_0$ is the resonance frequency and $B$ the bandwidth of the tuned circuit, $\varepsilon_0$ is the free-space permittivity, $w$ and $l$ are the width and length of the lever, and $A$ and $\Omega$ are the amplitude and frequency of the lever.

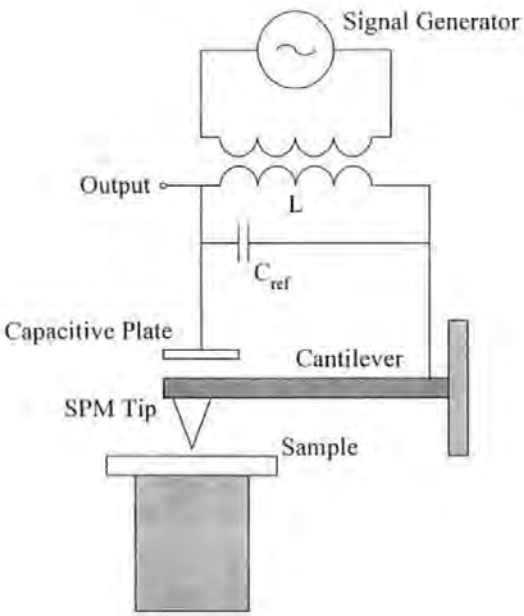


**Figure 10. Capacitance Detection Method.**

### *2.2.3 Laser Diode Feedback*

A laser diode is very sensitive to optical feedback. This can be used to detect the light reflected back from the cantilever, and hence the cantilever deflection [30]. The interference between the laser's front facet and light from the cantilever modulates the

output power of the laser, which can then be detected by monitoring the laser power at the rear facet. Whilst this method requires very few components, the optical and electronic processes occur within the laser cavity, complicating the theory behind its operation and so set up.

### *2.2.4 Interferometry - Homodyne/Heterodyne*

Both homodyne [31] [32] and heterodyne [33] [34] interferometer methods of detection have been used to detect cantilever deflections. A basic homodyne system is shown in Figure 11. A polarised laser beam passes through a beam splitter and is then incident on an optical flat, creating a reference beam, and the cantilever, creating the reflected force-sensing beam. A polarising beam splitter is used, in conjunction with a quarter-wave plate, to avoid the laser beam reflecting back to the laser, causing laser instability. The optical flat can be moved to adjust the phase between the two interfering beams. The photo-detector's output is monitored to detect the cantilever deflection. This produces an 'absolute' measure of the cantilever deflection. The method is sensitive to changes in laser power and noise, plus path length drift. It can be improved by adding a second beam splitter to monitor laser power, so producing a differential system. However, this is still susceptible to path length drift.

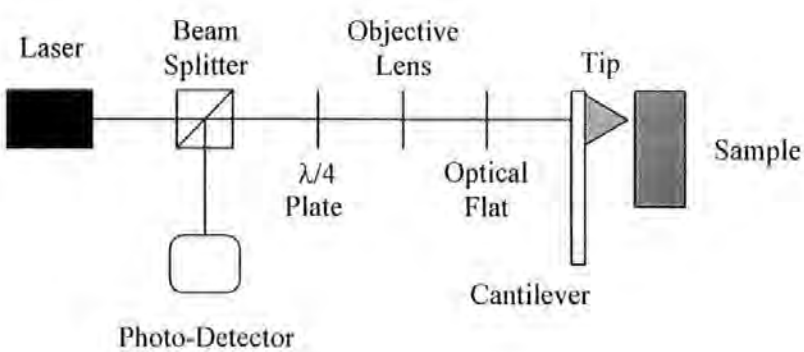


**Figure 11. Homodyne Interferometer.**

A heterodyne interferometer is shown in Figure 12. Here the laser beam is split into two components by the first beam splitter. One component is modulated using an Acousto Optic Frequency Shifter (Bragg Cell) to shift its frequency; the second component forms a reference beam remaining at the original laser frequency. The first component, the signal beam, passes through a second polarising beam splitter and a quarter-wave plate, and is then focussed onto the back of the cantilever. The reflection from the cantilever passes back through the wave plate, thus rotating a full 90°, and so is deflected by the second beam splitter. A polariser is then used as an analyser before the beam reaches the photo-detector. The reference beam passes through the second beam splitter and analyser to reach the same photo-detector. The two beams interfere at the detector, so generating a current containing a spectrum of frequencies. A single sideband receiver is then used to process this spectrum to extract the frequency of interest, thus eliminating path length drift. As such, this system requires no mechanical alignment to obtain the correct phase of the reference beam.

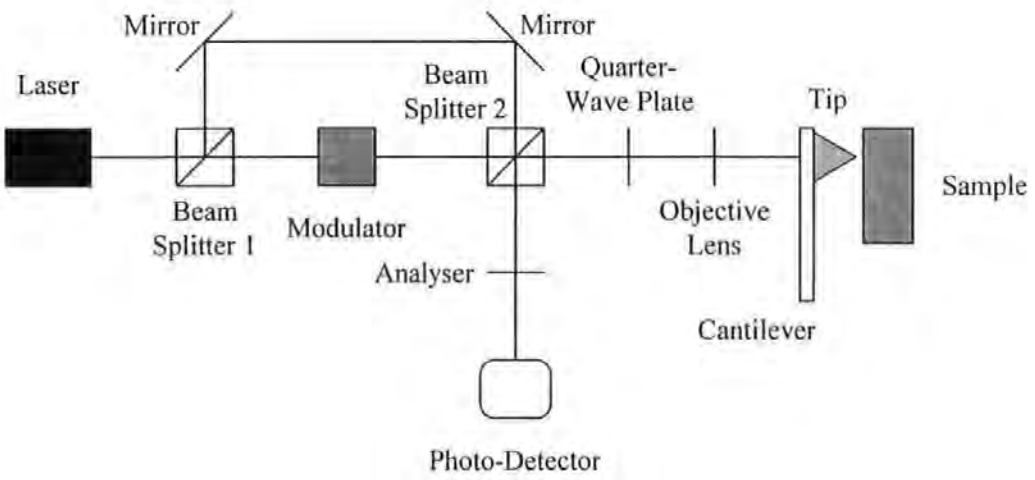


**Figure 12. Heterodyne Interferometer.**

A further interferometry technique is the dual beam homodyne interferometer. This makes a differential measurement, and so has good stability in both DC and AC measurements. Usually, one beam is focussed on the base of the cantilever, whilst a second is focussed

near the cantilever's tip. Although interferometric techniques can produce measurements of extremely high accuracy, their inherent problems are complexity and cost.

### *2.2.5 Optical Beam Deflection*

The optical beam deflection (OBD), also known as the beam bounce, detection system is shown in Figure 13 [36] [37]. A collimated laser beam is focussed onto the back of the cantilever, and reflected onto a lateral-split or quadrant photodiode. Using a lateral-split photodiode, the cantilever's deflection changes the laser position incident on the detector such that on one side of the photodiode it increases the irradiation and on the other decreases it. The current from the two halves can be connected to a differential amplifier, producing an output proportional to the cantilever deflection. This method can be augmented by using a quadrant photodiode, allowing the detection of lateral torsion in the cantilever.

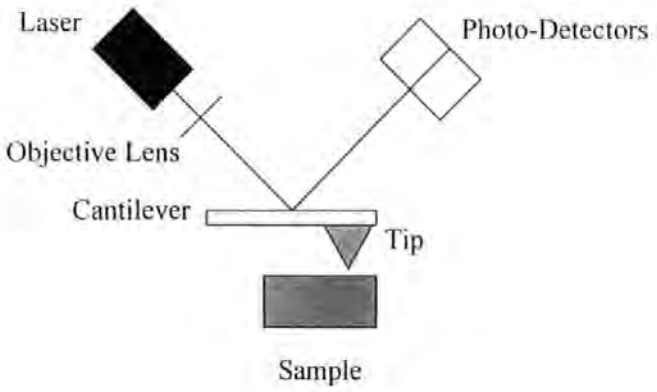


**Figure 13. Beam Deflection (Bounce) Detection Method.**

The differential nature of this arrangement reduces the effects of laser noise and power variation to a minimum. Also, as the system is only sensitive to angular deflections, it does not suffer from optical path length drift. It produces a relative measure of the cantilever's deflection, and a linear response for small displacements, as found in SPMs. Finally, the system requires relatively few components, all of which are kept at a large

distance from the cantilever allowing the safe set-up and running of the system without the risk of damage to the cantilever and its tip.

### *2.2.6 Choosing a Detection Method*

The different methods of cantilever deflection detection are compared in Table 1 below.

**Table 1. Comparison of different cantilever deflection detection methods.**

| Method | Pros | Cons | Deflection Resolution |
|---|---|---|---|
| Tunnelling Current | Resolution | Cantilever Image | $10^{-4}$ Å |
| Capacitance | | Noise, Resolution | 1 Å |
| Laser Diode Feedback | Easy to Build | Complicated Theory | 0.1 Å |
| Homodyne | Absolute Measure | Noise | 0.1 Å |
| Heterodyne | Resolution | Complicated to Build | 0.01 Å |
| Optical Beam Deflection | Easy to Build | | 0.1 Å |

As almost all the detection methods are capable of resolving sub-Angstrom deflections the choice of detection method does not depend on the resolution required. Rather, factors to be taken into consideration are ease of use, cost and the mechanical construction.

The tunnelling detection system has several intrinsic problems, as described in Section 2.2.1, and given this would not be used. The capacitance detection system requires complex electronics and is difficult to set up because of the capacitance plate's position close to the cantilever. This positioning requires complex mechanical construction and so can lead to the instrument becoming difficult to use and expensive to build.

The optical beam deflection system is the easiest to understand and implement of the optical detection methods. It provides a compact, easy to use and relatively cheap detection system that can monitor deflections as small as 0.1 Å. Therefore it was considered a good choice for a force microscope detection system. In fact, most commercial SPMs are based on this technique simply because its configuration is less sophisticated and requires few components.

## 2.3 *Modes of Operation*

Several modes of operation have been designed to detect and image the force interaction between the sample and the tip. The simplest and most straightforward method is the static or DC mode. This detects the force by measuring the static deflection of the cantilever, either when it is in 'contact' with the surface for purely topographic imaging, or scanning above the sample several 10's of nanometres to image the sample's stray magnetic fields. This mode follows Hooke's law, whereby a force causes the cantilever to be deflected by $\Delta z = \frac{F_n}{c}$, where $\Delta z$ is the deflection, $F_n$ is the force normal to the cantilever and $c$ is the cantilever's spring constant, typically 0.1 - 0.6 N/m (topographic contact mode) [38]. The minimum force that can be detected depends on the sensitivity of the deflection sensor, which is characteristically 0.1 Å, leading to a theoretical minimum force detection of 1 pN. The main inherent problem with this method for MFM is that of topographical information being captured and integrated into the magnetic information. As such it is generally only useful for samples such as computer hard drive platters as they produce relatively high magnetic stray fields that can be imaged from a scan height out of the range of the surface Van de Waals forces, e.g. 100 nm.

The second main mode is known as the resonant or AC mode, which has a much greater sensitivity, particularly to long range forces [39] [40]. This mode is accomplished by oscillating the cantilever at or near its resonant frequency and measuring the changes induced on the frequency, amplitude or phase due to the magnetic force gradient interaction. The cantilever is generally oscillated using a small piezoelectric element attached to the cantilever support structure. The force gradient changes the effective spring constant of the cantilever, and thus its mechanical response. This is normally detected in either of two ways. The first is to drive the cantilever in a feedback loop such that it remains at resonance, and therefore detect the shift in resonant frequency. This shift in the

resonant frequency ($\omega_0$), is given by the linear relationship $\Delta\omega_0 = -\frac{\omega_0}{2c}F'$, where $c$ is the spring constant and $F'$ is the force gradient. In the second mode the cantilever is driven at a constant frequency and the linear change in the detected amplitude or phase is observed. The change in amplitude ($A$) is given by $\Delta A = \frac{2A_0}{3\sqrt{3}c}\frac{\omega_0}{\gamma}F'$, where $\gamma$ is the damping factor for the medium surrounding the cantilever, and the change in phase ($\varphi$) is given by $\Delta\varphi = \frac{\omega_0}{c\gamma}F'$.

Resonant mode is by definition more complicated to apply than static mode, however its sensitivity is generally two orders of magnitude better than the static mode of operation [39]. This can be further improved by operating the cantilever in a low vacuum or low density gas (i.e. Helium), whereby the air damping effect on the resonating cantilever is reduced, and so the Q-factor increased significantly, and so sensitivity [36] [41].

A later adaptation of the resonant mode is LiftMode™, a method used in commercially available instruments manufactured by Digital Instruments [42]. An inherent problem in the use of MFMs is the influence of topography on the magnetic image. It is of course preferable to keep the topographic and magnetic data separate in order to produce enhanced magnetic images and to reveal any correlation between the sample structure and its magnetic features.

In the LiftMode™ technique, each line in the image scan is taken twice. First topographical information is taken using TappingMode™, a resonant mode of surface characterisation, in which the oscillating cantilever's tip lightly taps the surface [43]. In the second line scan magnetic force information is acquired. Here the tip is lifted to a pre-selected height above the sample. This 'lift' height is then added at each point to the previously stored topography data, ensuring that the tip-sample height is kept constant, so

preventing the tip from interacting with the surface and ensuring the sample's field is measured at a constant distance from the sample surface. This is done on every scan line to create completely separate topographic and magnetic force images of the same area of the sample. However, the method relies on the system's ability to reposition accurately the tip in the xy scan plane, while also locating the tip at the correct z position.

For the system implementation described in the following Chapters the ability to scan successfully in static mode (contact or non-contact) was considered of absolute importance, given the need to prove the concept of the novel MFM probe design that is the focus of this work. Although the system was designed with a resonant imaging capability, this was regarded as of secondary importance, given the time and labour limitations and the primary aim of the work (the novel probe). Therefore this mode has not yet been successfully implemented on the system. The system is equipped with a digital control system, described in Chapter 4, with the ability to replicate scan motion with very high accuracy, and recall height control output values. Because of this a LiftMode-like mode could be implemented, possibly using static scanning instead of the commercial resonant approach. This method is currently in the software design phase, and as of the time of writing no results are available.

# 3 Magnetic Force Microscope Hardware

## *3.1 Mechanical Construction & Vacuum*

The initial innovative SPM head specification and design shown in Figure 14 were created by Professor Warwick Clegg. The author has made some additions and alterations to the mechanical hardware, before designing the control and imaging components required to complete this system. The system is designed to be able to work under low vacuum or in a Helium environment. The benefits of vacuum operation are significant, since the removal of much of the normal viscous air damping enables a significant increase in the cantilever's effective Q-value, as operation moves into the molecular damping region (independent collisions of non-interacting air molecules) [41]. This in turn results in better resolution of images produced by resonant techniques.

**Figure 14. MFM under Vacuum Jar.**

A principle criterion of the SPM hardware was the ability to remove completely the optical head and cantilever to allow complete access to the scanner for sample exchange. The

head alignment is achieved with three screw mounted spherical ruby tooling balls locating in triangulated grooves, shown in Figure 15. Because of this kinematic design the head relocates within 1 μm when replaced. A later adaptation was the alternative of a DC-Motor to a manual screw and ball. The entire system is set on a vibration isolation table to minimise the effect of any mechanical noise from the surrounding laboratory.

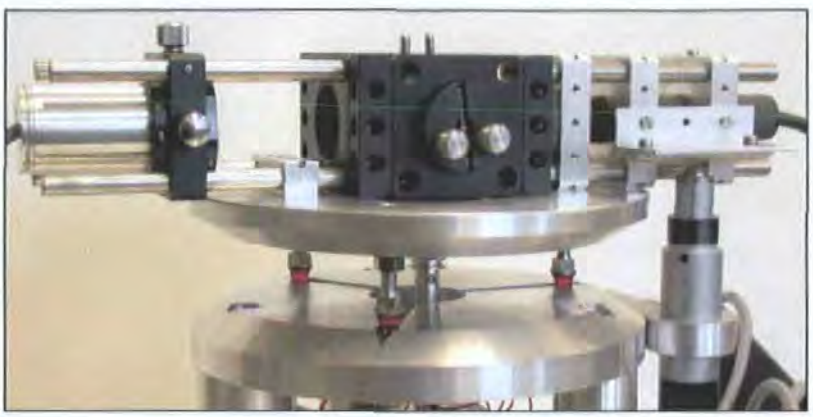

**Figure 15. Optical head showing ruby tooling balls for alignment, and DC Motor to bottom right.**

## *3.2 Cantilevers*

The cantilever and tip are the interface between the instrument and the sample, and as such form the most important part of the instrument. Standard batch-produced micro-fabricated cantilevers, commercially available at a reasonable cost, have been used in the development of this instrument. The cantilevers are fabricated on the edges of a 'chip', which then provides a base for mounting the cantilever to the SPM head. The cantilever chips are mounted onto specially designed holders using electrically-conductive silver paint. The holders bolt onto the bottom of the head such that a replacement cantilever is always located at the same inclination and position as the previous one. In this work two different sets of cantilevers have been utilised.

For contact mode imaging Silicon Nitride 'Microlever' cantilevers, produced by Park Scientific Instruments (now part of TM Microscopes (formerly Topometrix), owned by the

Veeco Group) are used. A diagram of a chip, and its cantilevers and tips is shown in Figure 16. Each chip contains four v-shaped cantilevers, two 100 μm long and two 200 μm long. The cantilevers used in this work are 0.6 μm thick providing force constants ranging from 0.032 to 0.37 N/m with resonance frequencies of 17 or 66 kHz. For the work shown in this thesis the 200 μm long, 36 μm wide cantilever is used since it provides the largest reflection area for the detection system and therefore provides the highest output signal. This cantilever has a force constant of 0.063 N/m and a resonant frequency of approximately 17 kHz. The Microlever tips are pyramidal in shape with the base of the pyramid measuring 4 x 4 μm. The radius of curvature at the end of the tip is approximately 40 nm.

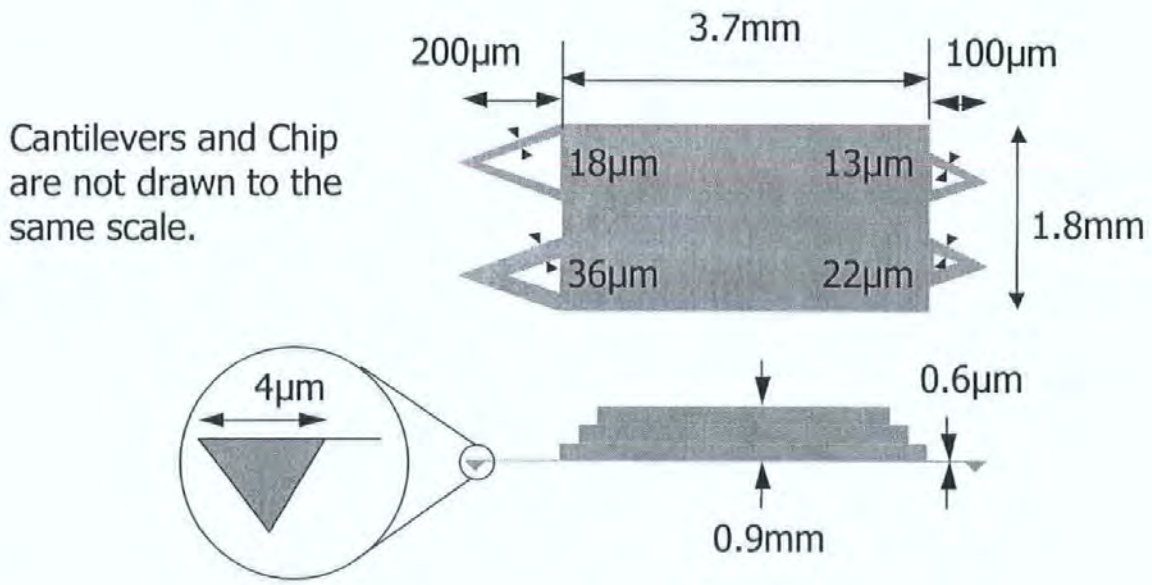


**Figure 16. Park Scientific Silicon Nitride 'Microlevers' and tips.**

In order to carry out static mode magnetic imaging, Microlever chips were sputter coated with Cobalt, with thickness ranging from 20 to 200 nm. The sputtering is performed on several chips simultaneously, which are held on a mounting plate inside the sputtering system. All four faces of the pyramidal tips were coated. The coercivity of Co is between 100 and 500 Oe. In order to magnetise the tip in a known direction, the chips were placed

between the pole pieces of a permanent magnet with a field of several thousand Oe, aligned so that the coating was magnetised along the tip axis. One of the problems with using these Microlever tips is that the cantilevers tend to bend due to the strains induced by the coating. Several levels of coating were tried, with the final MFM results shown in this thesis produced using a cantilever with a Co thickness of 50 nm, measured using the SPM.

I would like to credit and thank Mr Phil Brown for performing the coating work.

For future resonant magnetic imaging Silicon 'Ultrasharp' cantilevers (produced by MikroMasch) were purchased, as shown in Figure 17. In this case each chip contains only one bar shaped cantilever, 125 μm long (± 5 μm) and 35 μm (± 3 μm) wide. These cantilevers are typically between 1.5 and 2.5 μm thick providing force constants ranging from 1.8 to 12.5 N/m, with resonance frequencies of 110 to 220 kHz. The Ultrasharp tips are cone shaped with the base of the cone 10μm in diameter.

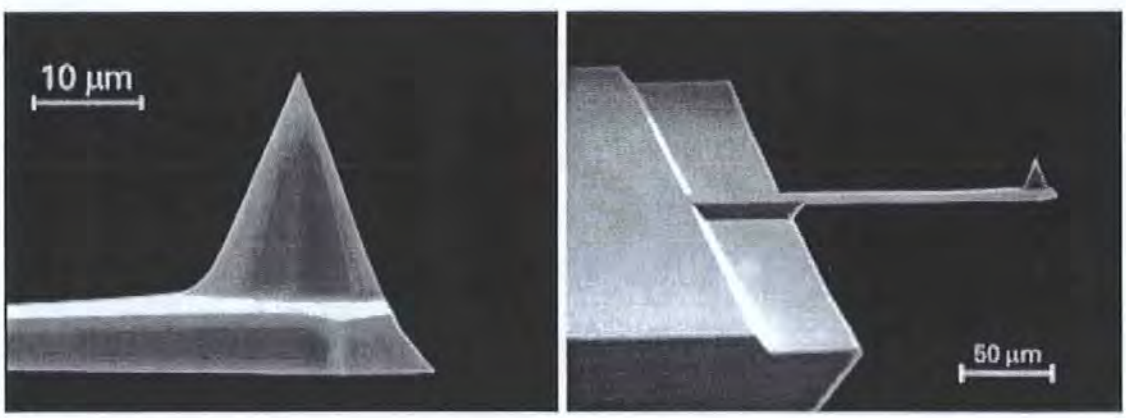


Figure 17. MikroMasch Ultralever © MikroMasch 2002.

The Ultrasharp cantilevers are supplied with a magnetic coating. This consists of a Cobalt layer of about 60 nm thickness on the tip side. The Co layer is formed as a polycrystalline film, which allows steady permanent magnetization in the direction of the tip axis. All of the chips are pre-magnetized at the factory before shipping. The Co coating is protected from oxidation by a 20 nm Chrome layer, resulting in longer cantilever lifetime. This

double coating also preserves the tip's magnetic properties when used in liquids, which is important for biological applications. The radius of curvature at the end of the tip is approximately 80 nm when coated.

## *3.3 Cantilever Detection*

The optical system used in the MFM to generate a signal relating to the movement of the probe, in this case a standard cantilever, follows an adaptation of the optical beam deflection detection form, as shown in Figure 18. A beam from a laser diode is focused onto the end of the cantilever, directed using an adjustable mirror. The laser is collimated using the diode's internal lens. The beam is then focussed using a lens mounted in a Royal Microscopical Society (RMS) focus lens attachment before the mirror. The RMS attachment, which moves the lens without rotating it, is used to reduce significantly the focal point's motion in the x-y or r-θ when focussing. A second mirror then redirects the reflected laser beam from the cantilever to a quadrant photo-detector. The reflected beam is focussed onto the detectors using a fixed collecting lens. Thus any changes in the attitude of the cantilever, due to magnetic or topographic features on the sample scanned beneath it, are indicated by a change in the photo-detector's output following a change in the path of the reflected laser beam. As the detector is made up of four quadrants, this could also be used to measure torsional motion in the cantilever. The quadrant photo-detector is located in a XY mount, so that its position can be changed using two screws on either side of it (Figure 18). This allows the reflected laser spot to be centred on the detector so that the dc offset from the differential amplifier is zero.

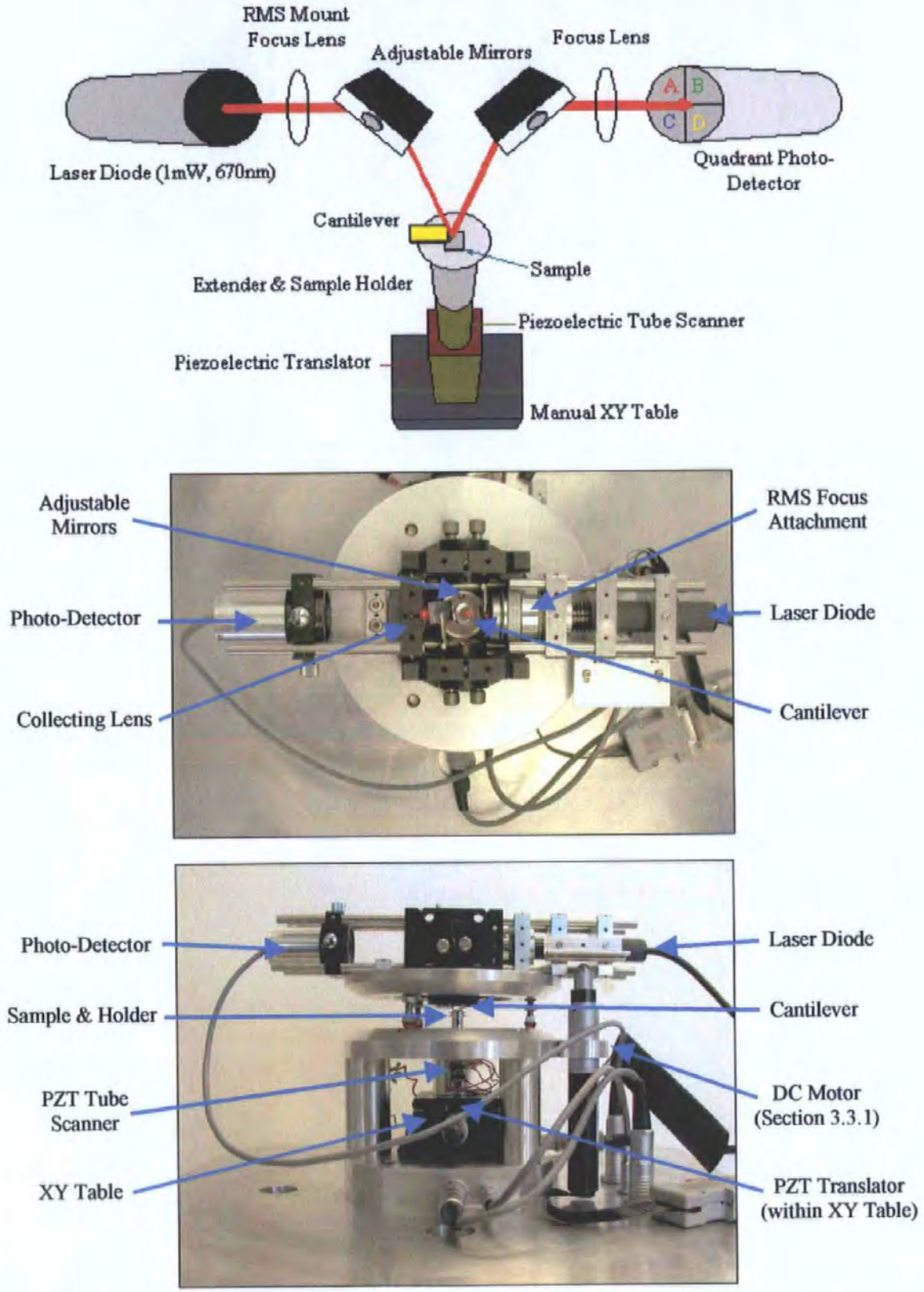


**Figure 18. Simplified diagram of MFM optical detection system and corresponding labelled photos of actual instrument, from above and side.**

A 1 mW, 670 nm laser diode, one of the Beta TX series manufactured by Vector Technology, is used in this system. This is a complete, self-contained laser diode system

that can operate in both continuous wave and modulation modes (up to 100 MHz). A high quality, aspheric collimating lens is fitted as standard, which is focussed using a simple key to prevent accidental adjustments. In the system described here the laser is collimated using its fitted lens before being focussed by the RMS mounted lens. The laser is constructed with a solid brass body that is designed to maximise heat dissipation, providing greater protection and thermal stability.

Given that the length of the cantilever is $l$, and $d$ is the distance between the cantilever and detector, then for a vertical movement of $z$ in the cantilever, the laser beam incident on the detectors will move by $2zd/l$. Thus the detection system acts as an optical lever with an amplification factor of $2d/l$. In the instrument described here the typical cantilever length is 200 μm and the distance between the cantilever and detector is 90 mm, giving an amplification factor of 900. This large amplification factor is the key to the high sensitivity of the optical beam deflection method.

In this system a Telefunken S239P quadrant photodiode detector is used. This device is particularly suitable as it has a large active area of 3 x 3 mm, with partitions between the quadrants of only 10 μm. In addition, its high sensitivity of 0.35 A/W to 670 nm light, its fast response speed of 150 ns rise and fall times, and its low noise (noise equivalent power $4 \times 10^{-14}$ W/Hz$^{1/2}$) make it a appropriate choice for this application. Figure 19 shows the circuit diagram for each of the four photodiodes, converting the photodiode current to voltage.

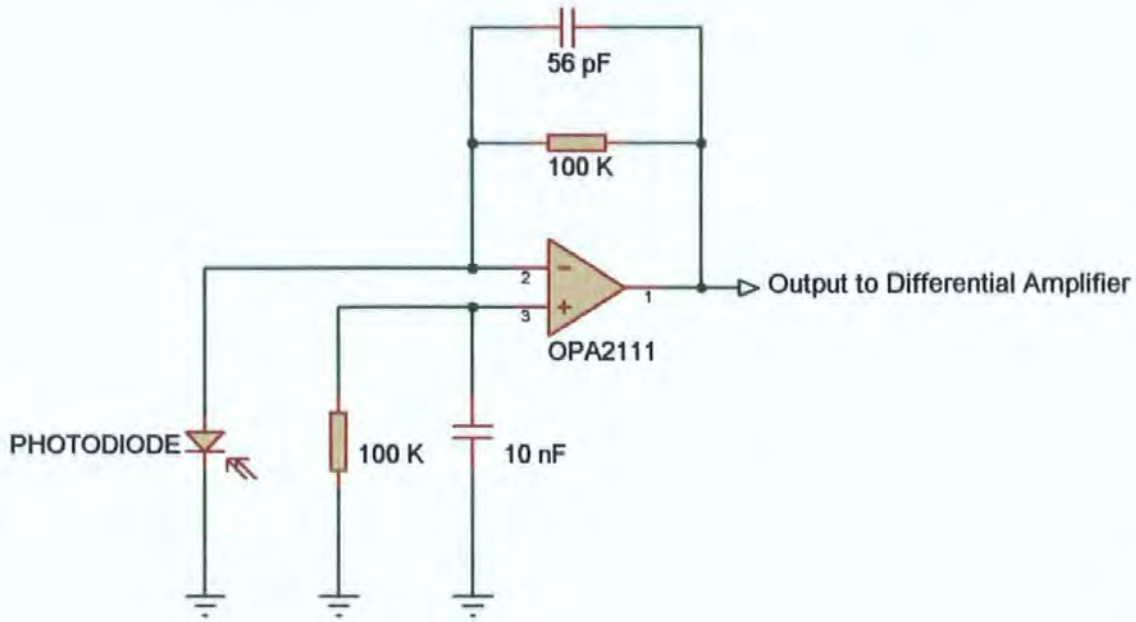


**Figure 19. Current to Voltage Converter for the Photodiode Detectors.**

The OPA2111 is a dual low noise precision DIFET operational amplifier supplied by Burr Brown. Noise (8 $nV/Hz^{1/2}$), bias current (±15 pA max), voltage offset (±500 μV max), drift (15 μV/°C max), open-loop gain (125 dB), common-mode rejection (110 dB) and power supply rejection (100 dB at 100Hz) are superior to BIFET amplifiers and its high performance characteristics are well suited to instrumentation applications.

The output voltages from the two quadrants on each half of the detector are summed together and then the difference between these two resulting voltages found, as shown in Figure 20. The output from the circuit in Figure 20 is therefore proportional to the difference in power intensity on each half of the detector.

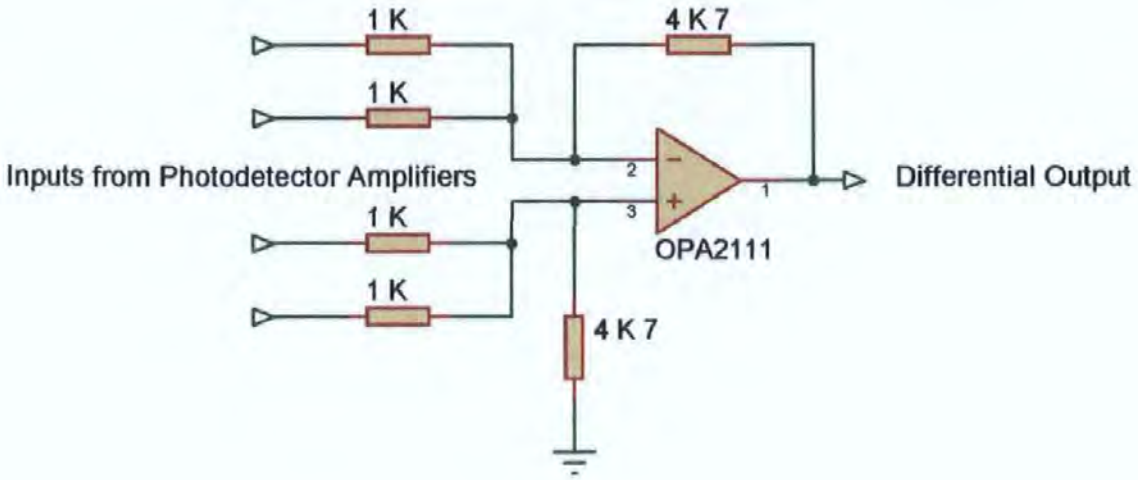


**Figure 20. Differential Amplifier for the Photodiode Detectors.**

The signal from the differential amplifier is then filtered and amplified. A second order active lowpass filter with a cut-off frequency of 20 kHz is used to eliminate any high frequency noise. This final filter circuitry is only used when imaging in static modes, resonant mode signals are dealt with using dedicated hardware, as described in the following Chapter. The final signal output is set to be between ±10 V to avoid saturation of the input to the computer data acquisition system described in Chapter 4.

## *3.4 Sample Approach and Scanning*

### *3.4.1 Sample Approach*

The system employs a two-stage vertical sample approach. The first coarse stage employs a single axis closed-loop DC-motor with a range of 10 mm and a resolution of 0.05 μm. The motor used is a Physik Instrumente M-227.10 High Resolution Closed-Loop DC-Mike Actuator. This consists of a micrometer with non-rotating tip driven by a closed-loop DC motor/gearhead combination with motor shaft mounted high-resolution encoder (2048 counts/rev). Although the motor resolution is 50 nm, the design of the MFM head is such that this is reduced considerably when considering the distance between sample and probe,

as shown in Figure 21. This shows the actual coarse approach range to be 2.857 mm, with a step size of 14.285 nm when calculated at the sample-probe interface.

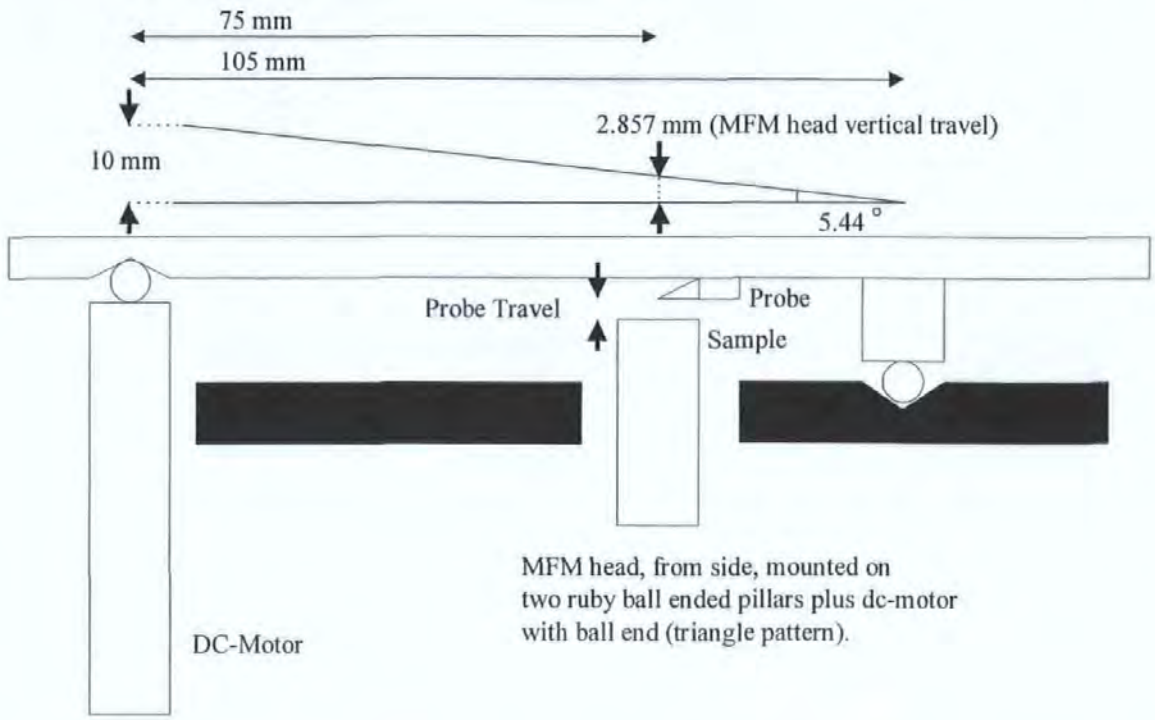


**Figure 21. Schematic of MFM head showing reduction of coarse sample approach, due to mounting of DC-Motor, to 2.857 mm, and so a step size of 14.285 nm.**

The DC-motor's controller uses a combination of small standalone PIC (Peripheral Interface Controller) microcontroller, running its own firmware, and a dedicated motion-control processor (LM629) providing high performance PID (Proportional Integral Derivative) motion control. The controller can be programmed using a set of standard ASCII commands, either via its own PC serial interface software or the LabVIEW interface written by the author. The coarse sample approach allows the user to bring the probe down to the sample until contact is detected via the optical system in 3.2. The sample can then be moved back by a pre-selected amount, e.g. 20 μm, ready for the second stage if required.

The second fine stage approach uses a piezoelectric translator (Physik Instrumente P-830.30 Open Loop Low Voltage Linear Translator) controlled using a 0-10 V analogue voltage from the controlling PC, which is buffered, then amplified by a factor of 10, to move the sample. The maximum travel provided is 0-45 μm with a voltage of 0-100 V. Thus with a single 16-bit ADC the fine approach resolution is 0.7 nm. Using a combination of control algorithm and the cantilever detection system, the sample can be moved into the required scanning position with great precision, stability and repeatability. The fine approach translator can be set to 50% prior to coarse approach, or the coarse approach DC-motor can move 'back' 20 μm, in either case allowing the fine approach translator ±50% travel.

### *3.3.2 Raster Scan*

The sample is raster scanned using a piezoelectric PZT tube scanner (PZT5H - Morgan Matroc), as described in Section 2.1, controlled by the PC's DSP data acquisition card (see Section 4.1). The scan range of the tube depends on its dimensions, material and, of course, voltage applied. Finite element analysis of these devices has been carried out by Carr [44]. From this the scanner motion in the x (y) and z axes can be described by the following equations,

$$\Delta x \approx 0.677 \frac{L^{2.066}}{D^{0.767} W^{1.086}} \tag{1}$$

$$\Delta z \approx 2.36 \frac{L^{1.005} D^{0.029}}{W^{1.01}} \tag{2}$$

where, $\Delta x$ is the extension in the x (or y) direction in Å/V, $\Delta z$ is the extension in z (Å/V), $L$ is the tube length (mm), $D$ is the tube diameter (mm), and $W$ is the wall thickness of the tube (mm). The tube scanner in use in the MFM has the following dimensions:

$L = 25.4$ mm, $D = 6.53$ mm, $W = 0.51$ mm.

So from Equation 1, the x and y deflection of the tube would be approximately 266.4 Å/V, and from Equation 2 the z movement would be approximately 127 Å/V.

The voltages applied by the control system have maximum limits of ±100 V. Therefore, if a voltage of 100 V were applied to a single quadrant electrode on the tube, the resulting deflection would be 2.664 μm. However, the tube scanner is connected with the inside electrode at ground and the four external quadrants each separately driven to ±100 V. These are configured so that opposite quadrants have opposite voltages, i.e. when the positive x-axis electrode is at 50 V, then the negative x-axis electrode is at –50 V. This in effect doubles the tube movement, and also, since each of the electrodes varies between 100 V and –100V, the actual maximum on each axis is four times 2.664 μm, or 10.656 μm. The scan resolution is governed by the DACs used in the system, as described in Section 4.1.2. These are 16-bit, and so over a range of ±100 V (amplified from ±10 V), the minimum voltage step is 3.05 mV, which at 266.4 Å/V is a scan step of four times 0.813 Å, therefore 3.25 Å.

As the tube is scanned in both x and y, one side of the tube contracts and the other side expands. This causes a tilt in the top of the tube, and so causes the sample to tilt. When imaging the sample directly above the tube's centre this tilt will not cause any movement in the z direction. However, when the image area of the sample is off-centre there will be a certain amount of z motion. When scanning at maximum range, with a voltage of ±100 V, the amount of expansion (or contraction) will be 200 V x 127 Å/V = 2.54 μm, at the tube's edge, reducing linearly to zero at the centre axis. Because this z movement is large compared with cantilever deflections due to surface features, it can cause the output signal to saturate, and so must be dealt with using feedback, described in Section 4.4. The tube scanner can be extended in the z direction by applying the same voltage to all four

quadrants. Each quadrant has a maximum limit of ±50 V applied for z movement, so the z range is therefore 1.27 μm.

In the system described here, the tube scanner has a passive extender 12 mm in length (including sample holder) mounted on top, as shown in Figure 22 below. This increases the effective scan range of the system from 10.656 μm to 15.77 μm, with a corresponding decrease in step resolution to 4.81 Å. In this system the extender and sample holder are grounded to the inside electrode, with the cantilever floating or grounded. This allows the introduction of a bias voltage (typically 1-10 V) between the cantilever and the sample, generating an attractive electrostatic force between the cantilever's tip and the sample surface. This is used because magnetic forces can be either attractive or repulsive, leading to problems with controller feedback stability when the system is operating with analogue feedback control [45] [46]. However, when using a digital feedback controller operating in LiftMode, as described in Section 2.3, the bias voltage need not be used as the controller only operates when the initial topography scan is made [47]. The sample holder is a standard SEM stub, an easily available and affordable item. Once a sample is mounted onto a stub, it is fixed on the scanner easily and quickly using an Allen key grub screw.

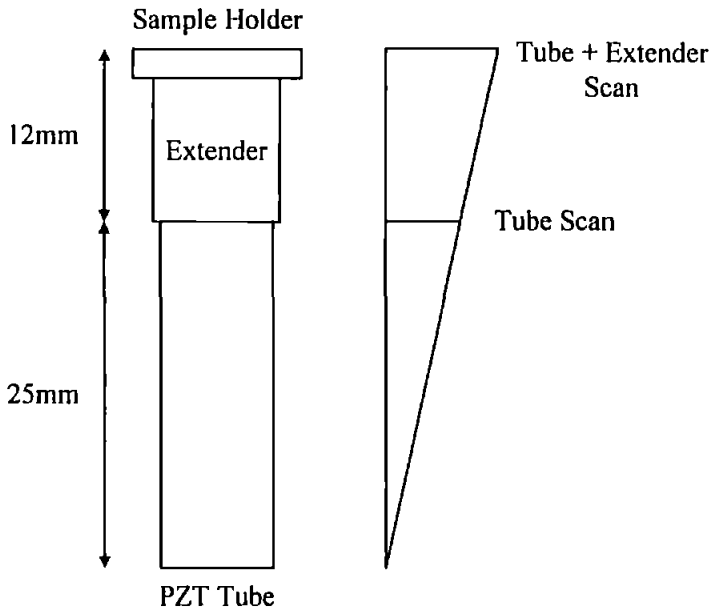


**Figure 22. Schematic of Tube Scanner with Extender.**

## *3.5 Observation*

The probe and sample can be observed using an Olympus SZ6045TR trinocular zoom stereo microscope mounted above the MFM head, utilising fibre-optic light guide illuminators, as shown in Figure 23. This provides a magnification of 30-189X using 30X eyepieces, with a working distance of 100 mm and a field of view of 1.1 mm at full magnification.

**Figure 23. Zoom Stereo Microscope above MFM head.**

It allows the operator to position the probe above the requisite sample area, and also align the first mirror so that the laser is reflected from the correct part of the probe, as shown in

Figure 24. In addition the operator can view the sample approach and scanning path to check for any problems. Finally, a Nikon CoolPix 3.34 MegaPixel CCD camera, with 4X optical zoom, can be fitted to the microscope in order to view and record both high-resolution still images and PAL video of the system in operation. To reduce the intensity of the focussed laser when viewed through the microscope a polarising filter is attached beneath the objective lenses.

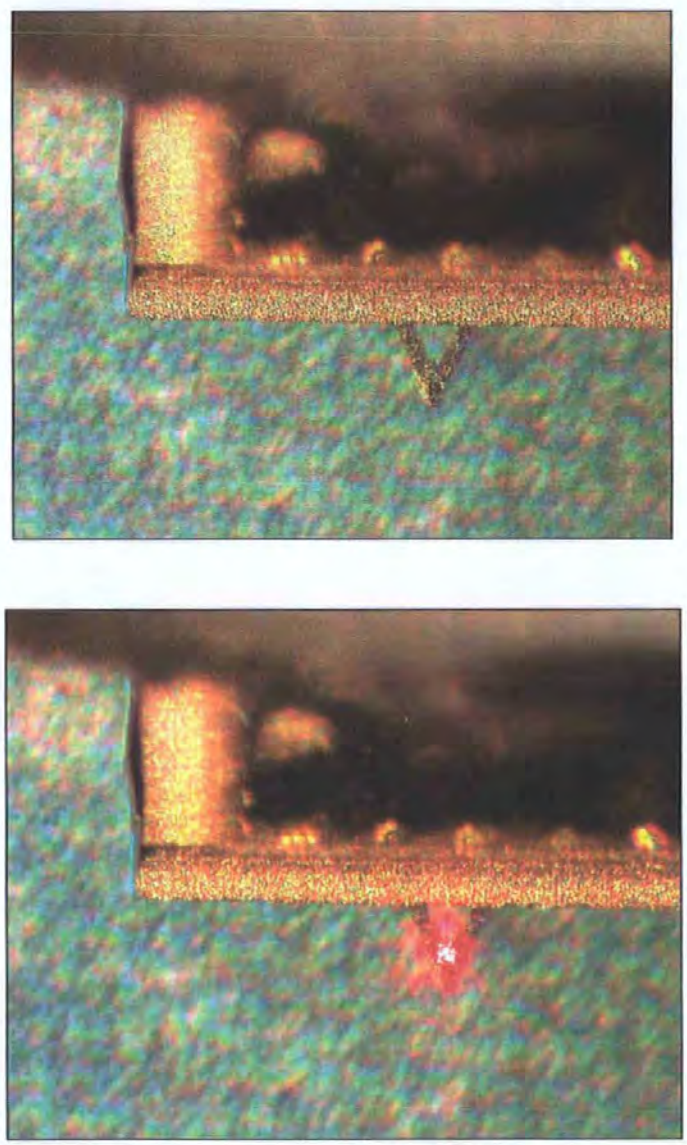

**Figure 24. Laser alignment captured by the Digital Camera via the Zoom Stereo Microscope. The top picture shows a standard probe, 200 μm length, and the bottom picture shows the same probe with the laser reflecting from its end point.**

# 4 Magnetic Force Microscope Control System

The following sections contain a detailed description of the MFM's control system. The system is largely computer-based, using plug-in cards, running as a Virtual Instrument on a PC. This is supported by other instruments, and allows for expansion, either through further internal plug-in cards or external instruments connected via a GPIB interface. A diagram of the overall system is shown below in Figure 25.

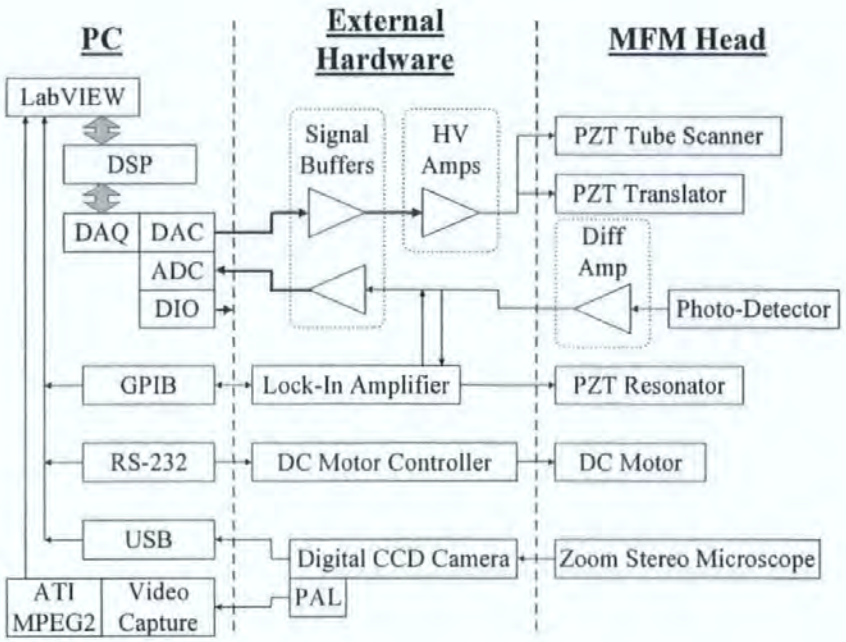


**Figure 25. Overall MFM system diagram.**

## *4.1 Computer Control*

The MFM's control system is Windows™ PC based. The control software is written using LabVIEW™ from National Instruments, interfaced using a variety of dedicated plug-in cards. The system is enhanced by the incorporation of a separate DSP board allowing time-critical control to be run separately from the host PC in a deterministic manner.

The computer has a 1 GHz AMD Athlon processor, 512 MB RAM, 64 MB accelerated graphics card and 60 GB ultra-fast hard drive. This platform was designed and built to

provide some of the fastest hardware support for the control system, with the best possible allowance for future upgrades. The computer runs a standard 32-bit Windows operating system, thus providing a platform for the widest possible range of industry-standard software and hardware. The computer is also network capable, such that in future remote Intranet/Internet operation of the system could be possible.

### *4.1.1 Digital Signal Processor - DSP*

To create a deterministic (see Section 4.4.2) control system a DSP host plug-in PCI board was used as a primary interface between the user and the system. This board, from Sheldon Instruments (USA), uses a Texas Instrument's TMS320VC33 32-bit floating point DSP IC running at 150 MHz, with 1 MB of onboard SRAM. Typical benchmarks for this DSP processor include the computation of the real portion of a 1024 point Radix-2 FFT in 400 μs. The DSP board also includes a DMA channel controller for full bi-directional PCI initiated bus mastering, with 132 MB/sec peak transfer rate and 12 MB/sec sustained transfer rate to the host PC [48].

The board was provided with all the necessary drivers, plus a library of LabVIEW Virtual Instruments (VIs) called QuVIEW. These VIs are used for implementing ultra-fast real-time processing, but with the added flexibility of using LabVIEW icons. The library of functions includes real-time data acquisition, signal processing and control, with functions for algebra, calculus, digital filtering, Z transforms, frequency domain analysis, numerical analysis, waveform generation, and process control. A program utilising these functions is thus written in LabVIEW, but downloads onto the DSP when run. This means that the DSP can continue to run, for example in a control loop, even if the host PC crashes (without power loss). As such the LabVIEW environment is used for pre and post data processing plus other auxiliary functions, whilst the DSP board runs the time-critical control of the MFM as it takes an image scan.

### *4.1.2 Data Acquisition - DAQ*

The Sheldon Instruments DSP board has a daughter board connector in addition to the normal DSP connectors, i.e. Joint Test Action Group (JTAG). This allows the connection of a data acquisition (DAQ) board, directly accessed by the DSP controller. The MFM system uses a board with 4 x 200 kHz 16-bit ADC ICs (successive approximation architecture), each with 8 multiplexed differential inputs (or 16 single-ended inputs) and a range of ±10 V, thus providing a resolution of 305 μV. All the ADCs are sampled simultaneously using a precision master clock on the DAQ board. Each ADC channel front-end has a variable gain amplifier on the input to its multiplexer. The board also includes 4 DAC ICs, each 100 kHz and 16-bit (±10 V), all simultaneously updated on the master clock and each with a low-pass linear phase smoothing filter. The DAQ board also includes a 16-bit digital IO interface (DIO).

The board can be used to sample the voltage input from the circuits following the photo-detector. Other signals could also be monitored, for example if cantilever torsion was being observed, as described in Section 3.2, all 4 voltages from the quadrant photo-detector could be sampled and analysed using the DSP. The 4 voltage outputs are used to control x and y on the PZT tube scanner, the fine z approach PZT translator, and finally a control feedback signal for the z direction of the tube scanner. The digital interface could be used, for example, to control an auxiliary external DAC.

### *4.1.3 General Purpose Interface Bus - GPIB*

The computer control system also includes a GPIB interface card. The GPIB, General Purpose Interface Bus, is an IEEE standard instrument interface based on Hewlett Packard's original HPIB system. This allows a huge variety of instruments from different manufacturers to be connected to a PC over a single bus and interface card. Typically up to fifteen instruments can be connected over 20 m, interfacing at a maximum speed of 1

Mbps (overall). However, the bus is usually slowed to the speed of the slowest instrument. In this case the GPIB card is controlled using the LabVIEW software interface, thus allowing integration of external instruments into the MFM's computer control system.

## *4.2 Instrumentation Electronics Interface*

The MFM system in general only uses a minimum of DAQ interface electronics. This limitation of the amount of electronic hardware is deliberate in order to provide for greater flexibility in the instrument by utilising the computer-based elements of the system. The DAQ interface between the computer and the rest of the microscope is shown in Figure 26.

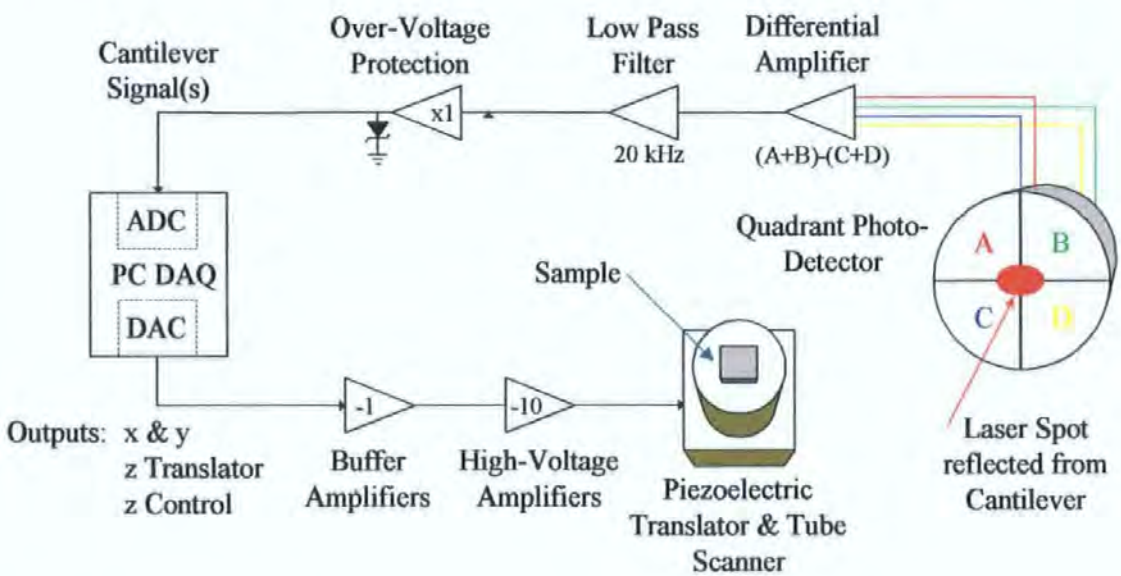


**Figure 26. Instrumentation Electronics Interface.**

The x, y and z translator outputs from the DAQ card are amplified to produce the high voltages required by the piezoelectric components. The high voltage amplifier and PSU circuits used were built by Dr P Crozier for an earlier SPM instrument [49]. As two pairs of inputs, one for x motion and one for y, drive the tube scanner, four signals are generated using a set of operational-amplifier inverter circuits with unity gain. The translator is driven from a single positive input. The control signal output is fed to all the tube scanner drivers in order to cause movement only in the z direction, (relative to the cantilever).

The outputs from the photo-detector are converted to voltage signals; a differential amplifier produces a single signal relating to the position of the cantilever, via the laser, thus eliminating common-mode noise. This signal is filtered to remove any high frequency noise then passed through over-voltage protection circuitry, protecting the inputs to the following DAQ board. Although the ADC inputs are rated to an absolute maximum of ±25 V, over-voltage protection circuitry is used as a 'better safe than sorry' policy. If using a resonant mode of operation the differential signal can be routed to the lock-in amplifier, which produces its own output to be monitored using the DAQ or GPIB.

As much care and attention as possible has been applied to the design of the electronics. In all cases low-noise high-precision instrumentation operational amplifiers have been used, i.e. the Burr Brown OPA2111. The signal paths throughout the system are all carefully shielded using core with earthing, and ground loops have been avoided. The laser diode is powered by a separate shielded PSU, with shielded power line, for maximum stability.

## *4.3 System Software*

During the early part of the research for this degree the author worked on a related magnetic imaging system, a magneto-optic SLM. Initially the instrument was almost completely constructed, but lacked a software control system. The SLM system had been built with a National Instrument's DAQ card for computer control, and the company's LabVIEW software suite purchased. The author had not used this software before, but over the early part of the PhD produced a fully working control suite for the SLM. This knowledge was therefore utilised for the MFM control system.

### *4.3.1 LabVIEW*

The MFM control instrumentation software has been implemented using National Instruments high-end graphical programming language, LabVIEW [50]. The software is

broken down into a set of functions, each known as a 'Virtual Instrument' or VI, whereby it has the potential to fulfil all the operations carried out by a standard instrument, i.e. an oscilloscope, given it has an interface to the necessary data acquisition hardware. However, whilst the software language was primarily designed as a method of virtual instrumentation, the language also provides standard programming functions.

Software is created using graphical symbols, as in Figure 27. Functions, often complex VI's in themselves, are picked from a toolbox, then using a 'drag and drop' technique, placed on the program's worksheet. The programmer builds a diagram, the program code, by picking the functions required and wiring their respective inputs and outputs together. This creates a 'dataflow' program, where the execution of the software's functions is determined by the flow of data through the diagram, not by the sequential listings of text as in standard languages. This allows the programmer to create multithreaded software code, where tasks can run in parallel. The software also supports hierarchical design, such that a programmer may create functions (sub-VIs) that can be included in others. Whilst the programmer is creating the diagrammatic code, graphical controls and indicators are created on a 'front panel'. These are automatically linked to the code created, such that after formatting the graphical front end of the software to comply with their standard, the programmer has a working Graphical User Interface (GUI), as shown in Figure 27.

LabVIEW is an easy to understand industry standard software language, and allows a novice to produce quickly working, useful, software. It claims to be equivalent in terms of processing speed to programming in C, dependent on machine, and allowing for the skill of the programmer. However, when complex functions are required the level of programming needed in order to produce viable software is increased significantly. This level can take time and considerable effort to attain. Also, given certain weaknesses in the LabVIEW environment, most notably software timing problems, the required result is not always satisfactory. In general the LabVIEW language's benefits, such as speed of

development and ease of use, outweigh its costs, such as the learning curve and timing restrictions.

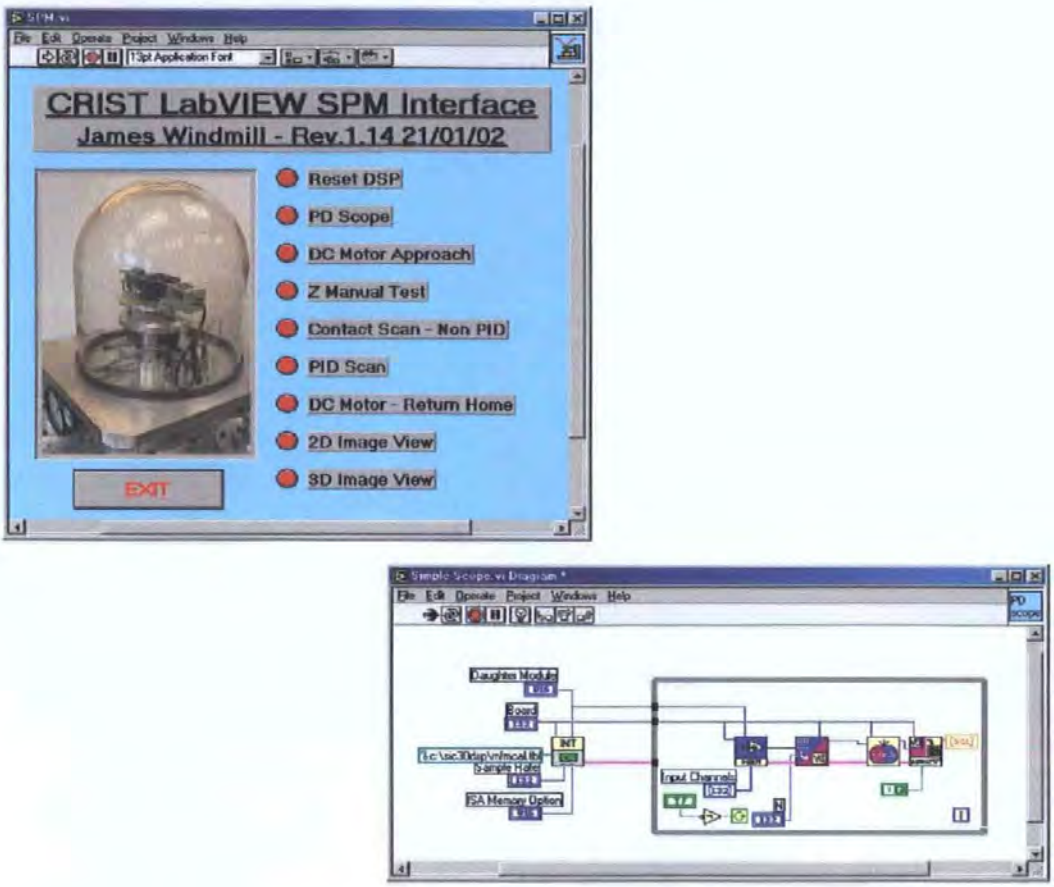


**Figure 27. LabVIEW Front Panel Interface & Background Graphical Code.**

### *4.3.2 MFM Interface*

The control software for the MFM has been created as a set of modules. Each module, after being separately tested, was introduced into the main program. Therefore, each can be run as a stable standalone piece of software. This modular method has made the software easy to update and keep organised. For example, updating any of the modules can be done with no effect on the rest of the control software. All of the modules adhere to a standard in both their graphical front panel and code. Thus the presentation of the software is that of a commercial application. Each module, either referring to a mode of image capture, or an auxiliary function, has been created with user friendliness foremost in

mind. The general rule of thumb has been to reduce unnecessary user interaction where possible, making the software easier to navigate and use. A summary list of the modules is given in Section 5.3.

## *4.4 Scanning & PID Control*

### *4.4.1 XY Motion Scanning*

The MFM software directs the DSP card to output x and y voltage 'waveforms' such that the PZT tube scanner moves in a raster scan. The two waveforms are simultaneously ramped to whichever image start point is specified, e.g. -1, -1 V (-1.58, -1.58 μm). The x-axis runs as the 'fast-scan', whereby the voltage is repetitively ramped up and down. As image data is only collected in one direction of x-axis motion the return ramp, or 'flyback', is run at a higher speed to reduce scan time. During this flyback the y-axis voltage is incremented one step, as the 'slow-scan' direction. A typical 500 x 500 pixel scan is made in a time of 5 minutes 50 seconds, however this can be altered by the user selecting a slower or faster scan speed.

The scanning waveforms can be updated in two ways. If no (digital) control is used, i.e. the system is run open-loop or with analogue feedback, the scan voltage waveforms are downloaded to the DSP, which then completes the scan independent of the LabVIEW software. If digital feedback control is implemented on the DSP, then a different strategy is used. In this case the controlling LabVIEW software is used to update the x and y voltage waveform values, and download them to the DSP, whilst the DSP runs the control loop, data from which is then uploaded to the LabVIEW software. This method is used primarily to separate the scanner update speed from the control loop speed. At the same time it allows the LabVIEW software to monitor the digital control loop and pause and generate an alert if an error is detected. The LabVIEW software collects and arranges both

the photo-detector voltage signal and the controller signal for viewing as images. The controller signal could be used during the image capture process to employ a LiftMode-like mode of operation, as described in Section 2.3.

The disadvantage of this second method is that the overall scan time is determined by the speed of interaction between LabVIEW and the DSP card, through the Windows operating system, rather than the much faster speed possible with the DSP operating on its own. It should be possible to use the DSP to calculate and so generate the necessary x and y voltage values as the scan is made, whilst also running the control loop, thus significantly decreasing the scan time. However, this approach has not been implemented in this work due to time constraints.

### *4.4.2 Deterministic Control - Real Time*

A real-time system response is the ability to respond reliably, and without fail, to an event within a guaranteed time period. As this period varies depending on the system application, there is no one universal time constraint that makes something real-time, nor is there any special operating system or hardware that makes the system real-time.

So, when executing a digital control loop, it must be such that the controller output responds to a measured input value within a specified time interval, known as the control loop cycle time. If this loop cycle time can be guaranteed, then the system is deterministic. If a control loop is not deterministic, then the control system is not guaranteed to be stable. Note that real-time does not necessarily mean extremely fast. Many data acquisition and control applications have cycle times that are slow. For example, temperature controllers commonly sample and control temperature a few times a second. Therefore, for a temperature controller to be stable, it must execute control loops on the order of a few Hertz, as thermal processes are slow. It is the degree of uncertainty or "jitter" with each control loop cycle time that defines the real-time requirements of the system.

### *4.4.3 Control System Design*

Digital feedback in SPM systems has been investigated in previous work, and has been standard in commercial instruments for some time [51] [52]. The successful use of a digital Proportional Integral Derivative (PID) controller has been reported, for example by Baselt et al [53]. The PID function is now commonly implemented in DSP libraries, i.e. the QuVIEW software described in Section 4.1.1. Because of these factors a PID controller, or derivative of such, is implemented in this system. This allows the use of previous works for reference, so implementing a digital feedback controller in a short period, giving more time for further experimental work utilising the system. The block diagram of a PID controller is shown in Figure 28. The equation for an analogue PID controller is given by,

$$m(t) = K_P e(t) + K_I \int_0 e(\tau)d\tau + K_D \frac{de(\tau)}{dt} \tag{3}$$

where, $K_P$ is the proportional gain, $K_I$ is the integral gain, $K_D$ is the derivative gain, $e$ is the error input signal, $m$ is the controller output signal and $\tau$ is the time period. The open loop transfer function, $G_c(s)$, of the controller in the analogue (s) domain is given by:

$$G_C(s) = K_P + \frac{K_I}{s} + K_D s \tag{4}$$

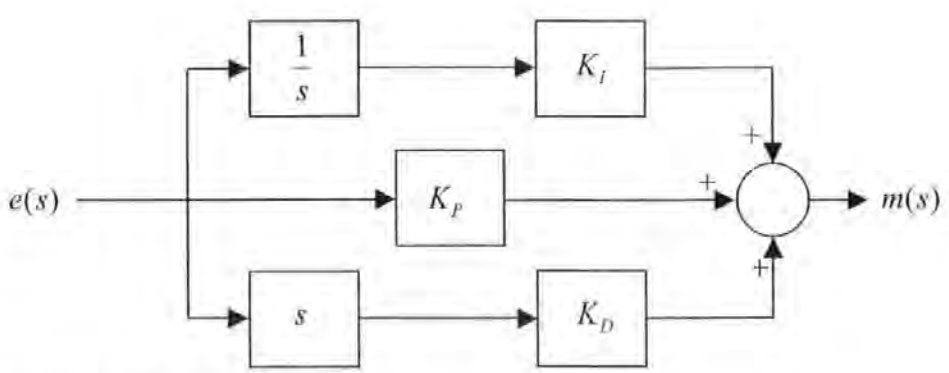


**Figure 28. The PID Controller.**

Three parameters of the controller are determined by the design process; $K_P$, $K_I$, and $K_D$. For a particular control regime one or more of the controller gains may be set to zero. For an inherently stable control system generally only the P and I gains are implemented in SPM feedback. The derivative is rarely used as it may amplify high frequency noise [54]. If a digital system has a sufficiently small sampling period, an analogue control design method can be used to estimate $K_P$ and $K_I$. The design can be tested and tuned, such that to begin with only a simple system model is required for gain parameter estimation.

The electrical behaviour of a piezoelectric transducer can be considered as capacitive when operated below resonance. Closer to resonance it can be modelled as an R, L, C equivalent circuit. There are generally several resonance frequencies for a piezoelectric transducer, ranging from several kHz to 10's of kHz, although in this case the lowest is of interest [55]. Therefore, the piezoelectric's characteristics can be described as a flat response at low frequency, a resonance at frequency $\omega_r$, and a 20 dB/decade roll off after resonance. This can be simulated using a standard second-order transfer function $G_P(s)$ with two conjugate poles,

$$G_P(s) = \frac{k\omega_r^2}{s^2 + 2\zeta\omega_r s + \omega_r^2} \tag{5}$$

where $k$ is the piezoelectric gain constant, $\omega_r$ is the resonance frequency and $\zeta$ is the damping ratio.

Following previous work [47], the resonance frequency and damping ratio for the piezoelectric were estimated by applying a small sinusoidal signal of 0.5 V peak, causing a displacement in the vertical (z) plane of approximately 6.35 nm peak at very low frequency. The gain $G(\omega_r)$ at resonance $\omega_r$ was then measured. To increase the accuracy of the gain estimation this testing was carried out with the piezoelectric tube loaded with

the passive extender and sample, as in normal image scanning. Given the gain at resonance the damping ratio is calculated using Equation 6 [56] [57].

$$|G(j\omega)| = \frac{1}{2\zeta} \tag{6}$$

From the test on the piezoelectric in this MFM, $\omega_r$ is 47.9 krad/s and the gain at resonance is 3.5. Therefore, the damping ratio $\zeta$ is approximately 0.14. For a fast and steady response, with a favourable settling time this can be increased.

The gain constant *H(s)* of the OBD detection system used in this MFM was measured at approximately 35 mV/nm. This value was measured by bringing the tip into contact with a sample surface, then driving the cantilever in the z plane using the tube scanner. Later, calibration (see Section 5.2) would allow the value to be measured again, and if necessary the controller gain estimation process reviewed. Substituting $\omega_r$, $\zeta$, *H(s)*, and *k* (as defined in Section 3.2.2) into Equation 5, the transfer function is given by,

$$G(s)H(s) = \frac{1.1\times10^9}{s^2 + 1.3\times10^4 s + 2.3\times10^9} \tag{7}$$

The transfer function of a PI controller is given by

$$G_C(s) = \frac{K_P s + K_I}{s} \tag{8}$$

The gains $K_P$ and $K_I$ can be estimated using the frequency response design method [58]. The PI controller is assumed to behave like a phase-lag controller. In this case the design is based on the Bode diagram of the open loop transfer function (Equation 7), as shown in Figure 29.

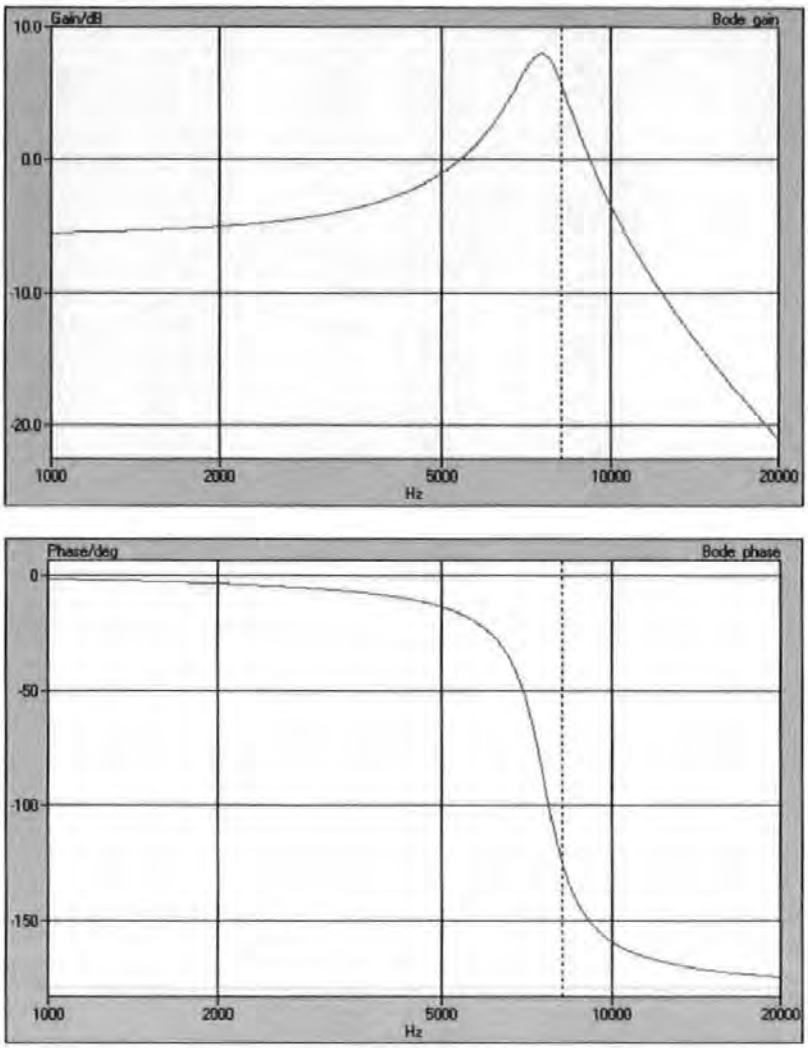


**Figure 29. Bode plots of z piezoelectric, using transfer function of Equation 7.**

First the frequency $\omega_1$ at which the angle of $G_P(j\omega_1)H(j\omega_1)$ is equal to -180° + $\phi_m$ + 5° is found, where $\phi_m$ is the phase margin (set at 50° for stability), in this case $\omega_1$ is 49.9 krad/sec. Then the gain at $G_P(j\omega_1)H(j\omega_1)$ is found, here it is 6.75 dB, i.e. 2.2. From this $K_P$ is given by

$$K_P = \frac{1}{|G_P(j\omega_1)H(j\omega_1)|} \tag{9}$$

such that in this case $K_P$ is 0.45.

$K_I$ is found using the magnitude of the controller's zero, chosen to be much lower than $\omega_1$.

Applying the general rule of controller design [58], the following equation is used,

$$\frac{K_I}{K_P} = 0.1\omega_1 \tag{10}$$

so that in this case $K_I$ is estimated to be 2250.

This gives the controller transfer function as,

$$G_C(s) = \frac{0.45s + 2250}{s} \tag{11}$$

The open loop Bode plot of the compensated system is shown in Figure 30. These values were then tested in the system using a step response test.

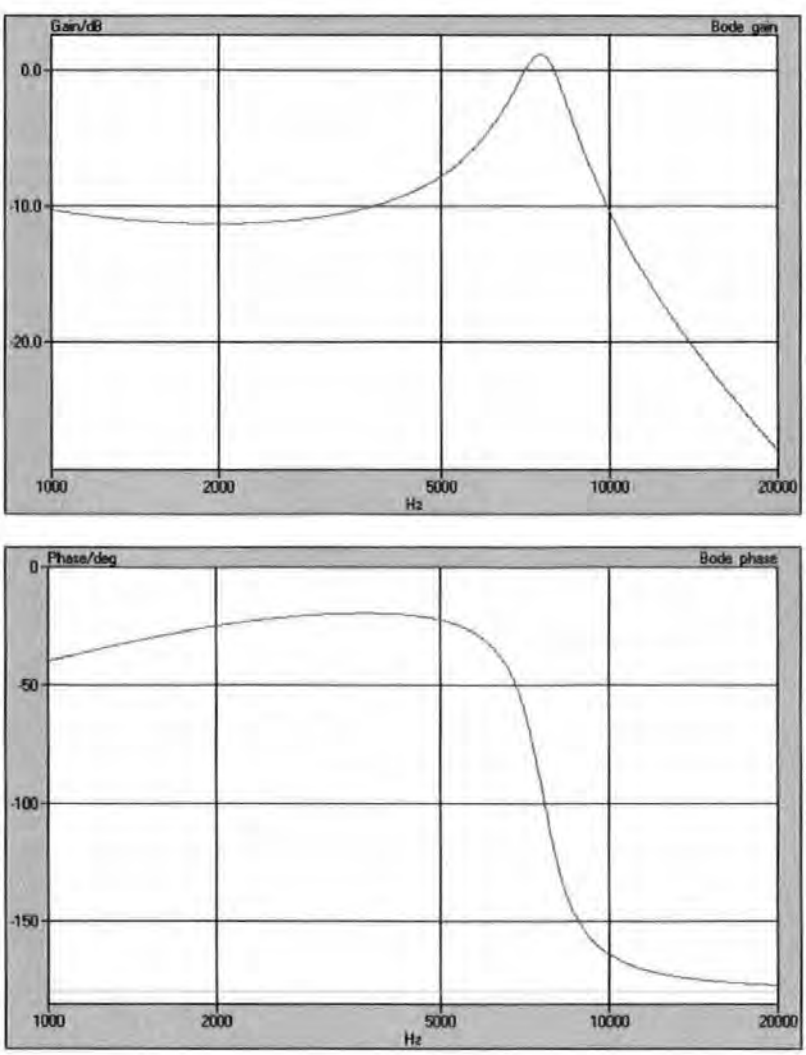


**Figure 30. Open loop Bode plots of the compensated system.**

### *4.4.4 Control System Testing and Tuning*

The controller's performance was tested and tuned using a step response test, as suggested by Baselt et al [53]. The test was carried out by applying a voltage step to the piezoelectric translator generating a cantilever deflection of approximately 30 nm. The PI controller, using the values from Equation 11, then cancels this deflection. Initially the sampling period was set at 10 μs, and hence $K_I T$ was 0.0225 for $K_I = 2250$. Figure 31 shows the step response of the system for these initial gain estimations.

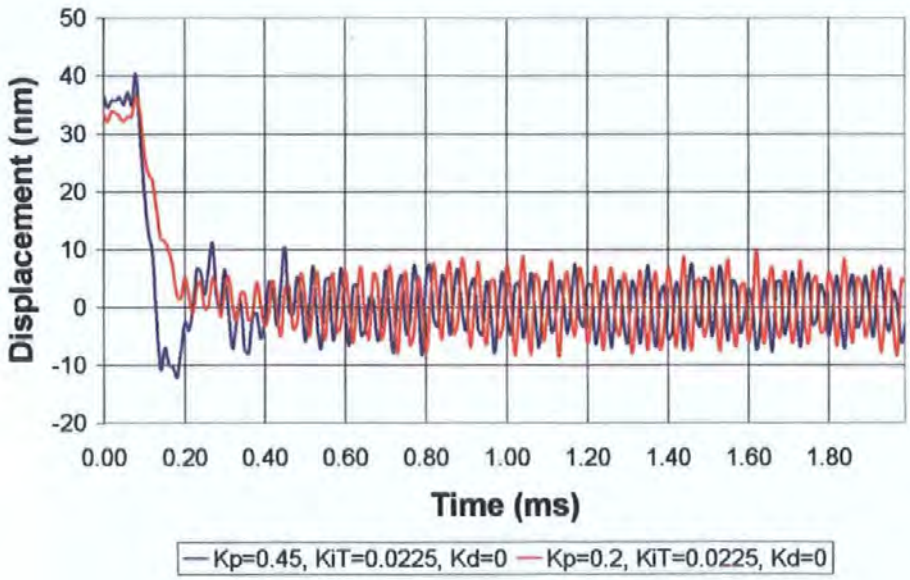


**Figure 31. Step response for $K_P = 0.45$, $K_I T = 0.0225$ and $K_D = 0$, and $K_P = 0.2$, $K_I T = 0.0225$ and $K_D = 0$.**

The results in Figure 31 show a large overshoot for the initial gains estimation (the blue line). In addition, the system stability is inadequate, as shown by the 'ringing' occurring while the system is at a constant height; this is due to noise feeding back through the controller. This sort of response can occur due to the sampling process in a digital control implementation that uses gains estimation based on a linear system [56] [57]. The sampling frequency in this system is approximately 13 times the system bandwidth, but for a discrete system to exactly duplicate a linear design the minimum sampling frequency should be at least 20 times the system bandwidth [56] [57]. Nevertheless, the step

response test does provide a useful guide for estimating the controller's gains. The second (red) line on the graph in Figure 31 shows that by reducing $K_P$ to 0.2 the overshoot is almost completely removed, however the system is still unstable. Further step tests were carried out to improve the PI controller's response.

Figure 32 shows the step responses for $K_P$ at 0.1 and 0.05. The first (blue) line still shows system instability after the step is complete. This is removed, leaving only noise in the second (red) line, but with a much longer settling time. These results indicate that the optimum value for $K_P$, such that there is no overshoot or system instability, is between 0.1 and 0.05.

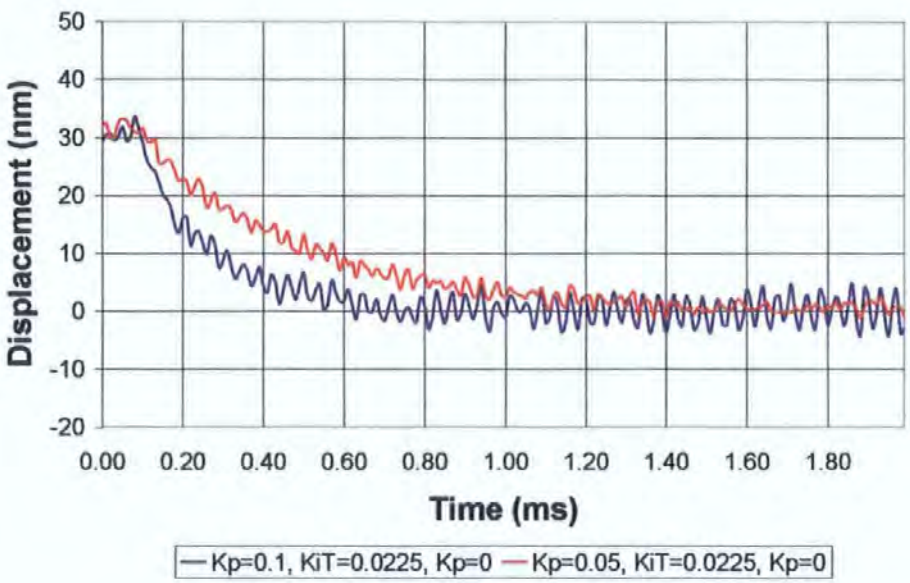


**Figure 32. Step response for $K_P = 0.1$, $K_IT = 0.0225$ and $K_D = 0$, and $K_P = 0.05$, $K_IT = 0.0225$ and $K_D = 0$.**

In Figure 33 the step response for $K_P$ optimised at 0.07 is shown. In this case the system instability, or 'ringing' is not evident, and the settling time is reduced to within 1 ms. The two lines in Figure 33 show a variation in $K_IT$, at 0.012 and 0.0225. Very little difference can be seen, except that in the second case (the red line) the system once settled seems more stable. These final values were used in the results shown in following Chapters. The system settles within 1 ms, a figure that is comparable to other work [47] [53]. As the

system dynamics are altered by different samples, the step response test will provide a useful and simple method of quickly optimising the PI controller's $K_P$ and $K_I$ gains [49].

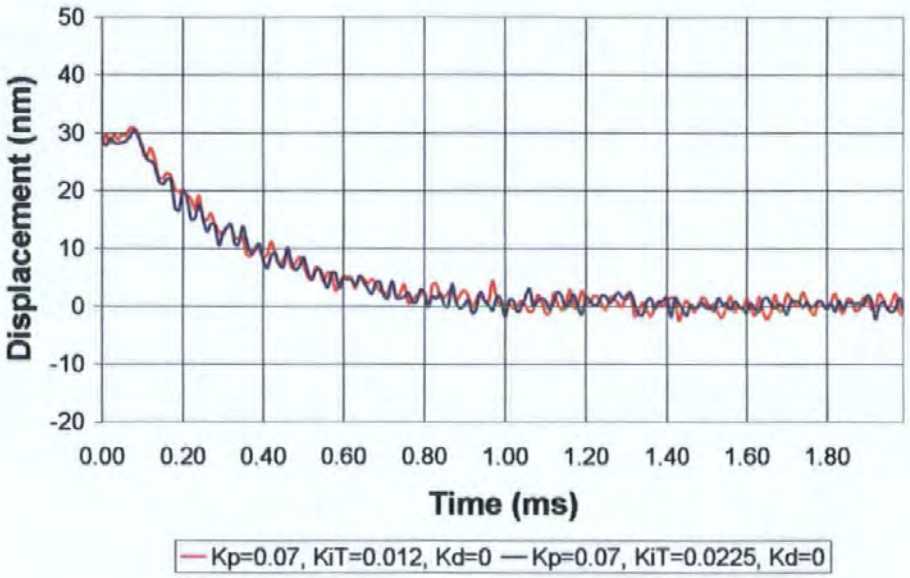


**Figure 33. Step response for $K_P = 0.07$, $K_I T = 0.012$ and $K_D = 0$, and $K_P = 0.07$, $K_I T = 0.0225$ and $K_D = 0$.**

# 5 MFM Instrument Development

## *5.1 System Noise*

The OBD detection system suffers from noise contributions from the laser, the detectors, the amplifiers and the cantilever. These noise sources have previously been described in depth by Sarid [59]. A brief description of these sources, following from the work of Sarid, together with typical figures for the detection system used in this instrument, is presented here. This is followed by a discussion of other sources of noise in the system. Finally, an evaluation of the measured levels of noise within the system is carried out. Note that these calculations consider the Microlever contact mode cantilever described in Section 3.2.

### *5.1.1 Johnson Noise*

Johnson noise is caused by the thermal agitation of electrons in the load resistor, R (100 KΩ), in the first stage of the photo-detector amplifiers and gives rise to a current noise in each of the four amplifiers given by

$$\left\langle \delta i^2 \right\rangle_J = \frac{4KTB}{R} \tag{12}$$

where $\left\langle \delta i^2 \right\rangle$ is the mean square current noise.

Therefore the total noise fed into the differential amplifier is

$$\left\langle \delta i^2 \right\rangle_J = \frac{16KTB}{R} \tag{13}$$

where $K$ is Boltzmann's constant (1.38 x $10^{-23}$ J/K), $T$ is the absolute temperature (293.15 K) and $B$ is the bandwidth of the filter at the output of the amplifier (125.66 krad/s).

Using the typical system values gives $\langle \delta i^2 \rangle_J = 8.13 \times 10^{-20}\ A^2$.

### *5.1.2 Laser Noise*

Laser diodes behave like a thermal source and amplify noise. Noise is caused by spontaneous-emission, mode-partition, mode-hopping and flicker noise (low frequency noise whose power spectrum is inversely proportional to frequency, sometimes called 1/f noise). The photo-current noise in each half (two quadrants) of the photo-detector caused by the laser intensity noise is

$$\langle \delta i_1^{\,2} \rangle_L = \frac{1}{4}\eta^2 RINP^2\left(1+\frac{\delta d}{d}\right)^2 \tag{14}$$

and

$$\langle \delta i_2^{\,2} \rangle_L = \frac{1}{4}\eta^2 RINP^2\left(1-\frac{\delta d}{d}\right)^2 \tag{15}$$

where $\eta$ is the sensitivity of the photo detector (0.35 A/W at 670 nm), $RIN$ is the relative intensity noise of the laser $RIN = \dfrac{\langle \Delta P^2 \rangle}{\langle P \rangle^2}$, ($\Delta P^2$ is the mean square optical intensity noise and $P$ is the average optical power of the laser), typically $10^{-10}$, $P$ is the optical power incident on the detector (0.5 mW), $d$ is the laser spot size on the detector (2 mm) and $\delta d$ is the deflection of the spot from the centre of the detector (900 nm for a cantilever deflection of 1 nm).

The noise at the output of the differential amplifier is obtained by subtracting Equation 14 from 15 giving

$$\langle \delta i^2 \rangle_L = \frac{1}{2}\eta^2 RINP^2\left(\frac{\delta d}{d}\right)^2 \tag{16}$$

If the laser spot is centred on the detector then $\delta d << d$, and the noise at the output of the differential amplifier is small, giving a good common-mode rejection.

Using the typical system values, $\langle \delta i^2 \rangle_L = 3.1 \times 10^{-25}$ A$^2$.

### *5.1.3 Cantilever Thermal Noise*

The cantilever thermal noise is caused because of the cantilever acting as a harmonic oscillator. The cantilever thermal noise will be greatest when the cantilever is oscillating at its resonance, 106.814 krad/s (17 kHz). The thermal noise of the cantilever causes a noise current in each of the four detectors given by:

$$\langle \delta i^2 \rangle_t = \eta^2 P^2 \frac{9s^2}{4l^2 d^2} \frac{4KTBQ}{\omega_0 k} \tag{17}$$

where $s$ is the distance from the cantilever to the detector (90 mm), $l$ is the cantilever length (200 μm), $Q$ is the quality factor of the cantilever (100) and $k$ is the force constant of the cantilever (0.063 N/m).

The thermal noise at the output of the differential amplifier will be

$$\langle \delta i^2 \rangle_t = \eta^2 P^2 \frac{9s^2}{4l^2 d^2} \frac{16KTBQ}{\omega_0 k} \tag{18}$$

Using typical values gives $\langle \delta i^2 \rangle_t = 4.22 \times 10^{-13}$ A$^2$.

### *5.1.4 Shot Noise*

Shot noise is caused by the varying number of photons arriving at the photo-detector at any one time. The shot noise generated by each photo-detector is

$$\langle \delta i^2 \rangle_s = 2e\eta B \frac{P}{4} \tag{19}$$

where $e$ is the electronic charge ($1.6 \times 10^{-19}$ C).

The noise at the output of the differential amplifier is therefore

$$\left\langle \delta i^2 \right\rangle_s = 2e\eta BP \tag{20}$$

Using typical values gives $\left\langle \delta i^2 \right\rangle_s = 7.04 \times 10^{-18}$ A$^2$.

Comparing the noise values for the detection system the Johnson noise, laser noise and shot noise are several magnitudes smaller than the cantilever thermal noise. This means that the resolution of the instrument will not be limited by the detection technique but by the thermal vibrations of the cantilever.

### *5.1.5 Other Sources of Noise*

Care has been taken in the design of the instrument to eliminate or reduce any other sources of noise. Electrical pickup has been reduced by the careful shielding of cables and the enclosure of the photodiode amplifiers in a die cast aluminium box. All grounds in the system have been connected in the standard star formation to eliminate the possibility of noise caused by ground loop currents. The high voltage power supply used to drive the instrument's tube scanner was designed to remove as much noise as viable. The output of each amplifier has a 2.5 μV ripple that will cause a movement on the piezoelectric tube scanner of only 0.0007 Å, a figure negligible compared to other sources of noise.

Building vibrations have been reduced by mounting the instrument on a Newport Research Corporation (NRC) optical table measuring 1200 x 2400 x 300 mm and weighing 460 Kg. The optical table has a stainless steel top plate, tapped with M6 holes spaced 1 inch between centres, a steel-honeycomb core which provides an extremely stiff table top and rolled steel sides and bottom plate. The table also has integral damping mechanisms, which rapidly damp out any vibrations that reach the table.

Four NRC Vibration Isolators support the optical table. These use air pressure to provide excellent vibration isolation in both vertical and horizontal planes. Their resonant frequency in both the horizontal and vertical planes are between 1.5 and 1.7 Hz and they will quickly damp out vibrations between 2 and 50 Hz, including large amplitude floor and building vibrations.

Air currents and acoustic noise can cause problems during image acquisition. Motion in the laboratory, or the opening of doors, causes air currents that result in movement of the cantilever. Enclosing the instrument in a glass vacuum jar at all times, i.e. when scanning in air, has reduced these air currents. As acoustic noise such as speech can have an effect on the image quality the glass also reduces this noise.

### *5.1.6 System Noise Analysis*

A power spectrum of the photo-detector circuit output signal can be obtained using a combination of the QuVIEW software provided with the DSP board and LabVIEW. The input signal can be sampled at different frequencies, making it possible to examine the low frequency and high frequency noise separately.

The power spectrum shown in Figure 34 was measured with only the instrumentation electronics, including the photo-detector and high-voltage piezoelectric driver circuits, and computer operating. This shows a noise floor of approximately -100 dB, equivalent to 4 mV (0.12 nm at the lever end) when measured in the time domain. The main source of this noise is the computer system, such that it cannot easily be decreased. However, compared to other sources of noise dealt with in the rest of this section the background noise is negligible.

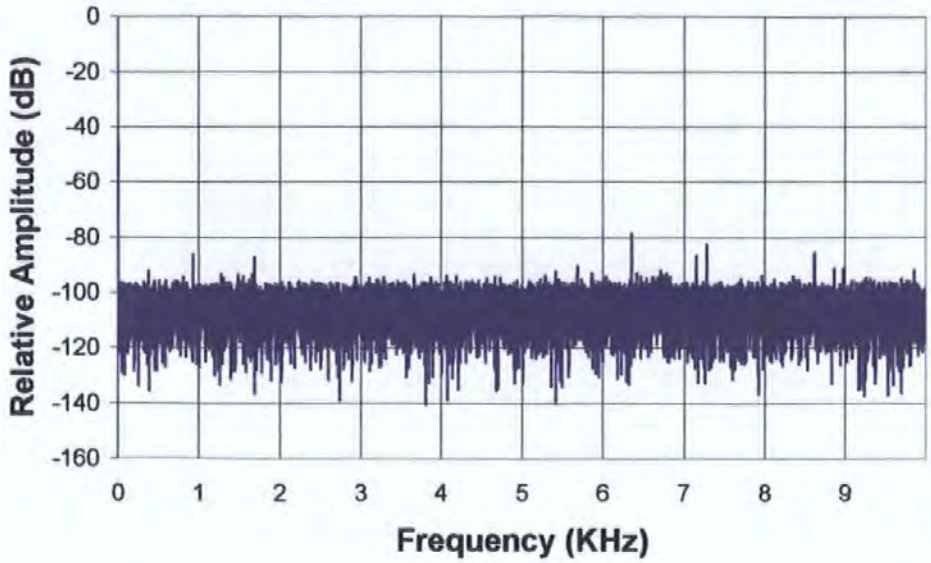


**Figure 34. Power spectrum of noise with only instrument electronics and computer active, no laser.**

The overall noise from the cantilever is shown by the power spectrums in Figure 35. The noise is even across the entire spectrum; further tests were conducted at higher frequencies, with the same result. The noise from the laser adds approximately 20 dB, when compared against Figure 34, and from the cantilever adds approximately 10 dB. These noise sources could be reduced, e.g. changing the laser is possible, although this laser is standard for this work, and using resonant imaging would improve the signal to noise ratio (Section 2.3). The level of measured noise shown here is significantly higher than that calculated in the previous sections. The explanation for this is that those calculations only took into account the noise at the output of the quadrant photo-detector circuit. After this circuit the signal is passed through a long transmission path, including connectors, a low-pass filter with a gain of 8 dB, an over-voltage protection buffer amplifier and further low-pass filtering on the DAQ board. All of this acts to increase the noise signal to the levels measured here.

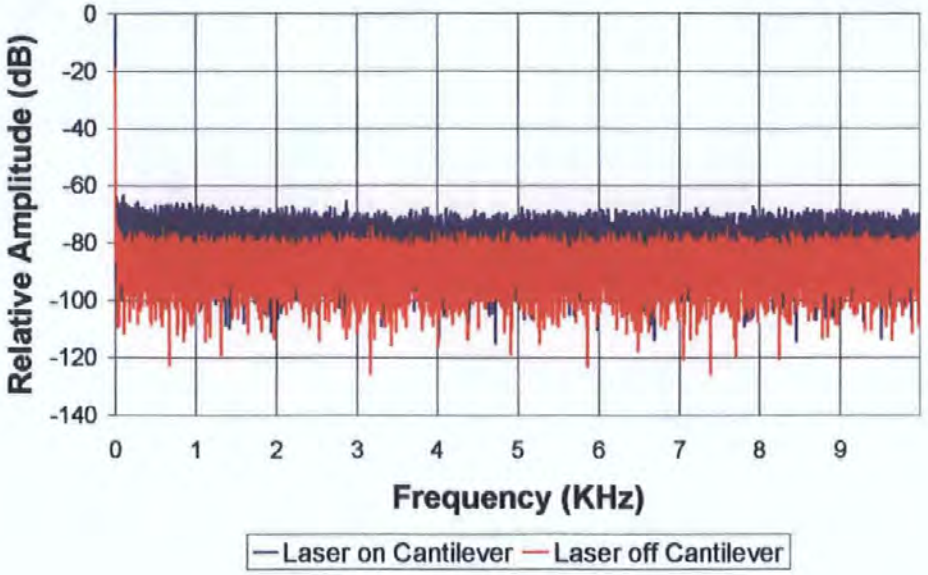


**Figure 35. Power spectrum of noise with laser deflection from cantilever and stationary point.**

When the cantilever is positioned in contact with the sample, with the tube scanner stationary, periodic noise is seen on the output signal. This noise appears at approximately 50 and 300 Hz and is not present if the tip is not touching the sample, as can be seen from Figure 36. This suggests that the sample is vibrating, but that these vibrations are not transmitted through the system to the cantilever, as long as the tip is not in contact.

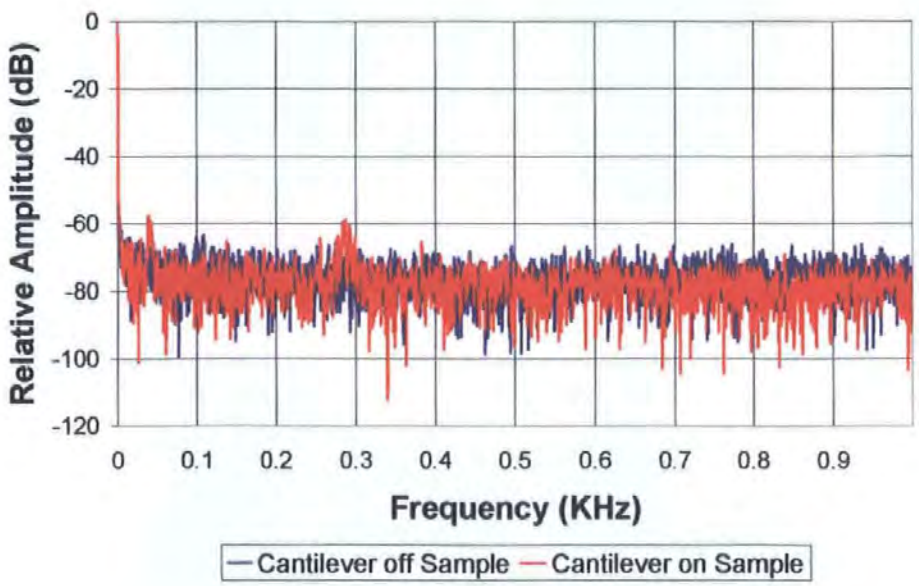


**Figure 36. Power spectrum of noise with cantilever touching and above sample surface.**

If the high voltage power supply to the piezoelectric translator and tube scanner is switched off when the cantilever tip is in contact, the noise at these frequencies is reduced, as shown in Figure 37. This suggests that the vibrations are coming from the tube scanner, and/or the piezoelectric translator. However, the amplitude of this noise is very low, i.e. less than 2 nm, also, if feedback is used when imaging in contact mode then the vibrations will be cancelled out by the feedback system.

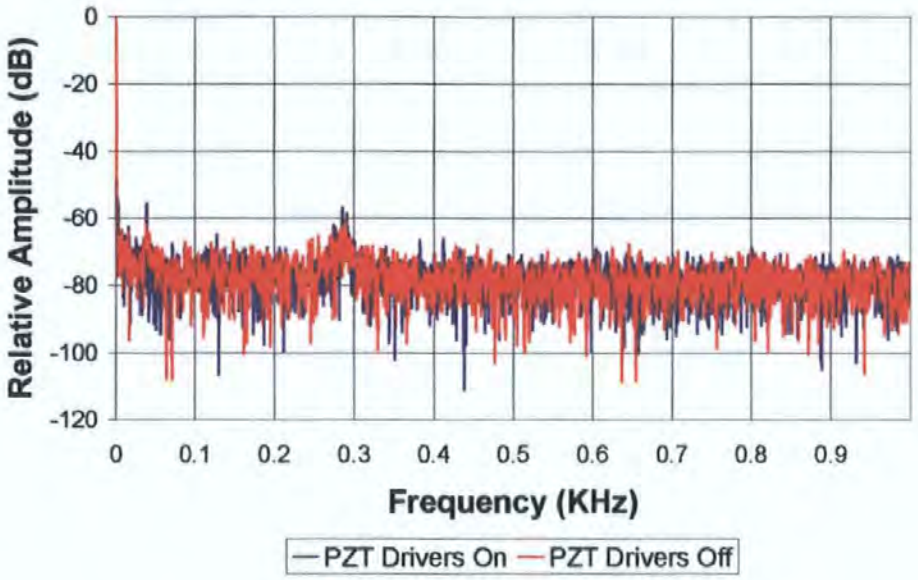


**Figure 37. Power spectrum of noise with PZT high-voltage drivers active and off.**

The effect of the vibration isolation optical table can be seen in Figure 38 where the low frequency noise was measured, at a sampling frequency of 1 kHz, with the cantilever touching the sample and the instrument covered with the vacuum jar. The graph of the undamped table power spectrum in Figure 38 clearly shows low frequency vibrations between approximately 1 and 67 Hz, plus frequencies at 110 Hz. General building structure vibrations, people moving around and machinery operating (e.g. lifts) produce these frequencies. Pumping the table up (damped) eliminates the majority of these low frequency vibrations as expected. The overall noise level is also reduced over the spectrum shown.

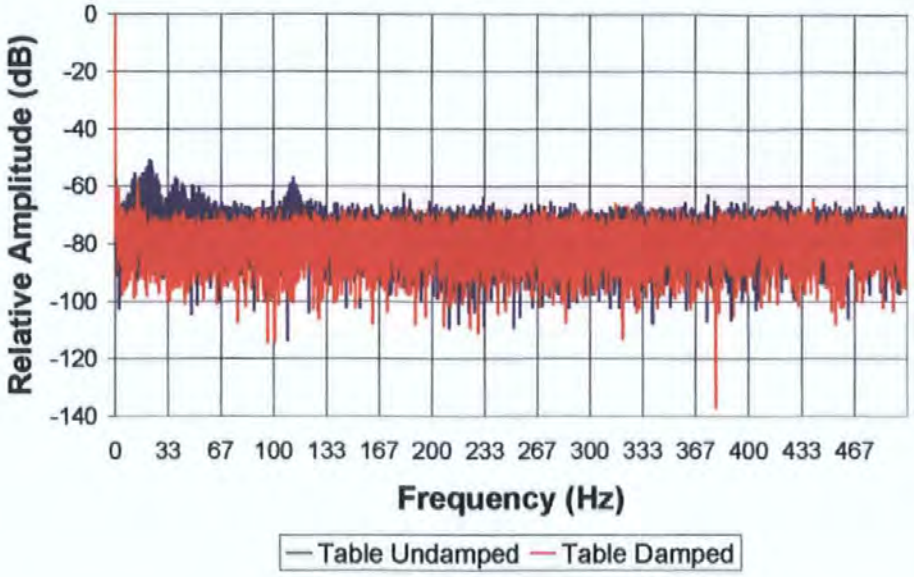


**Figure 38. Power spectrum of noise with optical table vibration damping system active and turned off.**

The noise from background light on the photo-detector signal is revealed in Figure 39. Spikes in the power spectrum when the background light is let through to the system can be made out at multiples of 100 Hz. These are most probably due to the artificial lighting in the lab, however in normal imaging acquisition the system is used under a blackout cover, as seen in the second spectrum in Figure 39.

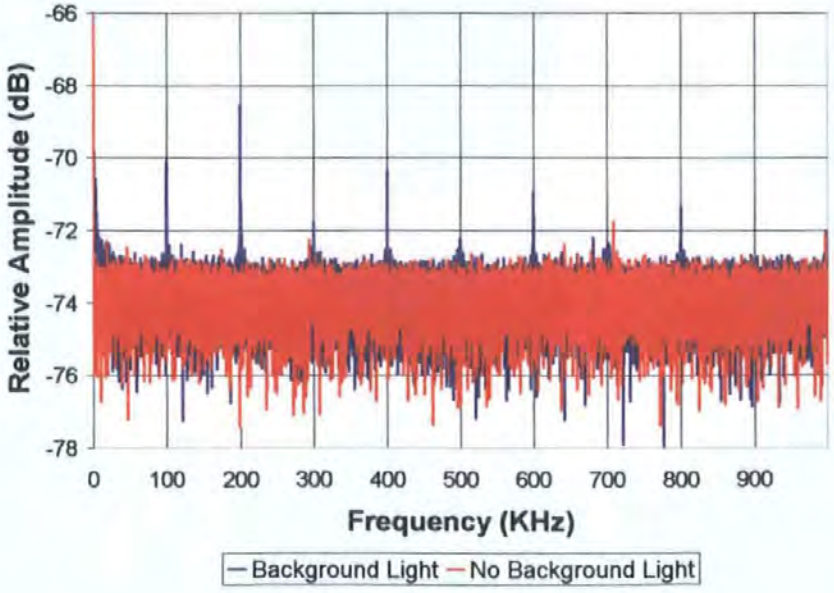


**Figure 39. Power spectrum of noise with and without background light (including artificial and natural).**

The power spectrums in Figure 40 show the effect of placing the vacuum jar (with no vacuum applied) over the MFM head during all image acquisition. Several low frequency spikes can be seen in the spectrum taken without the vacuum jar, these are caused by air currents and acoustic noise moving the cantilever. In the spectrum taken with the vacuum jar in place these effects have been removed or at least reduced.

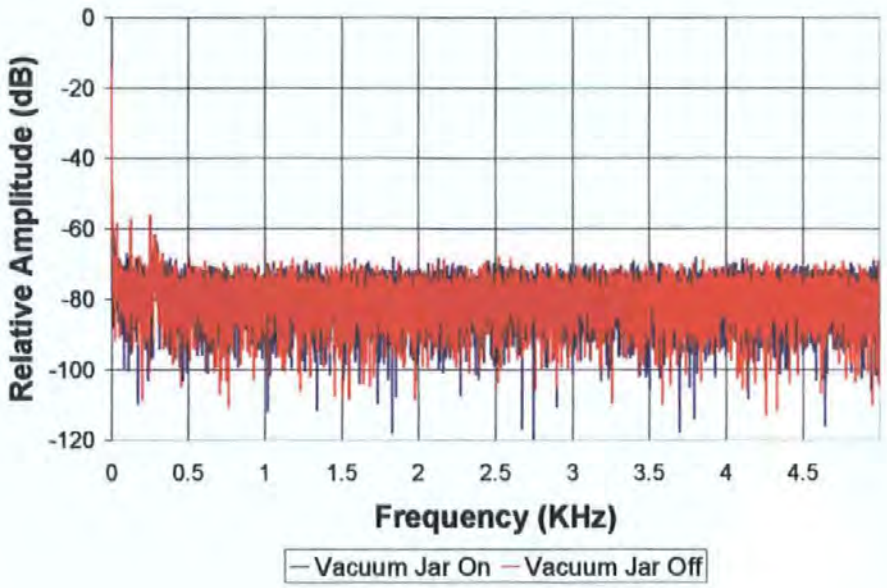


**Figure 40. Power spectrum of noise with and without vacuum jar present.**

Figure 41 shows the drift in the photo-detector signal at the PC over a period of five minutes. The measurements were made at constant ambient room temperature (25°C), with the MFM enclosed by the vacuum jar. The tube scanner and piezoelectric translator were stationary, with zero volts on each electrode. Before measuring the drift the instrument was allowed to warm up for one hour. When the tip is in contact with the sample the drift is due to the tube scanner and translator drifting. When the tip is not in contact with the sample, any drift is mainly due to drifting in the instrumentation electronics. As the output signal drifts relatively slowly, the feedback system will compensate and so this source of noise will not cause problems during image acquisition.

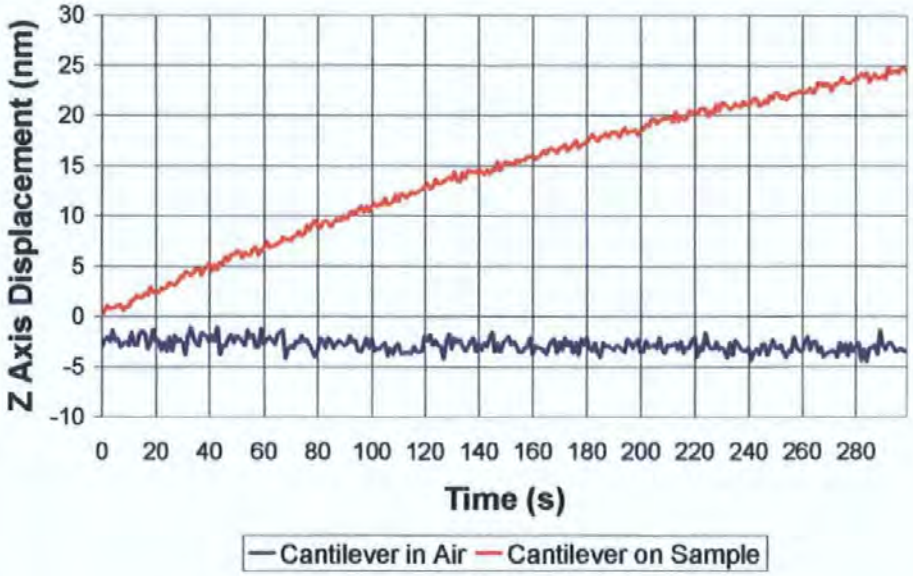


**Figure 41. Output signal drift with cantilever suspended above surface and in contact with surface.**

## *5.2 System Calibration*

### *5.2.1 Initial Z Calculations*

The OBD detection system used in this work does not provide any inherent calibration information. Therefore, it is necessary to calibrate the detection system so that the photo-detector circuit output voltage can be converted into a cantilever deflection measurement. As the magnitude of the output voltage is dependent on the amount of incident laser power, it is necessary to recalibrate the deflection signal each time the cantilever is changed or the laser spot on the cantilever is moved.

The initial z calibration of the detection system was achieved using the calculation of the z extension (12.7 nm/volt) of the tube scanner from Section 3.3.2. Thus, with the cantilever in contact with a sample, by applying a step of 5 V to the z inputs of the tube scanner, and thus a physical z step calculated to be 63.5 nm to the tube, a step change of 2.22 V was observed from the photo-detector circuit. So we can define the voltage from the detector in terms of volts per step height change, in this case 35 mV/nm, a value that is comparable to previous work on similar systems [49]. This provided a basic starting point for using the

system, and was used in the initial estimation of the PI controller gains, as shown in Section 4.4.3. It was also used to scale initial contact mode AFM images, particularly of a CD data pit, as shown in Section 6.1. These images show that the initial calibration was of the correct order of magnitude, accurate to at worst ±10%.

### *5.2.2 SPM Z Calibration*

The instrument's z calibration was later tested using a SPM vertical calibration grating, supplied by MikroMasch Ltd. (Estonia) [60]. This provides a one-dimensional array of rectangular $SiO_2$ steps on a Si wafer with a calibrated height value over the whole active area (3 mm x 3 mm). In this case a 100 nm series grating (±1.5 nm) was employed, as depicted in Figure 42. The actual step height for the grating used, as specified by the manufacturer, was 104.5 nm. The height accuracy given is a standard deviation calculated over the whole active area, whereby it shows the deviation from the actual (not nominal) step height value.

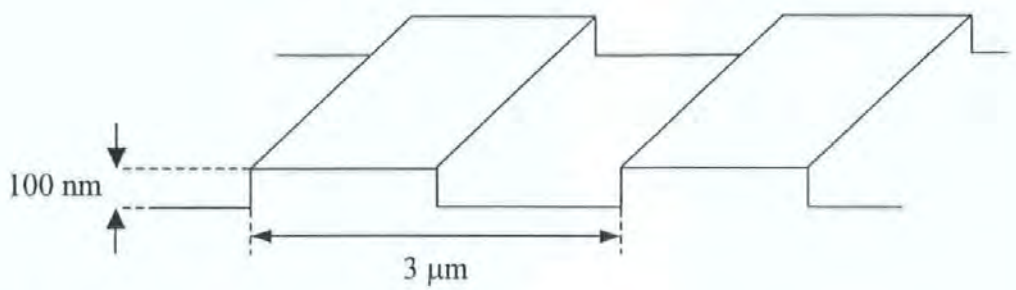


**Figure 42. Diagram of Vertical Calibration Sample.**

A contact mode AFM image of the vertical calibration sample taken by the system is shown in Figure 43. This clearly shows the one-dimensional array of steps. Some scanner non-linearity in the form of creep is visible, as the steps appear to curve across the image. The image also shows the step boundaries are not perfectly straight. When compared with

a similar image, supplied by the manufacturer, of this type of calibration sample, as shown in Figure 44, the image of Figure 43 can be regarded as the actual topography.

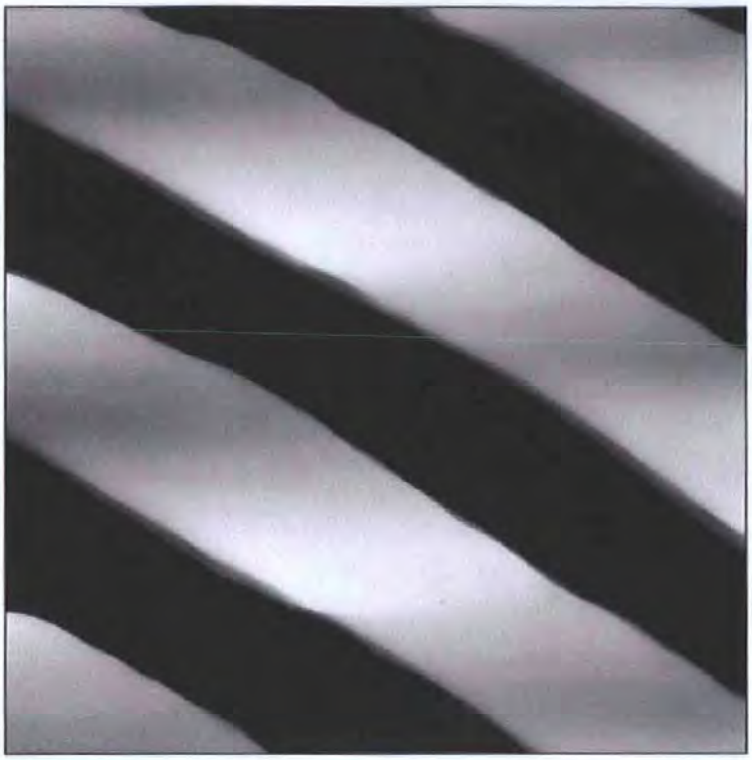

**Figure 43. AFM Image of Vertical Calibration Sample.**

**Contact-mode (PID) image, 6 μm x 6 μm scan area, showing rectangular 104.5 nm steps on Z calibration grating, pitch 3 μm.**

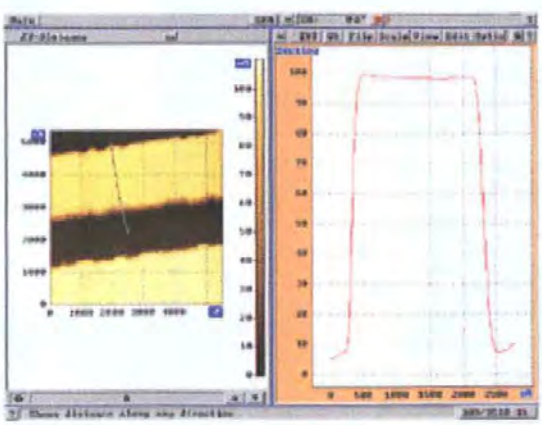

**Figure 44. Manufacturer AFM Image and Line Scan of Vertical Calibration Sample.**

In this case the actual x-y topography is not the primary consideration, rather the grating is designed specifically for z calibration. Figure 45 shows the photo-detector signal voltage

for a single line scan across the Z calibration grating. Given a manufacturer specified calibrated step height of 104.5 nm, the voltage step found in Figure 45 produces a gain constant (volts per step height change) of 33.5 mV/nm. The line scan graph appears to show the step corners are rounded. This is an imaging artefact caused by the integration of the pyramidal tip used with the step.

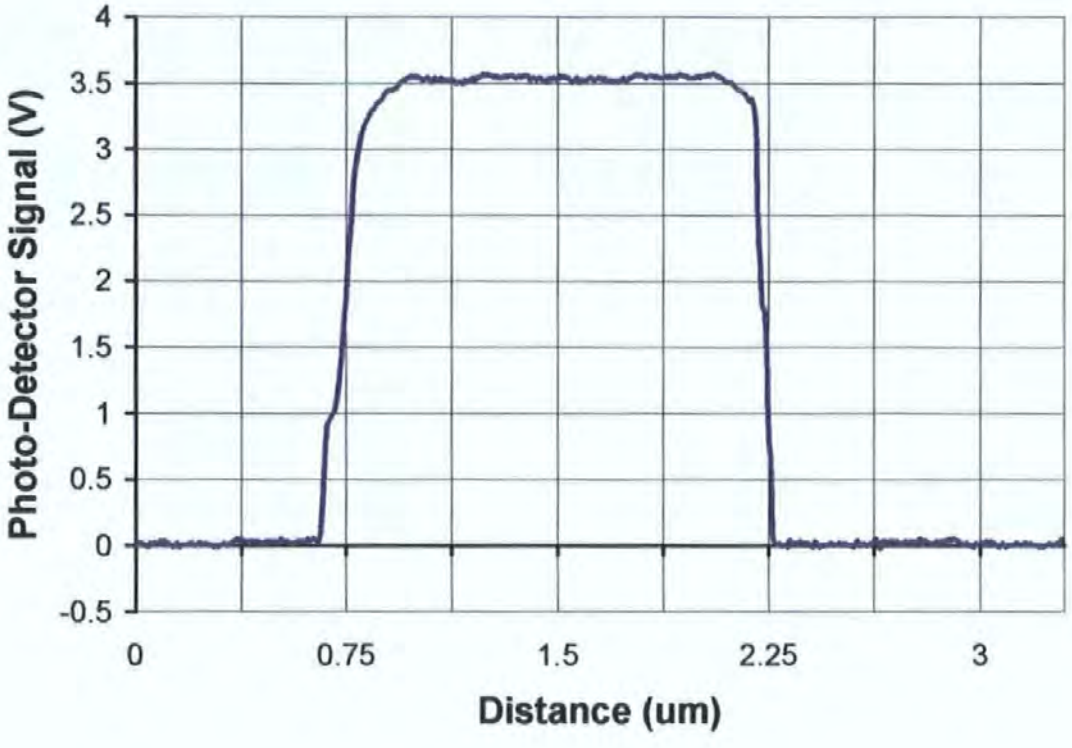


**Figure 45. Line scan of the photo-detector signal (V) across a step on the Z calibration grating.**

### *5.2.3 Z Calibration Conclusion*

The z calibration tests described in the two previous sections show a very satisfactory agreement of within 5% between the value calculated in the first section and that measured from the calibrated grating in the second section. This shows that the calculations from Section 3.3.2 are reliable, and also the initial gain estimations for the DSP control system described in Chapter 4 are justified. These results allow all images from the system to be accurately calibrated for height, and additionally provide a calibrated measure of scan height when using a non-contact mode for magnetic imaging.

### *5.2.4 XY Calibration*

The x and y axes of tube scanner motion were tested using a crossed line grating replica calibration (XY) sample. This commercially available sample has 2160 lines/mm in orthogonal directions, which equates to a line every 463 nm in both the x and y axis. The sample was scanned four times, each time with a different scan range, as shown in Figure 46. Images a, b and c clearly show the grid pattern as expected, with the approximately correct size grid for the scan voltages used.

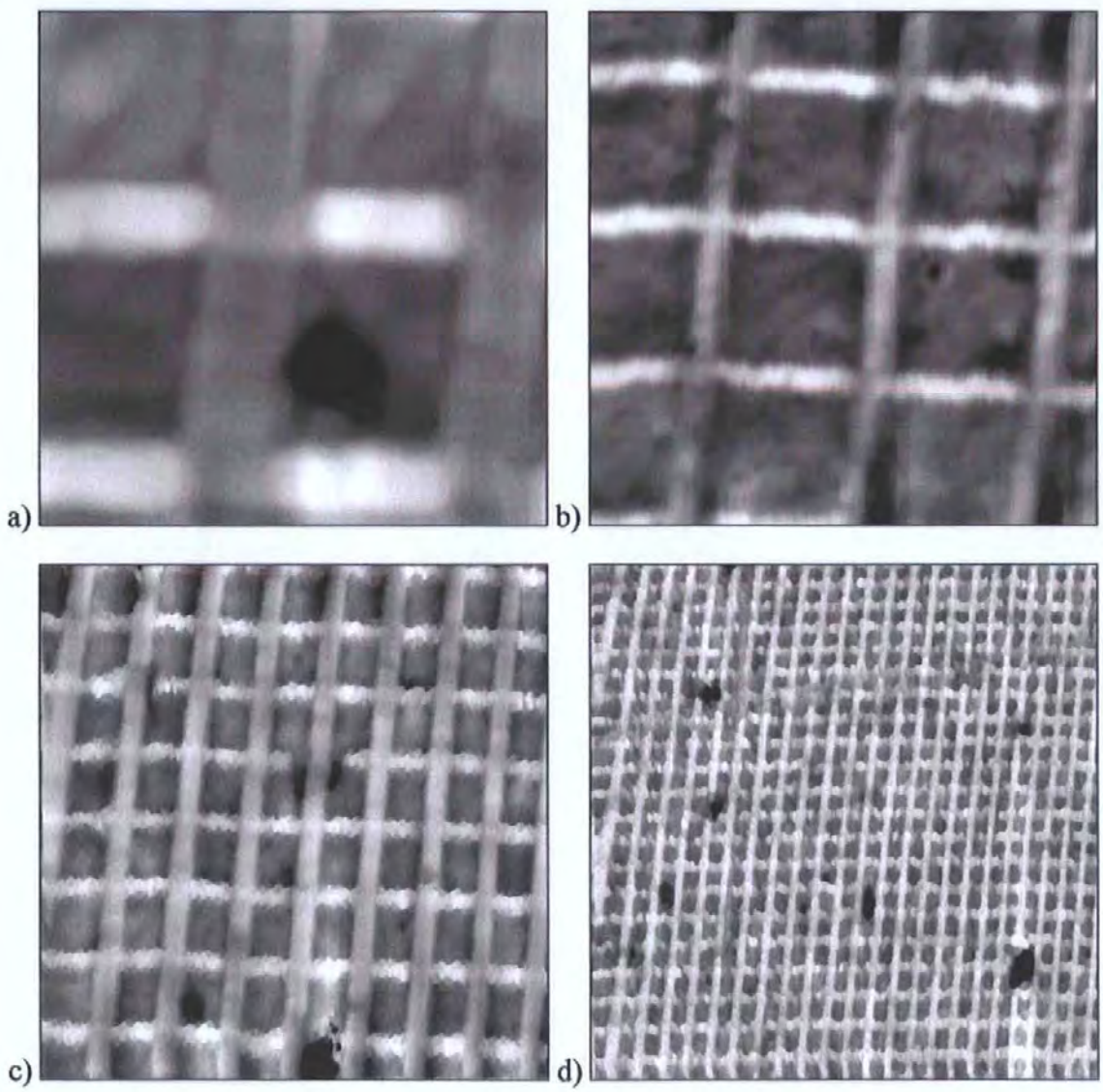


**Figure 46. Images of XY calibration sample.**

**Fast scan direction vertical on image; a) 1 x 1 μm, b) 1.5 x 1.5 μm, c) 4 x 4 μm, d) 10 x 10 μm (Actual 10 x 11 μm).**

The images in Figure 46 do appear 'unfocussed' to the human eye, probably due to the use of an older blunted pyramidal tip, however they contain the information necessary to verify the calibration of the system. In image d the slow scan axis (horizontal on image) actually shows 23 grid lines, against the 21 lines in the fast scan axis, an increase of almost 1 μm (10%) over the expected range. This image required a long overall scan time; for accuracy with relatively low resolution (compared to images a, b & c), and because the DSP feedback loop was used in this case (but not images a, b or c) as the scan area was relatively large and so subject to much greater tube scanner bowing. This long scan time would have introduced a large creep non-linearity to the slow axis, as described in Section 2.1.

From Figure 47 it can be seen that a measurement was taken over 16 grating lines in both the x and y direction (with no feedback control), with a measured scan size of 7.4 μm by 7.4 μm, corresponding to a tube scanner response of 148 nm/V. The difference in the non-linearity in the two scan directions is probably due to the different line scanning speeds causing different amounts of hysteresis in the tube scanner. The measured scanner response value compares to the response of 157.7 nm/V calculated in Section 3.3.2, this reduction in the actual system value may be due to PZT ageing as described in Section 2.1.

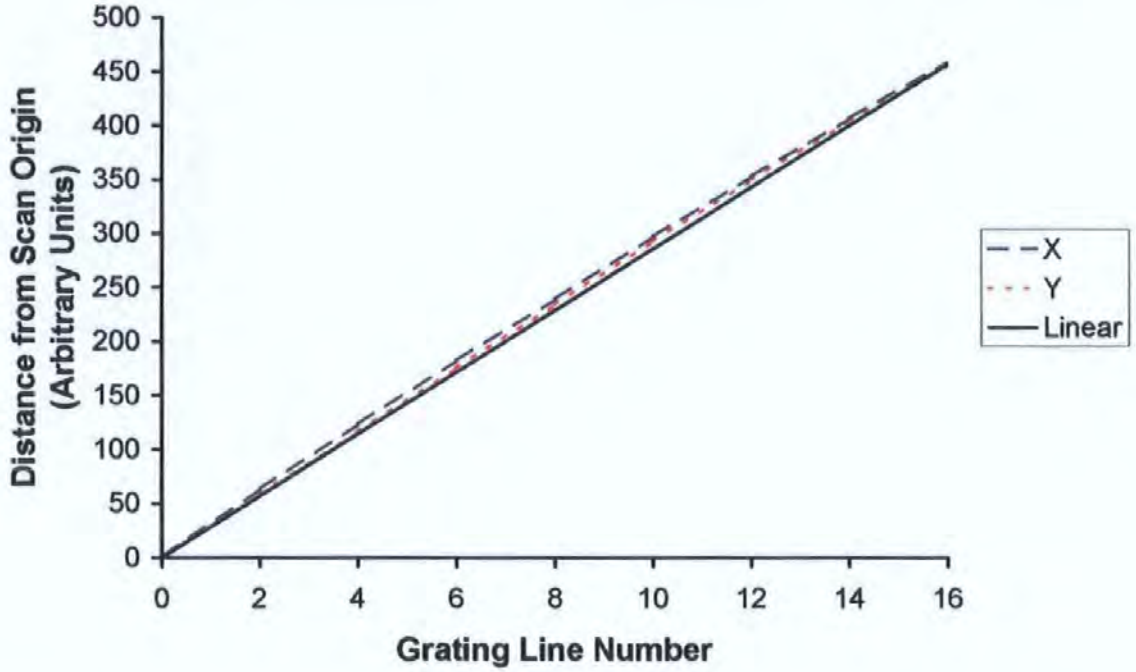


**Figure 47. Graph showing linearity of scan axes from XY sample measurements.**

The images taken of the XY calibration grating also allowed some basic quantitative z-axis calibration, as each grating line is specified as approximately 31 nm in height. This corresponds to a photo-detector response of approximately 1 V in this system, (see Sections 5.2.1-3), a value which is comparable to that shown in Figure 48. Given that the XY calibration sample documentation did not specify the tolerance of the grating line height, merely stating an approximation, the result shown in Figure 48 is taken as supportive of the work in previous sections, but not affecting those results in terms of the final instrument calibration.

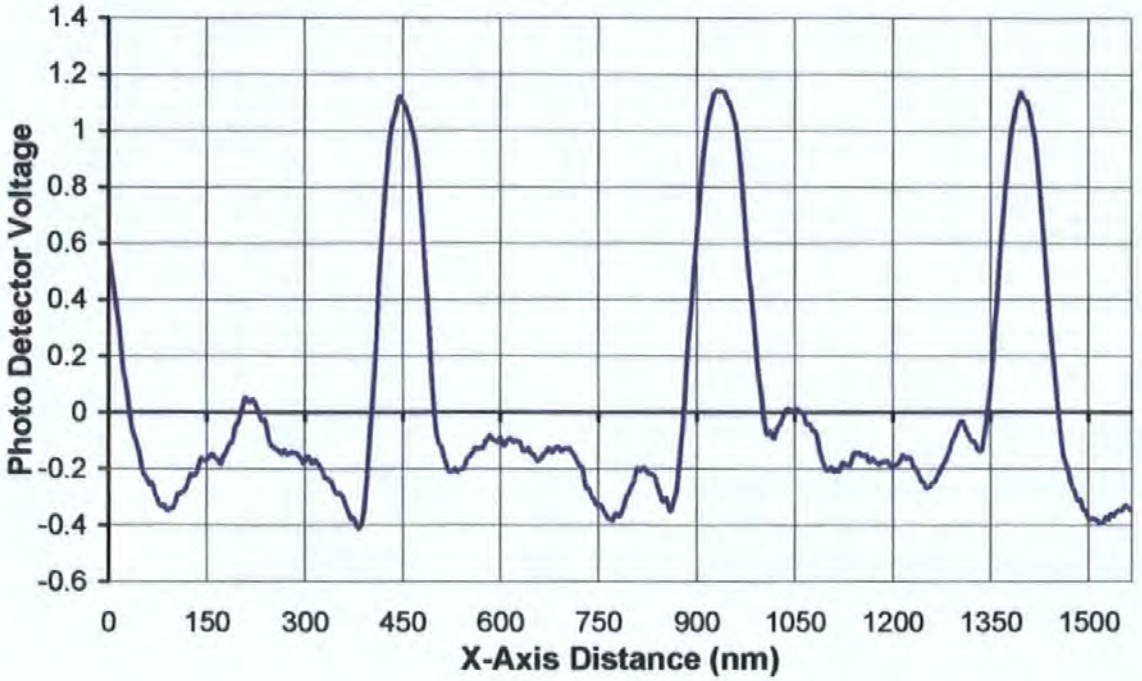


**Figure 48. Profile (signal voltage) of a line from an image of the XY calibration grating.**

## *5.3 System Operation & Specification*

The system described in this work is designed for anyone to use with very little prior experience in SPM instrumentation. The mechanical set-up of the system is straight forward, for example including cantilever mounting, laser alignment and head positioning as has been described in the previous Chapter. The electronic part of the system is completely self-contained and fine-tuned such that it only requires power to the different components (PZT High Voltage Drivers, Instrument Rack, Laser Diode and DC-Motor) to operate. The system's computer interface uses a GUI that only requires familiarity with the operations being controlled. The software is modular, with all components accessed from a common menu screen.

The modules can be summarised as follows:

- **Reset DSP**

  Resets DSP card and DAQ daughter card ready for new imaging session.

- **PC Oscilloscope**

  Computer based oscilloscope to check signal(s) from system electronics.

- **DC Motor Approach**

  Displays photo-detector signal and controls DC-Motor for cantilever coarse approach. Computer can also display video feed from CCD camera simultaneously.

- **Z Approach/Signal Test**

  Displays photo-detector signal and controls PZT translator for fine approach and cantilever positioning. Also used for test signals to z-axis for calibration and so forth.

- **Static Non-PID Scan (Contact/Non-Contact)**

  Sample raster-scan with no PID control, real-time imaging and image save, with limited image processing options.

- **Static PID Scan (Contact/Non-Contact)**

  Sample raster-scan with PID control loop, real-time imaging and image save, with limited image processing options.

- **DC-Motor Withdrawal**

  Sends DC-motor to original start position, moving cantilever away from sample.

- **Quick Image View**

  View in 2d or 3d image data, usually from images taken in current session. Includes calibrated scaling of image in x, y and z.

- **Image Processor Suite**

  Link to Scanning Microscope Image Processing Suite (LabVIEW based) - BSc Final Year Project by Sam Glasser, 2002 (University of Plymouth).

To conclude this section, Table 2 outlines the specifications of the SPM instrument described in this work.

**Table 2. SPM Specifications.**

| | |
|---|---|
| Detection System | Focussed Laser Optical Beam Deflection |
| Scanning Mechanism | Piezoelectric Tube Scanner with Passive Extender |
| Maximum Scan Size | 15.77 µm x 15.77 µm<br>Resolution 30.54 nm (500 steps) |
| Minimum Scan Size | 240.5 nm x 240.5 nm<br>Resolution 4.81 Å (500 steps) |
| Image Resolution | Image Size - 500 x 500 Pixels<br>(Typical, can be 1000 - 5000 per side)<br>Number of Image Scales – 65535 |
| Sample Coarse Approach Mechanism | Closed Loop DC-Motor |
| Sample Fine Approach Mechanism | Piezoelectric Translator |
| Sample Positioning Resolution | Coarse Approach - 14.3 nm<br>Fine Approach - 0.7 nm |
| Measured Lateral Resolution | Topographic Mode - 10 nm (Contact)<br>Magnetic Mode - 50 nm (Non-Contact) |
| Vertical Sensitivity | 1 nm (Static mode measured noise figure) |

The specifications outlined in Table 2 show that a functional SPM instrument has been produced that is capable of high-resolution imaging comparable to previous similar systems [47] [49]. One point to note is the measured vertical sensitivity of 1 nm, which appears relatively poor when compared to the original specification in Section 2.2.6. This value is the actual overall measured level when in normal static mode operation. If a resonant mode was implemented the sensitivity of the instrument would be expected to increase by two orders of magnitude, i.e. to a possible 0.1 Å, as identified in Section 2.2.6.

## 5.4 *Future Work*

At the time of writing the microscope system was working in contact force microscopy mode for topographical studies and static magnetic force microscopy mode for imaging magnetic structures. These are the two simplest methods of acquiring images. In the magnetic case, this mode of operation is only effective for samples with strong magnetic fields, however for the further work described in the following Chapters this method is acceptable for proof of concept. It must be taken into account that the main contribution to knowledge of this work is not the development of the instrument, but rather the new probe for MFM discussed in later Chapters. The system is designed to operate in a LiftMode style, using the DSP control structure, however this has yet to be successfully implemented. In addition, it should also be possible to implement resonant modes of imaging, both for magnetic studies and topographic (Tapping™ mode), producing much greater sensitivity in the z plane. A further possibility is to implement laser modulation, using lock-in techniques to reduce noise and hence increase the instrument's sensitivity.

Although the mechanical and electronic systems are completely operational, there are several possible enhancements that could be made. For example, the instrument currently uses a manual micrometer based XY table for sample positioning. This could be motorised, and hence computer controlled, using DC-motors similar to that used for coarse approach of the cantilever. In a similar vein, it would be possible to do the same for the mirror laser alignment and photo-detector alignment. Also the laser focus could be enhanced using a PZT fine-focus attachment. All of these additions would be computer controlled by the user. This opens the possibility of automating certain processes, for example laser alignment and laser focussing. It could also allow the instrument to be operated remotely, although of course to change the sample and cantilever would still require a physical presence.

The instrument is designed to be used to implement the novel electromagnetic MFM probe described in following Chapters. The probe is based on a standard cantilever chip form that can directly replace the industry-supplied AFM/MFM cantilevers used in the instrument. The probe is also designed to utilise the standard modes of imaging discussed in the preceding work, requiring no operational changes. The probe will require additional signal wiring, however the instrument has the necessary spare capacity for this. Further design considerations for implementing the novel probe and new methods of operation are discussed in later Chapters.

# 6 Conventional SPM Results

## *6.1 Atomic Force Imaging*

The very first tests of the MFM's imaging capability were carried out in AFM contact mode. This was primarily to calibrate the instrument in terms of lateral and vertical scan, but also provides a useful imaging routine. The very first successful image of this sort is shown in Figure 49 below, showing a 1.5 μm x 1.5 μm contact mode scan of a sample of hard disk drive platter. It shows the granular structure of the CoCr surface. In addition, grooves from the texturing process are also clearly visible running diagonally across the image.

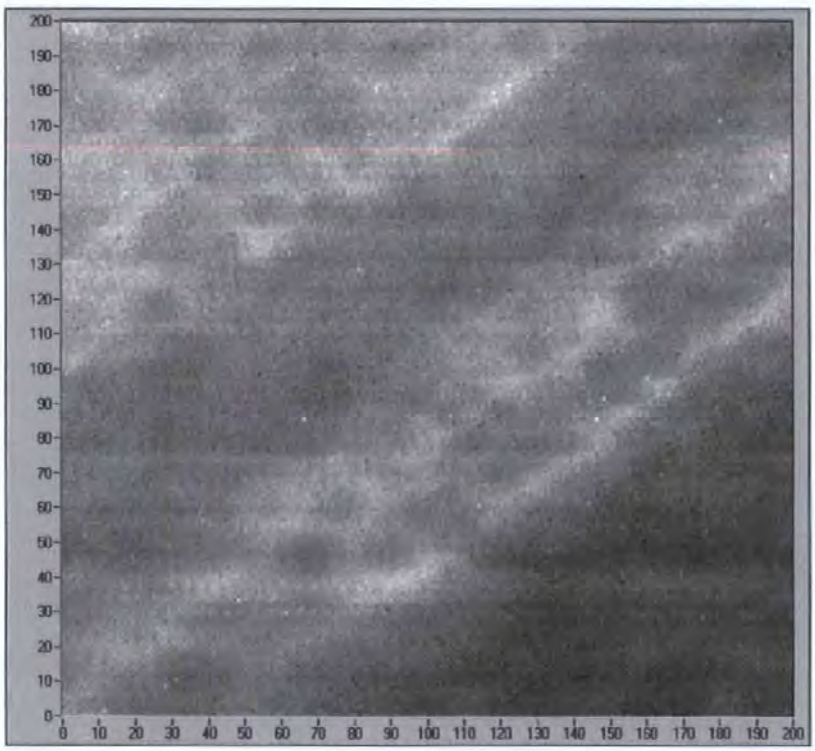


**Figure 49. First successful AFM contact mode image - Hard Disk Platter Topography (1.5 x 1.5 μm).**

Figure 50 shows later images of the hard disk platter, with two different scan areas. The grain structure is much clearer in this later case. The images compare reasonably well with previous work by Crozier [49]. Images by Crozier of the same structure are shown in

Figure 51. The grain structure is clearer in the Crozier image, however comparison with the images in Figure 50 shows that the system reported here is working correctly, and capable of imaging structures to the same level as past instruments.

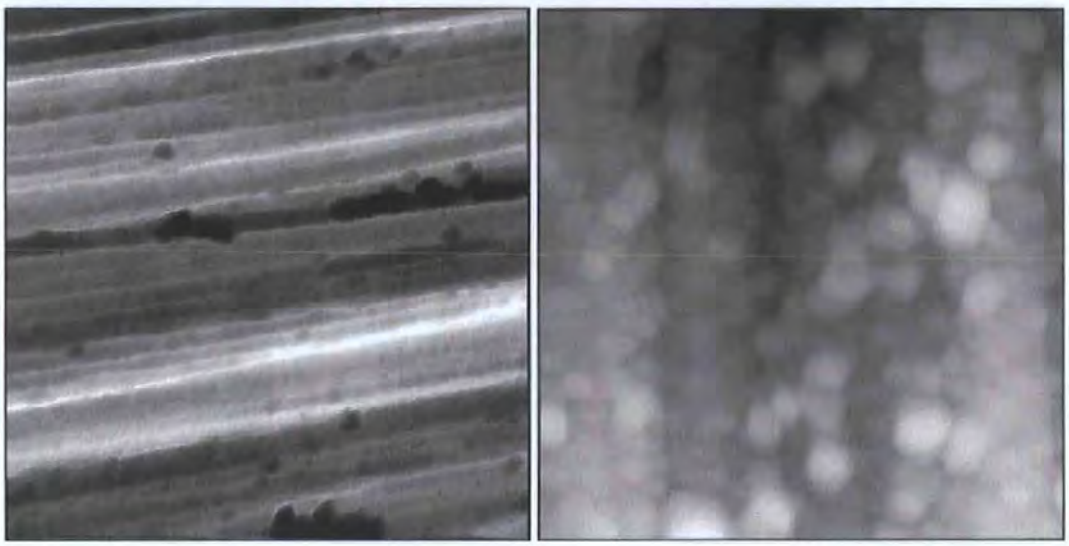

**Figure 50. AFM contact mode images - Hard Disk Platter Topography 4.5 x 4.5 μm (left) & 1.5 x 1.5 μm (right).**

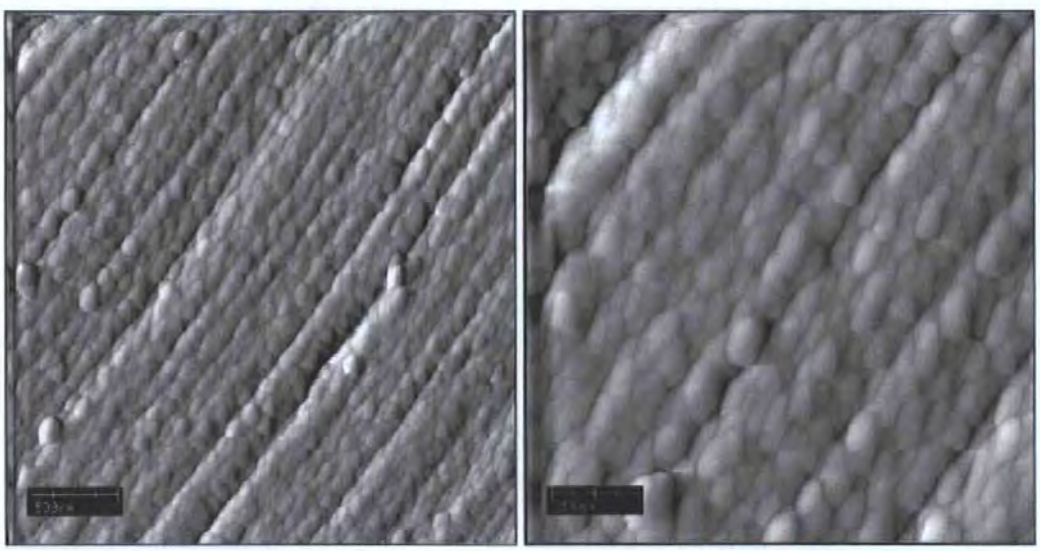

**Figure 51. AFM contact mode images - Hard Disk Platter Topography 3 x 3 μm (left) & 1.5 x 1.5 μm (right) - © P Crozier [50].**

Further AFM contact mode images were taken of the surface of a CD supplied by the manufacturer without its lacquer layer applied. Figure 52 below shows a three dimensional image of a single data pit, note that as the microscope imaged the label side of the CD the

pit appears as an actual indentation (pit), not the bump seen from the polycarbonate side of the CD by the reading laser. The depth of the pit, measured at approximately 140 nm by the instrument, is very close to the theoretical pit depth of 130 nm ($\lambda/4$). As the image is from the lacquer side, i.e. in contact with the aluminium layer, this discrepancy is possibly due to the edge profile of the sputtered aluminium layer. This image shows that the microscope was calibrated and working as expected.

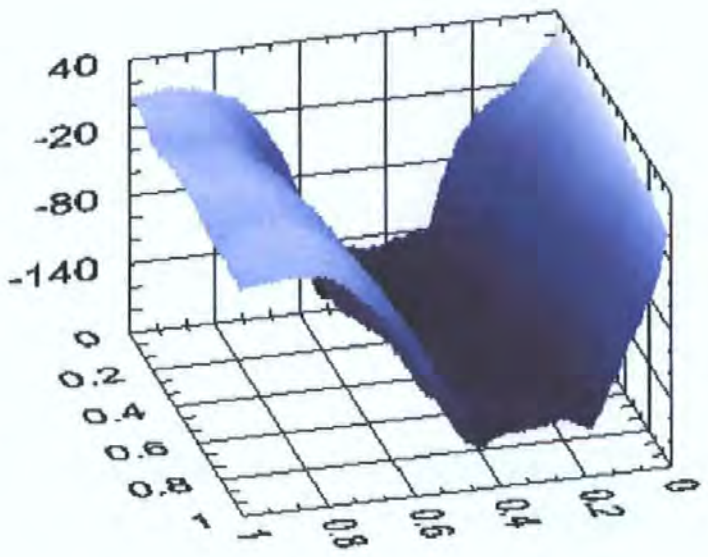


**Figure 52. AFM contact mode image (3D) - CD Data Pit (x, y: μm, z: nm).**

The feature shown in Figure 52 was imaged again but over a larger area of 1.5 μm x 1.5 μm, shown in Figure 53. Again this image shows the pit with approximately 140 nm depth. Unfortunately the end points of the pit were not revealed in this image, however, CD data pits can be up to 3.56 μm long. Figure 54 shows an image of a much larger area of the CD surface, approximately 8 x 8 μm, taken using the DSP control loop in order to keep the tip-surface interaction constant against the sample bowing effect (see Section 2.1). In this case the image shows the feedback signal. The CD pits and tracks (track width 1.6 μm) can clearly be seen as dark features, whereas the white marks are contamination (dust particles).

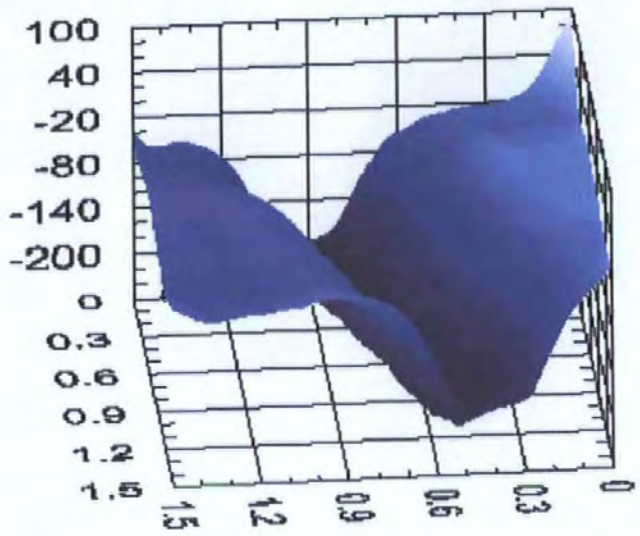


**Figure 53. AFM contact mode image (3D) - CD Data Pit (x, y: μm, z: nm).**

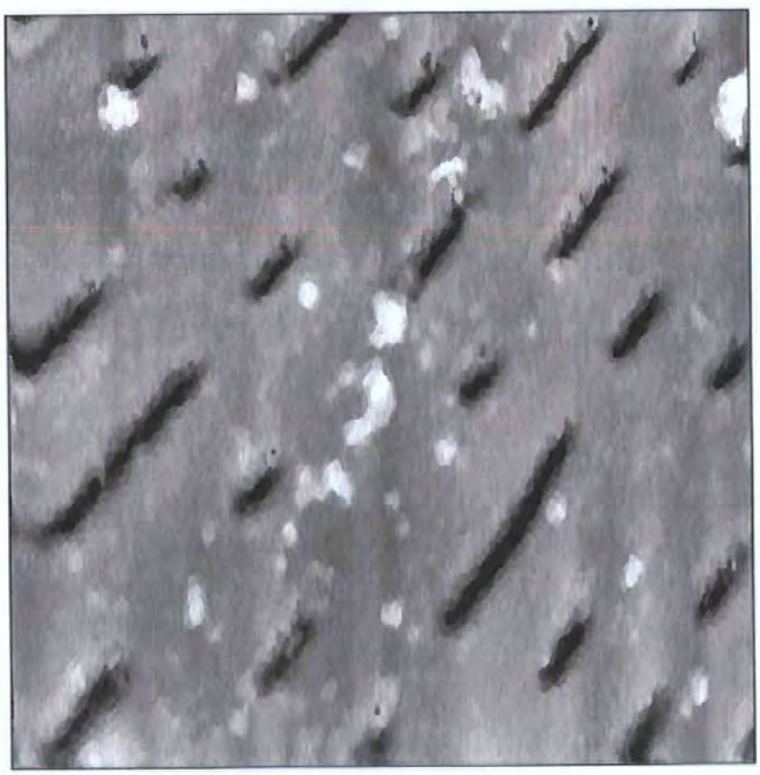

**Figure 54. AFM contact mode image - CD Data Tracks (8 x 8 μm).**

## 6.2 *Magnetic Force Imaging*

The first magnetic images by the instrument were of the garnet layer of a bubble memory chip. These were acquired using static mode magnetic imaging with a cobalt coated Microlever. Two examples are shown in Figure 55, where the perpendicular domain pattern can clearly be seen as white and black bands.

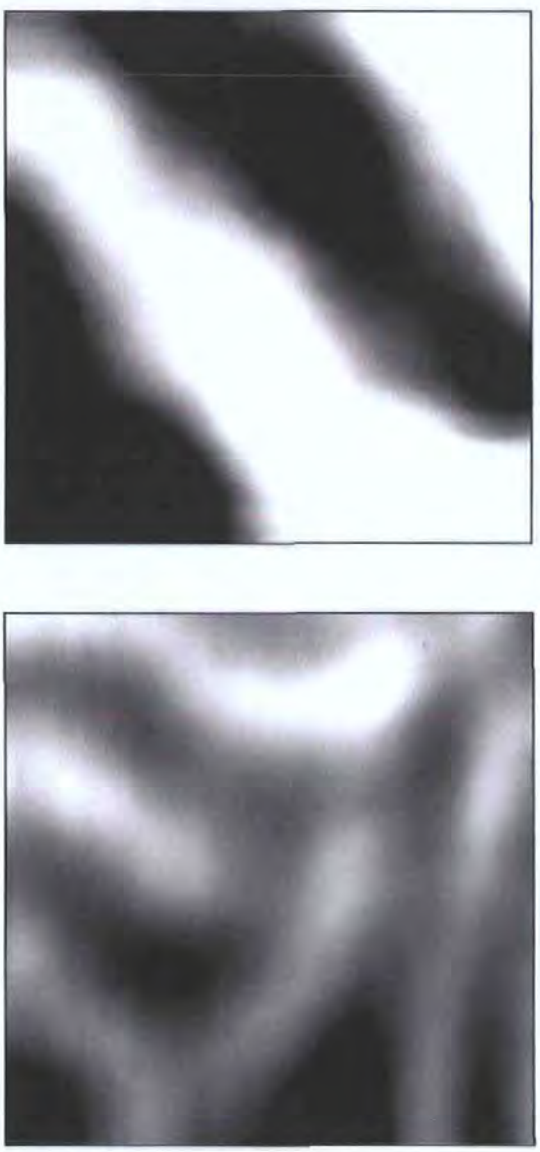

**Figure 55. Static mode MFM images of Garnet Layer on Bubble Memory, 6 x 6 μm (top) & 15 x 15 μm (bottom).**

This allows us to compare the results with an earlier image, shown in Figure 56, taken using a Magneto-Optic Kerr Effect Scanning Laser Microscope (SLM) by the author [61].

The image also clearly shows the same domain structure as that found by the MFM. The SLM produces an image over a much larger area, but at a reduced, diffraction-limited, resolution.

**Figure 56. Kerr Effect image of Garnet Layer on Bubble Memory (30 x 40 μm).**

Further work is required to improve the magnetic imaging capability of the system, however the results in Figure 55 show that the system is capable of magnetic contrast. The Systems and Materials for Information storage (SMI) group at the University of Twente, the Netherlands, have been contacted regarding the CAMST MFM Reference Sample that they manufacture. This would provide a standard to use to improve the MFM, allowing it to be compared against other systems. Unfortunately at time of writing SMI did not have any CAMST samples left, but will supply one as soon as they have finished preparing new ones.

# 7 The New Electromagnetic MFM Probe

One of the fundamental subjects in MFM research is the design and function of the probe used to interact with a magnetic sample's stray fields. Standard MFM probes, based on AFM cantilevers, use silicon tips that are magnetically sensitised using ferromagnetic thin films. Unfortunately this design has several inherent problems. First of all a variety of different designs and coatings need to be used depending on the magnetic properties of the sample being imaged, most significantly if the sample is magnetically 'hard' or 'soft', as, for example, the magnetisation of the tip may alter the magnetisation state of the sample being imaged. This means that an instrument must be reconfigured with a new probe each time a new type of sample is to be imaged. Furthermore, the magnetisation of the standard probe's tip can suffer from hysteresis over time, as well as wear and damage during its useful life. Also, the domain structure at the tip may change even during scanning, because of its interaction with the sample's stray field, making imaging inconsistent. These imperfections can have serious consequences in the acquisition of useful and quantifiable data. The following sections present a novel design as an answer to the standard probe's weaknesses.

## *7.1 The Initial Idea*

The new probe uses an electromagnetically-induced field as a replacement for the standard probe's stray field. Although electromagnetic MFM probes have been reported before, this design is unique [62]. The uniqueness of this new design is now discussed. The field is induced around a micro-fabricated aperture in a conductor sheet using a controlled current. The aperture is situated near the end of a standard cantilever that has been coated in a conductive material, for example gold. This design has the advantage that the probe's field intensity is standardised, and can be varied, and hence its interaction with the specimen can be controlled. The field distribution can be calculated to high accuracy since it arises

solely from the geometry of the current flow and aperture, not from a highly non-linear magnetic material. This means that the results will be both repeatable and quantifiable. In addition, it may be possible to vary the probe's magnetic characteristics during imaging, allowing many different measurements to be made on a single sample during the same scan session.

## *7.2 Modelling the eMFM's Field Distribution*

Using the Biot-Savart law, a change in magnetic field intensity, **H**, normal to the conductive material's surface is produced by changing the current density within it, given by,

$$\mathbf{H} = \frac{1}{4\pi} \cdot \int_S \frac{\mathbf{J} \cdot \mathbf{R}}{|\mathbf{R}|^3} ds \tag{20}$$

where, **J** is current density vector and **R** is the vector describing the position in space at which **H** is calculated.

By placing an aperture in a sheet of conductive material with constant linear current density, such that the current flows parallel to the sides of the conductor, current must flow around the aperture, resulting in a change in its density. This is depicted in Figure 57, where a cantilever is coated top, base and end with a conductor, such that the current flows down the base and past the aperture, where in this case the aperture is placed on a pyramidal tip, therefore allowing the probe to be used for topographic scanning. The current then returns by flowing around the end of the coated cantilever and along its top surface.

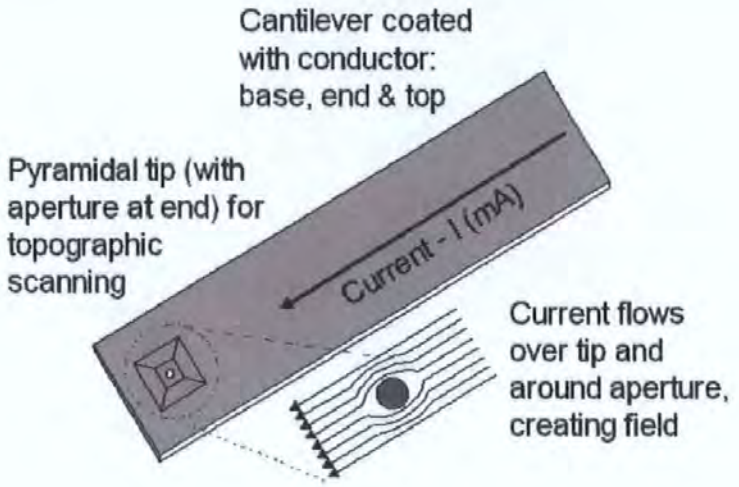


**Figure 57. Simplified diagram of basic probe design viewed from below. Current flows around an aperture, causing a change in its density and thus a change in magnetic field intensity normal to the surface.**

The first model used in this work to calculate the field intensity for the proposed probe was based on previous work by Bobeck et al. [63]. In their work on current access bubble memory the magnetic field intensity normal to the plane of an aperture, $H_z$, in Oersteds, is calculated above a circular aperture in a flat surface. This considered an infinitely thin conducting sheet, in the plane z = 0, extending to infinity, with a circular hole in its centre, supporting a constant current density $\mathbf{J} = J_o\hat{i}$ at points infinitely removed from the hole. The problem of obtaining the z component of the magnetic field at any point above the sheet was taken in two parts. Firstly, the solution of a boundary-value problem to calculate the linear current density in the plane of the sheet, secondly, integration over the source distribution to obtain the field. To solve the current density distribution Bobeck et al. used theoretical hydrodynamics to calculate the two-dimensional fluid flow about a cylindrical obstacle. This gives the current density as

$$\mathbf{J} = J_o\left[1-\left(a/\rho\right)^2\cos 2\phi\right]\hat{i} - J_o\left(a/\rho\right)^2\cos 2\phi\hat{j} \qquad (21)$$

where, $J_o$ is the constant linear current density at infinity, $a$ is the hole radius, $\rho$ is the radial source coordinate and $\phi$ is the angular source coordinate. Note that the current density is tangential at $\rho = a$ and $\mathbf{J} \to J_o \hat{i}$ as $\rho \to \infty$.

Bobeck et al. then obtained the magnetic field by projecting Equation 20 onto the z axis and expressing all components in cylindrical coordinates, obtaining the double integral in Equation 22.

$$H_z = \frac{J_o}{4\pi} \int_0^{2\pi} d\phi \int_a^{\infty} \Phi(r, \theta, z, \rho, \phi) d\rho \tag{22}$$

This equation was then simplified using radial integral tables, however the remaining angular integration must be done numerically. The full, reduced version of (22) is shown in Appendix 1, however it can be condensed to the following,

$$H_z = \frac{J_o}{4\pi} H \sin\theta \tag{23}$$

where $H$ is described in Appendix 1, and $\theta$ is the angle of the point with respect to the current flow as shown in Figure 58 below.

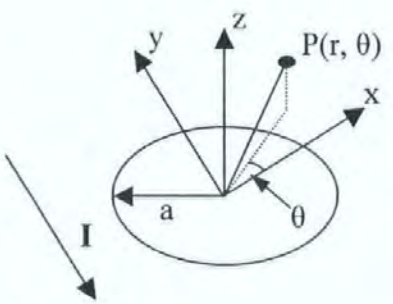


**Figure 58. Coordinate system for the model.**

**Where r is the distance from the aperture centre, a is the aperture radius and z is the height above the aperture. Also, I is planar current flow, P is a point position in space, $\theta$ is the angle of point P projected onto the plane of aperture against current flow I.**

The calculations were implemented in MathCAD for this work. The calculations performed showed that the work of Bobeck et al. had been reproduced correctly. This then allowed the mapping of $H$ from (23), across the plane of a circular aperture, at different heights, as shown in Figure 59. Given this, it is possible, knowing $J_o$ and $\theta$, to estimate $H_z$, although in this work once a specific aperture and scanning height (z distance above aperture) was defined the field was calculated using Equation 23.

The graph in Figure 59 shows that two opposite peaks in the magnetic field intensity will occur at the edge of the circular aperture, due to the splitting of the current flow around the aperture, as such the value calculated is dependant on $\theta$. The field intensity is much greater closer to the plane of the aperture, and additionally presents peaks of greater intensity with a lower spatial distribution.

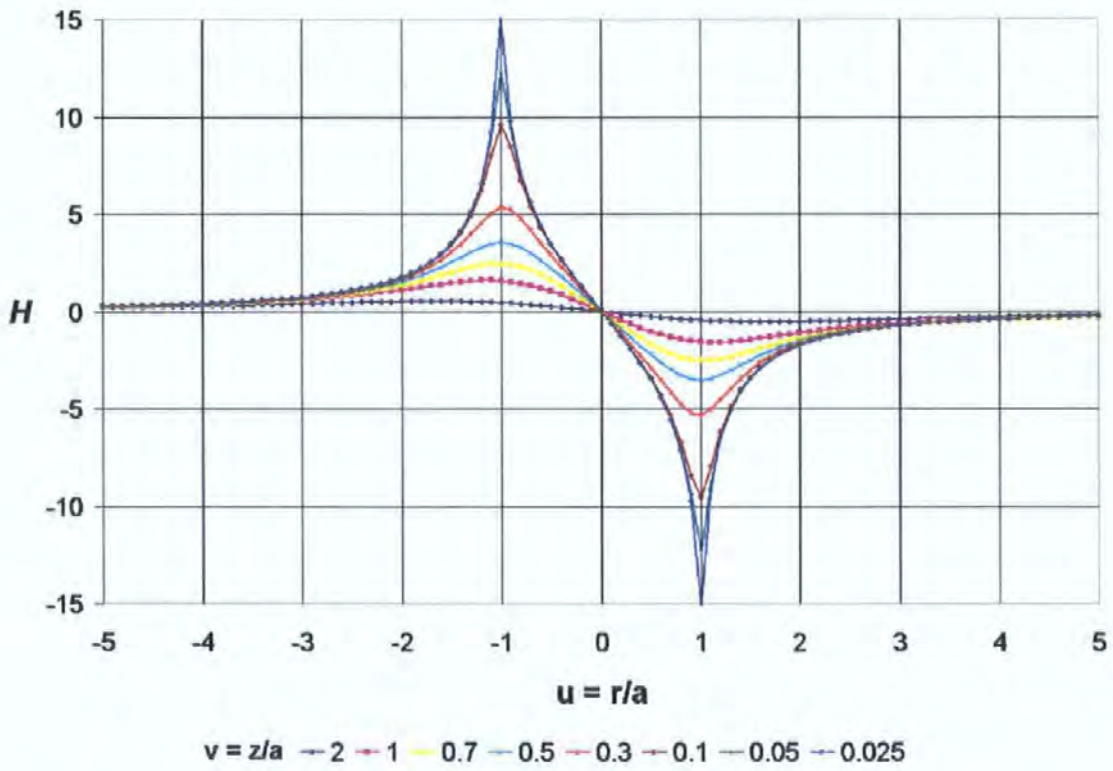


**Figure 59. Current sheet with circular aperture calculation of *H*.**

**The dimensionless *H* of the modelled magnetic field intensity $H_z$ is shown as a function of distance from the centre of the aperture (r/a) and height above the plane of the aperture (z/a).**

Figure 60 shows the relationship between the applied current density and the magnetic field intensity about a 2 μm circular aperture. Clearly the intensity increases linearly with the applied current density, as shown in the graph inset. Figure 60 also shows that the probe can be used to produce a field intensity comparable to standard probes, as discussed by Hill [64].

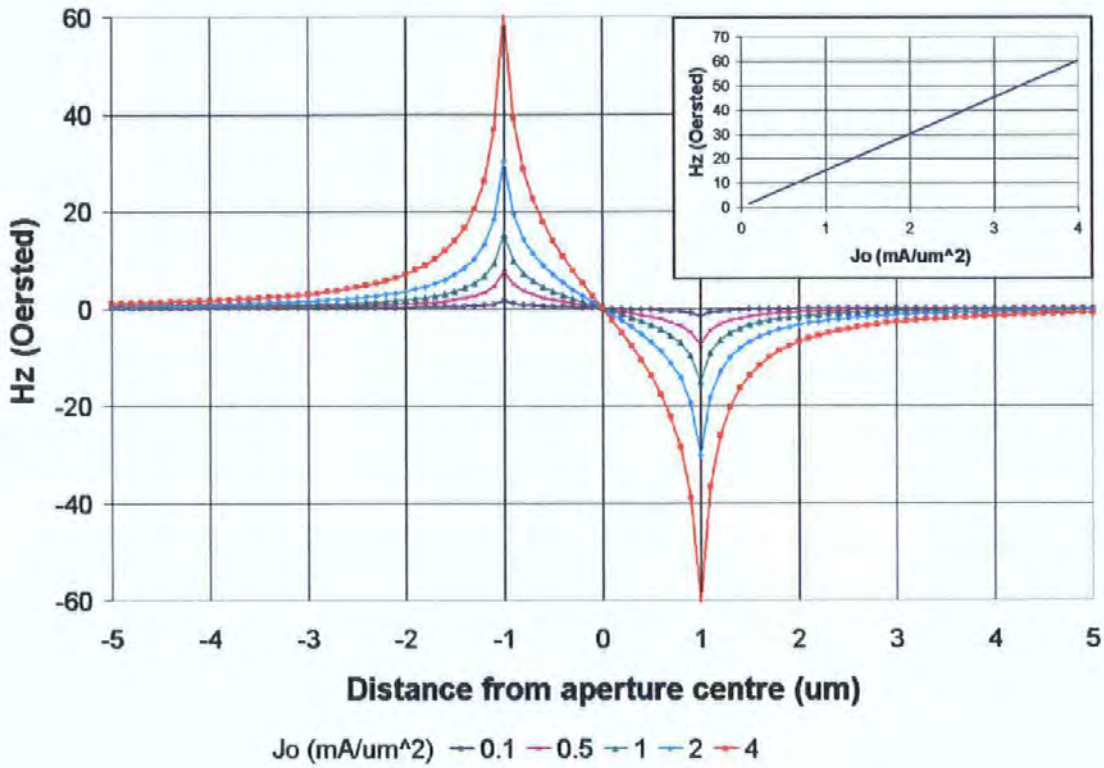


**Figure 60. Current sheet with circular aperture calculation of $H_z$ for I.**

**The magnetic field intensity $H_z$ shown as a function of current density $J_o$ (mA/μm$^2$) for an aperture of 1 μm radius.**

The lines in Figure 61 show that the peak field intensity and the peak spatial distribution diminish as the aperture diameter decreases. The field is still at a valuable level for the smallest aperture shown, indicating that for the circular aperture probe the resolution will be related to the minimum aperture size physically possible.

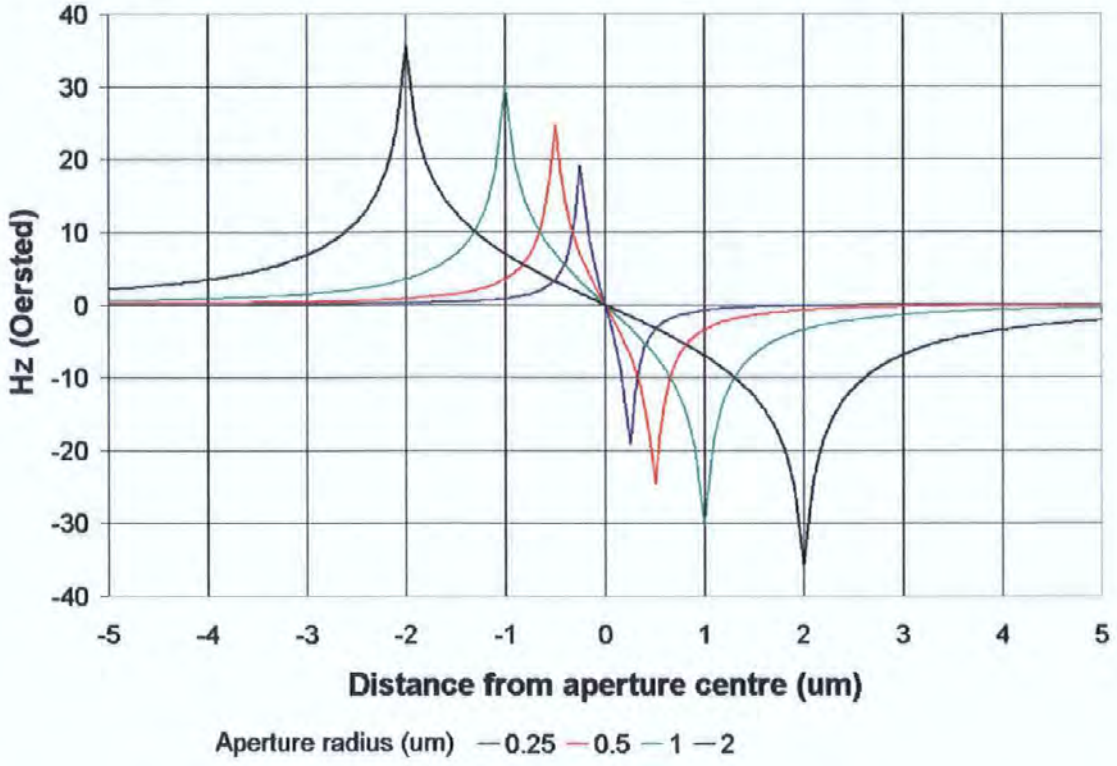


**Figure 61. Current sheet showing $H_z$ for different circular apertures.**

**The magnetic field intensity $H_z$ shown as a function of aperture radius (μm) for a constant current density of 2 mA/μm², and height of 25 nm.**

The results from the MathCAD model suggest that there are three primary variables to define for a circular aperture in order to generate adequate field intensity, $H_z$, over the smallest area, i.e. given that resolution is proportional to spatial field distribution. These three variables are the linear current density ($J_o$), scanning height ($z$) and the size (diameter) of the circular aperture ($a$). Clearly generating adequate field strength, defined by Equation 23, is determined by increasing the current density, as shown in Figure 60, and decreasing the scanning height, as in Figure 59. To increase resolution the aperture diameter must be set as small as possible, see Figure 61.

There are practical limits to the amount of current, discussed further in Section 8.1, and of course the size of aperture possible in this design. So, for primary image modelling purposes, $H_z$ was calculated for a height of 25 nm above the surface of an aperture of

radius 250 nm, with a current density of 2 mA/μm$^2$, whereby all three variables are at reasonable practical physical levels. The field intensity $H_z$ for this model in two dimensions about the aperture is shown in Figure 62. Of course, by controlling the applied current, and hence the linear current density, the field strength can be varied, and even reversed, if required.

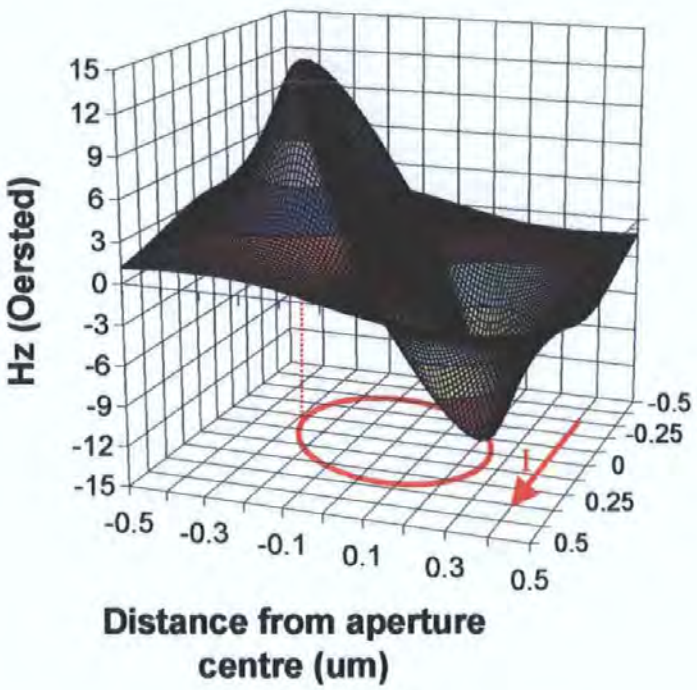


**Figure 62. Magnetic Field Intensity, $H_z$ (Oe), normal to a circular aperture. Shown as a function of the sheet density of the current. $H_z$ is shown at 25 nm above the surface of a 0.5 μm diameter aperture, with a current density of 2 mA/μm$^2$.**

The magnetic field intensity has been shown in Oersteds in this work to allow comparison with previous work on MFM probes. The field intensity and distribution from Figure 62 shows that this design is comparable to a standard MFM probe, as discussed by Hill [64]. The two dimensional graph in Figure 62 clearly demonstrates the effect of the current flowing around the aperture, whereby the current density, and hence field intensity, is greatest at the two points on the edge of the aperture at ±90° ($\theta$) to the current flow. It should be noted at this point that standard coated MFM tips have been described with

apertured tips, which were used to image in-plane stray fields [65], showing at this early stage that manufacturing techniques are available to create the new probe.

## *7.3 MFM Interaction - The Reciprocity Principle*

In general, the simulation of MFM images has been realised by considering the interaction between the magnetisation of the MFM's tip and a specimen's stray field. This allows the calculation of the force acting on the tip due to the field from the specimen. However, given Newton's third law, which states that every action has an equal and opposite reaction, the principle of reciprocity, as discussed by Wright and Hill, can be used [66] [67]. As such the force acting on the specimen due to the tip's stray field is calculated, which is the inverse of the force acting on the tip. The tip-sample configuration and notation used in this work is shown in Figure 63 below.

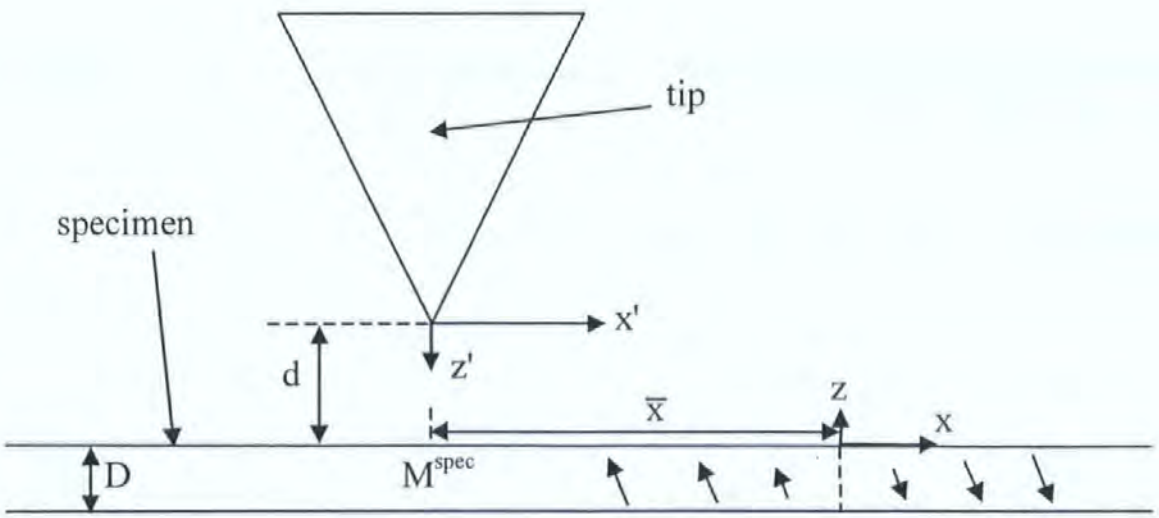


**Figure 63. MFM tip and specimen geometry and coordinate system.**

The reciprocal force acting in the vertical, z, direction between the tip and the specimen can be expressed by,

$$F_z^{tip} = -F_z^{spec} = -\int_{spec} \sum_i M_i^{spec}(r') \frac{\partial H_i^{tip}(r+r')}{\partial z'} d^3r' \qquad (24)$$

where $i$ corresponds to the directions x, y, or z, $M_i^{spec}$ is the x, y or z component of the magnetisation of a specimen volume element and $H_i^{tip}(r+r')$ is the stray field from the tip at that specimen volume element.

This then allows the simulation of the new probe, since the calculated field intensity, as shown in Figure 62, can be used with (24). Note that the force calculated in (24) is that produced when an MFM is operating in static, or DC, mode. The resonant, i.e. force gradient, or AC, mode can be described by taking the second derivative of the tip's stray field.

## *7.4 Computer Image Simulation*

In order to create image simulations a model is needed for the magnetisation of the specimen. In this work both perpendicular and longitudinal magnetic media bit transitions have been considered [68]. Each uses a simple arctangent model, as for example for a perpendicular transition in the x (along track) direction, as given in Equation 25,

$$M_z = \frac{2}{\pi} \cdot M_o \cdot \arctan\left(\frac{x}{a_p}\right) \tag{25}$$

where $M_z$ is the vertical magnetisation component, $M_o$ is the remanent magnetisation state, $x$ is the position on the transition and $a_p$ is the transition width parameter. This is then extended in the y direction to produce a model magnetic specimen.

To produce a quick, efficient computer image simulation of the interaction between the probe and a magnetic specimen, a FFT convolution of the probe's gradient field and the specimen magnetisation distribution is performed [67].

Firstly it is assumed that the tip-specimen system is two-dimensional, unvarying in the y direction, then the force, following Equation 24 is given by

$$F_z^{spec}(\bar{x}) = \int_{-\infty}^{\infty}\int_{d}^{d+D} M_z^{spec}(x'-\bar{x})\frac{\partial H_z^{tip}(x',z')}{\partial z'}dz'dx' \tag{26}$$

If it is then assumed that the tip field gradients are in effect constant throughout the specimen, then Equation 26 becomes

$$F_z^{spec}(\bar{x}) = D\int_{-\infty}^{\infty} M_z^{spec}(x'-\bar{x})\frac{\partial H_z^{tip}(x',z'=d)}{\partial z'}dx' \tag{27}$$

which is a correlation of the specimen magnetisation and the derivative of the tip field at the surface of the specimen.

To obtain the transfer function for this system we take the Fourier transform of (27) to give

$$F_z^{spec}(k) = DM_z^{spec}(k)^* \frac{\partial}{\partial z'} H_z^{tip}(k,z'=d) \tag{28}$$

where $k$ is the wavenumber or spatial frequency and * denotes complex conjugation. This complex conjugation can then be calculated using a FFT convolution. In this work National Instrument's LabVIEW software was used to perform this function on the raw data from the aperture field and specimen magnetisation models.

To take this further, in this form the field at a distance $z'$ below the surface of a two-dimensional field source in free space is equal to the field at the surface of that source multiplied by an exponential spacing loss term $\exp(-|k|z')$.

This allows (28) to be rewritten as

$$F_z^{spec}(k) = -|k|DM_z^{spec}(k)^* H_z^{tip}(k,z'=0)\exp(-|k|d) \tag{29}$$

so that the transfer function is actually $|k|$D times the product of the transform of the tip surface field and the exponential loss factor due to tip-specimen spacing. Therefore, in cases where the variation in stray field gradients through the specimen cannot be ignored, (29) is taken and transformed to obtain

$$F_z^{spec}(k) = M_z^{spec}(k) * H_z^{tip}(k, z'=0) \times \int_d^{d+D} \frac{\partial}{\partial z'} \exp(-|k|z') dz' \tag{30}$$

which can be solved as

$$F_z^{spec}(k) = M_z^{spec}(k) * H_z^{tip}(k, z'=0) \times \exp(-|k|d)[\exp(-|k|D) - 1] \tag{31}$$

this now contains an additional term due to the finite thickness of the specimen.

In the work that follows Equation 28 was used to simulate the MFM images, with the assumption that errors due to variation of the field through the sample will not greatly affect the overall result, i.e. to give a basic proof of the validity of this probe as an imaging mechanism.

Prior to running computer simulations, the probe imaging process, for a perpendicular domain transition, was considered as illustrated in Figure 64, to provide a check on the expected result. In this case, as the twin peaks from a circular aperture pass over the domain transition, it can be anticipated that their effect is cumulative, either negatively or in this case positively, because the magnetisation is either matched with the field peaks, or their inverse.

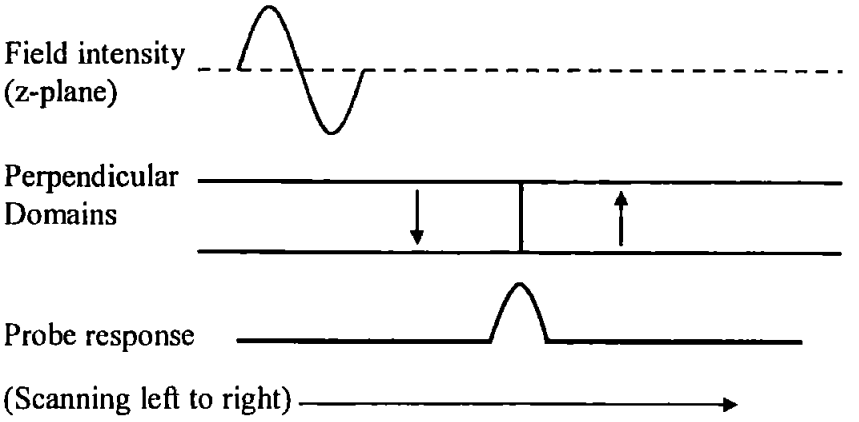


**Figure 64. Simplified 2-d illustration of probe response simulation.**

## *7.5 Initial Results*

The simulated static mode MFM images shown in Figure 65 and Figure 66 were created using the technique described in Section 7.4, using an aperture field similar to that shown in Figure 62. In Figure 65 an image of a perpendicular bit pattern has been created. The aperture 'probe', with a scanning height of 25 nm, has successfully imaged the pattern, specifically highlighting the bit domain transitions as dark or light lines, as discussed in 7.4 above. The shading of the line indicates the transition direction, although this depends on the orientation of the probe field, i.e. the direction of the current flow past the aperture. In this case the probe scanned left to right, with the negative field peak leading. Changing the direction of current flow, whereby the field is inverted, only reverses the contrast, not the resolution.

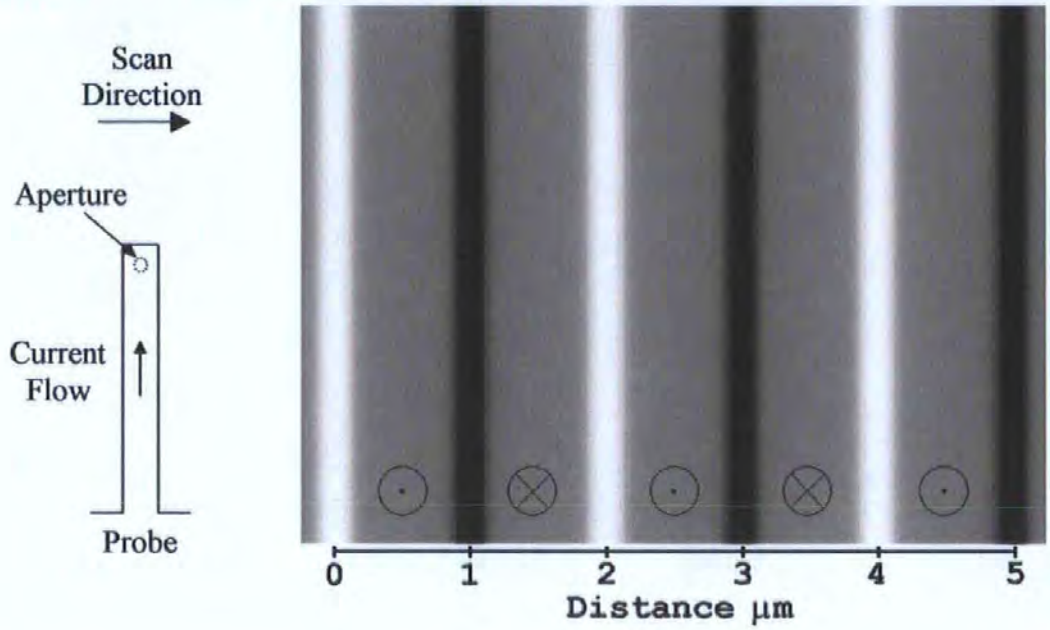


**Figure 65. Simulated MFM image of five 1 μm long perpendicular bits.**

**Uses the new probe, with a 250 nm diameter aperture. The probe scans the image from left to right. A dark or light line, depending on transition and probe field orientation, shows each transition; therefore contrast would be reversed if the probe field was inverted.**

In Figure 66 the new probe has been used to image a longitudinal bit. There is however a large artefact created by the probe's 'double-peak' field intensity. The transitions, shown by the dark and light shaded lines, are imaged twice, once by each of the field peaks, so creating a pair of lines for each transition. The distance between each line in a pair gives a good indication of the probe aperture size. This artefact could be removed using computer image filtering, although further artefacts may be introduced. A further answer, would be to adjust the aperture such that one peak is dominant over the other, e.g. a semicircular aperture to increase current density on one aperture side, whilst reducing it on the other.

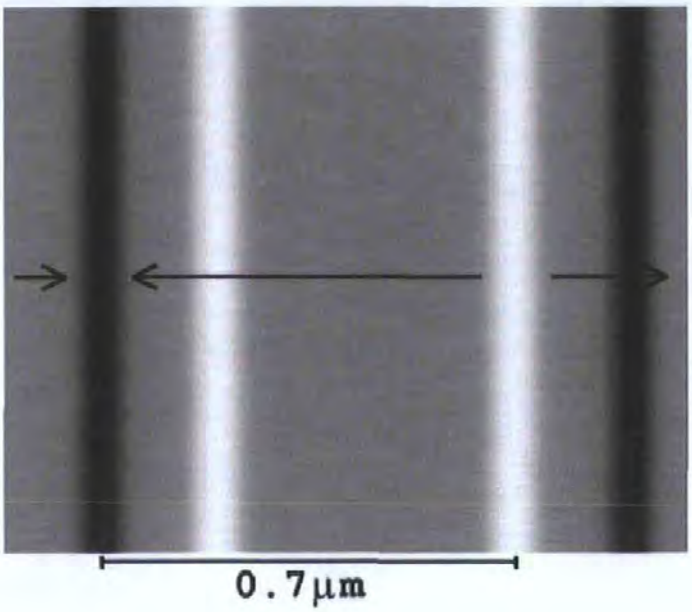


**Figure 66. Simulated MFM image of a 0.7 μm long longitudinal bit.**

**Uses the new probe, with a 250 nm diameter aperture. Note the double-peak effect, where each domain transition is imaged twice.**

In the case of the circular aperture the image resolution is directly related to the aperture's diameter because of the cumulative effect of the two opposite but equal peaks in field intensity. These occur at the two points directly above the edge of the aperture where the current density is greatest. In order to limit the physical problems of manufacturing a probe with sub-micrometer apertures, plus solving the longitudinal domain imaging artefact, changes in aperture geometry, e.g. semicircular, will be investigated in the following Chapter.

# 8 Developing the Electromagnetic MFM Probe

## *8.1 Practical Design*

Before attempting to build a probe an examination of its practical implementation was carried out. It was foreseen that the probe aperture would be placed on a tip, near the end of a standard bar or v-shaped cantilever, coated with a conductive material, e.g. gold, in such a way that the design allows for current flow down past the aperture, then back to its source. Because of this design, the fields from the coating on the whole of the cantilever must be taken into account. Also, the conductive material must be able to tolerate sufficient current to create the required field intensity, without damaging the probe, e.g. through thermal effects or electromigration.

### *8.1.1 Cantilever Fields*

One potential problem of the new probe is the effect and possible interference of the cantilever design and its conductive coating on the specimen magnetisation, the probe field and their interaction. In Figure 67 the magnetic field intensity normal to the surface of a bar shape cantilever is shown. This field intensity is of similar magnitude to the probe field, depending on the size of probe aperture and cantilever. However, this is considerably reduced, since with this design it is necessary to have a conductor on the top, end and base of the cantilever to create a current flow past the aperture. For example, a cantilever 20 μm wide, with a 0.5 μm thick conductive coating, and current density of 2 $mA/\mu m^2$, would have field peaks of approximately 7 Oe reduced to 2 Oe. A further step will be to place the aperture on a coated tip, moving it away from the cantilever surface, reducing the field from the sides of the cantilever further, as seen in Figure 67. This tip would also act as a topography probe for pre-MFM scanning in a LiftMode type mode of operation.

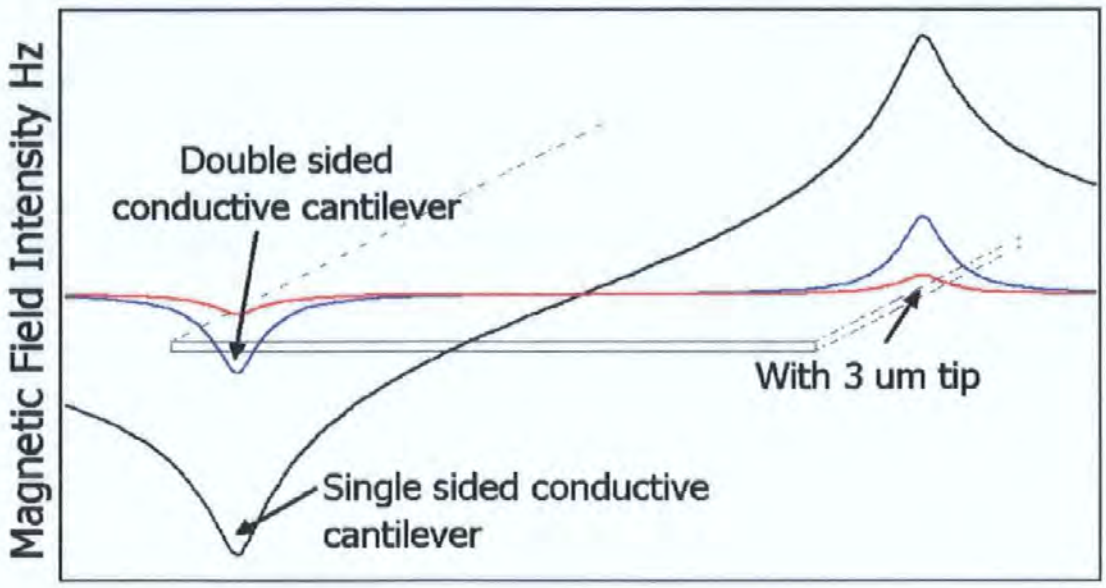


**Figure 67. Magnetic field intensity, $H_z$, 25 nm below a bar shape cantilever. Current flowing along a conductive material covering the base (black line), with current along the top, end and base (blue line), and with aperture on 3 μm tip (red line).**

### *8.1.2 Thermal Effects*

Due to the energy into the probe from the current flow, i.e. $J^2\rho$, where $J$ is current density and $\rho$ is resistivity, it follows that a Joule heating effect will occur. This may give concern over the possible effect on the cantilever in terms of reliability and lifetime, and also noise due to thermal effects as discussed in Section 5.1.3. Therefore a calculation of the heat generated within a simple probe design has been made. A simple one-dimensional model for heat dissipation in a flat conductor is used for proof of concept, considering a conductor connected between two semi-infinite heatsinks (the cantilever's leadouts) [69]. The steady-state excess temperature ($T$) is described by Poisson's equation as

$$\nabla^2 T - m^2 T + \frac{Q}{k} = 0 \tag{32}$$

where,

$$m = \sqrt{\frac{k_s}{ktd}}$$

given $Q = J^2\rho$, and $k$, $k_s$, $t$ and $d$ are the thermal conductivity and thickness of the conductor and substrate respectively. Given a probe conductor thickness ($t$) of 500 nm, as used in Section 8.2, grain boundary scattering and the Fuchs size effect will not produce a significant effect on the resistivity, allowing the use of the bulk value [70]. Therefore it is taken that the thermal conductivity is also not affected, following the Wiedemann-Franz law [71]. The solution of (32) for the temperature from the conductor, $T_c$, is then as given in (33) below.

$$T_c = -\frac{Q}{2km^2}e^{-mL}(e^{mx} + e^{-mx}) + Qe^{-mx}\left(\frac{td}{k_s} - \frac{1}{km^2}\right) + \frac{Q}{km^2} \qquad (33)$$

where, $x$ is 0 at the centre of the conductor, and $L$ is half the length of the conductor. Considering a gold conductor ($k$ = 320 W/m.K, $\rho$ = 2.2 x $10^{-8}$ Ω.μm) on a silicon substrate ($k_s$ = 1 W/m.K, $d$ = 1 μm), the temperature at the conductor is calculated to be 0.29 x $10^{-3}$ °C over ambient, with a dc current density ($J$) of 2 mA/μm$^2$, as used to simulate imaging successfully in Section 7.5. It was calculated that the conductor temperature would reach a temperature of 220 °C above ambient at a current density of 1.74 A/μm$^2$, a temperature at which previous research has shown that a thin film conductor would fail [69].

### *8.1.3 Electromigration*

A metal thin-film has a polycrystalline structure, wherein the orientation differs for each crystal grain, such that defects are scattered around the grain boundaries and some of the metal atoms in these defects have weak inter-atomic bonds. Electromigration, as described by Lloyd [72], is the transport of those metal atoms due to the momentum transfer from collisions between conducting electrons and those metal atoms. Lloyd describes this

momentum transfer with the help of a simplified argument. Considering an electron in a metal conductor; if there is no current flowing the electron can be treated as being at rest. Obviously there are no electrons at rest in any conductor, but an 'averaged' electron is imagined as an entity that possesses the average momentum of all the electrons that are equally distributed in all directions, such that this imaginary entity is considered as being at rest. Thus, although any specific electron is not at rest, the 'averaged' electron is, when calculated from the vector sum of all the moments. Upon application of an electric field and the passage of current this imaginary averaged electron would be accelerated by the electric field until it collides with a defect. When this collision occurs, the entire momentum gained from the field is transferred to a metal atom at the defect. Metal atoms with this momentum then migrate in the direction of the electron flow along the crystal grain boundaries where diffusion is easy. This migration can cause voids to form and grow, producing the problems of increased resistance and eventually open circuits.

Electromigration in the integrated circuit industry is usually considered in terms of the mean-time-to-failure of a circuit, and is calculated using scaling factors generated by experimental tests of the circuit's physical structure [72]. Whilst modelling work has been carried out to support this, it has not yet reached the point of replacing empirical data [73]. However, rule-of-thumb electromigration limits for dc current density in integrated circuitry, including large safety margins, have been given in the literature; these range between 10 and 100 $mA/\mu m^2$ [73] [74] [75]. It is these values that have been taken into account when using the new probe's field model, thus ensuring that the new probe is a feasible concept.

To take this further, for an ac signal, the electromigration conditions are different. Most importantly, given a symmetrical ac current, there is effectively no electromigration [72]. Thus, for symmetrical ac signals, current limitations should be based on thermal effects only [76]. This would still place a limit on the maximum rms current, as discussed in

Section 8.1.2, but the limit is considerably higher than the current limitations given in the literature. For asymmetrical ac signals, e.g. pulse trains, the frequency, and duty cycle (therefore average current value), require consideration. Low frequency asymmetric signals (e.g. <100 kHz) can be considered as very similar to dc, because any relaxation is significantly less than the electromigration caused by the current. At higher frequencies the system cannot respond dynamically, to the current 'pulse' or relaxation, so that in this case the limit due to electromigration is the average current. This fact has been used in industry to simplify testing procedures, as only a dc current equivalent need be applied in experimental testing of circuits.

Returning to the new probe, this discussion shows that if an ac current signal (symmetrical or asymmetrical) were used then the maximum limit on current and therefore field intensity could be greatly increased, an important factor which is exploited in later sections.

### *8.1.4 Controlling the Probe Current*

In order to test the new probes a regulated current source was required, which could be controlled either by computer or manually. The initial circuit design to accomplish this is shown in Figure 68. The current regulator uses a low-dropout voltage regulator (U2) whose voltage feedback is derived from the input current by a current-sense amplifier (U1). This connection allows the regulator IC to oppose any change in output current. When powered from 5 V, the current source has a compliance range of 0 V to 4.7 V. A specific, regulated output level, between 0 mA and 250 mA, is set by applying 0 V to 5 V at the DAC Voltage Control Input, where 0 V = 250 mA and 5 V = 0 mA, thus providing digital control of the output current. Therefore, with a 16-bit resolution DAC (0-10 V), 7.6 μA current resolution is obtained at the Current Output.

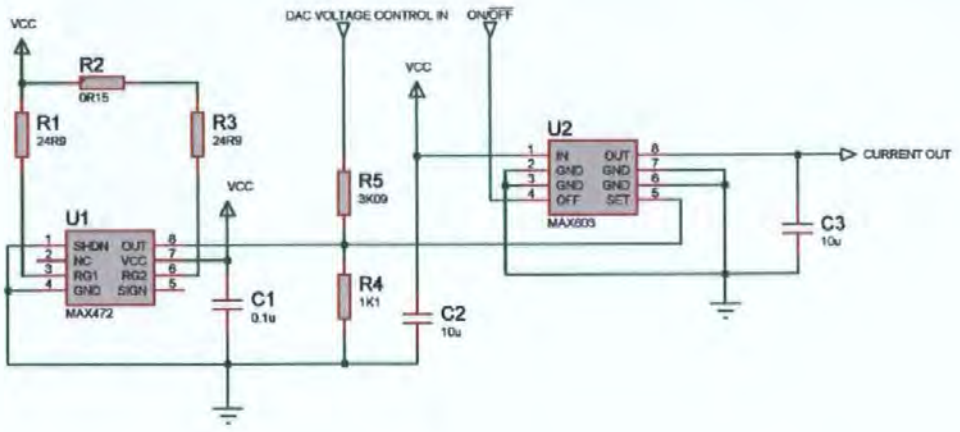


**Figure 68. Regulated linear current supply, 0 – 250 mA, operating on 5 V ($V_{cc}$).**

**U1 converts R2 current to a proportional output voltage, enabling the voltage regulator (U2) to produce a regulated output current.**

## *8.2 Finite Element Modelling of Probes*

As previously described in Section 7.2, one potential probe design combined a circular aperture with a topographic tip, and later in Section 7.5 a semicircular aperture is suggested. The work reported in Chapter 7 was based on a two dimensional model of the conductive material. Rather than expend a large amount of effort to expand this model technique into three-dimensions, with the ability to change the aperture geometry, a different, faster, approach was sought. The answer was to model the magnetic field intensity using three-dimensional finite element analysis. Using the Vector Fields Opera-3d Electromagnetic Finite Element Model (FEM) design software, any number of different 3d geometry probe models could be created. A simple model, starting with a blank page, could be created in a few hours (given practice). In addition, models could easily be deconstructed by the software to be rebuilt with alterations in much less time. The time to analyse a model depended on the size of the model and the computer, with a 650 MHz PC running Windows NT 4 taking from a few seconds to a minute at most. Once the main analysis is complete additional tools to create and view the field distribution are used; these can also take several seconds to within a minute to run.

The FEM software allows the creation of 'conductor' structures, for example as coils or simpler building blocks. Initial modelling attempts used these to build more complicated probe structures. Unfortunately, the system was too simplistic to create structures with apertures such that the software would actually analyse the current flow around that aperture. The eventual model technique used the Opera-3d TOSCA magnetostatics current-flow simulation package. This calculates the flow of current through the entire probe structure, based on voltages set at specified facets on the edges of the design, shown by way of example in Figure 69. The standard analysis only calculates the current, and the field due to that current at the surface of the structure. However, a later secondary analysis can be run that calculates the field at a distance from the structure by integrating across its current distribution. This technique was used for all the work shown in this section. I would like to take this opportunity to thank Klaus Hoffer of Vector Fields Ltd., without his help and guidance this work would not have been possible.

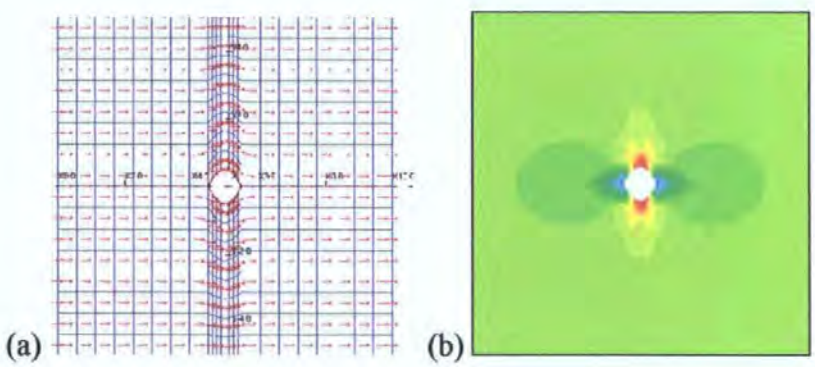


**Figure 69. Graphical representations of current density through a 3d structure.**

**(a) Vector representation of current flow & density, (b) Surface map of current density.**

### *8.2.1 FEM Compared to Original Model*

The first result required from the three-dimensional FEM work was to replicate the original two-dimensional model and compare it to the original calculations. A simple structure, shown in Figure 70 was modelled, and the resulting field intensity distribution calculated. This shows a result directly comparable to that in Figure 62, Section 7.2. It was found that

a conductor thickness of 500 nm was required to produce this result. Note that in all the following examples, unless otherwise declared, the conductor thickness is 500 nm, and the current density is 2 mA/μm$^2$ and scanning height 25 nm, as suggested in Section 7.2.

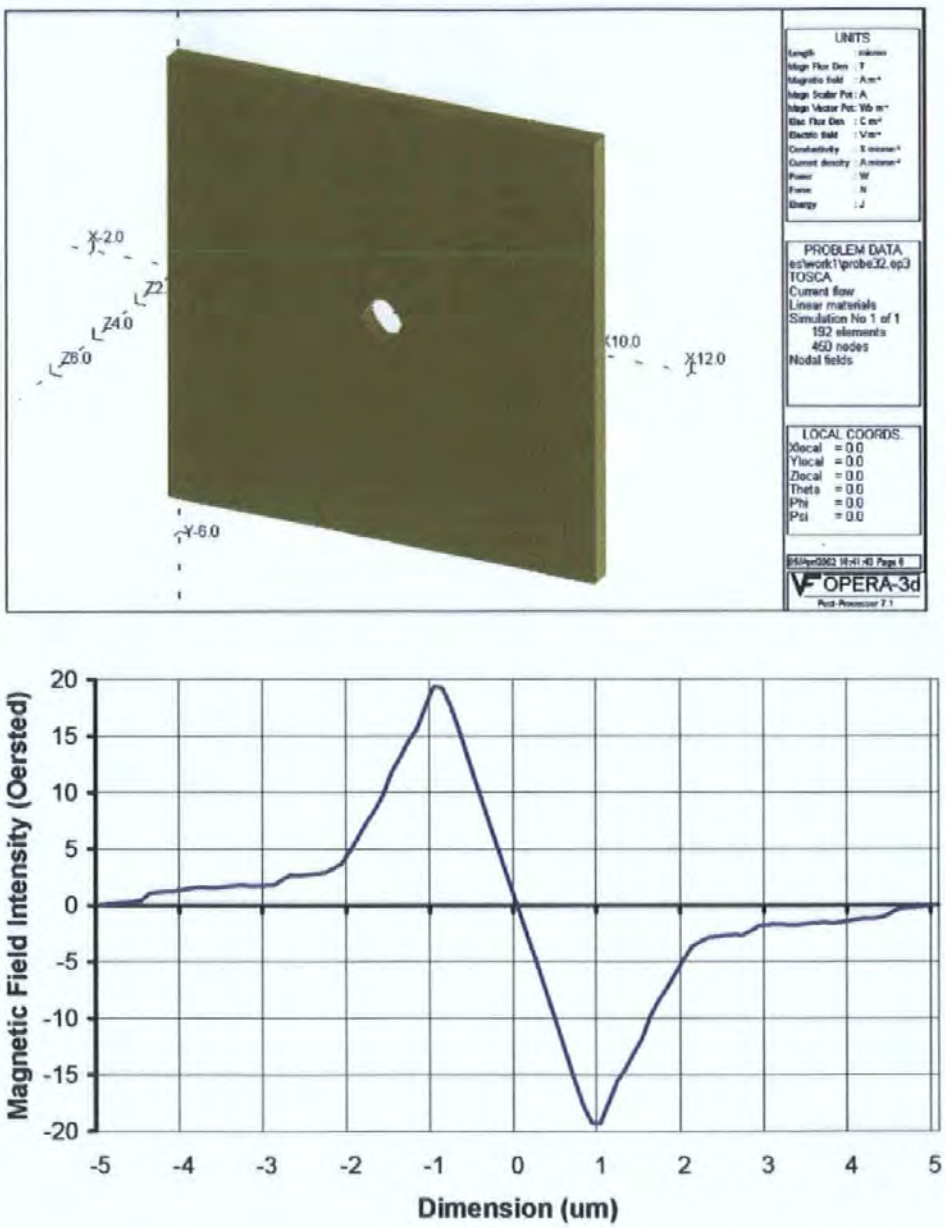


**Figure 70. 3d structure comparable to original 2d model, and the resulting field distribution.**

### *8.2.2 Semicircular Aperture Design*

In the previous Chapter simulations using a circular aperture are shown. A large image artefact appeared for longitudinal domain structures, where each domain transition was imaged separately by each peak, so creating a pair of lines on the image for each transition.

An answer to this problem is to change the design such that one field intensity peak is dominant over the other. Using a semicircular aperture, as shown in Figure 71, the current density past the semicircle's straight edge is lower than that past the circular edge.

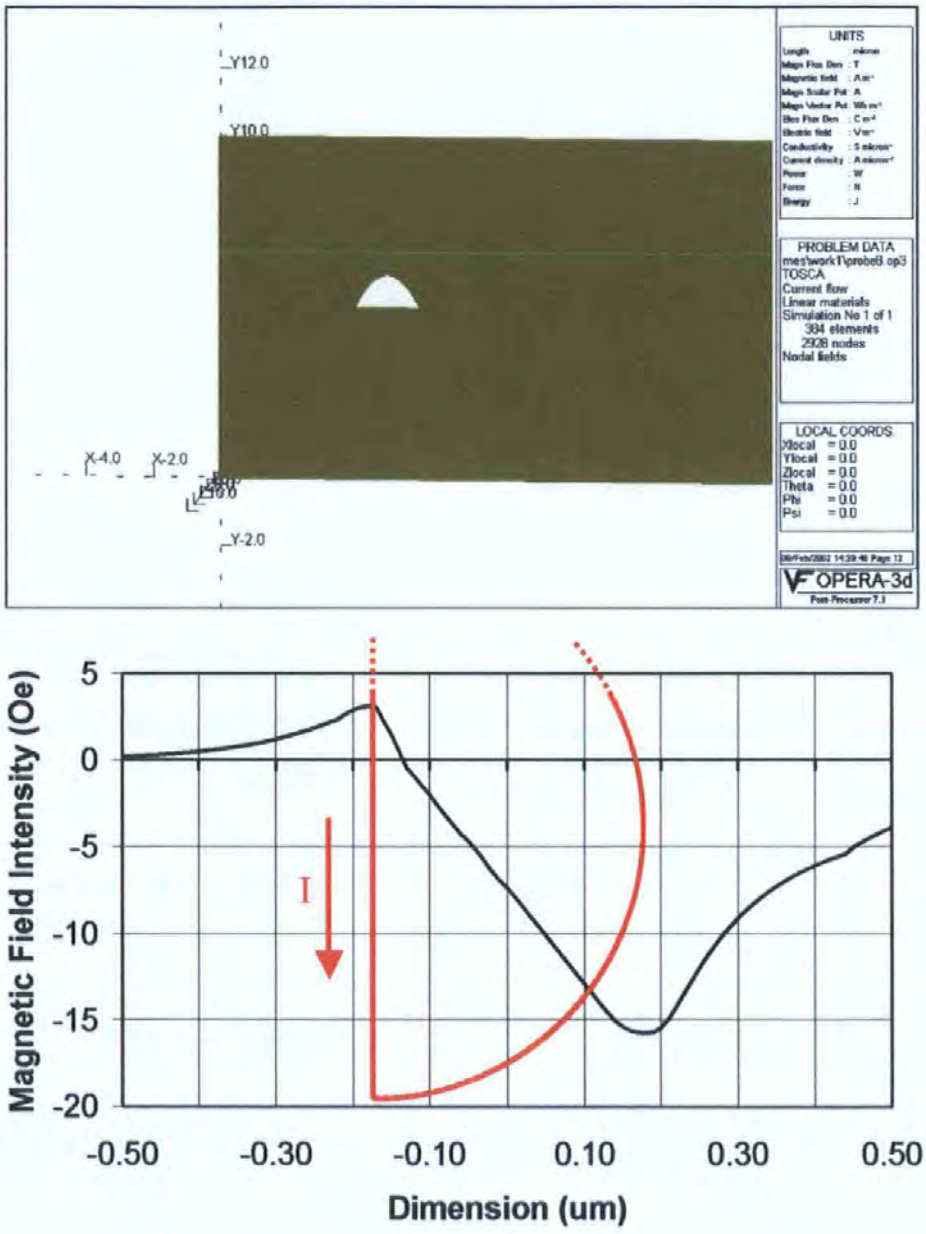


**Figure 71. Semicircular Aperture Magnetic Field Intensity, Hz (Oe).**

**0.5 μm semicircular aperture, at height 25 nm from probe surface and current density of 2 mA/μm$^2$.**

The resulting image simulations for the semicircular aperture are shown in Figure 72 and Figure 73. When compared with the first simulations in Section 7.5, these clearly

demonstrate that the semicircular aperture can successfully image both perpendicular and longitudinal domains.

In Figure 72 the semicircular aperture field distribution shows a clear interaction, this time based on the domain direction, rather than the domain transition as shown in the previous Chapter. This interaction occurs because of the dominance of one peak in the field distribution, and so provides a much clearer picture of the different domains. In this case the imaging resolution will depend on the spatial field distribution of the dominant field intensity peak, assuming the secondary peak has no discernible effect.

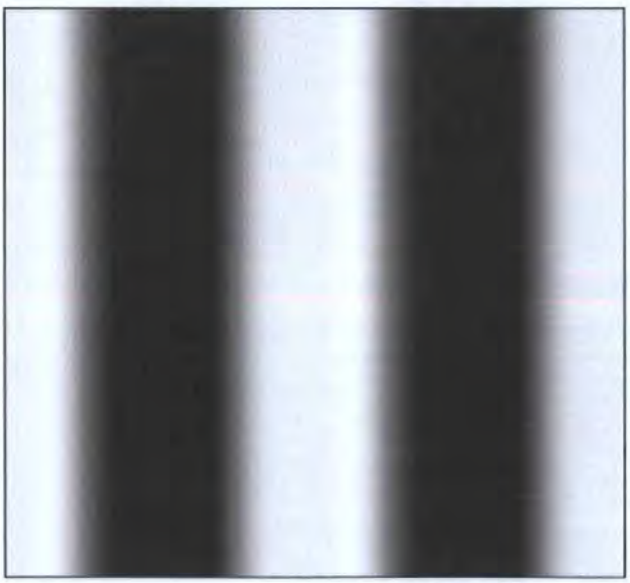

**Figure 72. Perpendicular bits (1 μm) imaged with the semicircular probe.**

**Probe with a 0.5 μm-diameter semicircular aperture. A dark or light line indicates each domain, depending on probe scan and orientation.**

In Figure 73 the semicircular aperture has imaged the longitudinal domain transitions without the artefact seen in Figure 66, where each transition was imaged twice due to the dual peaks in field intensity. Again in this case the distribution of the dominant peak in the field will determine the imaging resolution.

**Figure 73. Longitudinal bits (0.7 μm long) imaged with the semicircular probe.**

**Image does not show artefacts of circular aperture field distribution, with in this case only a single line on the image for each transition.**

### *8.2.3 3D FEM of Tips with Apertures*

The work started on semicircular apertures in the previous section was then expanded into further 3D modelling with apertures and tips. This allowed experimentation with the aperture size and shape, and coating depth, over an entire tip. A three-dimensional model of a 3 μm tip was produced, in this case with a 0.5 μm coating of gold. An almost ovoid aperture was used, whereby the sharper end of the aperture lies over the end of the tip, while the blunter, rounded end of the aperture covers one side of the tip. In this ovoid aperture design, the current density, and so the field intensity, is greatest at the sharper end of the aperture, plus the blunter end of the aperture is vertically much further away from the sample surface, reducing the secondary field intensity peak's influence even more. The result shown in Figure 74 shows that it was possible to refine the structure to produce a much improved, sharper, field intensity distribution. As image simulations have shown the potential requirements for a new probe, it was decided that comparing field distributions was easily sufficient to compare the later designs against each other.

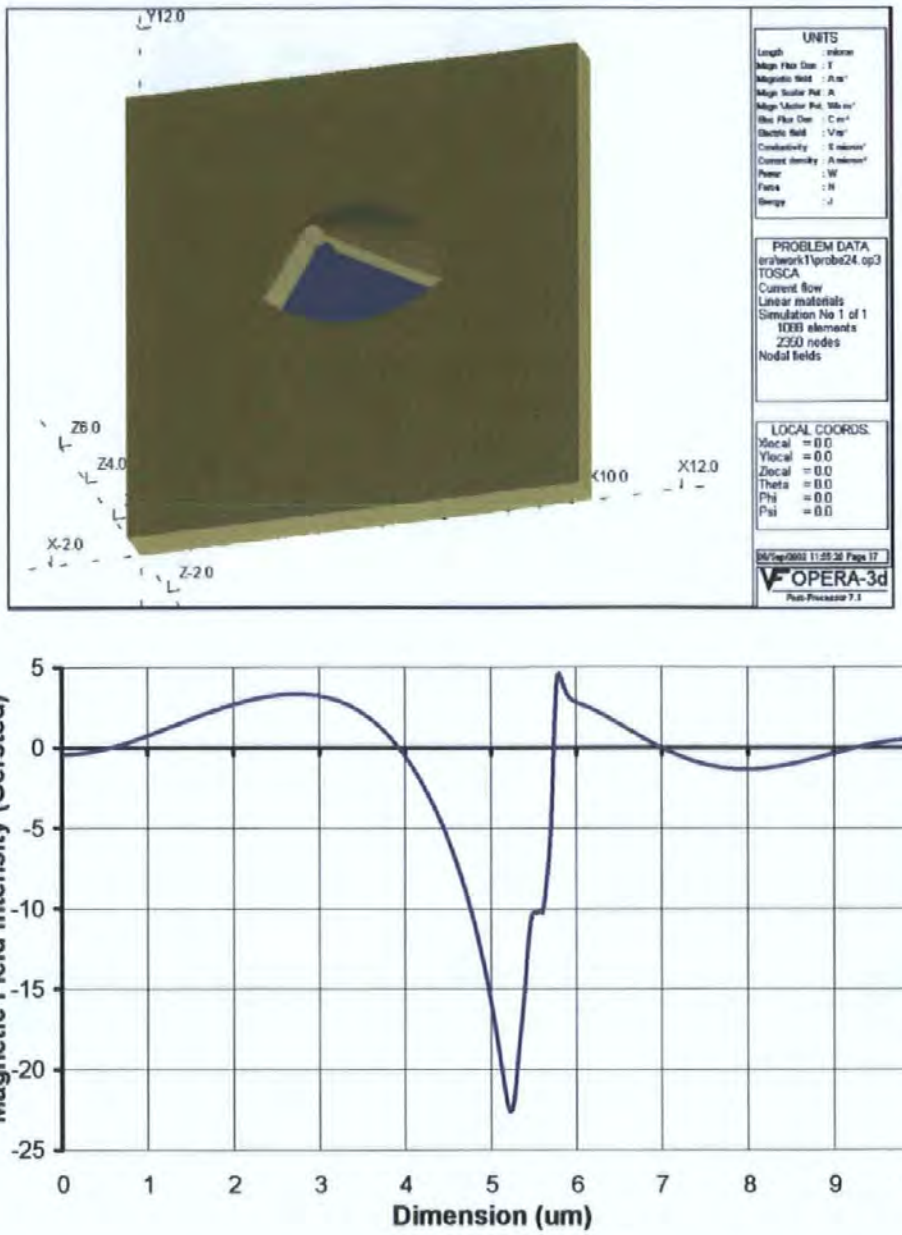


**Figure 74. 3d tip with semicircular aperture, and the resulting field distribution 25 nm from the tip's end.**

Following discussions with a SPM probe manufacturer, explained in Section 9.3, modelling work based on conductive coatings of only 50 nm was carried out, but is described here for continuity. The result, shown in Figure 75, shows that with this coating structure it is possible to produce a valid field distribution. However, in this and the following model the current density is increased by a factor of five. Although this is a large increase, based on the work in Section 8.1 it is within acceptable limits.

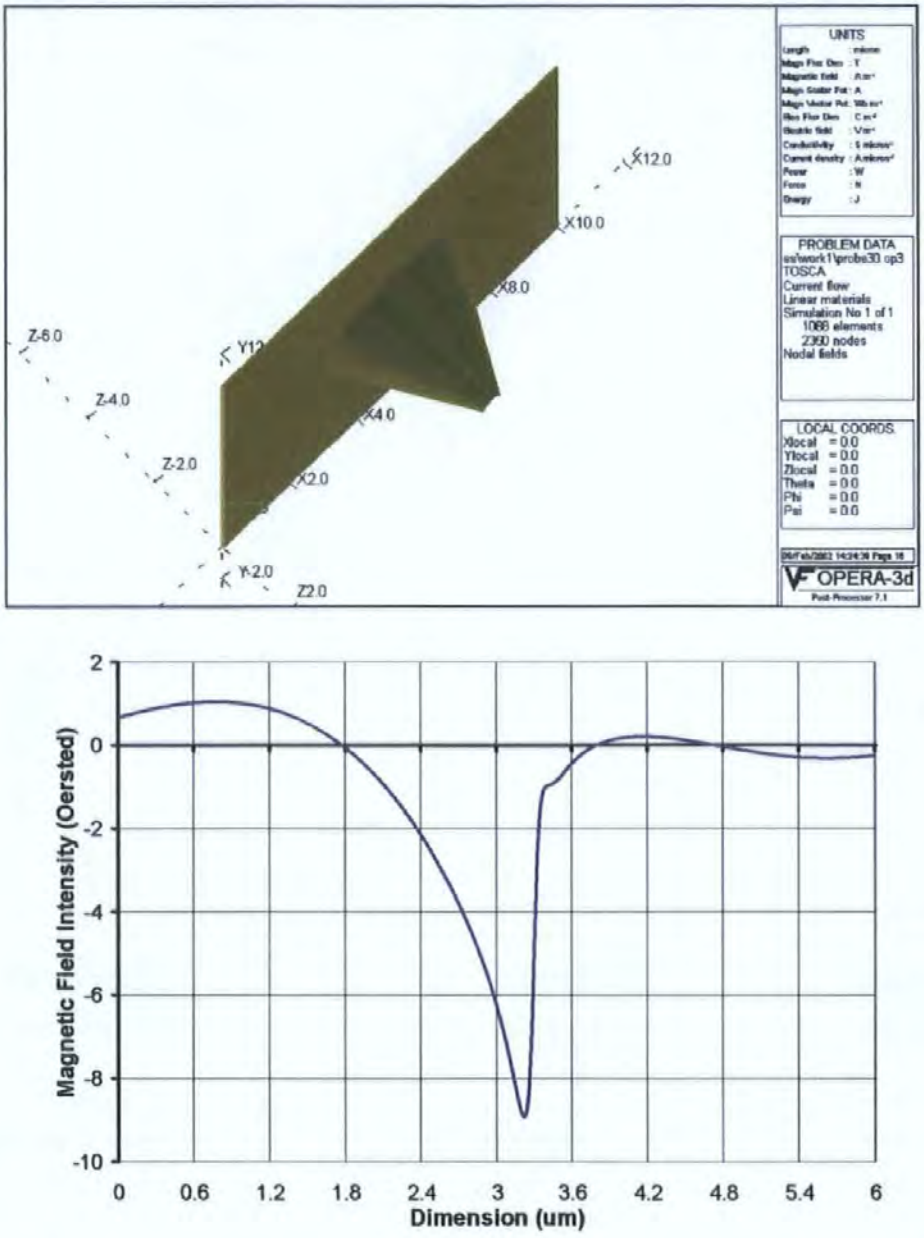


**Figure 75. 3d tip with semicircular aperture in 50 nm coating, and the resulting field distribution.**

Finally the thin coating model was repeated with a tip of 4 μm length. The result, shown in Figure 76, shows that the field distribution is again suitable for imaging following the preceding work, albeit with a reduced field intensity.

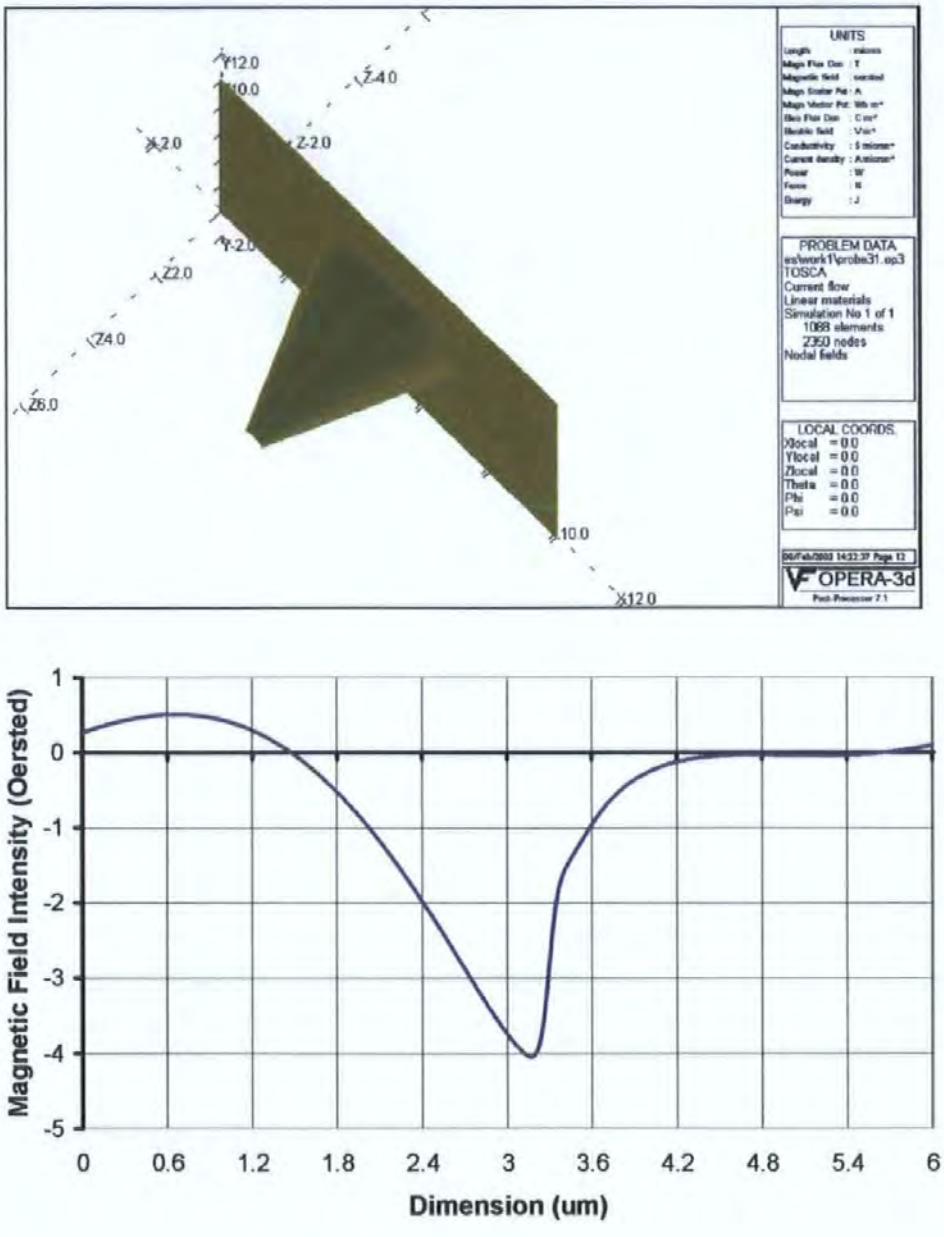


**Figure 76. 3d tip of 4 μm length with semicircular aperture in 50 nm coating, and the resulting field distribution.**

The modelling software also allows the user to generate a two-dimensional field distribution, so for example the thin-film coating tip in Figure 76 produces the distribution shown in Figure 77.

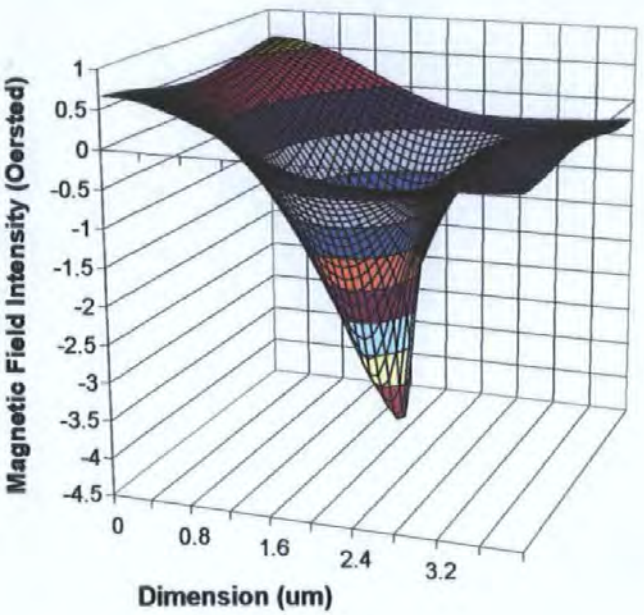


**Figure 77. 2d field distribution from 3d model of a 4 μm tip with 50 nm coating.**

The relationship between the thickness of the conductive coating and the field intensity generated by the FEM modelling is shown in Figure 78. This shows the relationship to be essentially linear, except when sub-μm. In the sub-100 nm region this is expected, due to various physical size effects, such as electron mean-free path considerations. Although in Figure 78 the relationship appears non-linear above this region (100 - 500 nm), this could be due to a scaling artefact of the FEM model.

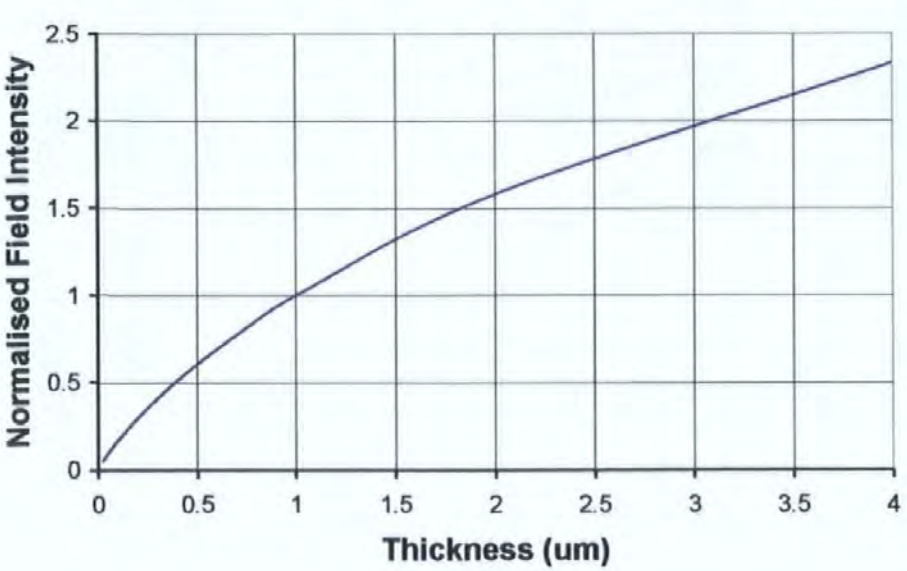


**Figure 78. Graph of FEM modelled relationship between field intensity and conductor thickness.**

The modelling work covered in this Chapter describes only a small variety of the actual number of models created. It has shown that the FEM agrees with the classical theoretical calculations previously done. This then allowed the extension into different three-dimensional structures, more closely resembling the physical design put forward. These designs have allowed the proof of concept for probes of the physical structure planned, and allowed further improvements in the field distribution, physical manufacturing constraints allowing. The work shows that a good system for modelling this type of probe was achieved, producing valuable and reliable results. In the following Chapter a practical field result is obtained from a micrometer sized aperture in a conducting sheet. The author has been involved in the investigation of other types of electromagnetic probe, as described for example in [77], work that has also used the modelling techniques described in this thesis.

# 9 Further Work on the New Probe

## *9.1 eMFM Prototype Apertures*

In order to prove the theory behind the new eMFM probe described in Chapters 7 and 8 prototype apertures were created in flat conductive sheets. These are larger than those modelled, ranging from 5 to 30 μm, due to the manufacturing processes available. However, they were intended to provide experimental results to confirm the field modelling. These apertures were created in the University of Plymouth's own clean room facility, with the generous help of Mr Nick Fry. The processes used in their manufacture are described in Appendix 2.

An AFM image of a 10 μm aperture is shown in Figure 79 below. The aperture is very clearly seen at the bottom left of the image. The aperture is shown to be reasonably circular, however there are some deposits around its edge. This unevenness is probably due in part to the age of the aperture, i.e. several months, at the time of imaging.

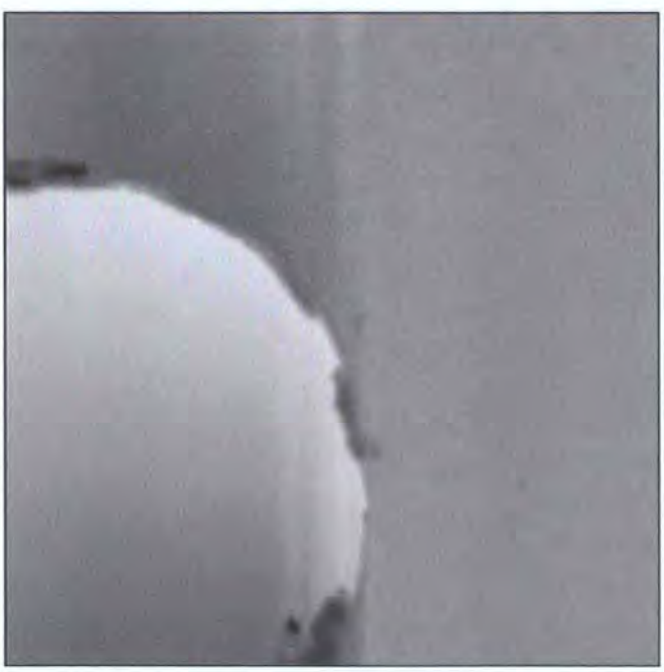

**Figure 79. AFM Image (8 x 8 μm) of part of a 10 μm diameter prototype aperture.**

## *9.2 Practical Tests of EM Apertures*

A MFM static mode image, and corresponding AFM image, of the aperture shown in Figure 79, with a current applied, are shown in Figure 80 below.

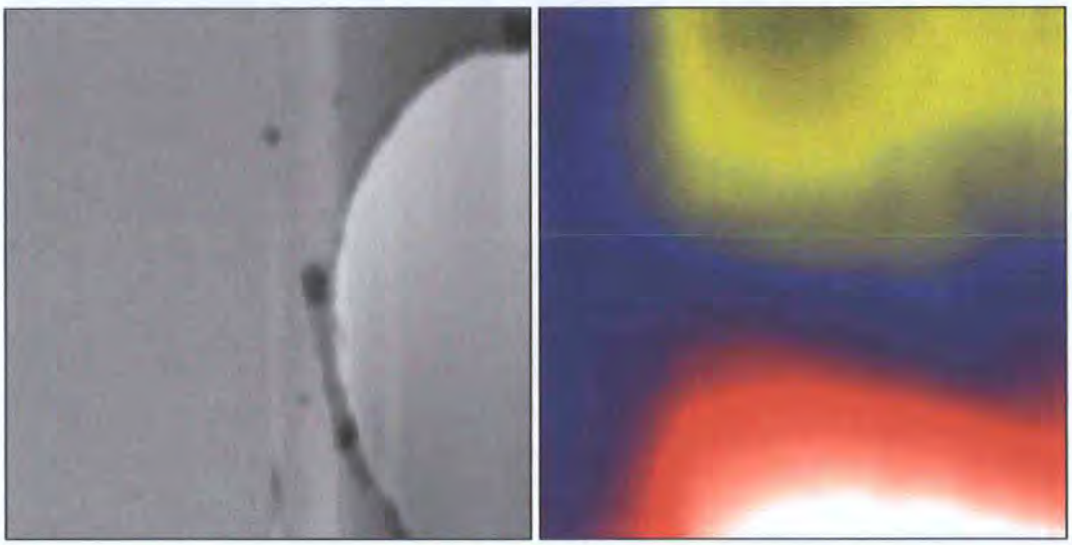

**Figure 80. AFM (left) and MFM (right) of Aperture with current applied (across image).**

The MFM image on the right shows the two peaks of field generated on either side of the aperture as the current passes around it, flowing from left to right. The MFM image was taken at a large distance (several hundred nanometres) from the surface to remove artefacts produced by the large topographic step of the aperture wall. Unfortunately this leads not only to a low signal level, but also to a large integration of the tip domains with the stray field from the aperture, and thus a low level of contrast in the image. Given this problem, false colouring has been used to help indicate the cantilever deflection. The result in Figure 80 was found to be both repeatable and controllable. Changing the applied current or the flying height of the MFM tip were seen to alter the contrast, however the effect is difficult to quantify with the current system and so is not reported here. This preliminary result does provide physical evidence that the aperture is producing a field effect as described in the theoretical findings. It is therefore hoped that future enhancement to the imaging system will further confirm this result.

## *9.3 Future Probe Manufacture*

A small company in the USA called NovaScan Technologies produces conductive-coated AFM cantilevers for use in Scanning Capacitance Microscopy. Using original v-shaped silicon nitride cantilevers (Microlevers manufactured by TM Microscopes), they first chemically etch all of the gold from the probe surfaces (if required). Then specialised v-shaped masks are applied to the probe surface using customised optics and micromanipulators. In addition to coating the cantilever two electrical contact pad regions are created, one pad extending from each cantilever leg over the chip. Gold, plus an adhesion layer if required, is then sputter-coated so that the bottom surface of the cantilever/tip and the pad regions are coated. Finally the mask is removed and the gold 'circuit' is scribed and cleaned using micromanipulators. There are inherent problems with this technique; firstly it is very easy to warp the cantilever beyond use. If a fairly thick layer of Au (greater than 100 nm) is required this becomes a real concern (particularly with very soft cantilevers). Fortunately if warping occurs it can usually be addressed by canting the chip in order to get the right angle to compensate for warpage. Secondly, the coating must be confined to the right areas or shorts may occur, thus the masking must be as accurate as possible. Thirdly a chip holder must be fabricated that allows electrical contacts with the pads while still allowing clearance to make sure the tip touches the sample surface and not the leads to the contacts. As everything is on the bottom of the chip, the leads have to be made fairly thin.

NovaScan can produce apertures in the gold coating, but only with a minimum size of 1-2 microns in diameter. In the case of the new probe, the author proposes that Focussed Ion Beam (FIB) milling is used to create the aperture instead. A FIB system is similar to that of a Scanning Electron Microscope (SEM), where the major difference is the use of a gallium ion beam instead of an electron beam. In imaging mode, the best image resolution that can be obtained by FIB is approximately 5 - 7 nm. The ion beam is raster-scanned

over a sample, which is mounted in a vacuum chamber at pressures of around $10^{-7}$ mbar. When the beam strikes the sample, secondary electrons and secondary ions are emitted from its surface. The intensity of these electrons or ions is monitored and used to generate an image of the surface. Secondary electrons are generated in much greater quantities than ions, providing images of better quality and resolution; consequently the secondary electron mode is used for most imaging applications. Of course, for our purpose, ion beams can also be used to remove material, i.e. milling, from the surface of the sample, again at resolutions of approximately 10 nm. FIB systems do have drawbacks; including damage to the milled surfaces from ion implantation, and the fact that some milling will occur during the imaging process. The latter problem can be avoided by using dual-beam FIB systems. These combine a FIB and a SEM, where the ion beam can be used for milling and the electron beam for imaging.

NovaScan strip all the original gold coating from the cantilevers; whereas this design calls for a conductive coating on both the top and bottom of the cantilever, see Section 8.1.1. Discussions with NovaScan confirm that the only reason for removing the top gold coating is the possibility of shorting between the different conductive surfaces. Again, in this case the use of FIB, to trim and remove electrical shorts, is a conceivable answer to the problem. Several chips incorporating cantilevers with different levels (30 - 100 nm) and design of coating (top etched or not) are being purchased from NovaScan. These will then be imaged and apertures created using one of the FIB facilities in the UK. The probes will then be tested within the microscope system described here. If these tests are successful it is hoped that future work will continue with both probes from NovaScan, possibly including gold coating onto MFM (ferromagnetic tip) cantilevers, and also an investigation into manufacturing eMFM probes from start to finish in the UK.

## *9.4 Using the Probe for Data Storage*

Probe storage has been discussed as a potential candidate for future recording systems, and work has progressed in several laboratories around the world [78] [79] [80]. Given the ability of the novel probe described in this work to vary the field strength about the aperture, an additional aspect that merits investigation is whether the probe can be used not only as an image or 'read' mechanism, but also if it can be used to write data in a reproducible manner.

The typical coercivity of the latest commercial hard drive media is now in the region of at least 3.2 KOe. The field strength to write to this reliably can be taken as twice $H_c$ [81]. It would be impossible to generate this field reliably with the new probe because of the practical limits of the current density. However, a field of 130 Oe, as shown in Figure 81, can be achieved using this probe, given a current density of 50 $mA/\mu m^2$. This appears to be a large current to take into consideration, but when writing only a very short pulse is required, reducing the energy used. Using the calculation from Section 8.1.2, a steady-state temperature rise of 1.5 °C over ambient would occur with a steady-state current of 50 $mA/\mu m^2$. In addition, electromigration would not be a factor, due to the use of an ac current, as discussed in Section 8.1.3. Therefore the probe can withstand the recording current pulse suggested above.

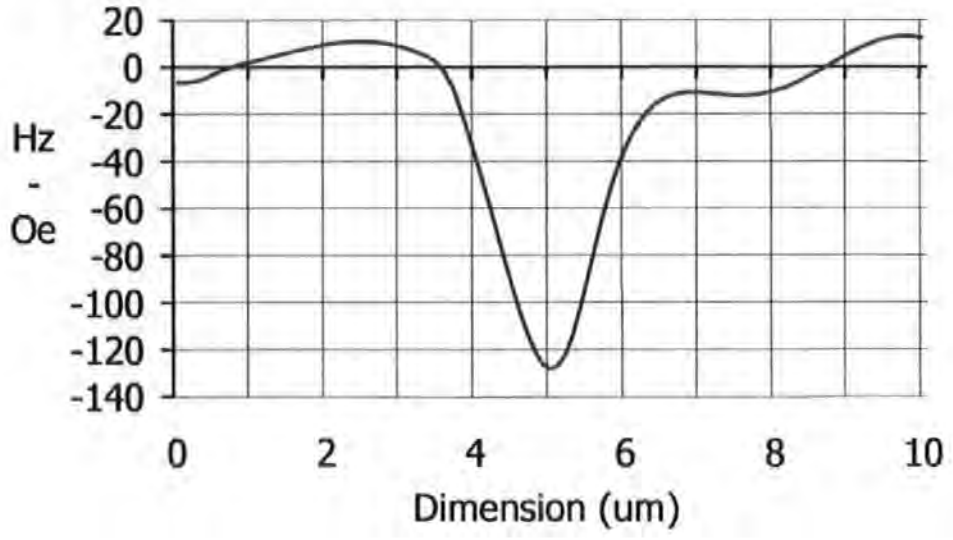


**Figure 81. Field intensity 25 nm from probe surface, current density of 50 mA/μm².**

Magneto-Optic recording uses thermo-magnetic materials, which require only small switching fields of typically 100 Oe when heated, such as that shown in Figure 81. As such a form of 'hybrid recording' with the probe could be used [82]. In this case a laser will be required to provide the heat necessary to write to the medium. Two methods have been considered for this process. The first utilises a laser through the probe's aperture, as used in a micro-cantilever Scanning Near-field Optical Microscope [83] [84]. This can be considered a type of Dual Gradient hybrid recording, whereby the data track width is determined by the thermal gradient and the bit length dependent on the magnetic field gradient [85]. Previous work shows that sufficient laser power is delivered to the sample through this type of device [86]. Two variations of this proposal are shown in Figure 82. In the first a Silicon Dioxide wave-guide is manufactured within the probe, which is technically more challenging and expensive, but provides a single complete solution. In the second variation the laser is incident on the rear of the probe's cantilever, this design is simpler and thus lower in cost, but requires the incident laser to be correctly aligned [87].

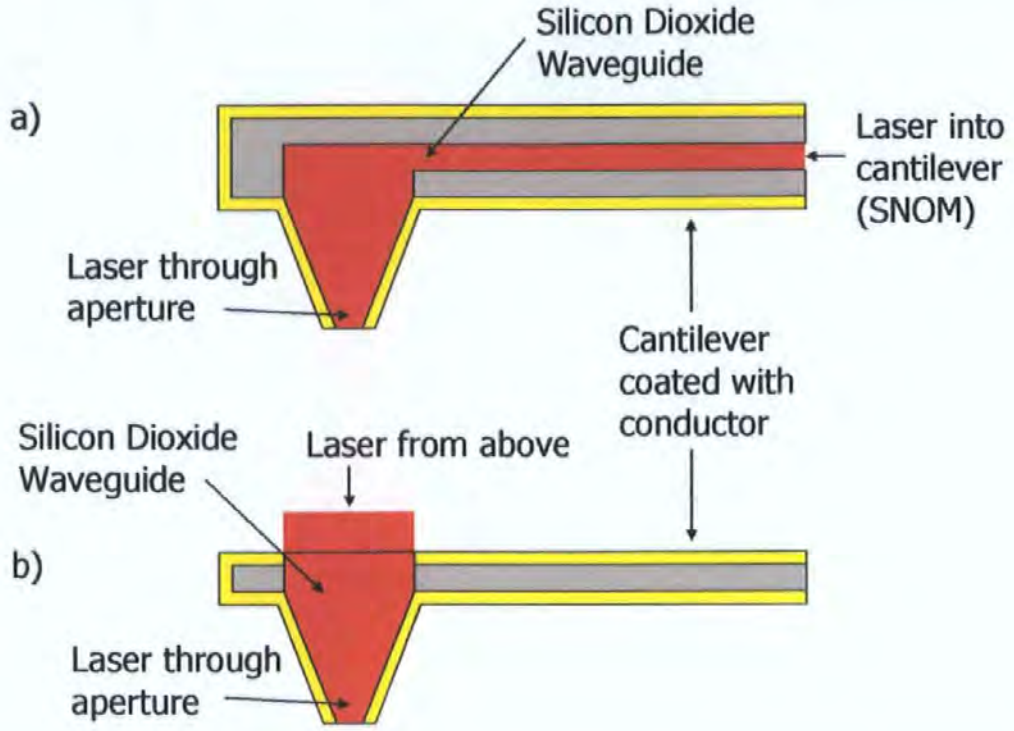


**Figure 82. Probe designs for MO-probe recording, using a laser through the probe's aperture. (a) shows the first method, using an integrated waveguide running the length of the cantilever. (b) shows the second method, with the laser from the rear of the cantilever.**

The second write method is shown in Figure 83. Here the laser is incident on the rear of the MO material through the substrate (disc). This method type is that of Thermally Assisted (or Magnetic-Field Gradient) hybrid recording, in which the track width and transition parameters are dependent on the applied field, and the thermal profile is essentially constant [88] [89]. This allows for much simpler probes, although the heating effect, and laser aim and focus are more problematic. In this case, although the focused laser spot, and so thermal profile on the material is much larger in area than that of the probe's write field distribution, previous work has shown that this method can be applied [89]. However, the alignment of the laser spot and probe, and the focus of the laser due to macroscopic fluctuations in the substrate surface are problems that would require attention.

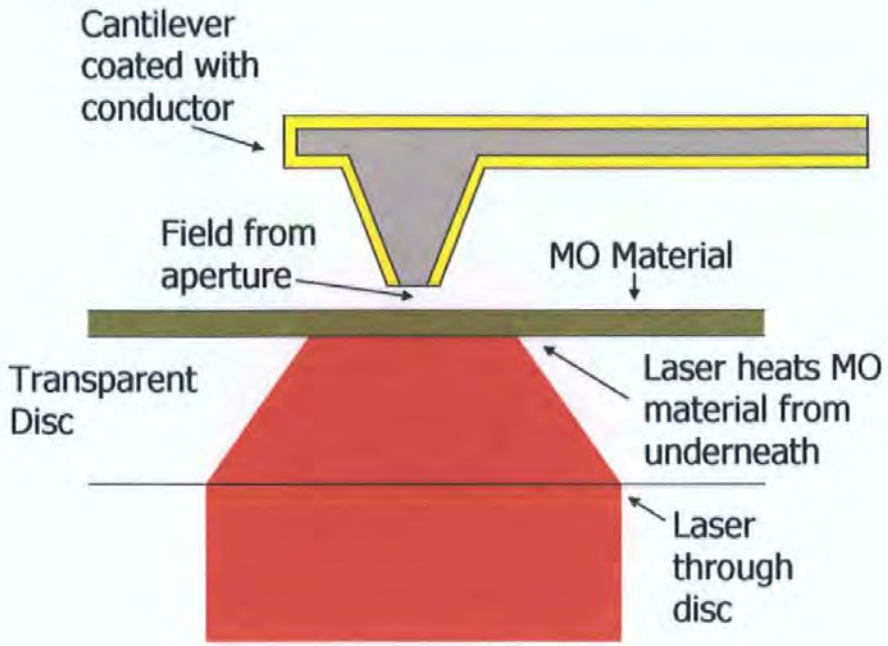


**Figure 83. Probe design for MO recording, using a laser through the MO substrate.**

Note that in none of the methods of writing, as envisaged here, is the laser combined with the aperture probe used to detect the magnetic information, only to heat the thermo-magnetic material, and so does not require the complex optical detection used in SNOM, as described by Betzig et al. [86]. The read mechanism is thus akin to that of an MFM operating in its standard imaging mode, albeit using the apertured-conductor method as described herein. Research into hybrid recording techniques is continuing, as many data storage companies regard it as a potential successor to contemporary methods [90].

## *9.5 Other Future Work*

Operating with an ac current the sample could be probed with an ac or combined ac/dc magnetic field, which is of course not possible with standard MFM probes. This would then allow an investigation of the new probe as a Magnetic Resonance Force Microscope (MRFM). Previous research into MRFM systems, by workers at IBM, shows them as a potential future method of imaging individual atoms, elementally specific, in three dimensions [91]. This would be a remarkably useful tool with numerous applications, for example, not just limited to magnetic storage media analysis, but extending to life sciences

and drug development. The very latest work in the area has focussed on the theoretical use of MRFM in quantum computers, as it is predicted they will be capable of single-electron spin measurement. The new probe design, proposed here, will allow integration of the resonant field with a spatial distribution proportionate with the intrinsic imaging resolution, as against a system using a macroscopic external coil.

The new eMFM probes may also offer additional sensing modes, which could ultimately alleviate the requirement for optical sensing. The impedance of the current-driven probe will change according to the interaction between the magnetisation of the sample and the field associated with the probing current. This potential ability to integrate the sensing of the cantilever's deflection into the probe design itself would be particularly advantageous as it simplifies the system, thus removing several noise sources, i.e. the laser, and other elements, sensitive to physical vibration. In addition, it should be noted that a possible avenue of exploration is to apply the new eMFM aperture tip design to a cantilever whose tip is also coated with a low coercivity magnetic material. This could potentially increase the field intensity of the tip, but still retaining the controllability of the eMFM probe.

The probe could also be used in a micro- or nano- manipulation technique utilising its integrated and controllable field for localised positioning of micron-sized magnetic objects, in a similar manner to that discussed by Barbic et al. [92]. This could provide a non-invasive, low cost alternative to the optical trapping techniques normally used in such manipulation. Possible advantages could include reduced heating of the manipulated sample and the ability to perform studies in a fluid.

# 10 Conclusions

## *10.1 The New Instrument*

A new Atomic/Magnetic Force Microscope has been designed and constructed, based on previous work in this field. This uses the Optical Beam Deflection detection technique incorporated on a novel removable head assembly containing the cantilever and detection system. The head is mounted via a kinematic design onto a lower section that includes the sample, tube scanner, piezoelectric translator, and DC-motor. The ability to remove the head assembly allows easy replacement of both the sample and the cantilever. These two sections are constructed within a vacuum system to allow for improved imaging sensitivity in resonant imaging modes. The instrument comprises a computer controlled DC-motor for coarse sample approach, a piezoelectric translator for fine sample approach, a piezoelectric tube scanner for sample motion, a DSP based proportional-integral feedback and data acquisition system, and an overall control software suite implemented in LabVIEW on a host PC. In addition, the sample and cantilever can be viewed via a stereo microscope and digital camera, thus allowing live video, and still picture, capture via the host PC.

The instrument can be set up, including power-on, computer boot-up and software load, changing the cantilever and sample, laser beam alignment and sample approach in less than 10 minutes.

The instrument is capable of scanning a maximum area of 15.77 μm by 15.77 μm (30.54 nm step) and a minimum DAC limited area of 240.5 nm by 240.5 nm (0.481 nm step). A lateral resolution of 10 nm has been achieved in contact topographic mode (1 μm by 1 μm scan) and approximately 50 nm has been achieved in the static magnetic mode of operation. The vertical resolution or sensitivity of the instrument, limited by vibrations of

the cantilever and the noise in the detection system, has been found to be 1 nm (static mode).

The control, operation and image formation of the whole system is undertaken by an AMD Athlon Windows PC, with the appropriate development of hardware for electronic interfacing to the DSP/DAQ cards, and the coding of an extensive amount of LabVIEW software to facilitate a friendly and efficient user interface. An image is built up, pixel by pixel, and stored in the memory of the DSP card, which simultaneously controls the scan operation, before being streamed to the host PC. The DSP card can be used to implement a proportional-integral control system. Images are generally 500 pixels square with 65536 grey scales, although higher pixel counts are possible. It is also possible to enhance images by adding false colour, or applying image filtering.

The instrument has successfully imaged both topographic and magnetic samples including CD Audio data tracks and bubble memory garnet layers. The cantilever deflection was initially calibrated using calculations of the tube scanner motion. Samples with known features were imaged in order to calibrate the instrument. The cantilever deflection and piezoelectric z motion were calibrated against a z step calibration grating with rectangular steps 100 nm high. This was in general agreement with results from scanning CD Audio data pits. The x-y scanning range has been calibrated using a calibration grating with 2160 lines/mm in two orthogonal directions. This has given an accurate figure for the scan size and has also produced figures for the non-linearity of the tube scanner.

There are a number of improvements that could to be made to the instrument. The system is designed to operate in a LiftMode™ style, separating the topographic and magnetic features, using the DSP control structure, however this has yet to be successfully implemented. Additionally, the implementation of resonant modes of imaging, both for magnetic studies and topographic (Tapping™ mode), would produce much greater

sensitivity in the z plane than the static imaging mode used in the work presented here. There are also several possible enhancements to the current mechanical and electronic systems. The instrument currently uses a manual micrometer based XY table for sample positioning. This could be motorised and computer controlled, possibly providing a method of image scanning a larger area either at a low resolution, or by building up an image from several normal scans. Also, mirror and photo-detector alignment and laser focus could be powered via computer control. Non-linearities in the tube scanner, e.g. creep and ageing, have been shown to cause distortions in images; these could be reduced using movement detectors and a closed loop feedback system on the tube scanner. This would produce accurately calibrated images and allow certainty in the results from repeated scans of the same area of a sample.

## *10.2 The New Probe*

The development of a novel design of electromagnetic MFM probe, to complement the current standard coated tip probe, has been presented. The standard coated MFM tip suffers several inherent problems, for example different tips are required to match different sample characteristics, tip coatings can suffer hysteresis and wear and damage, in addition tip domain alteration can occur due to interaction with a magnetic sample. These weaknesses can affect the acquisition of useful and quantifiable images. The new design presented in this work employs a field induced around a micro-fabricated aperture using a controlled current as a replacement for the standard tip's stray field. The advantage of this design is that the field intensity can be standardised, and varied, and hence the sample-tip interaction can be controlled. As the field distribution is due solely to the geometry of the current flow about the aperture, i.e. is not from a highly non-linear magnetic material, it can be calculated to high accuracy. This means that the results will be both repeatable and quantifiable.

Two methods of modelling the field intensity distribution from the new design have been used. Initially a two-dimensional calculation based on previous work was implemented in MathCAD. This calculated the field above a circular aperture in a flat conducting sheet. The results from the MathCAD model show that there are three primary variables to define for a circular aperture in order to generate adequate field intensity, over the smallest area, whereby image resolution is proportional to spatial field distribution. These variables are the initial linear current density, the scanning height and the diameter of the aperture. A field model was generated, that applied practical limits to these variables, and agreed with previous work on standard MFM tip field distributions. A current density of 2 $mA/\mu m^2$, with a scanning height of 25 nm, and a circular aperture of 0.5 μm diameter, were chosen as the optimum levels, given practical limits, for the new probe design.

MFM images were simulated of the interaction between the field distribution of the initial design and simple models of both perpendicular and longitudinal magnetic domains, using the reciprocity principle. These show that perpendicular magnetic domains can be observed by way of their transitions. Furthermore, the transition direction can be determined, given that the probe field distribution is known. Unfortunately, the simulated images of longitudinal domains contained a large artefact produced by the two peaks of field intensity generated above a circular aperture. As an answer to this problem a semicircular aperture was suggested in order to produce a dominant 'imaging' field intensity peak. Also, it was seen that the resolution of the new probe with a circular aperture is related to the minimum possible aperture diameter, due to the cumulative effect of the two peaks in field distribution, which in the case of a single dominant peak in the field intensity from a semicircular aperture would no longer be relevant. Rather with a single dominant field intensity peak the resolution would be determined by the spatial distribution of that one peak.

The initial practical problems of implementing the new probe were discussed and solutions put forward. From accepted design standards and literature the level of current used in the field model was taken not to generate electromigration effects. In addition to the work reviewed, a short investigation of the thermal effects of the current was also undertaken, which showed the current level to be non-critical. The effect from the fields due to the conductor on the entire cantilever was also considered. This work suggested that placing the aperture on the end of a tip on the cantilever, in addition to coating conductor on both sides of the cantilever, would reduce the influence of these fields significantly. Finally, a circuit was designed to generate the constant current required by a probe. This was then used in later prototype work.

To develop the probe design further a second method of modelling the field distribution was implemented. In order to investigate the field from three-dimensional structures, with different aperture morphologies, an electromagnetic finite element analysis package was used (Opera-3d). This package calculates the current flow through the entire probe structure. From this the field intensity can be calculated at any point around the probe. The finite element work was first used to replicate the original circular model and found to agree with the MathCAD calculation. This then allowed the creation of many different probe shapes, however this thesis concentrates on semicircular and then ovoid apertures. The semicircular aperture design was proven to produce a superior field distribution, eliminating the artefact found in longitudinal imaging by circular aperture. This was enhanced further by using an ovoid aperture lying over a cantilever tip. Finally, field distributions for possible prototype probes were modelled. These also produced reasonable results, but at the cost of an increased current load on the probe. The finite element modelling system allows the relatively fast construction of varied probe-aperture morphologies and generation of field distributions for comparison.

To prove the theoretical field distributions prototype apertures were created in flat conductive sheets. Although larger than the modelled designs they have allowed practical tests of the general field distribution. This very preliminary work does support the theoretical modelling, indicating that the probe design could be successfully implemented.

This thesis has presented a completely novel design of MFM probe, which has been successfully modelled and simulated, with practical prototype results verifying the new research to this point. The following section discusses the continued development, and possible future avenues of research, for the new probe design.

## *10.3 Future Research*

Discussions were undertaken with a company, NovaScan Technologies, involved in coating standard cantilevers for use in different methods of SPM. This has led to the purchase of several chips incorporating cantilevers with different levels and design of coating. Future work will include the use of focussed ion beam milling to create apertures on the tips of these cantilevers, and their subsequent characterisation and testing as working eMFM probes.

Variations of the new probe design were also considered for use as a mechanism for probe data storage via hybrid recording. Probe storage is one of the contenders to replace conventional magnetic or optical data storage techniques in the future. As current techniques move ever closer to their physical limits, research into probe storage is being undertaken in some of the world's top storage research establishments such as IBM's Zurich Laboratories, Carnegie Mellon University and University of Twente (Netherlands). The brief investigatory work shown here discussed the encouraging potential the probe has for writing to recording media in a thermally assisted manner, with the data read back accomplished using the probe in a standard MFM mode.

The use of the probe with an ac or ac/dc current, hence probing the sample with an ac or ac/dc field, is also suggested as an area for future investigation. For example, this could potentially allow the probe to operate as a MRFM to image individual atoms in three dimensions. This would not only be extremely useful for magnetic data storage media analysis, but also life sciences, drug development and possibly quantum computing. The new probe may also offer an additional impedance-sensing mode, which could remove the requirement for optical sensing, as the impedance of the probe will change according to the interaction between the sample magnetisation and the probe's field. This integration of the sensing of the cantilever's deflection into the probe design would be valuable because it simplifies the system, removing several noise sources such as the laser. An investigation into using tips coated with an additional magnetic layer, potentially increasing the field strength, while retaining the eMFM's worthy characteristics, could also be considered. Finally, the probe could also potentially be used as a method of micro- or nano-manipulation of micrometre and sub-micrometre magnetic objects, thus providing an alternative to current optical trapping techniques.

# Appendix 1 - Initial Numerical Model of Field $H_z$

Equation 22 from Section 7.2,

$$H_z = \frac{J_o}{4\pi}\int_0^{2\pi} d\phi \int_a^{\infty} \Phi(r,\theta,z,\rho,\phi)\,d\rho,$$

was reduced by Bobeck et al. [63], with appropriate changes of the variables and collecting terms, to

$$H_z = \frac{J_o}{4\pi} H \sin\theta$$

where

$$H = 2\int_0^{\pi} (F_1 + F_2 + F_3)\,d\psi = H(\mu, v),$$

$$F_1 = \frac{C_0 + C_1 C + C_2 C^2 + C_3 C^3 + C_4 C^4}{\sigma^2\left(\sigma^2 - \mu^2 C^2\right)\left(\sigma^2 + 1 - 2\mu C\right)^{0.5}},$$

$$F_2 = C \ln\left[\left(\sigma^2 + 1 - 2\mu C\right)^{0.5} + 1 - \mu C\right],$$

$$F_3 = \mu\left(2C^2 - 1\right)\sigma^{-3} \ln\left[\frac{\sigma\left(\sigma^2 + 1 - 2\mu C\right)^{0.5} + \sigma^2 - \mu C}{\sigma - \mu C}\right],$$

$$\mu = \frac{r}{a},$$

$$v = \frac{z}{a},$$

$$\sigma = \left(\mu^2 + v^2\right)^{0.5},$$

$C = \cos\psi$,

$C_0 = \mu\sigma^2\left(1+\sigma^2\right)$,

$C_1 = \left(\sigma^2+\mu^2\right)\left(1-\sigma^2\right)$,

$C_2 = -\mu\left[\sigma^2\left(\sigma^2+3\right)+2\mu^2\right]$,

$C_3 = 2\mu^2\left(\sigma^2-1\right)$,

$C_4 = 4\mu^3$.

# Appendix 2 - Prototype Aperture Manufacture

All substrate processing was carried out under Class 10 laminar flow hoods in Class 100 rooms. The sputter deposition and ion milling machines occupy an adjacent Class 1000 room. The entire process is shown in Figure A2-1 below.

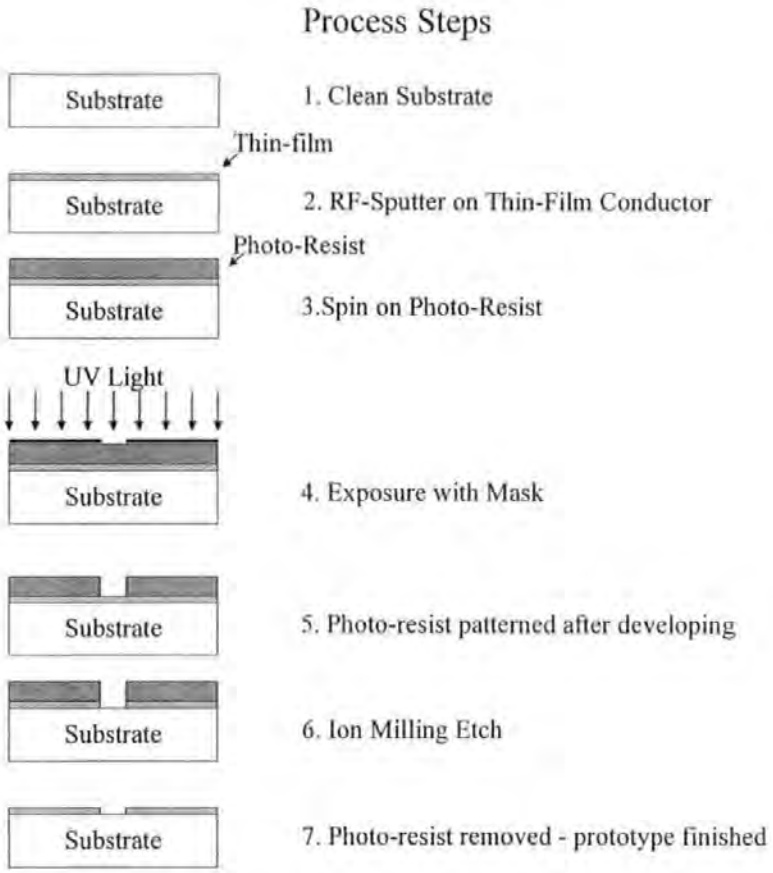


**Figure A2-1. The manufacture process used to produce the prototype apertures.**

### *Mask Design*

The aperture masks are designed using CorelDraw on a standard PC. This easily allows feature sizes down below 1 μm, although in this case the smallest apertures designed were 5 μm in diameter. This size was dictated by the minimum reliable size that the clean room processes in University of Plymouth could produce at that time. Once complete the mask

designs were sent to the Rutherford Appleton Laboratories to be processed. The masks were made at the Electron Beam Lithography Facility (EBLF) at Rutherford.

The mask plate size is 100 mm by 100 mm for use in the in-contact mask-aligner described later. In order to reduce cost, the prototype apertures shared a mask with other devices being produced by the clean room facility. As 50 mm by 50 mm glass substrates were used, a single mask can be used for at least four layer processes. The masks were made of extremely high quality flat glass with an 80 nm thick Chromium layer on one side. This layer was patterned using electron beam lithography, with a beam size of 1.8 μm.

The prototype aperture masks are shown in Figure A2-2. Each aperture was set in its own solderable leadout. A variety of sizes of aperture were put on the mask, ranging from 5 μm to 50 μm. This allowed the testing of scalability, although on the necessarily larger scale than perceived for the final probe design. It also provided leeway for any problems in the clean room facilities processes.

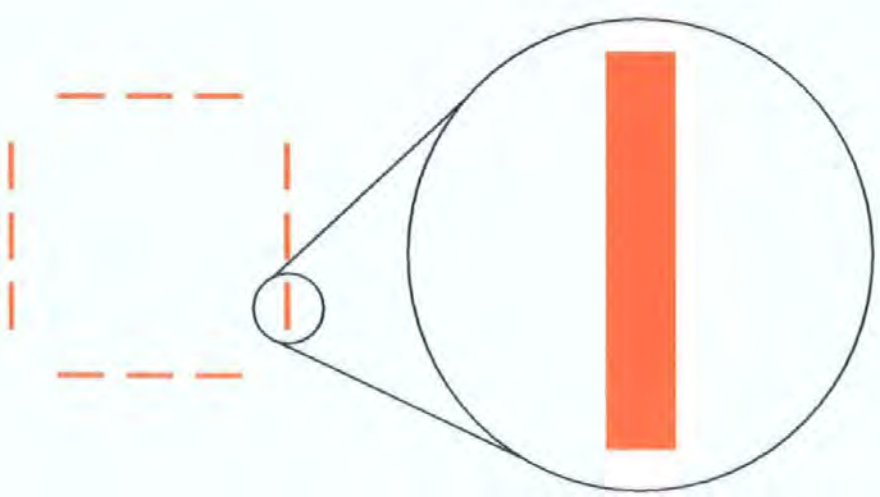

**Figure A2-2. The prototype probe designs, in actual and zoomed in size (pad length 5 mm).**

### *Substrate Preparation*

In the manufacturing process substrate cleanliness is imperative to ensure the quality, reproduction and amalgamation of coated films. A standard routine has been instigated in the clean room. After the glass substrates are removed from their sealed packaging they

are cleaned using a hot detergent, such as neutracon, applied with a soft non-shedding clean room cloth. This removes any particles and grease marks on the surface. The substrates are then rinsed in de-ionised water before being placed in an ultrasonic bath, containing a warm solution of weak detergent, for 15 minutes. When removed they are again rinsed, and then dried with a Nitrogen gun. At this point they are examined under an optical microscope, whereby if they are not completely clean the procedure is repeated. Before a substrate is used it is placed in an oven at 135 °C for 30 minutes to remove any moisture contamination. Finally, when the substrate is first placed in the sputtering chamber before deposition, it is sputter etched to remove any contamination that may still remain after the cleansing process.

***Deposition – RF Sputtering***

The sputtering process is the removal of a deposition material from a target to form a coating on a substrate. This is carried out in a vacuum chamber containing two electrodes, where the target is cathode, and substrate is anode. The atoms on the surface of the target are bombarded by fast moving particles. This collision releases some of the target surface atoms to condense on the substrate surface. Immersing the target, with a high negative voltage applied, in a gas plasma produces the particle bombardment. An inert gas, usually Argon, is introduced into the vacuum chamber at a particular pressure. The plasma's electric field ionises the gas particles. These heavy ions are then attracted to the negative potential at the target surface; bombardment takes place, ejecting target atoms out to condense on the substrate. This process is carried out at a low pressure, whereby the number of gas molecules is low, such that the released target atoms do not collide with the gas molecules to be scattered back to the target surface.

The sputtering process is a very reliable and versatile method of depositing thin films, particularly for alloys. Although sputter deposition rates are relatively slow, i.e. 5 to 50

nm a minute, the control of deposition characteristics and reliability of the method made it the correct choice for the manufacture of the aperture prototypes. RF sputtering, see Figure A2-3, was used for depositing the thin conductor film used in the prototypes. RF sputtering is more efficient than dc and can be used to deposit insulators as RF can be coupled through non-conductors.

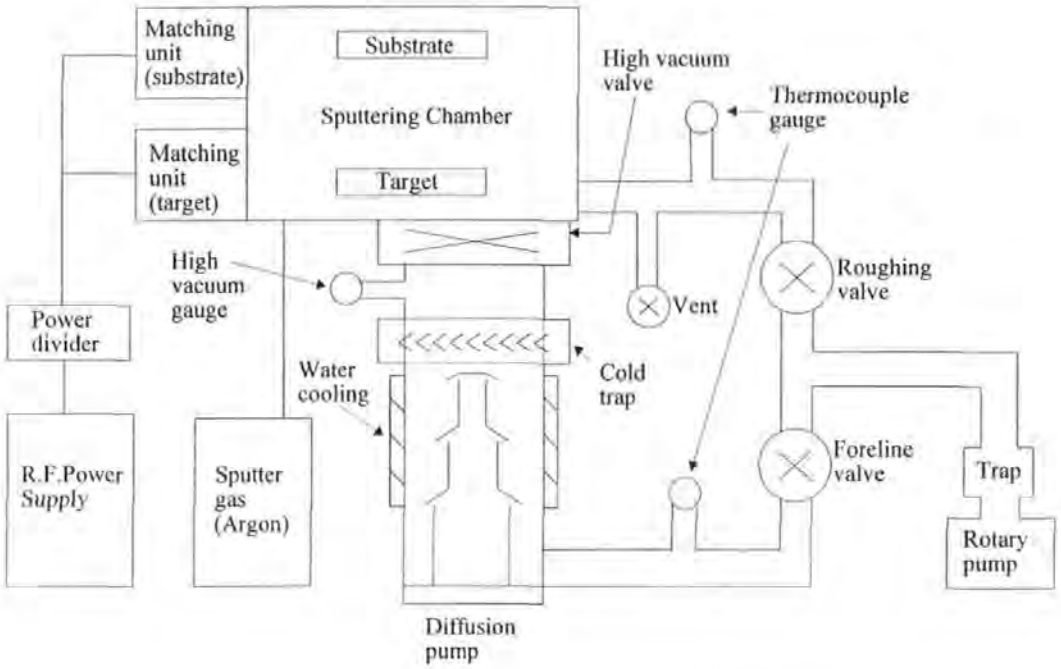


**Figure A2-3. A schematic diagram of the RF sputtering system, © N Fry 1996.**

### *Photo-Resist Process*

A positive photo-resist was used so that the mask aperture was directly duplicated on the coated substrate. Therefore, the photo-resist was used as a covering mask so that exposed regions, i.e. the aperture, were etched. An appropriate photo-resist was selected for the required spin-on thickness. In this case Shipley AZ1813 was used with a thickness of 1.3 μm. The substrate is held down using a vacuum chuck and the photo-resist placed on its centre. The substrate was then spun for 20 seconds at 4000 rpm, thus producing a uniform thickness of resist across the substrate. Once the spinning was completed the substrate and

its covering of photo-resist were baked at 100 °C for 1 minute. This removes any residual solvent contained in the resist.

The substrate is exposed to ultra-violet light using a Dage Precima in-contact mask aligner. The substrate holder floats on an air cushion allowing the substrate and mask to be brought together and levelled. Once this is done the air is turned off, and the substrate can be aligned by micrometers. The mask and substrate are then held together by vacuum. The pattern on the mask then blocks the exposure of regions of the photo-resist by the ultra-violet source, a timed 200 W mercury lamp. After exposure the substrate is developed in a solution of Shipley AZ developer for 30 seconds to reveal the mask pattern of photo-resist on top of the coated film.

***Etching***

In ion milling, see Figure A2-4, Argon molecules are injected into a source discharge chamber and struck by electrons from a cathode, so generating a plasma. Although some ions recombine with electrons at the chamber's walls, others form beamlets by passing through aperture in a screen grid. These beamlets are then attracted to a high negative voltage at an accelerator grid. However, due to the alignment of the grids, most pass through without hitting it. These individual beamlets then form an ion beam as they leave the accelerator grid. The ion beam is neutralised by electrons from the neutraliser, thus stopping the beam from expanding by Coulomb repulsion, and preventing charge build up at the substrate surface. The water-cooled substrate and ion source are located in a vacuum chamber such that the ion beam is aimed at the substrate. The angle of incidence can be adjusted to obtain the correct edge profile.

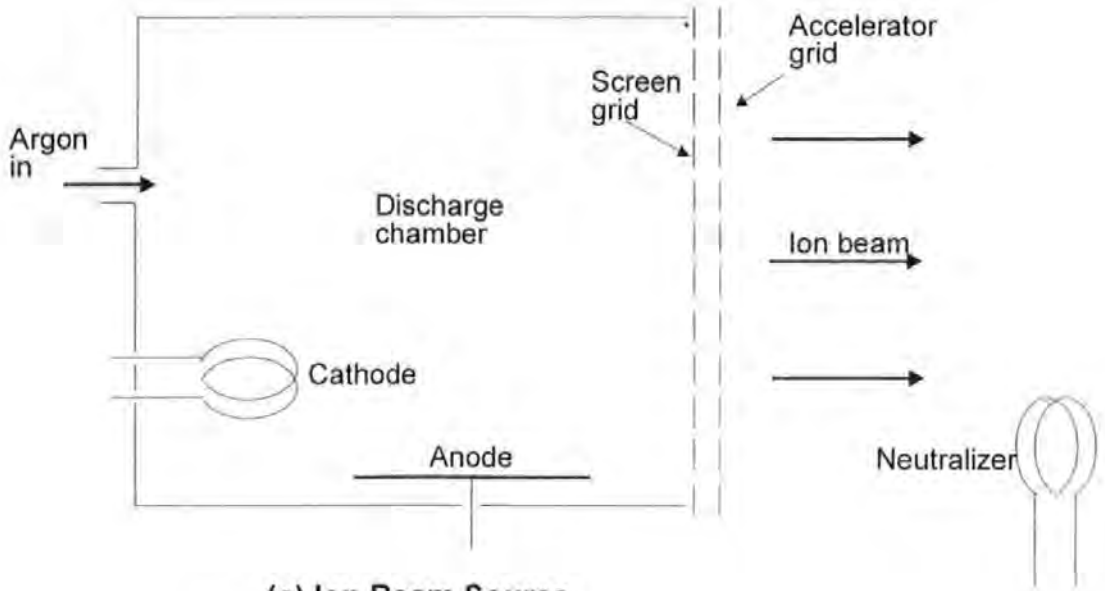


**(a) Ion Beam Source**

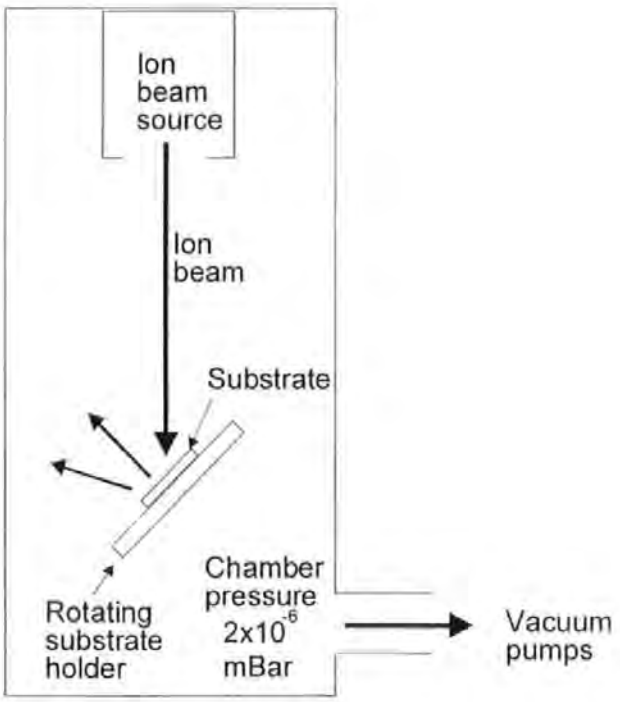


**(b) Ion Beam Etcher Configuration**

**Figure A2-4. Ion beam source (a) and etching (b), © N Fry 1996.**

A Commonwealth Vacuum Corporation ion-milling system was used to dry etch the aperture designs. This provides an anisotropic etch, producing accurate edge profiles with minimum undercutting. This method is employed, as it is the best available process in the Plymouth clean facility for the production of the prototype apertures.

After etching the photo-resist is removed by soaking the entire substrate in Acetone, thus revealing the final prototype aperture geometry. This was then rinsed and dried for storage in the Class 100 rooms within the clean room. If the resist proves difficult to remove, as may happen if the resist is partly baked by the ion milling process, the substrate is soaked overnight or immersed in warm acetone or photo-resist stripper to remove the remaining resist.

# References


[1] Toshiba Corporation Press Release, "Toshiba's New HDD Offers World's Highest 2.5-inch Platter Capacity", Tokyo, April 9th 2002.

[2] T. M. Coughlin, "High Density Hard Disk Drive Trends in the USA", The Institute for Information Storage Technology, Santa Clara University, 2001.

[3] R. Wood, "The Feasibility of Magnetic Recording at 1 Terabit per Square Inch", IEEE Transactions on Magnetics, vol. 36 (1), pp. 36-42, 2000.

[4] F. A. Jenkins, H. E. White, Fundamentals of Optics, McGraw-Hill, 1957.

[5] R. Carey, E. D. Isaac, Magnetic Domains and Techniques for their Observation, English Universities Press Ltd., 1966.

[6] W. W. Clegg, N. A. E. Heyes, E. W. Hill, C. D. Wright, "Development of a scanning laser microscope for magneto-optic studies of thin magnetic films", Journal of Magnetism and Magnetic Materials, vol. 95, pp. 49-57, 1991.

[7] C. D. Wright, N. A. E. Heyes, W. W. Clegg, E. W. Hill, "Magneto-Optic Scanning Laser Microscopy", Microscopy and Analysis, pp. 21-23, March 1995.

[8] M. Bauer, R. Lopusnik, H. Dotsch, B. A. Kalinikos, C. E. Patton, J. Fassbender, B. Hillebrands, "Time domain MOKE detection of spin wave modes and precession control for magnetization switching in ferrite films", Journal of Magnetism and Magnetic Materials, vol. 226, pp. 507-509, 2001.

[9] N. A. E. Heyes, C. D. Wright, W. W. Clegg, J. Zhao, "A Short-Wavelength R-Theta Scanning Laser Microscope And Optical Disc Tester For The Characterization Of

Optical-Recording Media", IEEE Transactions on Magnetics, vol. 31 (6), pp. 3271-3273, 1995.

[10] Toptica Photonics AG, Fraunhoferstr. 14, D-82152 Martinsried/Munich, Germany, VersaTest (Optical Data Storage Media Versatile Dynamic test system), 2002.

[11] C. J. R. Sheppard & D. M. Shotton, Confocal Laser Scanning Microscopy, BIOS Scientific, 1997.

[12] E. H. Synge, "A suggested method for extending microscopic resolution into the ultra-microscopic region", Philosophical Magazine, vol. 6, pp. 356-362, 1928.

[13] E. Betzig, J. K. Trautman, "Near-Field Optics: Microscopy, Spectroscopy, and Surface Modification Beyond the Diffraction Limit", Science, vol. 257, pp. 189-195, 1992.

[14] H. Heinzelmann, D. W. Pohl, "Scanning near-field optical microscopy", Journal of Applied Physics A: Solids & Surfaces, vol. 59, pp. 89-101, 1994.

[15] D. Drews, W. Ehrfeld, M. Lacher, K. Mayr, W. Noell, S. Schmitt, M. Abraham, "Nanostructured probes for scanning near-field optical microscopy", Nanotechnology, vol. 10, pp. 61-64, 1999.

[16] B. Knoll, F. Keilmann, "Mid-infrared scanning near-field optical microscope resolves 30nm", Journal of Microscopy, vol. 194, pp. 512-515, 1999.

[17] G. Eggers, A. Rosenberger, N. Held, A. Münnemann, G. Güntherodt, P. Fumagalli, "Scanning near-field magneto-optic microscopy using illuminated fiber tips", Ultramicroscopy, vol. 71, pp. 249-256, 1998.

[18] K. Wang, X. Wang, N. Jin, W. Huang, J. Xu, "The height regulation of a near-field scanning optical microscope probe tip", Journal of Microscopy, vol. 194, pp. 317-320, 1999.

[19] G. Binnig, H. Rohrer, C. Gerber, E. Weibel, "Surface Studies by Scanning Tunneling Microscopy", Physical Review Letters, vol. 49 (1), pp. 57-61, 1982.

[20] G. Binnig, C. H. Gerber, E. Stoll, T. R. Albrecht, C. F. Quate, "Atomic Resolution with Atomic Force Microscope", Europhysics Letters, vol. 3 (12), pp. 1281-1286, 1987.

[21] Y. Martin, H. K. Wickramasinghe, "Magnetic imaging by "force microscopy" with 1000 Å resolution", Applied Physics Letters, vol. 50 (20), pp. 1455-1457, 1987.

[22] Physik Instrumente Ceramic, Lindenstrasse, D-07589 Lederhose, Germany, Piezoelectric Ceramics & Components - Data Sheet, 2002.

[23] TM Microscopes, 1171 Borregas Avenue, Sunnyvale, CA 94089, USA, "A Practical Guide to Scanning Probe Microscopy", 2001.

[24] T. Fujii, M. Suzuki, M. Yamaguchi, R. Kawaguchi, H. Yamada, K. Nakayama, "Three-dimensional displacement measurement of a tube scanner for a scanning tunneling microscope by optical interferometer", Nanotechnology, vol. 6, pp. 121-126, 1995.

[25] M. D. Kirk, T. R. Albrecht, C. F. Quate, "Low-Temperature Atomic Force Microscopy", Review of Scientific Instruments, vol. 59 (6), pp. 833-835, 1988.

[26] O. Marti, B. Drake, P. K. Hansma, "Atomic Force Microscopy of Liquid-Covered Surfaces: Atomic Resolution Images", Applied Physics Letters, vol. 51 (7), pp. 484-486, 1987.

[27] G. Neubauer, S. R. Cohen, G. M. McClelland, D. Horne, C. M. Mate, "Force Microscopy With A Bidirectional Capacitance Sensor", Review of Scientific Instruments, vol. 61 (9), pp. 2296-2308, 1990.

[28] A. DiCarlo, M. R. Scheinfein, R. V. Chamberlin, "Magnetic Force Microscopy Utilizing An Ultrasensitive Vertical Cantilever Geometry", Applied Physics Letters, vol. 61 (17), pp. 2108-2110, 1992.

[29] T. Göddenhenrich, H. Lemke, U. Hartmann, C. Heiden, "Force Microscope with Capacitive Displacement Detection", Journal of Vacuum Science & Technology, vol. A8, pp. 383-387, 1990.

[30] D. Sarid, P. Pax, L. Yai, S. Howells, M. Gallagher, T. Chen, V. Elings, D. Bocek, "Improved Atomic Force Microscope Using A Laser Diode Interferometer", Review of Scientific Instruments, vol. 63 (8), pp. 3905-3908, 1992.

[31] C. M. Mate, G. M. McClelland, R. Erlandsson, S. Chiang, "Atomic-Scale Friction of a Tungsten Tip on a Graphite Surface", Physics Review Letters, vol. 59 (17), pp. 1942-1945, 1987.

[32] R. Erlandsson, G. M. McClelland, C. M. Mate, S. Chiang, "Atomic Force Microscopy Using Optical Interferometry", Journal of Vacuum Science & Technology, vol. A6 (2), pp. 266-270, 1988.

[33] Y. Martin, C. C. Williams, H. K. Wickramasinghe, "Atomic Force Microscope-Force Mapping and Profiling on a Sub 100Å Scale", Journal of Applied Physics, vol. 61 (10), pp. 4723-4729, 1987.

[34] P. C. D. Hobbs, D. W. Abraham, H. K. Wickramasinghe, "Magnetic Force Microscopy with 25nm Resolution", Applied Physics Letters, vol. 55 (22), pp. 2357-2359, 1989.

[35] D. W. Abraham, C. C. Williams, H. K. Wickramasinghe, "Measurement of In-Plane Magnetisation by Force Microscopy", Applied Physics Letters, vol. 53 (15), pp. 1446-1448, 1988.

[36] G. Meyer, N. M. Amer, "Novel Optical Approach to Atomic Force Microscopy", Applied Physics Letters, vol. 53 (12), pp. 1045-1047, 1988.

[37] S. Alexander, L. Hellemans, O. Marti, J. Schneir, V. Elings, P. K. Hansma, M. Longmire, J. Gurley, "An Atomic-Resolution Atomic-Force Microscope Implemented Using an Optical Lever", Journal of Applied Physics, vol. 65 (1), pp. 164-167, 1989.

[38] MikroMasch Eesti, Narva mnt. 13 10151 Tallinn, Estonia - Scanning Probe Microscope Tips - 2002.

[39] G. Binnig, C. F. Quate, C. Gerber, "Atomic Force Microscope", Physical Review Letters, vol. 56(9), pp. 930-933, 1986.

[40] M. S. Valera, A. N. Farley, "A high performance magnetic force microscope", Measurement Science and Technology, vol. 7, pp. 30-35, 1996.

[41] T. Weber, Development and Instrumentation of Resonant Force Microscope, Studienarbeit Thesis Technische Universität Hamburg-Harburg, 1996.

[42] Digital Instruments, 112 Robin Hill Road, Santa Barbara, CA 93117, USA, NanoScope MultiMode - LiftMode™ (1995).

[43] C. B. Prater, P. G. Maivald, K. J. Kjoller, M. G. Heaton, "TappingMode™ Imaging Applications and Technology", Digital Instruments Application Note (AN04), 2001.

[44] R. G. Carr, "Finite Element Analysis of PZT Tube Scanner Motion for Scanning Tunnelling Microscopy", Journal of Microscopy, vol. 152, no. 2, pp. 379-385, 1988.

[45] R. Wiesendanger, Scanning Probe Microscopy and Spectroscopy, Cambridge University Press, 1994.

[46] D. Rugar, H. J. Mamin, P. Guethner, S. E. Lambert, J. E. Stern, I. Mcfadyen, T. Yogi, "Magnetic force microscopy: General principles and application to longitudinal recording media", Journal of Applied Physics, vol. 68, pp. 1169-1183, 1990.

[47] M. Khalid, "The Development of Scanning Probe Microscopy Instrumentation and Techniques", PhD Thesis, University of Manchester, page 46, 1997.

[48] Sheldon Instruments, 609 West Date Street, San Diego, CA. 92101-2525, USA, - SIC33DSP Data Sheet - 2001.

[49] P. J. Crozier, "The Development of a High Resolution Scanning Force Imaging System", PhD Thesis, University of Manchester, 1994.

[50] G. W. Johnson, LabVIEW Graphical Programming (3rd Ed.), McGraw-Hill Inc., 2001.

[51] T. M. H. Wong, M. E. Welland, "A digital control system for scanning tunnelling microscopy and atomic force microscopy", Measurement Science & Technology, vol. 4, pp 270-280, 1993.

[52] RHK Technology Inc., 1050 East Maple Road, Troy, MI 48083, USA, - SPM 1000 SPM Controller & Software - 2002.

[53] D. R. Baselt, S. M. Clark, M. G. Youngquist, C. F. Spence, J. D. Baldèschwieler, "Digital signal processor control of scanned probe microscopes", Review of Scientific Instruments, vol. 64, pp.1874-1882, 1993.

[54] G. Ping, M. A. Player, "Control system analysis of a scanning tunnelling microscope", Measurement Science & Technology, vol. 4, pp. 677-681, 1993.

[55] M. E. Taylor, "Dynamics of Piezoelectric Tube Scanners for Scanning Probe Microscopy", Review of Scientific Instruments, vol. 64 (1), pp. 154-158, 1993.

[56] G. F. Franklin, J. D. Powell, A. Emami-Naeini, Feedback Control of Dynamic Systems (3rd Ed.), Addison-Wesley, 1994.

[57] B. C. Kuo, Digital Control Systems, Holt, Rinehart & Winston Inc, 1980.

[58] C. L. Philips, R. D. Harbor, Feedback Control Systems, Prentice-Hall, 1988.

[59] D. Sarid, Scanning Force Microscopy with Applications to Electric, Magnetic and Atomic Forces (Revised Edition), Oxford University Press, 1994.

[60] MikroMasch - Scanning Probe Microscope TGZ Vertical Calibration Gratings - 2002.

[61] W. W. Clegg, D. F. L. Jenkins, L. He, J. F. C. Windmill, N. Fry, R. Atkinson, W. R. Hendren, C. D. Wright, "A Scanning Laser Microscope System to Observe Static and Dynamic Magnetic Domain Behaviour", IEEE Transactions on Instrumentation and Measurement, vol. 51 (1), pp. 10-13, 2002.

[62] H. Zhou, G. Mills, B. K. Chong, A. Midha, L. Donaldson, J. M. R. Weaver, "Recent progress in the functionalization of atomic force microscope probes using electron-beam nanolithography", Journal of Vacuum Science & Technology A, vol. 17 (4), pp. 2233-2239, 1999.

[63] A. H. Bobeck, S. L. Blank, A. D. Butherus, F. J. Ciak, W. Strauss, "Current-Access magnetic bubble circuits", Bell Systems Technical Journal, vol. 56, pp. 1453-1540, 1979.

[64] E. W. Hill, "Modeling damaged MFM tips using triangular charge sheets", IEEE Transactions on Magnetics, vol. 31, pp. 3355-3357, 1995.

[65] L. Folks, M. E. Best, P. M. Rice, B. D. Terris, D. Weller, J. N. Chapman, "Perforated tips for high-resolution in-plane magnetic force microscopy", Applied Physics Letters, vol. 76 (7), pp. 909-911, 2000.

[66] C. D. Wright, E. W. Hill, "Reciprocity in magnetic force microscopy", Applied Physics Letters, vol. 67 (3), pp. 433-435, 1995.

[67] C. D. Wright, E. W. Hill, "A reciprocity-based approach to understanding magnetic force microscopy", IEEE Transactions on Magnetics, vol. 32, pp. 4144-4146, 1996.

[68] J. G. Zhu, H. N. Bertram, "Reversal mechanisms and domain-structures in thin-film recording media", Journal of Applied Physics, vol. 69, pp. 6084-6089, 1991.

[69] C. Durkan, M. Schneider, M. Welland, "Analysis of failure mechanisms in electrically stressed Au nanowires", Journal of Applied Physics, vol. 86 (3), pp. 1280-1286, 1999.

[70] K. Fuchs, "The conductivity of thin metallic films according to the electron theory of metals", Proceedings of the Cambridge Philosophical Society, vol. 34, pp. 100-108, 1938.

[71] C. Kittel, Introduction to solid state physics, 6th Edition, Wiley, 1986.

[72] J. R. Lloyd, "Electromigration in integrated circuit conductors", Journal of Physics D: Applied Physics, vol. 32, pp. R109–R118, 1999.

[73] J. R. Lloyd, "Electromigration in thin film conductors", Semiconductor Science & Technology, vol. 12, pp. 1177–1185, 1997.

[74] D. A. Fraser, The Physics of Semiconductor Devices, 4th Edition, Oxford University Press, 1986.

[75] R. L. Geiger, P. E. Allen, N. R. Strader, VLSI design techniques for analog and digital circuits, McGraw-Hill, 1990.

[76] K. Seshan, T. J. Maloney, K. J. Wu, "The Quality and Reliability of Intel's Quarter Micron Process", Intel Technology Journal, Quarter 3, 1998.

[77] F. Wang, N. Helian, W. W. Clegg, J. F. C. Windmill, D. F. L. Jenkins, "A current-modulating magnetic force microscope probe", Journal of Applied Physics, Vol. 89, No. 11, pp. 6778-6780, 2001.

[78] S. Hosaka, "SPM Based Storage", IEEE Transactions on Magnetics, vol. 32 (3), pp. 1873-1877, 1996.

[79] B. W. Chui, T. D. Stowe, Y. S. Ju, K. E. Goodson, T. W. Kenny, H. J. Mamin, B. D. Terris, R. P. Ried, D. Rugar, "Low-Stiffness Silicon Cantilevers with Integrated Heaters and Piezoresistive Sensors for High-Density AFM Thermomechanical Data Storage", Journal of Microelectromechanical Systems, vol. 7 (1), pp 69-77, 1998.

[80] U. Durig, G. Cross, M. Despont, U. Drechsler, W. Haberle, M. I. Lutwyche, H. Rothuizen, R. Stutz, R. Widmer, P. Vettiger, G. K. Binnig, W. P. King, K. E. Goodson, "Millipede - an AFM data storage system at the frontier of nanotribology", Tribology Letters, vol. 9 (1-2), pp. 25-32, 2000.

[81] M. Williams, E. Growchowski, "Design of Magnetic Inductive Write Heads for High Density Storage", DataTech, 2nd Edition, 1999.

[82] T. Rausch, J. A. Bain, T. E. Schlesinger, "Advances in hybrid recording may overcome barriers to commercialization", Data Storage Magazine, June 2001.

[83] A. Vollkopf, O. Rudow, T. Leinhos, C. Mihalcea, E. Oesterschulze, "Modified fabrication process for aperture probe cantilevers", Journal of Microscopy, vol. 194 (2/3), pp. 344-348, 1999.

[84] M. Stopka, D. Drews, K. Mayr, M. Lacher, W. Ehrfeld, T. Kalkbrenner, M. Graf, V. Sandoghdar, J. Mlynek, "Multifunctional AFM/SNOM cantilever probes: Fabrication and measurements", Microelectronic Engineering, vol. 53 (1-4), pp. 183-186, 2000.

[85] T. Rausch, P. Herget, J. A. Bain, J. Zhu, D. D. Stancil, T. E. Schlesinger, "Experimental Test Bed for Hybrid Recording", Optical Data Storage 2001, Proceedings of SPIE, vol. 4342, pp. 502-510, 2002.

[86] E. Betzig, J. K. Trautman, R. Wolfe, E. M. Gyorgy, P. L. Finn, M. H. Kryder, C. H. Chang, "Near-field magneto-optics and high density data storage", Applied Physics Letters, vol. 61, pp. 142-144, 1992.

[87] S. Munster, S. Werner, C. Mihalcea, W. Scholz, E. Oesterschulze, "Novel micromachined cantilever sensors for scanning near-field optical microscopy", Journal of Microscopy, vol. 186, pp. 17-22, 1997.

[88] H. Katayama, M. Hamamoto, J. Sato, Y. Murakami, K. Kojima, "New Developments in Laser-Assisted Magnetic Recording", IEEE Transactions on Magnetics, vol., 36 (1), pp. 195-199, 2000.

[89] S. R. Cumpson, P. Hidding, R. Coehoorn, "A Hybrid Recording Method Using Thermally Assisted Writing and Flux Sensitive Detection", IEEE Transactions on Magnetics, vol. 36 (5), pp. 2271-2275, 2000.

[90] NIST ATP Project 00004601 - Heat Assisted Magnetic Recording, Sponsor: National Storage Industry Consortium, October 2001.

[91] J. A. Sidles, J. L. Garbini, K. J. Bruland, D. Rugar, O. Zuger, S. Hoen, C. S. Yannoni, "Magnetic-resonance force microscopy", Reviews of Modern Physics, vol. 67 (1), pp. 249-265, 1995.

[92] M. Barbic, J. J. Mock, A. P. Gray, S. Schultz, "Scanning probe electromagnetic tweezers", Applied Physics Letters, vol. 79 (12), pp. 1897-1899, 2001.

# Publications


1. J. F. C. Windmill, W. W. Clegg, "A Novel Magnetic Force Microscope Probe Design", IEEE Transactions on Magnetics, vol. 36 (5), pp. 2984-2986 (Part 1), September 2000.

2. D. F. L. Jenkins, W. W. Clegg, L. He, J. Windmill, G. Tunstall, X. Liu, C. Chilumbu, A. Li, "Sensors For Dynamic Characterisation Of Magnetic Storage Systems", Sensor Review, vol. 20 (4), pp. 307-317, 2000 (invited paper).

3. F. Wang, N. Helian, W. W. Clegg, J. F. C. Windmill, D. Jenkins, "A current-modulating magnetic force microscope probe", Journal of Applied Physics, vol. 89 (11), pp. 6778-6780, 2001.

4. J. F. C. Windmill, W. W. Clegg, D. F. L. Jenkins, P. Davey, "A New Theoretical Probe for the Magnetic Force Microscope", Journal of Magnetism and Magnetic Materials, vol. 226-0, pp. 1267-1269, 2001.

5. W. W. Clegg, D. F. L. Jenkins, L. He, J. F. C. Windmill, N. Fry, R. Atkinson, W. R. Hendren, C. D. Wright, "A Scanning Laser Microscope System to Observe Static and Dynamic Magnetic Domain Behaviour", IEEE Transactions on Instrumentation and Measurement, vol. 51 (1), pp. 10-13, 2002.

6. W. Clegg, D. Jenkins, N. Helian, J. Windmill, R. Windmill, R. Atkinson, B. Hendren, C. D. Wright, "Scanning Laser Techniques For Dynamic Thermo-Magnetic Recording Onto Stationary Media", Journal of Magnetism and Magnetic Materials, vol. 249-3, pp. 42-45, 2002.

# A Novel Magnetic Force Microscope Probe Design

James F. C. Windmill and Warwick W. Clegg, *Senior Member, IEEE*

***Abstract*—A new theoretical electromagnetic probe for the Magnetic Force Microscope (MFM) is presented here. The magnetic field intensity normal to the probe, $H_z$ (Oe), has been modeled. The reciprocity principle was used to obtain the force acting on the sample due to the probe field when scanned over a magnetic specimen. Thus, images of specimen magnetic distribution were created by the convolution of the distribution and the probe's gradient field. These show that in the case of perpendicular magnetization the new probe was successful. However, in longitudinal magnetization there was an image artifact problem. The practical use of the new probe is discussed, and future work outlined.**

***Index Terms*—Magnetic force microscopy, magnetic force microscopy tip.**

## I. Introduction

OVER the last ten years since its conception, the Magnetic force Microscope (MFM) has gained recognition as a useful research tool in many fields. The main area that has provided the impetus for the expansion of MFM's from interesting research concept to practical commercial instrument is magnetic data storage. The continuing effort to increase data density, and so remain in competition, has led to commercially available densities of 14 GigaBytes per square inch. As a result the imaging instruments used in data recording research have had to improve. A large amount of research continues into MFM, in both the theories behind its operation, and the practical issues of improving its operation.

One of the fundamental MFM research subjects is the design and function of the probe used to interact with a magnetic sample's stray fields. Standard MFM probes (cantilevers) use silicon tips that are magnetically sensitized using ferromagnetic thin films. Unfortunately this design has several inherent problems. First of all a variety of different designs and coatings need to be used depending on the magnetic properties of the sample being imaged, i.e., if the sample is magnetically "hard" or "soft." This means that an instrument must be reconfigured each time a new type of sample is to be imaged. Furthermore, the magnetization of the tip can suffer from hysteresis over time, as well as wear and damage during its useful life. These imperfections can have serious consequences in the acquisition of useful and quantifiable data. This paper presents a new theoretical design as a possible answer to the standard probe's weaknesses.

Manuscript received May 15, 2000. This work was supported in part by an Engineering & Physical Sciences Research Council (UK) Research Studentship.

The authors are with the Centre for Research in Information Storage Technology (CRIST), University of Plymouth, Plymouth, PL4 8AA, UK (e-mail: {jwindmill; wclegg}@plymouth.ac.uk).

Publisher Item Identifier S 0018-9464(00)08648-9.

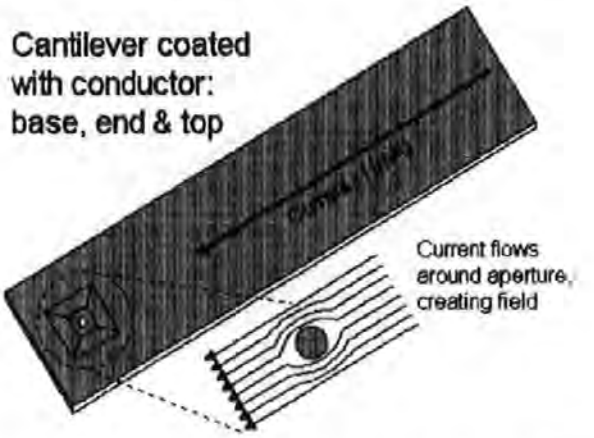


Fig. 1. Simplified diagram of basic probe design viewed from below. Current flows around an aperture, causing a change in its density and thus a change in magnetic field intensity normal to the surface.

## II. The New Probe

### A. Initial Idea

The new probe uses an electromagnetically induced field as a replacement for the standard probe's stray field. Although, electromagnetic MFM probes have been reported before, this design is unique [1]. The field is induced around a micro-fabricated aperture using a controlled current. The aperture would be situated near the end of a standard cantilever that has been coated in a conductive material, e.g., gold. This design has the advantage that the field intensity, and hence specimen interaction, is variable, and also the results should be repeatable. Using the Biot–Savart law, as given in (1), a change in magnetic field intensity normal to the conductive material's surface is produced by changing the current density within it.

$$\mathbf{H} = \frac{1}{4\pi} \cdot \int_S \frac{\mathbf{J} \cdot \mathbf{R}}{|\mathbf{R}|^3}\, ds \tag{1}$$

### B. Field Modeling

By placing an aperture in a sheet of conductive material of constant current density, current must flow around the aperture, resulting in a change in its density, as shown in Fig. 1.

The model uses a simple circular aperture in a flat surface, producing the magnetic field intensity, $H_z$, in Oersteds, as shown in Fig. 2 [2]. $H_z$ is shown for a height of 25 nm above the surface of an aperture of radius 250 nm, with a sheet current density of 2 mA/$\mu$m. Note that by controlling the applied current, and hence the linear current density, the field strength can be varied. The aperture design gives a "double-peak" effect, where the splitting of the current flow causes two inverse peaks

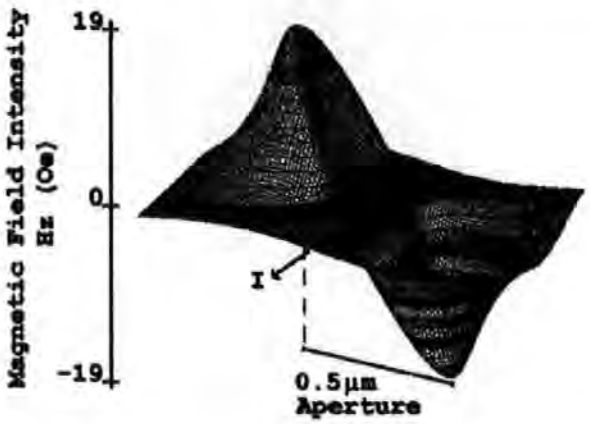


Fig. 2. Magnetic Field Intensity, $H_z$ (Oe), normal to a circular aperture as a function of the sheet density of the current. $H_z$ is shown at 25 nm above the surface of a 0.5 $\mu$m aperture, with a sheet current density of 2 mA/$\mu$m.

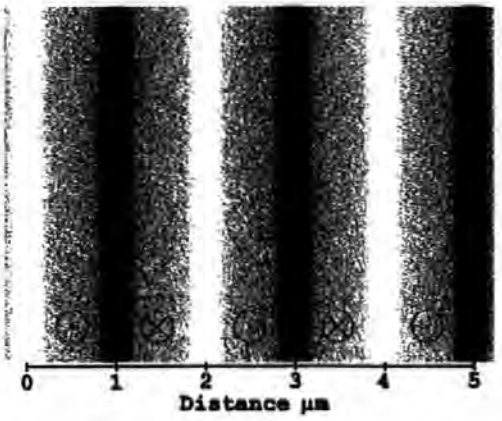


Fig. 3. Simulated MFM image of five 1 $\mu$m long perpendicular bits using the new probe, with a 250 nm-diameter aperture. A dark or light line, depending on transition and probe travel direction, shows each transition.

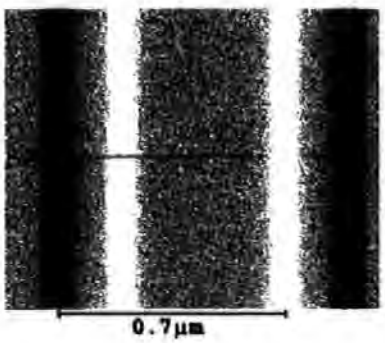


Fig. 4. Simulated MFM image of a 0.7 $\mu$m long longitudinal bit using the new probe, with a 250 nm-diameter aperture. Note the double-peak effect, where each domain transition is imaged twice.

in $H_z$ to be produced. Standard MFM tips have been described with aperture tips, which are used to image in-plane stray fields [3]. This shows that the manufacturing techniques are available to create our new probe. The magnetic field intensity has been shown in Oersteds to allow comparison with previous work on MFM probes, and as such shows that this design is comparable to a standard MFM probe, as discussed by others [4].

## III. MFM Simulation

### A. Theory of MFM Interaction

In general, the simulation of MFM images has been realized by considering the interaction between the magnetization of the MFM's tip and a specimen's stray field. This allows the calculation of the force acting on the tip due to the field from the specimen. However, given Newton's third law, the principle of reciprocity that has been discussed in previous work can be used [5]. As such the force acting on the specimen due to the tip's stray field is calculated, which is the inverse of the force acting on the tip. This reciprocal force acting in the vertical, $z$, direction can be expressed as in

$$F_z^{tip} = -\int_{spec} \sum_i M_i^{spec}(r') \frac{\partial H_i^{tip}(r+r')}{\partial z'} d^3r', \qquad (2)$$

where $i$ corresponds to the directions $x$, $y$, or $z$, $M_i^{spec}$ is the $x$, $y$, or $z$ component of the magnetization of a specimen volume element and $H_i^{tip}(r+r')$ is the stray field from the tip at that specimen volume element.

This then allows the simulation of the new probe, since the calculated field intensity, as shown in Fig. 2, can be used with (2). Note that the force calculated in (2) is that produced when an MFM is operating in static, or DC, mode. The resonant, i.e., force gradient AC, mode can be described by taking the second derivative of the tip's stray field.

### B. Computer Image Simulation

In order to create image simulations a model is needed for the magnetization of the specimen. In this work both perpendicular and longitudinal magnetic media bit transitions have been used [6]. Each use a simple arctangent model, for example the first, for a perpendicular transition, is given in (3), but extended in the $y$ direction to produce an image.

$$M_z = \frac{2}{\pi} \cdot M_o \cdot \arctan\left(\frac{x_o}{a_p}\right) \qquad (3)$$

To produce a quick, efficient computer image simulation of the interaction between the probe and a magnetic specimen, a FFT convolution of the probe's gradient field and the specimen magnetization distribution is performed.

## IV. Image Results

The simulated DC MFM images shown in Figs. 3 and 4 were created using the above technique. In Fig. 3 an image of a perpendicular bit pattern has been created. The new probe, with a flying height of 25 nm, has successfully imaged the pattern, specifically highlighting the bit domain transitions as dark or light lines. The shading of the line indicates the transition direction, although this depends on the direction of the probe's travel relative to a transition. In this case the probe flew left to right, with the negative field peak leading.

In Fig. 4 the new probe has been used to image a longitudinal bit. There is however a large artifact created by the probe's "double-peak" field intensity. The transitions, shown by the dark

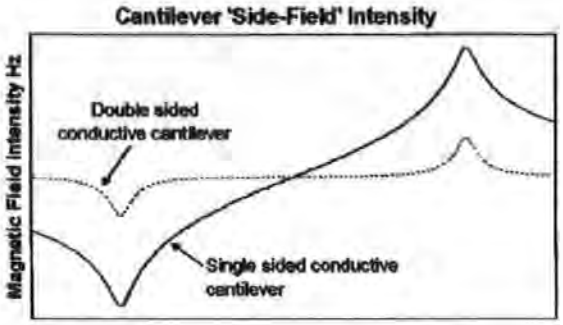


Fig. 5. Magnetic field intensity, $H_z$, 25 nm below a bar shape cantilever, with current flowing along a conductive material covering the base (solid line), and with current along the top, end and base (dotted line).

and light shaded lines, are imaged twice, once by each of the field peaks, so creating a pair of lines for each transition. The distance between each line in a pair gives a good indication of the probe aperture size. This artifact could be removed using computer image filtering, although further artifacts may be introduced. A further answer, would be to adjust the aperture such that one peak is dominant over the other, e.g. a semicircular aperture to increase current density on one aperture side, whilst reducing it on the other.

## V. Practical Design Issues

So far the theoretical probe and its interaction with magnetic specimens has been considered. An examination of the practical use of the probe is also in progress. It is foreseen that the probe would be placed near the end of a standard bar or v-shape cantilever, coated with a conductive material, e.g. gold, in such a way that the design allows for current flow down past the aperture, then back to its source. The conductive material must be able to tolerate sufficient current to create the required field intensity, without damaging the probe, e.g. through electromigration effects. However, given the currents used in this modeling, e.g. that for Fig. 1, it is accepted that this problem will not occur [7].

Another potential problem is the effect and possible interference of the cantilever design and its conductive coating on the specimen magnetization, the probe field and their interaction. In Fig. 5 the magnetic field intensity normal to the surface of a bar shape cantilever is shown. This field intensity is typically several magnitudes larger than the probe field, depending on the size of probe aperture and cantilever. However, this is considerably reduced, since with this design it is necessary to have a conductor on the top, end and base of the cantilever to create a current flow past the aperture. For example, a cantilever 20 $\mu$m wide, with a 0.5 $\mu$m thick conductive coating, and current density of 2 mA/$\mu$m$^2$, would have field peaks of approximately 7 Oe reduced to 2 Oe. A further step will be to create a blunt tip on the cantilever below the aperture, moving it away from the cantilever surface, reducing the field from the sides of the cantilever. This would also act as a topography probe for pre-MFM scanning, increasing the flying height of the cantilever.

## VI. Conclusion

A new theoretical design for an electromagnetic MFM probe has been presented. MFM images have then been simulated using this new design. This has shown that perpendicular magnetic domains can be observed by way of their transitions. Furthermore, the transition direction can be determined, given that the probe dynamics are known. Unfortunately, longitudinal domains were not as successfully imaged. However, in the next phase of modeling this issue will be examined, i.e. through aperture morphology design. The initial practical problems of the probe have been discussed and solutions put forward. It is anticipated that the design covered in this paper will in time be put through practical tests. The results from this, and further modeling enhancements will be published in the near future.

## Acknowledgment

The authors would like to thank D. Jenkins and H. Shute of CRIST, University of Plymouth, UK, and D. Wright of the School of Engineering & Computer Science, University of Exeter, UK. The assistance of the support staff from Vector Fields Ltd., Oxford, UK is also greatly appreciated.

## References

[1] H. Zhou *et al.*, "Recent progress in the functionalization of atomic force microscope probes using electron-beam nanolithography," *J. Vac. Sci. Technol. A*, vol. 17, no. 4, pp. 2233–2239, 1999.
[2] A. H. Bobeck, S. L. Blank, A. D. Butherus, F. J. Ciak, and W. Strauss, "Current-access magnetic bubble circuits," *Bell Systems Tech. J.*, vol. 56, pp. 1453–1540, 1979.
[3] L. Folks *et al.*, "Perforated tips for high-resolution in-plane magnetic force microscopy," *Appl. Phy. Lett.*, vol. 76, no. 7, pp. 909–911, 2000.
[4] E. W. Hill, "Modeling damaged MFM tips using triangular charge sheets," *IEEE Trans. Magn.*, vol. 31, pp. 3355–3357, 1995.
[5] C. D. Wright and E. W. Hill, "A reciprocity-based approach to understanding magnetic force microscopy," *IEEE Trans. Magn.*, vol. 32, pp. 4144–4146, 1996.
[6] J. G. Zhu and H. N. Bertram, "Reversal mechanisms and domain-structures in thin-film recording media," *J. Appl. Phy.*, vol. 69, pp. 6084–6089, 1991.
[7] R. L. Geiger, P. E. Allen, and N. R. Strader, *VLSI Design Techniques for Analog and Digital Circuits*. New York: McGraw-Hill, 1990.

Research articles

# Sensors for dynamic characterisation of magnetic storage systems

*D.F.L Jenkins*
*W.W. Clegg*
*L. He*
*J. Windmill*
*G. Tunstall*
*X. Liu*
*C. Chilumbu and*
*A. Li*

The authors

**D.F.L Jenkins, W.W. Clegg, L. He, J. Windmill, G. Tunstall, X. Liu, C. Chilumbu and A. Li** are all at the Centre for Research in Information Storage Technology (CRIST), University of Plymouth, Plymouth, UK.

Keywords

Inspection, Magnetic, Distance measurement

Abstract

The areal (surface area density of bits) storage density of magnetic hard disks is continually increasing, with typical available commercial storage densities being around 10Gbits/in$^2$. It is predicted that densities in excess of 40Gbits/in$^2$ will be possible before the year 2003. A number of key issues arise from this development, such as the need to determine and control accurately the dynamic flying height (*z*-axis) of the read-write head, which is affected by the apparent distortion of the disk surface due to rotation-induced disk resonance. As a result of the increasing storage density the positional control of the head in the plane of the disk (*x-y* plane) also becomes more critical. This paper deals generally, but with a particular emphasis on optical and piezoelectric sensors used in our laboratory for characterisation of storage media and systems.

Electronic access

The research register for this journal is available at http://www.mcbup.com/research_registers/aa.asp

The current issue and full text archive of this journal is available at http://www.emerald-library.com

Sensor Review
Volume 20 · Number 4 · 2000 · pp. 307–315
 · ISSN 0260-2288

## Introduction

There is a vast array of sensors available to us at present. Sensors are selected according to the particular measurand and in many cases, the particular application, e.g. interfacing to a control system. Sensors are generally required to work in parallel with signal conditioning electronics, and may then be either used as a stand-alone measurement system or incorporated into a control system for real-time sensory feedback.

Depending on the measurand there is a vast array of sensors that can be used for surface and textural characterisation. One of the standard methods for investigating the surface profile is to use a profilometer[1]. A profilometer utilises a stylus much in the same way as a record player follows the variations along the track of a record, the main difference being that the profilometer uses optical sensing to determine the attitude of the stylus. In a record player the stylus generates a signal by electromagnetic induction (moving coil or moving magnet). The potential disadvantage of the stylus-based systems is modification of the surface, due to contact being made by the stylus. However, the use of optical based profilometry is able to circumvent this, and a number of systems have been developed so far. Abou-Zeid and Wiese developed a compact interference profilometer that uses a wavelength-tunable diode laser as an optical stylus, with a measurement uncertainty of around 10nm[2]. A number of profilometry systems based on interferometry have also been reported[3,4]. Cuthbert and Huynh[5] have designed an optical system for fast non-contact measurement of surface texture, based on the optical Fourier transform pattern of the surface, which is correlated with the surface roughness obtained using a stylus based instrument.

Moving into the new millennium we are faced with the increasing demands of hard disk drive technology. Data storage density continues to increase, necessitating that the head flies even closer to the disk surface: state-of-the-art flying heights currently being around 15nm. This is coupled with the increasing demand for faster track access, which means that the disk drive is required to operate at increasingly higher speed. This represents a challenge for PCs operating in the office environment, but presents more

Sensor Review
Volume 20 · Number 4 · 2000 · 307–315

serious difficulties for computers working in conditions where they are subjected to shock and vibration. This is of particular interest to military and aerospace applications; and to a lesser extent will also affect users of laptop computers.

This paper looks at a variety of sensor systems used in the CRIST research laboratory for the characterisation of magnetic media and data storage systems, namely: scanning laser microscopy, magnetic force microscopy, dual beam polarisation interferometry, CD-ROM optics and thick film piezoelectric sensors. Finally, there is a brief look at a complete sensor-control-actuator system, which includes optical beam deflection for displacement (or topography) sensing, which is currently being investigated for the improved operation of hard disk drives.

## A. Dynamic scanning laser microscopy

Scanning laser microscopes are extremely useful tools for high-resolution point-by-point imaging of sample surfaces. The most common configuration employs a stationary laser beam, which can have either continuous or modulated (intensity or polarisation) output. The laser is brought to a focus using a microscope objective to yield a diffraction-limited spot, which is typically around 1mm on the sample surface. The sample can then be micro-positioned, with a motorised *x-y* stage, with respect to the sample and the reflected light collected by one or more detectors. An alternative configuration employs a pair of scan mirrors to move the spot on the sample surface. This set-up is significantly more complex as it requires auto focusing to maintain the same size spot at all points of the scan, and there is a trade-off between scan area and resolution. For example a 5mm × 5mm area can be scanned with a resolution of around 30mm[6]. However, the two systems are often combined: scan mirrors (high speed scanning) and *x-y* stage (large area scan). The use of different detectors and polarisation sensitive/insensitive optics enables different information to be acquired.

In our laboratory a scanning laser microscope has been designed and built to observe the dynamic behaviour of domain switching during the thermo-magnetic write process and the subsequent magnetisation state (domain orientation) in thin-films and devices[7-9]. It can also be used to write to magneto-optic disk material thermo-magnetically prior to imaging. Images are derived from the longitudinal and polar magneto-optic Kerr effects, which are wavelength dependent.

The microscope system has been made modular, which enables the imaging system to be flexible and allows further functionality to be added as required. An overview of the system is shown in Figure 1. The scanning laser microscope is constructed around the basic frame of a Leitz Metalloplan optical microscope, mounted on optical breadboard along with other optical and mechanical components, as shown in Plate 1.

The various modes of operation of the SLM are as follows:

- *XY table scanning mode.* In the XY scan mode a sample is raster scanned beneath the laser spot via a Burleigh XY Worm Table, with a resolution of 4nm. The

**Figure 1** Block diagram of SLM component parts

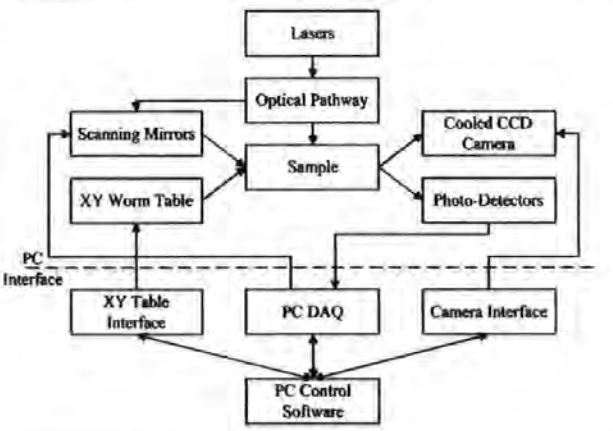


**Plate 1** The scanning laser microscope system in the CRIST laboratory

magnetic or intensity (pseudo-topographic) information is then extracted by sampling all the photo-detector outputs using the computer I/O board, then applying the required algorithm to the data. Plate 2 shows bubble memory magnetic domain patterns using the polar Kerr effect (scan area 32$\mu$m × 40$\mu$m). The reflected light intensity is a function of the sample magnetisation (domain orientation), and LabView enables the reflected intensity to be represented by a grey scale image. The change in intensity represented here is typically less than 1 per cent.

- *Galvanometer scanning mode.* In the galvanometer scan mode the sample is held stationary whilst the laser spot is raster scanned over it via the scanning mirrors. The galvanometer position is controlled using the computer I/O board voltage outputs. Again the computer processes magnetic or topographic information after it is sampled to create an image. Plate 3 shows a pseudo-topographic (reflected intensity) image of an integrated circuit layout (galvanometer scan area 100$\mu$m$^2$).
- *Dye pulse laser.* A further imaging mode of the SLM utilises a dye pulse laser. This requires the software to trigger a waveform generator, and at a set time period later trigger the laser. Finally, at some point in time after this, data are acquired from the photo-detectors. Each of these time periods must be accurately related to the others. The magnetic image is retrieved from the quadrant photo-detectors as for other modes of operation.
- *CCD camera image acquisition.* Another mode of image acquisition uses a super-cooled CCD camera, triggered after a pulse of light has illuminated a sample. The camera is supplied with a set of functions in the form of a Windows dynamic link library (DLL), also known as an application program interface (API). These functions cover all that is required to operate the camera.

Plate 2 Bubble memory magnetic domain patterns using Kerr effect static laser XY table scan 32$\mu$m × 40$\mu$m

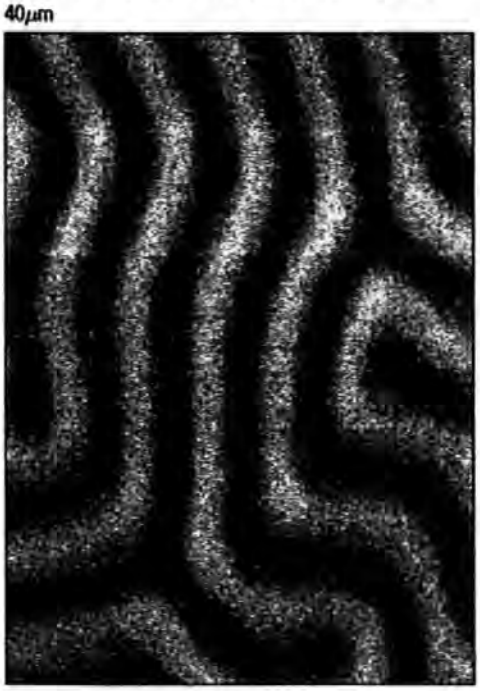

Plate 3 Integrated circuit layout pseudo-topography (intensity) using galvanometer scan – 100$\mu$m$^2$

## B. Magnetic force microscopy

The magnetic force microscope (MFM) is based on the atomic force microscope (AFM)[10]. In the AFM a small probe, a silicon cantilever with an atomically sharp tip, is brought into contact with a sample surface, and raster scanned across it. The resultant deflection of the tip is recorded and used to create an image of the surface topography. In magnetic force imaging the tip is coated in a ferromagnetic material, and moved away from the surface several tens of nanometres. It is then raster scanned, and the interaction between the magnetic field of the sample and the tip recorded to create an image of the magnetic forces.

The development of our MFM, shown in Plate 4, is based on a versatile, modular form,

Sensor Review
Volume 20 · Number 4 · 2000 · 307–315

Plate 4 The magnetic force microscope

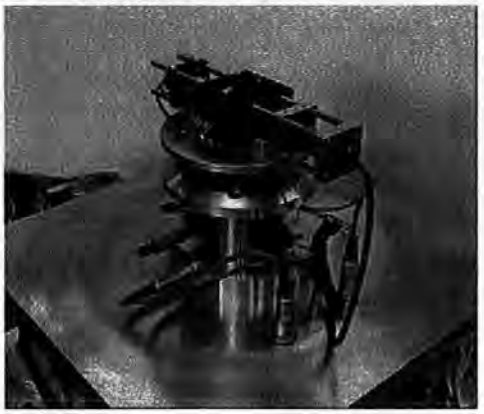

enabling easy access to the specimen and easy change of tips/cantilevers[11]. It uses optical beam deflection to sense cantilever movement and is designed to operate in either topographic or magnetic force imaging modes. This system is also designed to work in low vacuum (or in a helium atmosphere). The benefits of vacuum (and helium) operation are significant, since the removal of much of the normal viscous air damping enables a significant increase in the cantilever's effective Q-value, as operation moves into the molecular damping region (independent collisions of non-interacting air molecules). This in turn results in better resolution of images produced by resonant techniques. Plate 5 shows an image of the topography of a hard disk surface (scan area 1$\mu$m × 1$\mu$m), showing granular structure of surface and diagonal grooves from texturing process.

Plate 5 Hard disk topography, 1$\mu$m × 1$\mu$m surface scan, showing granular structure of surface and diagonal grooves from texturing process

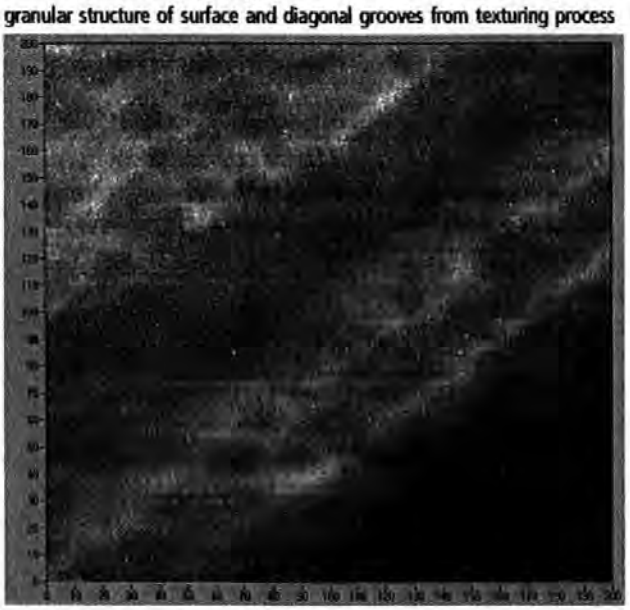

A variety of scanning modes exist for the MFM. The "static" scan, as described above, is the simplest; however, this requires samples with relatively powerful magnetic fields. Resonant scanning is a standard mode of operation, where the cantilever is resonated, and the effects of the sample's fields on that resonance are monitored in different ways to create an image. In recent years LiftMode™ has being recognised as a very useful mode of operation[12]. In this case the topography of the sample is mapped out with an initial scan, from which the data are used to control the height of the MFM probe, in resonant mode, to do a second magnetic scan. This results in removal of topographic effects from the resulting magnetic image.

The design and function of the probe used to interact with the stray fields from a magnetic sample are a major MFM research subject. The standard ferromagnetic design has several inherent problems. The tip magnetisation can suffer from hysteresis over time, together with wear and damage during its useful life. The magnetic properties of different samples, i.e. if the sample is magnetically "hard" or "soft", mean that a range of different designs and coatings need to be employed. Therefore, an instrument must be reconfigured each time a new type of sample is imaged. Furthermore, these imperfections may have serious consequences in the acquisition of useful, quantifiable data.

We are currently investigating a new type of MFM probe that uses an electromagnetically induced field as a replacement for the standard probe's stray field. Although electromagnetic MFM probes have been described before, this design is unique[13]. The field is induced around a micro-fabricated aperture using a controlled current. The aperture would be situated near the end of a standard cantilever that has been coated in a conductive material, e.g. gold. This design has the advantage that the specimen interaction is variable, giving controllable field intensity, and as such the results would be repeatable. The new probe has been theoretically simulated to create images of magnetic domain patterns, and it is anticipated that work on the fabrication of these new and innovative probes will begin soon. The practical issues of using the probe in our MFM instrument are also undergoing analysis.

## C. Dual beam polarisation interferometry

Optical interferometry is a well established technique for precise and non-contact measurement. Various types of interferometry, such as heterodyne interferometry[14], sinusoidal phase modulating interferometry[15], and phase-shifting interferometry[16], have been developed to make high resolution measurement of small displacements. However, apart from the complexity of the system construction, these existing methods are generally feasible only for low-speed measurement applications. When a high-speed measurement is needed, it is difficult to find a suitable technique if the measurement accuracy requirement is high. The speed limitation in these displacement measurement interferometers is mainly due to the use of slow modulation or scanning techniques. In the CRIST laboratory, a dual beam polarisation interferometer has been constructed, which can be used for high-speed measurement of dynamic morphology/topography, and in our case for the complex measurement dynamic disk head flying height[17,18].

The polarisation interferometer configuration utilises two orthogonally-polarized light beams to remove the directional ambiguity of the displacement, and is shown schematically in Figure 2. The main part of the interferometer utilises a polarising beam splitter PBS1, two quarter-wave plates QW1 and QW2, two mirrors M1 and M2, and a non-polarising beam splitter NPBS1 as both a beam splitter and phase shifter.

Employing a polarising beam splitter PBS1 makes the best use of the laser beam and prevents the returning beam from feeding back into the laser diode. The mirror M2 is driven by a piezoelectric translator (PZT1), which can be used to perform system calibration. Mirror M3 is used as a reference plane when single point displacement is measured. When the system is used to measure the relative displacement of two adjacent points, such as the vertical movement of the hard-disk read/write head relative to the disk surface, M3 is removed and the reference beam is extracted by NPBS1 to the second measurement point. Mirror M2 can also be micro-positioned manually to adjust the spacing of the two measurement points. A 670nm wavelength laser diode is used as the light source. The laser beam passes through the polariser and enters the polarising beam splitter PBS1. Then the s-polarised component is coupled out and reflected by mirror M1 and focused on the measurement point on the sample. The p-polarised component passes through and is focused on to the reference mirror or another measurement point. The returning beam enters the interferometric receiver, which is used to measure the intensity and phase difference between the two polarised beams. The interferometric receiver consists of a non-polarising beam splitter NPBS2, two polarising beam splitters PBS2 and PBS3, a quarter-wave plate QW3 and four photo-detectors. The detected voltage signals are amplified and equalised, then sampled in by the computer through a 12-bit A/D converter board. The sampling rate of the A/D converter will determine the measurement speed of the system. The A/D converter board with a sampling rate of 20MS/s is commercially available at present. The computer, through a 12-bit D/A converter board and a high voltage (150V) amplifier also controls the piezoelectric translators.

We take the electric field of the two orthogonally polarised beams to be of the standard form:

$$E_p = A_p \exp(i(\omega t)) \tag{1}$$

$$E_s = A_s \exp(i(\omega t + \phi)) \tag{2}$$

where $\omega$ is the angular frequency of the radiation, $A_p$ and $A_s$ are the amplitudes of $E_p$ and $E_s$ respectively, and

$$\phi = 4\pi(d + \Delta d)/\lambda. \tag{3}$$

**Figure 2** Dual-beam polarisation interferometer

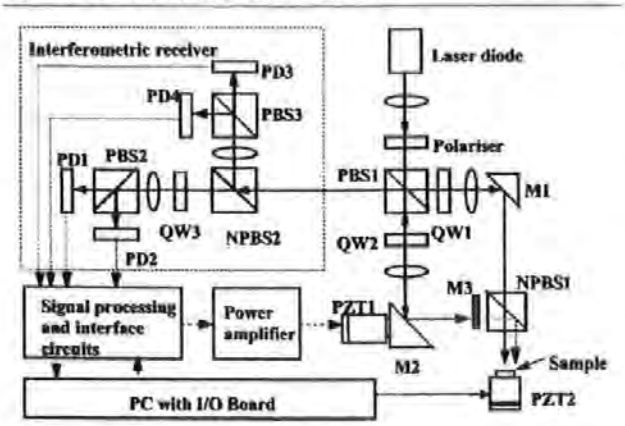

In equation (3), $\lambda$ is the wavelength of the laser beam, $d$ is the static optical path difference between the two polarised beams and $\Delta d$ is the displacement to be measured. The wave intensity being received by each of the four photo-detectors ($P_{PD1}$ to $P_{PD4}$) is proportional to the square of the electric field, and by simple signal conditioning and processing quadrature signals $P_{PD2} - P_{PD1}b_2/b_1$ and $P_{PD3} - P_{PD4}b_3/b_4$ are obtained. The computer samples these signals with two channels of the A/D converter board. The displacement $\Delta d$ is then determined by phase evaluation and unwrapping[19].

To test the ability and effectiveness of this interferometer, several experiments have been conducted. A 12-bit D/A converter, with a 0-10V voltage output, drives another piezoelectric translator, PZT2, to move the sample. One of the measurement results is shown in Figure 3, in which PZT2 moves the sample in a saw-wave form with amplitude of about 8.5nm.

The dual beam polarisation laser interferometer can be used for accurate high-speed measurement of small displacements, vibration, and disk flying height. Theoretically, a 12-bit A/D converter can provide a measurement resolution higher than $\lambda$/4,096. However, because of the system noise, especially the electrical noise, the system in its present configuration has a general measurement resolution of about 0.5nm. The dual beam polarisation interferometer in its first version has been demonstrated to work effectively in our application. However, there are a number of issues to be addressed in order to realise its true potential. The interferometer will be developed from its present state to include a frequency stable He-Ne laser and the interferometer itself will be made to be compact and from thermally stable materials (invar as opposed to aluminium). These improvements will significantly improve the signal-to-noise ratio available, enabling more precise measurements of small displacements to be made. Choosing a higher sampling rate A/D board can also increase the system's measurement bandwidth.

## D. CD-ROM optics

The interaction between the read-write head and the disc surface causes the flying height of the head above the surface to change, and so the dynamic morphology of the rotating disk(s) is extremely important. As the head moves outside its operating margin data-transfer becomes a problem, eventually leading to data-transfer error, as shown in Figure 4. As the disk (aluminium-magnesium, coated with a thin magnetic layer and thin lubrication layer) rotates at speeds of up to 10,000rpm the disk flexes radially and circumferentially and the CD-ROM optics will be utilised to measure these rotation-induced effects.

A CD-ROM drive utilises a laser with photodiodes to read data from the disk. The photo detector comprises four sensors and when the disk is perfectly focused the laser spot reflected off the disk will be centrally placed on the four sensors. The spot will then move either left or right to cover one pair of spots depending on the distance of the disk.

**Figure 3** Measurement result for displacement amplitude of about 8.5nm

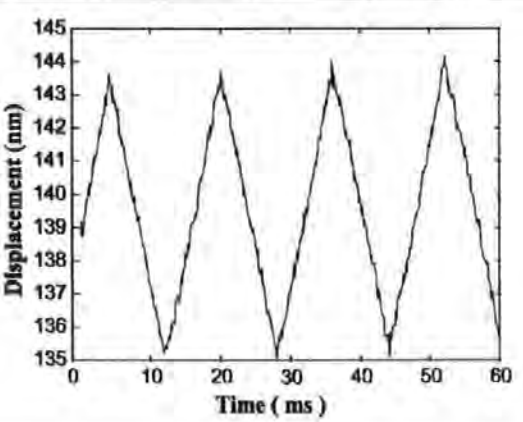


**Figure 4** Effect of vibration on disk drive operations: 3.5" hard disk

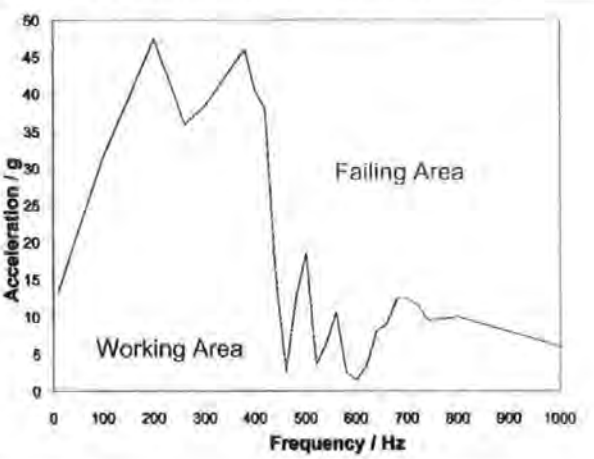

The CD head is mounted to a micrometer controlled sliding table and aligned so as to reflect off of a typical hard disk drive disk. In normal operation two of the segments are summed and the difference from the other two segments is compared, to yield a signal four times greater than that observed from just the one segment.

Using an oscilloscope to monitor the signal on one of the photodiodes it was recorded that a peak voltage of 30mV was measured when the lens was 2.80mm away from the disks' surface. The response from the detectors is linear with distance, with a change of ± 0.2mm yielding a change in output of ± 20mV, a response therefore of 0.1mV/$\mu$m. After signal conditioning, the response becomes 0.4mV/$\mu$m. Work in this area is part of ongoing research.

## E. Piezoelectric sensors

An alternative means of characterising hard disk flutter is to use a thick film piezoelectric sensor, in this case polyvinylidene di-fluoride (PVdF). The sensor, in the form of a 110$\mu$m sheet, was used as a cantilever. When a piezoelectric material is deformed the potential difference across its electrodes is proportional to the average induced strain. The fixed end of the sensor was bonded to the drive's chassis such that the cantilever is pre-tensioned against the disk. Any movement of the disk would therefore bend the cantilever from its static position. Because the cantilever is pre-tensioned, when the disk is static there is always a DC voltage. If the disc causes the cantilever to move from its static position there will be a change in the cantilever's induced stress; the output voltage will increase as the strain increases and vice-versa. The end of the cantilever rests on the edge of the disk to sense maximum displacement. Figure 5 shows the results obtained using this sensor arrangement, for a 3.5" hard disk drive rotating at 4,500rpm. The first peak (at 75Hz) corresponds to disk rotation (disk clamping and spindle bearing), the second peak at around 500Hz corresponds to disk flutter, as predicted by finite element analysis, and the peaks at higher frequencies are attributed to disk-suspension arm interaction.

**Figure 5** Response from piezoelectric sensor showing the effect of disk flutter. Inset shows the actual sensor at the edge of the disk

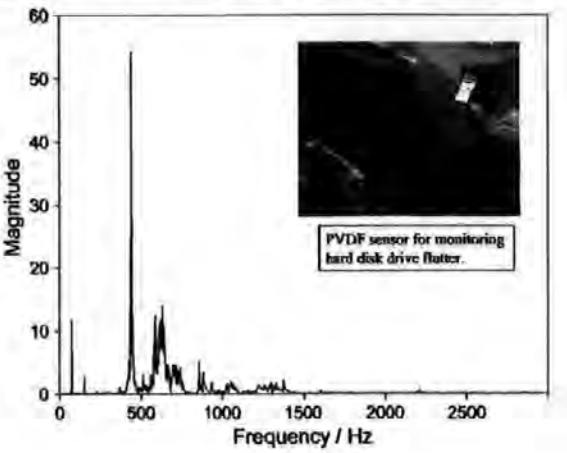


## F. Hard disk drive control system

It is appropriate now to look at the control system that is being developed for active control of the read-write head for both track following and flying height[20]. Current hard disk drives utilise a voice coil motor for positioning the head with respect to the data tracks, and design the head suspension system such that air flow, due to the rapidly rotating disk, "lifts" the head to the desired height above the disk surface. The system developed in the CRIST laboratory will still use the voice coil motor for coarse track following, but fine positioning and flying height control will be affected using piezoelectric stack actuators, as shown in Plate 6. Stack actuators offer advantages of useful actuation at low voltage (< 3V) and wide bandwidth operation.

The attitude of the head is monitored using optical beam deflection (OBD), whereby a laser beam is deflected by a small mirror above "the head" on to a position sensing quadrant photodetector, capable of simultaneously measuring displacements in the horizontal and vertical planes. The output of the detector, which is linear for small displacements, and has spatial resolution comparable with interferometers (i.e. sub nm), is applied to the DSP implemented proportional integral and derivative (PID) controller for real time active control of the head suspension system. The suspension arm is set into resonance by applying bursts of band-limited white noise to the piezoelectric stacks and the resonant modes are sensed

**Plate 6** Suspension arm incorporating stack actuators for simultaneous head positioning and flying height control

optically, for both data tracking and flying height control. However, actuation in one plane can induce resonance effects in the orthogonal plane, and vice versa.

Modified PID controllers have been implemented to control and position the suspension arm with adequate bandwidth and stability. Bode plots show that the PID servo system's control loop for the tracking stage can be closed with a 25.6kHz gain cross-over frequency and phase and gain margins of 54° and infinity respectively. The flying height control stage is closed with a gain cross-over frequency of 2.33kHz and phase and gain margins of 51° and infinity respectively. Figure 6 shows the experimental open loop response and the theoretical closed loop response for track following, with the response for the flying height control similar to that for track following.

In an actual hard disk drive, position sensing would be achieved via the read/write head for flying height and from the tracking servo for track positioning. If data are read back from the disk, then according to the Wallace spacing loss equation[21], the amplitude of the read-back signal will be modulated by the spacing variations between the head and the disk due to the surface irregularities of the disk. The read-back signal from the magnetic head reflects the surface

**Figure 6** Open and closed loop response for track positioning

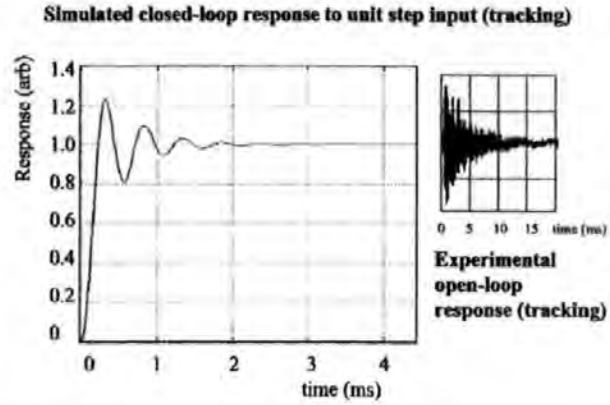


topography of the disk, and will provide a feedback signal for the control system.

## Conclusion

In the CRIST laboratory a number of sensor systems have been developed for the characterisation of magnetic media and data storage systems. An SLM, with dynamic read-write capability, and an MFM have principally been developed for the characterisation of magnetic and magneto-optical thin films. By utilising the intensity imaging mode, the SLM is able to characterise the surface reflectivity with a spatial resolution of around 1$\mu$m. The MFM operates with the probe at constant height and so a prerequisite is that the surface topography is known. This is determined from a pre-imaging scan in AFM mode, whereby the probe tip is brought into contact with a sample surface, and raster scanned across it. The resultant deflection of the tip is recorded and used to create an image of the surface topography. The dual beam interferometer, for measuring head flying height, is so far able to measure dynamic surface topography of a rotating hard disk, with sub-nanometre resolution. Current instrument development is focused towards the simultaneous measurement of the head position, to realise the determination of its actual height above the disk surface in real time.

In parallel with this is work on the dynamic characterisation of disk drives for ruggedised operations, such as in seismic data logging. Two experimental systems have been

developed for this based on CD-ROM optics and thick film piezoelectric sensors to measure the topography of the rotating disk drive under hostile operating conditions. Measurements of data-transfer to and from the disk will be used to further the understanding of data-transfer failure mechanisms under hostile operating conditions.

Operation of hard disk drives relies on the head-to-disk flying height being maintained at a constant height. A sensor-controller-actuator system has been developed to enable both the flying height and the track position to be maintained. Optical sensing is used at present to determine the attitude of the head and the response used to drive two independent actuators via a DSP implemented PID controller. Future developments of this system will include the replacement of the optical sensor by a direct measurement of the head's position from the actual head readout signal itself. This will form the basis of a realisable system that will be developed commercially in partnership with our collaborators, the Data Storage Institute, Singapore.

## References

1 Morrison, E., "The development of a prototype high-speed stylus profilometer and its application to rapid 3D surface measurement", *Nanotechnology*, Vol. 7 No. 1, 1996, pp. 37-42.
2 Zhang, J.-H. and Cai, L., "Profilometry using an optical stylus with interferometric readout", *Meas. Sci. Technol.*, Vol. 8 No. 5, 1997, pp. 546-9.
3 Jalocha, A. and Pieralli, C., "A scanning optical profilometer using the SNOM architecture", *Pure Appl. Opt.*, Vol. 3 No. 5, 1994, pp. 793-804.
4 Bowen, D.K., Chetwynd, D.G. and Schwarzenberger, D.R., "Sub-nanometre displacements calibration using X-ray interferometry", *Meas. Sci. Technol.*, Vol. 1 No. 2, 1990, pp. 107-19.
5 Cuthbert, L. and Huynh, V.M., "Statistical analysis of optical Fourier transform patterns for surface texture assessment", *Meas. Sci. Technol.*, Vol. 3 No. 8, 1992, pp. 740-45.
6 Carey, R.C., Jenkins, D.F.L., Newman, D.M. and Thomas, B.W.J., "Laser scanning at full objective aperture using 2-axis galvanometer mirrors", *Meas. Sci. and Technol.*, Vol. 4, 1993, pp. 488-91.
7 Clegg, W.W., He, L., Jenkins, D.F.L. and Windmill, J.F.C., "A magneto-optic scanning laser microscope to characterise static and dynamic behaviour in magnetic materials", poster presentation, CMMP 99 Conference, Leicester, 1999.
8 Clegg, W.W., He, L., Jenkins, D.F.L. and Windmill, J.F.C., "A magneto-optic scanning laser microscope facility for the time-resolved examination of domain dynamics", poster presentation at FOM 2000, Shirahama, Japan, April, 2000.
9 Clegg, W.W., He, L., Jenkins, D.F.L., Windmill, J.F.C. and Fry, N., "A scanning laser microscope system to observe static and dynamic magnetic somain behaviour", oral presentation at IMTC 2000, Baltimore, MA, submitted for *IEEE Trans. IMTC*, 2000.
10 Farley, V., "A high performance magnetic force microscope", *Meas, Sci. and Technol.*, Vol. 7, 1996, pp. 30-5.
11 Clegg, W.W. and Windmill, J.F.C., "A novel scanning force microscope head configuration compatible with vacuum operation", paper presented at CMMP Conference, UMIST, Manchester, 1998.
12 http://www.di.com (Digital Instruments).
13 Zhou, H. *et al.*, "Recent progress in the functionalization of atomic force microscope probes using electron-beam nanolithography", *J. Vac. Sci. Technol. A*, Vol. 17 No. 4, 1999, pp. 2233-9.
14 Dai, X. and Seta, K., "High-accuracy absolute distance measurement by means of wavelength scanning heterodyne interferometry", *Meas. Sci. Technol.*, No. 9, 1998, pp. 1031-5.
15 Wang, X., Sasaki, O., Takebayashi, Y., Suzuki, T. and Maruyama, T., "Sinusoidal phase-modulating Fizeau interferometer using self-pumped phase conjugator for surface profile measurements", *Optical Engineering*, Vol. 33, 1994, pp. 2670-74.
16 Creath, K., "Phase measurement interferometry techniques", *Progress in Optics*, Vol. 27, 1990, pp. 273-359.
17 Liu, X., Clegg, W., Jenkins, D. and Liu, B., "Polarization interferometer for measuring small displacement", IMTC/2000, Baltimore, MA, May 2000.
18 Clegg, W., Liu, X. and Liu, B., "Dual beam normal incidence polarization interferometry flying height testing", *IEEE International Conference on Magnetics*, Paper CP-04, Toronto, April 2000,.
19 Malacara, D., *Optical Shop Testing*, 2nd ed., John Wiley & Sons, New York, NY, 1992.
20 Chilumbu, C., Clegg, W.W., Jenkins, D.F.L. and Robinson, P., "A novel two-dimensional suspension arm for flying height control and high-bandwidth track following in advanced hard disk drives", oral presentation at IMTC/2000, Baltimore, MA, May 2000.
21 Wallace, R.L., "The reproduction of magnetically recorded signals", *The Bell Tech. J.*, 1951, pp. 1145-73.

# Current-modulating magnetic force microscope probe

Frank Z. Wang
*School of Informatics and Multimedia Technology, University of North London, 166-220 Holloway Road, London N7 8DB, United Kingdom*

Na Helian,[a] Warwick W Clegg, James F. C. Windmill, and David Jenkins
*Centre for Research in Information Storage Technology, DCEE, University of Plymouth, Drake Circus, Plymouth PL4 8AA, United Kingdom*

A new current-modulating probe for the magnetic force microscope (MFM) is proposed in this article. The magnetic field, which will be used to interact with a magnetic specimen's stray field, is induced on the sharp tip of the conical magnetic core surrounded by a microfabricated single turn conductive coil. The reciprocity principle is used to obtain the force acting on the probe due to the specimen's stray field when scanned over a magnetic specimen. The magnetic field intensity is adjustable by control of the applied current. Images of specimens have been modeled using this probe. The suitability to different specimens is seen to be the biggest advantage of this scheme over the conventional probe designs. © *2001 American Institute of Physics.*
[DOI: 10.1063/1.1358817]

## I. INTRODUCTION

The magnetic force microscope (MFM) is the tool of choice for many studies, not only of magnetic domain structures, but also written bit patterns in recording media.[1] Standard MFM probes (cantilevers) use silicon tips that are magnetically sensitised using ferromagnetic thin films. Unfortunately, this design has several inherent problems. First of all a variety of different designs and coatings need to be used depending on the magnetic properties of the specimen being imaged, i.e., if the specimen is magnetically "hard" or "soft." This means that an instrument must be reconfigured each time a new type of specimen is imaged. This imperfection can have serious consequences on the acquisition of useful and quantifiable data.

It is certainly important to find new ways to improve the resolution and sensitivity of magnetic field probes. Reliability, reproducibility and controllability are also desirable properties for MFM probe. Using MFM as a information storage mechanism would only be taken up by industry if the sensitivity were also improved. Thus, electromagnetically induced fields as a replacement for the standard probe's stray field have been proposed, using either a microfabricated single-turn coil around an atomic force microscope (AFM) tip,[1] or a microfabricated aperture situated near the end of a standard cantilever that has been coated with conductive material.[2] In the first case, a single-turn coil without any magnetic material's flux-concentrating effect just produces a weak magnetic field, thus causing low sensitivity. In the second case, the magnetic field is generated from the cantilever surface, rather than a tip as with standard probes, so there is some difficulty in controlling the separation distance between probe and specimen; in addition, the two-peak magnetic field distribution generated by the aperture causes difficulties when imaging longitudinal magnetization specimens. In order to overcome the weaknesses of these designs, this article presents a new concept as a possible answer.

## II. THE NEW PROBE

A current-modulating MFM probe is proposed, as shown in Fig. 1. An electromagnetically induced field, complementing the standard magnetically coated probe's stray field, is utilized. The magnetic field, which will be used to interact with a magnetic specimen's stray field, is induced on the sharp tip of the conical soft magnetic core, surrounded by a microfabricated single turn conductive coil. The conical core is situated near the end of a standard cantilever that could be simultaneously utilized as an AFM probe.

This design has the advantage that the field intensity, and hence specimen interaction, is variable, and also the results should be repeatable. Magnetic flux generated by the single turn conductive coil would be coupled to the tip by the soft magnetic material; therefore a sharp magnetic field can emanate from the tip with a signal peak. Using the commercial finite element method package TOSCA, the magnetic field distribution has been studied. In Fig. 2, magnetic field intensity

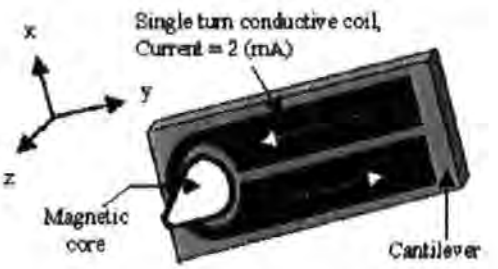


FIG. 1. Schematic diagram of the current-modulating MFM probe. The current flow around the magnetic core generates magnetic field at the sharp tip of the core.

[a]Author to whom correspondence should be addressed; electronic mail: lhe@plymouth.ac.uk

 

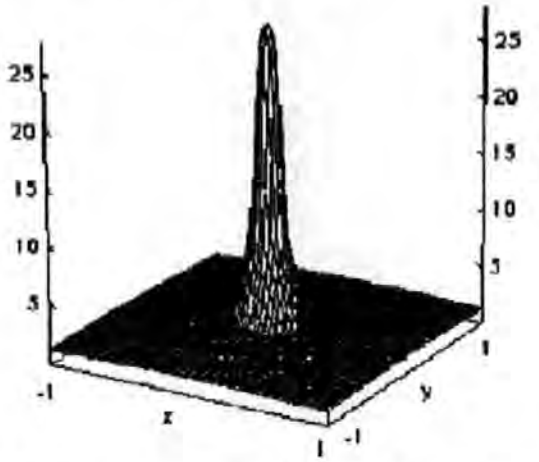


FIG. 2. The perpendicular magnetic field intensity, $H_z$(Oe), is shown at 25 nm above the sharp tip of the magnetic core with a current density of 2 mA/$\mu$m$^2$ over a 2 $\mu$m by 2$\mu$m range in the $xy$ plane.

$H_z$, normal to the cantilever plane, is shown for a height of 25 nm above the tip, where the tip diameter is 100 nm and the coil current density is 2 mA/$\mu$m$^2$. The bottom diameter and the height of the probe are 3.2 and 5 $\mu$m, respectively. The single turn conductive coil has a square cross section with an area of 1 $\mu$m$^2$. The soft magnetic conical core is assumed to be an FeN-based soft magnetic film, with a saturation magnetization $B_s$ of 21 KG and an initial permeability of 3400.[3] Note that by controlling the applied current, and hence the linear current density, the field strength can be varied. The current-modulating design gives a sharp single-peak magnetic field distribution as shown in Fig. 2.

## III. MFM IMAGE PRINCIPLE

In general, the simulation of MFM images has been realized by considering the interaction between the magnetization of the MFM's tip and a specimen's stray field. This allows the calculation of the force acting on the tip due to the field from the specimen. Given Newton's third law, the principle of reciprocity can be used.[4] The force acting on the specimen due to the tip's stray field when scanned over a magnetic specimen is calculated, which is the inverse of the force acting on the tip. This reciprocal force acting in the vertical, $z$, direction can be expressed as

$$F_z^{\text{tip}} = -\int_{\text{spec}} \sum_i M_i^{\text{spec}}(r') \frac{\partial H_i^{\text{tip}}(r+r')}{\partial z'} d^3r', \tag{1}$$

where $i$ corresponds to the direction $x$, $y$ or $z$, $M_i^{\text{spec}}$ is the $x$, $y$ or $z$ component of the magnetization of a specimen volume element and $H_i^{\text{tip}}(r+r')$ is the stray field from the tip at that specimen volume element. This then allows the simulation of the new probe, since the calculated field intensity, as shown in Fig. 2, can be used with Eq. (1).

In order to create image simulations a model is required for the magnetization of the specimen. In this work, perpendicular magnetic media has been used. It uses a simple arctangent model, given in Eq. (2), but extended in the $y$ direction to produce an image

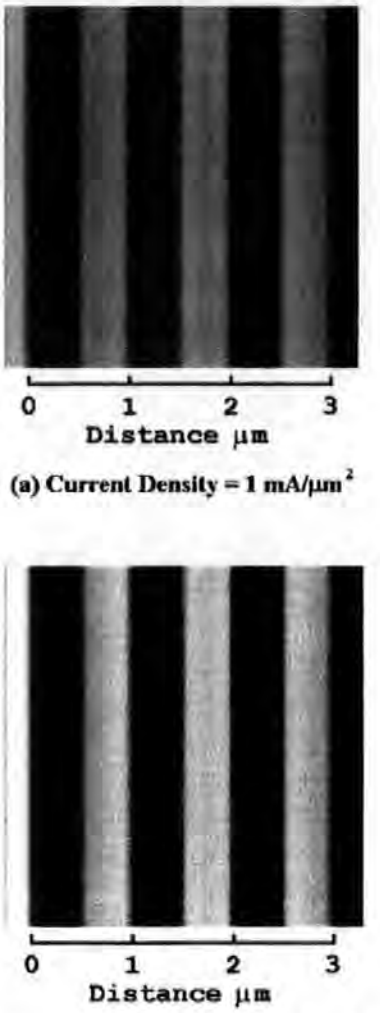


FIG. 3. Simulated MFM image of six 0.5-$\mu$m-long perpendicular bits using the current-modulating probe at 1 and 2 mA/$\mu$m$^2$ current density. The probe is a magnetic conical core with a 5 $\mu$m height, 100 nm tip diameter, and 3.2 $\mu$m bottom diameter. A dark or bright area, depending on magnetization direction, shows each bit. The darkness or brightness is proportional to the force acting on the tip.

$$M_z = \frac{2}{\pi} \times M_0 \times \arctan\left(\frac{x_0}{a_p}\right). \tag{2}$$

To produce a quick, efficient computer image simulation of the interaction between the probe and a magnetic specimen, a fast Fourier transform method has been used. The images of the specimen's magnetic distribution were created by the convolution of the probe's gradient field and the specimen magnetization distribution.[2]

## IV. IMAGE COMPARISON

The simulated MFM images shown in Fig. 3 were created using the above technique. Simulated MFM images of six 0.5-$\mu$m-long perpendicular bits using the current-modulating probe at 1 and 2 mA/$\mu$m$^2$ are shown in (a) and (b), respectively. The probe dimensions are as given earlier.

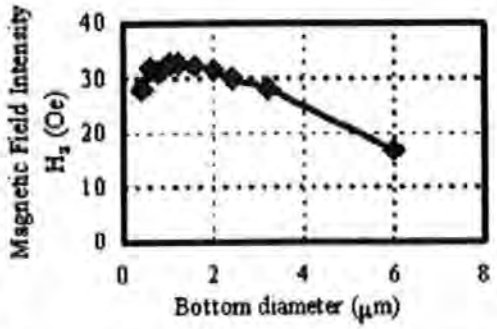


FIG. 4. Magnetic field intensity's dependence on the core bottom diameter. The height of the core is 5 $\mu$m and the tip diameter is 100 nm. The modulating current density is 2 mA/$\mu$m$^2$.

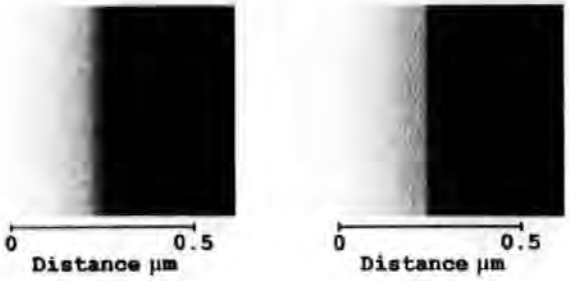


(a) Tip diameter = 100 nm (b) Tip diameter = 25 nm

FIG. 6. Simulated MFM image of a transition from one direction of magnetization to another using the current-modulating probe, with a tip diameter of 100 nm in (a) and 25 nm in (b), respectively. The bottom diameter is 1 $\mu$m and the height is 4 $\mu$m. The modulating current density is 2 mA/$\mu$m$^2$.

A dark or bright area, depending on magnetization direction, shows each bit. The darkness or brightness is proportional to the force acting on the tip. It is clear that the image with 2 mA/$\mu$m$^2$ current density is of better quality, in terms of contrast, than that of 1 mA/$\mu$m$^2$, which indicates that the optimal image can be achieved by adjusting the applied current according to different types of the specimen. Such a suitability to different specimens by adjusting the applied current to get the optimal image, no matter if the specimen is magnetically "hard" or "soft," is the biggest advantage of this scheme over a conventional design. Our purpose in this article is to detect, or read, the existing information rather than altering (writing) it. A criteria of choosing the optimal sense field strength has been set, i.e., the sense field should not be greater than the specimen's magnetic coercivity, otherwise the sense field will magnetize the specimen.

An examination of the practical use of the probe is in hand. The probe's geometric effects on the field intensity and resolution have been studied. For all the geometric investigations, the physical parameters of the core remain the same, which means that the saturation magnetization and the permeability remain unchanged. Also, the modulating current remains the same, i.e., the current density is 2 mA/$\mu$m$^2$ carried in the coil with cross-section area of 1 $\mu$m$^2$.

Figure 4 indicates the field intensity's dependence on the core bottom diameter. The height of the core is 5 $\mu$m and the tip diameter is 100 nm. As the bottom diameter decreases, the diameter of the coil decreases correspondingly to keep the same separation of 1 $\mu$m between the core and the coil. As shown in Fig. 4, the field increases as the bottom diameter's decreases to 1 $\mu$m, it then reaches a maximum, and decreases as the bottom diameter decreases further. There is a optimal bottom diameter around 1 $\mu$m. The first phase can be simply explained by the fact that the field intensity at the center is inversely proportional to the diameter of the coil by the Biot–Savart law. However, as the core bottom diameter decreases below 1 $\mu$m, the saturated smaller magnetic core transports less magnetic flux to the core tip.

A similar phenomenon has been found for the core height, as shown in Fig. 5. The tip and bottom diameters of the core are 100 nm and 3.2 $\mu$m, respectively. There is an optimal height of 4 $\mu$m. The shorter the magnetic path, the higher the transmission efficiency of magnetic flux. Nevertheless, too short means a vanishing sharp top and the shrinkage of the magnetic core, and hence less magnetic field emanating from the tip.

As mentioned above, the probe's sharp single peak field distribution ensures a high resolution. By optimizing the probe's geometric dimension, high-resolution imaging can be achieved. As shown in Fig. 6, which represents the transition from one direction of magnetization to another, the probe with tip diameter of 25 nm can obtain much better resolution than that with tip diameter of 100 nm.

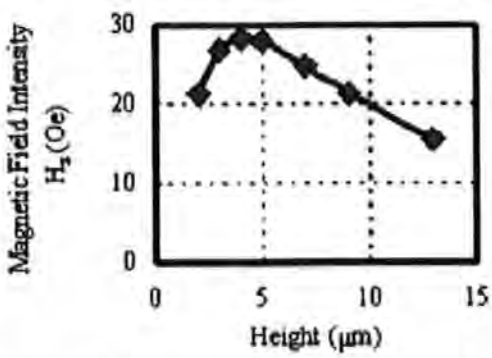


FIG. 5. Magnetic field intensity's dependence on the core height. The tip and bottom diameters of the core are 100 nm and 3.2 $\mu$m, respectively. The modulating current density is 2 mA/$\mu$m$^2$.

## V. CONCLUSIONS

A new design for an electromagnetic MFM probe has been presented. MFM images have then been simulated using this new design. This has shown that magnetic specimens can be observed at an optimal quality by adjusting the current. It is also shown that high-resolution imaging can be achieved by optimizing the probe's geometric dimension.

[1] H. Zhou, G. Mills, B. Chong, A. Midha, L. Donaidson, and J. Weaver, J. Vac. Sci. Technol. A **17**, 2233 (1999).
[2] J. Windmill and W. Clegg, Intermag 2000, Toronto, Canada (unpublished); IEEE Trans. Magn. (in press).
[3] M. H. Kryder, S. Wang, and K. Rook, J. Appl. Phys. **73**, 6212 (1993).
[4] E. W. Hill, IEEE Trans. Magn. **31**, 3355 (1995).

ELSEVIER

Journal of Magnetism and Magnetic Materials 226–230 (2001) 1267–1269

Journal of magnetism and magnetic materials

www.elsevier.com/locate/jmmm

# A new theoretical probe for the magnetic force microscope

J.F.C. Windmill*, W.W. Clegg, D.F.L. Jenkins, P.J. Davey

*CRIST, DCEE, University of Plymouth, Drake Circus, Plymouth, PL4 8AA, UK*

**Abstract**

The magnetic force microscope (MFM) is established as a valuable tool for the analysis of magnetic structures. The standard design of MFM incorporates a silicon tip coated with a magnetic material. However, these tips are subject to several inherent problems, e.g. changing characteristics over time due to damage or magnetic hysteresis. A new theoretical electromagnetic MFM probe is introduced here. Although electromagnetic MFM has been discussed before by Zhou et al. (J. Vac. Sci. Technol. A 17 (1999) 2233), the design presented here is a different approach. Two different probe iterations and their magnetic field intensity distribution are modelled. The probe imaging capability is compared using the reciprocity principle (Wright and Hill, Appl. Phys. Lett. 68 (1996) 1726) to image the simulated force interaction between a sample and the probe fields. Thus, images of a sample's magnetic distribution are produced by the convolution of the different probe gradient field distributions and the sample magnetisation. Both perpendicular and longitudinal magnetisation patterns were simulated with the different probe iterations. This clearly showed the improvement of the second probe iteration, particularly for longitudinal patterns. The practical use of the new probe is also discussed, and future work outlined. © 2001 Published by Elsevier Science B.V.

*Keywords:* MFM; Magnetic modelling; Electromagnetic MFM probe

The design of magnetic force microscope (MFM) probes is a continuing area of research interest. The standard MFM probe uses a silicon tip, magnetically sensitised using a ferromagnetic coating. This design has several inherent problems, for example, a range of probes are required to image different samples, and a probe's characteristics can change over time. As such it is difficult to obtain quantitative data using MFM. A possible answer to these problems is to use an electromagnetic probe to interact with a magnetic sample. An electromagnetic MFM probe has been reported before; however, it is a relatively new idea, and the design presented here is completely novel [1]. A field would be created about a micro-sized aperture in a conductor at the end of a cantilever. This follows the Biot–Savart law, where, by changing the current density in a conductive material, the magnetic field intensity normal to its surface is altered. So the current must flow around the aperture, changing the current density local to the aperture, generating a field. The probe has the advantage that the field intensity is variable, controllable, and should provide repeatable results.

The first probe field model, shown in Fig. 1, followed work done in the 1970s on current-access bubble memory, where a circular aperture was modelled [2]. This was then confirmed using three-dimensional finite element modelling. The next step was to simulate the imaging performance of the new probe. Most previous work has simulated the interaction between the probe tip magnetisation and a sample's stray field, and thus the force acting on the tip. However, the reciprocity principle can be used [3]. In this case the force on the sample due to the interaction of the probe stray field and the sample magnetisation is considered, i.e. the inverse of the force on the probe. Magnetisation distribution models for perpendicular and longitudinal magnetic media bit transitions have been used to simulate the imaging capability of the new probe [4]. A FFT convolution of the probe's gradient field and the sample magnetisation distribution then creates simulated DC-MFM images.

The simulated images shown in Fig. 2a and b were created using the above technique for a circular aperture

* Corresponding author. Fax: +44-1752-2325-83.
*E-mail address:* jwindmill@plymouth.ac.uk (J.F.C. Windmill).

0304-8853/01/$ - see front matter © 2001 Published by Elsevier Science B.V.
PII: S0304-8853(01)00074-9

probe. In Fig. 2a the new probe, with a flying height of 25 nm, images a perpendicular bit pattern. The pattern is successfully imaged, highlighting the domain transitions as dark or light lines, where the shading indicates the transition direction, depending on the probe's travel and orientation. In Fig. 2b the circular probe has imaged a longitudinal bit pattern. However, a large artefact is created by the twin peaks of field intensity. Each transition is imaged separately by each peak, so creating a pair of lines for each transition. The answer was to change the design such that one field intensity peak was dominant over the other. Using a semicircular aperture,

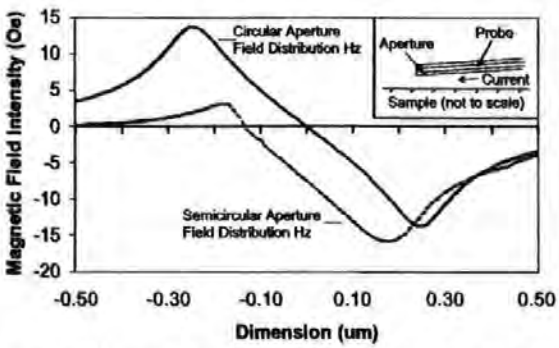


Fig. 1. (a) Magnetic field intensity, $H_z$ (Oe), for a 0.5 μm circular aperture, at height 25 nm from probe surface and sheet current density of 2 mA/μm. (b) $H_z$ (Oe) under same conditions for a 0.5 μm semicircular aperture.

Fig. 1, the current density past the semicircle's straight edge is lower than that past the circular edge. The resulting image simulations, Fig. 2c and d, demonstrate that the semicircular aperture can successfully image both perpendicular and longitudinal domains.

The practical use of the new probe is also under investigation. The probe would be sited near the end of a standard bar SPM cantilever coated with a conductor. The conductive material must be able to tolerate sufficient current, with no adverse effects due to, for example, electromigration, to create the required field intensity. Fortunately, given the currents used in the models, this problem will not arise. The possible interference due to the conductive cantilever on the imaging process is also a potential obstacle. However, although the cantilever does create a magnetic field, it is significantly smaller than that of the aperture. A further step is to use a blunt tip on the cantilever under the aperture. This reduces the field effects from the cantilever, whilst increasing its flying height, and would also act as a topography probe for pre-MFM scanning.

A theoretical design for a new electromagnetic MFM probe is presented. The design was used to simulate MFM images. Although the first circular aperture successfully imaged perpendicular magnetic domain transitions and their direction, unfortunately, longitudinal domains were not imaged correctly. The second, semicircular, aperture did successfully image both longitudinal and perpendicular domain patterns. The preliminary

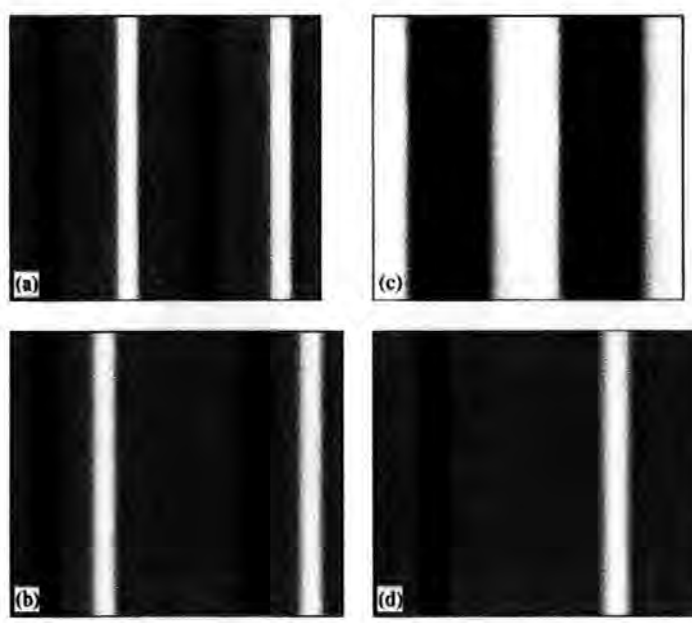


Fig. 2. (a) Simulated DC-MFM image of 1 μm perpendicular bits, with a 250-nm-diameter circular aperture. A dark or light line indicates transition direction, depending on probe flight and orientation. (b) Longitudinal bits imaged using probe of (a). Each domain transition is imaged twice, due to the twin peak effect. (c) Perpendicular pattern of (a), imaged with a 0.5-μm-diameter semicircular aperture. (d) Longitudinal bits imaged with probe of (c), in this case imaged correctly.

problems of using the probe in practice were discussed, with solutions suggested. In time the new MFM probe will hopefully be put through practical tests. As such, the results from this and advanced modelling developments will be published in the future.

The authors would like to acknowledge the support of the Wohlfarth fund.

## References

[1] H. Zhou, G. Mills, B.K. Chong, A. Midha, L. Donaldson, J.M.R. Weaver, J. Vac. Sci. Technol. A 17 (1999) 2233.
[2] A.H. Bobeck, S.L. Blank, A.D. Butherus, F.J. Ciak, W. Strauss, Bell Syst. Technol. J. 56 (1979) 1453.
[3] C.D. Wright, E.W. Hill, Appl. Phys. Lett. 68 (1996) 1726.
[4] J.G. Zhu, H.N. Bertram, J. Appl. Phys. 69 (1991) 6084.

# A Scanning Laser Microscope System to Observe Static and Dynamic Magnetic Domain Behavior

Warwick Clegg, *Senior Member, IEEE*, David F. L. Jenkins, Na Helian, James F. C. Windmill, *Student Member, IEEE*, Nick Fry, Ron Atkinson, *Senior Member, IEEE*, William R. Hendren, and C. David Wright

***Abstract*—Scanning laser microscopes (SLMs) have been used to characterize the magnetic properties of materials for some time. The first SLM built [1] was a purely static system capable of imaging magnetic domains. Dynamic capability was introduced with the development of the R-Theta microscope [2]. However, this microscope utilizes a rotating drive. A scanning laser microscope has been designed to observe the dynamic behavior of domain switching during the thermo-magnetic write process and the subsequent magnetization state (domain orientation) in stationary media, without the requirement for a rotating drive. It will also be used to write to the magneto-optic (MO) disk material thermo-magnetically prior to imaging. Images are derived from the longitudinal and polar magneto-optic Kerr effects. In this paper, the different configurations for imaging are described and some initial images are presented.**

***Index Terms*—Data storage, dynamic laser microscopy, magneto-optics.**

## I. Introduction

THE aim of the project is to develop a versatile imaging system that enables the observation of magnetic behavior for a variety of applications. Scanning laser microscopes (SLMs) are extremely well suited for this and are also able to write bits for subsequent imaging with either an SLM or a magnetic force microscope (MFM). While an SLM is able to image at a resolution of $\lambda/2$ (around 250 nm in this case), its writing resolution capability is greater than this limit, as it is principally a thermal process, as opposed to an optical one. The thermal profile of the laser-heated region mirrors that of the optical intensity profile of the laser, but only the central region, where the temperature is above the Curie point ($T_C$), is able to reverse domains. Compared to an SLM (without scanning near-field microscopy—SNOM—capability), an MFM offers high-resolution imaging at the nanometer level, but with a very limited scan area; typically, this is up to $100 \times 100$ $\mu$m. The SLM, however, is able to image a much larger area, up to $10 \times 10$ mm in 50 nm increments, by mounting the sample on a precision motorized $x$-$y$ sample stage.

Wherever possible, the microscope system has been made modular. This enables the imaging system to be flexible and allows functions to be added or changed for different applications.

Manuscript received May 4, 2000; revised November 12, 2001.

W. Clegg, D. F. L. Jenkins, N. Helian, J. F. C. Windmill, and N. Fry are with the Centre for Research in Information Storage Technology, University of Plymouth, Drake Circus, Plymouth, U.K.

R. Atkinson and W. R. Hendren are with the School of Mathematics and Physics, Queen's University Belfast, Belfast, U.K.

C. D. Wright is with the School of Engineering and Computer Science, Harrison Building, University of Exeter, U.K.

Publisher Item Identifier S 0018-9456(02)02299-4.

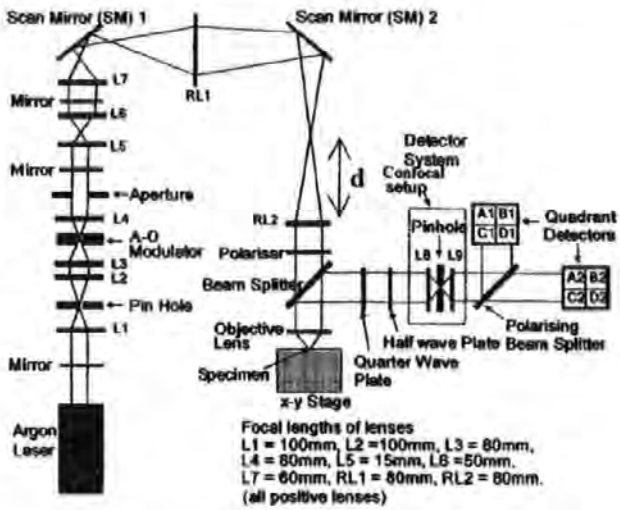


Fig. 1. Optical pathway for the SLM system.

This is also a consideration for future development and applications of the microscope, for example, a scanning near-field magneto-optic module.

The scanning laser microscope system is based around a central PC that uses National Instruments LabVIEW software as the user interface and development base. The component parts of the microscope system are controlled and monitored from the computer via both a data acquisition (DAQ) board and other dedicated control cards. The system is now largely complete and experimental testing of a variety of material specimens has begun.

## II. Optical System Design

The optical system incorporates both Gaussian beam optics (for beam transformation) and geometric optics (scanning and de-scanning) [3]. To enable the laser beam to both be completely stationary and completely fill the aperture of the final focusing objective, a small amount of beam over-spill is permissible. This is shown schematically in Fig. 1. The output beam from the laser is expanded, spatially filtered, then focused to a 5 $\mu$m spot at the midpoint of the AO modulator (AOM); the rise time of the AOM is directly proportional to the spot size. Geometric optics is used to image the scan mirror pivot points using relay lenses RL1 and RL2, to image both pivot points (or stationary points) onto the back focal plane of the final focusing objective lens, with unity magnification. Gaussian beam optics are simultaneously used to transform the beam wave fronts to produce a collimated beam at the back focal plane of the final focusing objective lens. A

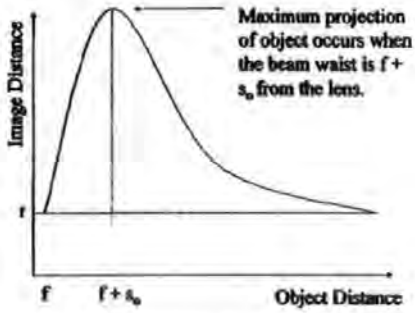


Fig. 2. Generation of collimated beam for diffraction limited spot scanning.

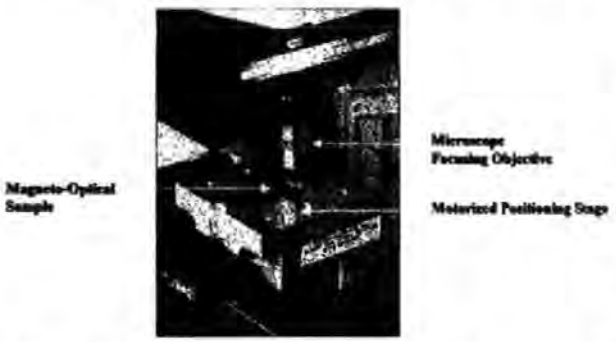


Fig. 3. Static imaging process. The sample is mounted on the $x$-$y$ stage and scanned under the diffraction limited laser spot.

critical requirement of this is the positioning (d) of the second relay lens (RL2). The positioning of this lens is absolutely crucial for the microscope's dynamic operation. Lenses L4–L7 are then used to transform the beam before relay lens RL1 produces a waist at a point $f + s_o$ from relay lens L2, where $f$ is the focal length of lens RL2 and $s_o$ is the Raleigh range associated with the beam waist. If $d \approx f + s_o$ (to a very good approximation), then this ensures that the projection of the waist by lens RL2 is a maximum, as shown in Fig. 2. This means that the divergence angle of the transformed beam is a minimum, ensuring optimum collimation of the beam. The system is now capable of scanning a diffraction-limited spot over the sample surface. A linear polarizer, between RL2 and the beam splitter, ensures that the incident beam is plane polarized.

Static imaging is then accomplished by means of moving the sample using the precision $x$-$y$ stage, as shown in Fig. 3. To enable dynamic imaging of samples the AOM and scan-mirrors are utilized. Geometric, or paraxial, optics are used to image mirror SM1 onto SM2, and, consequently, the pair to the back-focal plane of the objective lens. The laser spot can now be $x$-$y$ scanned on the sample surface. Further relay optics are then used to de-scan the returning laser beam before it reaches the detectors.

The microscope is designed to observe the dynamics of magnetic structures, both spatially and temporally. This can be accomplished by changing the instant of optical or electronic sampling slowly in phase with respect to the repetitive excitation of the magnetic structure. For example, a magnetic device is placed within a cyclic magnetic field and the laser pulse and consequent data capture are timed for a specific point in the field cycle. Another mode will use the Argon-Ion laser to simulate a dynamic

Fig. 4. Image of perpendicular domain patterns on a bubble.

Fig. 5. Intensity image of an magnetic integrated circuit layout (100 $\mu m^2$).

bit-write process on the MO disk. This can then be simultaneously imaged in real-time using the CCD camera and light reflected (from pulsed laser beam) onto the photo detectors at a specific time during the write procedure. Further work will use a scanning near-field module to image the change in magnetic structure over time, at a greatly increased spatial resolution, i.e., below the diffraction limit [4].

The static magnetic images are derived from any of the three Kerr magneto-optic effects. The polarized incident light is produced by either a fast pulsed (2–3 ns) Nitrogen/dye laser, illuminating the full observation field, or from an Argon Ion laser, operating in diffraction-limited scanned spot confocal mode. Both lasers are wavelength-tuneable. In the second case, either the specimen being imaged is raster-scanned under the laser spot via a Burleigh XY Worm Table, or the laser beam itself is scanned across the specimen using servo-mounted mirrors [3]. The returning light is then detected with quadrant photo-detectors, where a number of imaging modes are possible. A cooled CCD camera allows full-field low-level direct imaging of the sample, with integration over several frames if necessary for better noise performance.

## III. Initial Results

The microscope is able to obtain images of magnetic domains using the magneto-optic Kerr effects, or psuedo-topographic images of the sample surface using the microscope's intensity-only imaging mode. The initial image results from the microscope system are shown below. Fig. 4 shows a static image of the perpendicular magnetic domain pattern on the surface of a bubble memory chip, and Fig. 5 shows a secondary imaging mode, where the surface topography has been captured, from the reflectivity of the surface itself. This can be done at high speed using the servo-mounted mirrors. It allows the operator to map out the specimen under investigation and thus select areas of specific interest for further magnetic imaging.

Fig. 6 shows static images of the perpendicular magnetic domain pattern on the surface of a TbFeCo substrate. Image (a) of Fig. 6 shows the perpendicular domain pattern of a TbFeCo substrate captured using the SLM at Queens University Belfast (UK). This can be compared with the image in (b) obtained

Fig. 6. Comparative magneto-optic images of a TbFeCo substrate. (a) SLM image © Queens University Belfast ($40 \times 40$ $\mu$m); (b) SLM image ($60 \times 60$ $\mu$m) © University of Plymouth.

using the dynamic SLM in (static) polar Kerr mode. It is shown that the SLM is capable of imaging magnetic domains comparable to equivalent static imaging systems.

## IV. Discussion and Conclusion

A scanning laser microscope system has been designed to observe the static and dynamic magnetic domain behavior. At present, the electronics and LabVIEW control software are largely complete. However, the optical system is still under development to enable dynamic imaging of magneto-optical samples. The microscope is currently able to operate in static mode. In this mode the laser beam path is fixed and the sample under investigation is moved with respect to the focused laser spot. Preliminary results have shown that the system is capable of producing static images. Operation of the microscope was initially confirmed by surface topography observations, using the reflectivity of the surface itself. Subsequently, magnetic images were then obtained of domain patterns on the surface of a bubble memory chip. Currently, the dynamic operation of the microscope, for real-time observation of domain switching, is close to completion and the results will be presented in the near future.

## References

[1] W. Clegg, N. Heyes, E. Hill, and C. Wright, "Development of a scanning laser microscope for magneto-optic studies of magnetic thin films," *J. Magn. Magn. Mater.*, vol. 95, no. 1, 1991.

[2] N. Heyes, C. Wright, W. Clegg, and J. Zhao, "A short-wavelength R-theta scanning laser microscope and optical disc tester for the characterization of optical-recording media," *IEEE Trans. Magn.*, vol. 31, no. Nov., 1995.

[3] R. C. Carey, D. F. L. Jenkins, D. M. Newmand, and B. W. J. Thomas, "Laser scanning at full objective aperture using 2-axis galvanometer meters," *Meas. Sci. Technol.*, vol. 4, 1993.

[4] C. Durkan, I. V. Shvets, and J. C. Lodder, "Observation of magnetic domains using a reflection-mode scanning near-field optical microscope," *Appl. Phys. Lett.*, vol. 70, no. 10, 1997.

**Warwick Clegg** (SM'94) studied physics at the University of Liverpool, Liverpool, U.K., in the mid-1960s and then went on to received the M.S. and Ph.D. degrees at the University of Manchester, Manchester, U.K., for work on magnetic data stores.

He is currently with the University of Plymouth, Plymouth, U.K., where his research includes instrumentation for optical and magnetic recording and micro-imaging using scanning laser and scanning probe techniques. Following on from his appointment as Research Professor, he is now Head of the Department of Communication and Electronic Engineering.

**David F. L. Jenkins** received the B.Sc. (physics), M.Sc. (lasers and their applications) and Ph.D. (photothermal deflection spectroscopy) degrees.

After receiving Ph.D. research at Royal Military College of Science, Shrivenham, U.K., he became a post-doctoral Research Fellow at Coventry University, U.K., in 1990, working on magnetophotoacoustic spectroscopy. Between 1993 and 1997, he worked in the Information Storage Group, Division of Electrical Engineering at University of Manchester, Manchester, U.K., researching into active vibration control of micro-mechanical structures. In 1997, he moved to University of Plymouth, Plymouth, U.K., to take up the position of Lecturer in the Centre for Research in Information Storage Technology, where he has continued his research into micro-actuators and microsensors. He has recently been appointed to the position of Senior Lecturer.

**Na Helian** received the B.Sc. degree in computer science from Hauzhong University of Science and Technology, Wugan, China, in 1987. She received the Ph.D. degree in magnetic recording in 1993 and then she joined Akita Research Institute of Advanced Technology, Akito, Japan, as a Post-Doctoral Fellow.

During 1996, she was with Data Storage Institute, National University of Singapore, Singapore. Now, she is Research Fellow of Center for Research in Information Storage Technology, University of Plymouth, Plymouth, U.K. She has been engaged in magnetic recording by both theoretical and experimental approach, especially in high-density magnetic recording. Recent works include media, heads, signal processing, servo systems for ultra-high magnetic recording and instrumentation for micro-image using scanning laser.

**James F. C. Windmill** (S'00) received the B.Eng. (Hons) degree in electronic engineerin in 1998 from the University of Plymouth, Plymouth, U.K. He is currently pursuing the Ph.D. degree in information storage and his research is comprised of different magnetic microscopy imaging techniques. This includes published work on a magneto-optic scanning laser microscope, a magnetic force microscope, and a novel new probe for the latter.

He is a Research Assistant at the Centre for Research in Information Storage Technology, University of Plymouth. As a final year degree student, he created a device which was featured in a paper of which he was co-author ("Remote-Controlled Computer Mouse for Physically Disabled Children," ICCHP 98 Conference, Austria). Based on this project, he was shortlisted for Best Electronic Engineering Student, in The 1998 Science, Engineering & Technology Student of the Year Awards, Great Britain.

**Nick Fry** received the M. Phil. degree based on an investigation into multitrack thin film tape heads from the University of Plymouth, Plymouth, U.K., in 1996.

He joined the University of Plymouth, Plymouth, U.K., in 1983 as a Research Technician where he has supported research into magnetic devices and materials, specializing in the microfabrication of thin-film magnetic sensors and the design and development of their electronic measurement systems. Since 1996, he has been employed as a Research Officer. In this position, he has been involved in several research areas that include magnetic recording, magneto-optics, and, most recently, giant magnetic impedance (GMI).

**Ron Atkinson** (SM'99) is Head of the School of Mathematics and Physics at The Queen's University of Belfast (QUB), Belfast, U.K. He is also a Fellow of the Institute of Physics and Honorary Visiting Professor in the Department of Physics at the University of Salford, Salford, U.K.

He took up a lectureship in the School of Maths and Physics at QUB in 1973 and is leader of the Thin Film Magneto-Optics and Magnetics Group and QUB-Director of the Northern Ireland Centre for Advanced Materials. He has 28 years experimental and theoretical experience in thin film optics, magneto-optics, and magnetics of multilayered nanostructures.

**William R. Hendren** received the degree in physics in 1990, followed by the M.Sc. and Ph.D. degrees in 1991 and 1995, respectively, from the Queen's University of Belfast (QUB), Belfast, U.K.

After two years as a Consultant and Field Engineer, he returned QUB to take up his current position as a Postdoctoral Research Fellow. His research interests include dynamic, *in situ*, optical, and magneto-optical studies, during the growth of thin films and multilayer structures and materials useful as magneto-optical recording media.

**C. David Wright** was born in Thornaby-on-Tees, U.K., in 1957. He received the B.S. degree in physics from Imperial College, London, U.K., the M.S. degree in solid state physics from the University of Sheffield, Sheffield, U.K., and, in 1984, the Ph.D. degree in the area of perpendicular magnetic recording from Manchester Polytechnic, Manchester, U.K.

He worked in the Information Storage Research Group at the University of Manchester between 1986 and 1999. He is currently Professor of electronic and computer engineering and Head of the Electronic Systems Research Group at the University of Exeter, Exeter, U.K. His research interests lie in the areas of optical, magneto-optic, and magnetic recording and scanning probe microscopy.

# Scanning Laser Techniques for Dynamic Thermo-Magnetic Recording Onto Stationary Media

Warwick Clegg, David Jenkins, Na Helian, James Windmill, Robert Windmill, Ron Atkinson*, Bill Hendren* and C David Wright**

Centre for Research in Information Storage Technology, University of Plymouth, Drake Circus, Plymouth PL4 8AA,UK.
*School of Mathematics and Physics, Queen's University Belfast, Belfast, UK.
**School of Engineering and Computer Science, Harrison Building, University of Exeter, UK.

## Abstract

*Scanning laser microscopes (SLM) have been used to characterise the magnetic properties of materials for some time [1,2]. A scanning laser microscope has been designed to facilitate a number of operating modes: both for writing and reading magneto-optical data. The current SLM is capable of thermo-magnetically recording bits onto magneto-optical thin films. Unlike previous SLMs, the current instrument has been designed to write bits both statically and dynamically onto stationary media. It will be used to write to magneto-optic (MO) disk material thermo-magnetically prior to imaging. Images may be derived from the longitudinal and polar magneto-optic Kerr effects, which are wavelength dependent, using the appropriate laser wavelength. In this paper the two configurations for dynamic recording are described.*

## 1. Introduction

The overall aim of the project is to develop a magneto-optical scanning laser microscope system that enables the recording and subsequent observation of magnetic behaviour for a variety of applications. Wherever possible the microscope system has been made modular. This enables the imaging system to be flexible and allows functions to be added or changed for different applications. This is also a consideration for future development and applications of the microscope, for example Confocal Imaging and also a Scanning Near-Field Magneto-Optic module.

The scanning laser microscope system is based around a central computer that uses National Instruments LabVIEW software as the user interface and development base. The system is now largely complete, and the imaging capabilities of the microscope have been demonstrated for both magneto-optical and pseudo-topographic imaging [3]. In this paper we will demonstrate the use of the SLM for dynamic and static recording of bits onto TbFeCo thin films.

## 2. System Design

The general system design layout is shown in Figure 1. The following sections describe the design and operation of the microscope's two recording modes. The optical system is schematically shown in Figure 2. The imaging system has been described previously [3], however the key features of the imaging system [4] are utilised for dynamic recording. The principle requirement of the optical system is to deliver a collimated beam to the final objective lens, under both static and dynamic operating conditions. By slightly overfilling the objective lens with a collimated beam we can optimise the spatial resolution of the

microscope. The principles governing thermo-magnetic recording are now described, for both static and then dynamic operation.

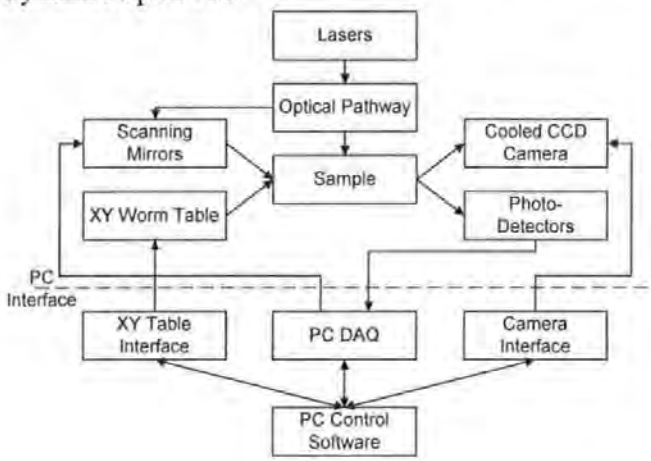


**Fig. 1 A block diagram of the system showing all the component parts making up the microscope.**

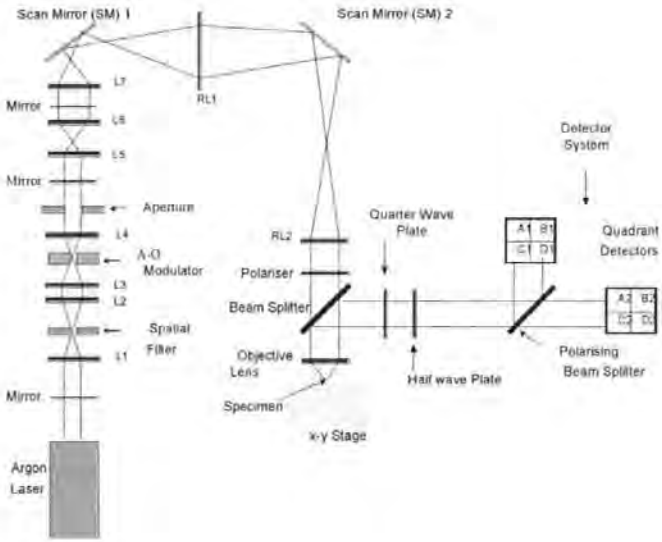


**Fig. 2 The optical pathway for the SLM system.**

**Static Thermo-Magnetic Recording:** This is the simplest recording arrangement using the SLM. The output beam is expanded, spatially filtered, then focused to a spot at the midpoint of the AO modulator (AOM). The rise time of the AOM is directly proportional to the spot size, with, for example, a 50 mm spot yielding rise time of 8 ns. The beam then passes via a series of beam transformation lenses and two relay lenses to produce a collimated beam that just over-fills the aperture of the objective lens, to produce a diffraction limited spot at the sample surface. The argon ion laser is operated in CW mode at 488 nm or 515 nm and the AOM set to deflect the laser beam out of the main optical path. In order to write a 'bit' the AOM is triggered and a pulse of light delivered to the sample surface. A piezoelectric focusing corrector, incorporated into the microscope for fine z-control of the objective lens, enables optimum delivery of the laser beam to the sample. To enable the localised reversal of the magnetisation state, a small coil is used to generate a bias field of around 50 Oe. However, depending on the induced temperature rise, it should also possible to switch the domains without the assistance of the bias field. Once the 'bit' has been written the sample is moved to the next point using the x-y stage

**Dynamic Thermo-Magnetic Recording:** For dynamic recording the arrangement is very similar to that used for static recording, although the implementation is considerably more difficult. The galvanometer mirrors are used in conjunction with AOM to simulate the recording process in a rotating disk drive. With the initial state being laser on and AOM deflecting beam out of path, the x-mirror only is triggered to scan at a speed equivalent to a rotating drive. The same trigger signal is delivered to the AOM, but in this case via a variable delay line, so that the AOM is triggered just as x-mirror approaches the near normal incidence condition. Thus, a focused spot is scanned over the sample surface, as in a normal magneto-optical drive. The beam spot size, on the sample surface, will vary slightly as the spot is scanned. The piezoelectric focusing facility will be developed to enable fast auto-focusing of the scanned spot, to maintain a constant spot size during scanning.

## 4. Results

The capability of the microscope to image magnetic domains has already been demonstrated. Figure 3 shows a static image of the perpendicular magnetic domain pattern on the surface of a bubble memory chip.

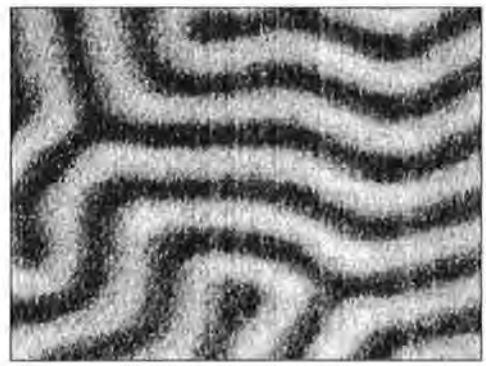

**Fig. 3 An image of perpendicular magnetic domain patterns on a bubble memory chip (40mm x 32mm).**

Magneto-optical films of TbFeCo and GdFeCo will be used to record bits thermo-magnetically, in both the static and dynamic configurations. These films have been characterised by their hysteresis loops as a function of temperature. This was over the temperature range 20° C to 280° C to determine the coercivity and compensation temperature (TC), which for these films is around 180° C. Figure 5 shows the hysteresis loops obtained during heating and the effect of increasing temperature on the coercive field. The microscope will be used to record bits both statically and dynamically on TbFeCo and GdFeCo thin films. The 'bits' recorded with both films will be presented and compared for both static and dynamical configurations.

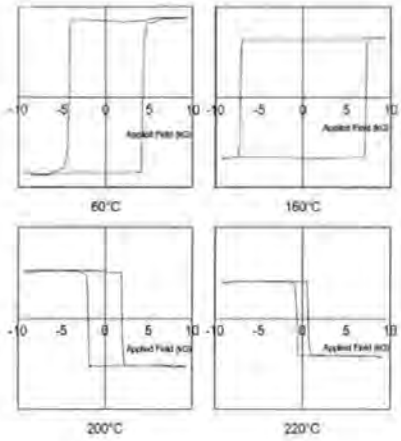


**Fig. 4. Magneto-optic Kerr effect loops of TbFeCo films at different temperatures, showing the effect on the coercivity with increasing temperature. All loops recorded during heating. The upper and lower loops are below and above TC respectively.**

## 5. Conclusions

A scanning laser microscope system has been designed for both the recording and observation of magnetic domains, under static or dynamic conditions. Operation of the microscope was initially confirmed by surface topography observations, using the reflectivity of the surface itself. Preliminary results have also shown that the system is capable of producing both static and pseudo-dynamic images [6]. TbFeCo and GdFeCo films have been grown on glass for investigating the recording capability of the SLM. Results will be presented for both films and the implications of dynamic recording and the limitations of static recording discussed.

## 6. References

[1] W Clegg, N Heyes, E Hill & C Wright. Development of a scanning laser microscope for magneto-optic studies of magnetic thin films. Journal of Magnetism and Magnetic Materials, Vol. 95, No. 1, 1991.

[2] N Heyes, C Wright, W Clegg & J Zhao. A Short-Wavelength R-Theta Scanning Laser Microscope and Optical Disc Tester for the Characterisation of Optical-Recording Media. IEEE Transactions on Magnetics, Vol.31, No. 6 Pt. 1, 1995.

[3] W W Clegg, D F L Jenkins, L He, J F C Windmill and N Fry. A scanning laser microscope system to observe static and dynamic magnetic domain behaviour. Presented at IMTC/2000, Baltimore, USA, May 2000. Submitted to IEEE Transactions on Instrumentation and Measurement.

[4] R C Carey, D F L Jenkins, D M Newman and & B W J Thomas. Laser Scanning at full objective aperture using 2-axis galvanometer meters. Measurement Science & Technology, Vol. 4, 1993.

[5] C Durkan, I V Shvets & J C Lodder. Observation of magnetic domains using a reflection-mode scanning near-field optical microscope. Applied Physics Letters, Vol. 70, No. 10, 1997.

[6] W W Clegg, L He, D F L Jenkins and J F C Windmill. Dynamic Thermo-Magnetic Recording Using A Magneto-Optic Scanning Laser Microscope. Presented at PELS-2000, Southampton, September 2000.